



INVESTIGATION OF ASPHALTENE AGGREGATION
WITH SYNTHETIC MODEL COMPOUNDS
AN EXPERIMENTAL AND COMPUTATIONAL STUDY

By

Dorin Simionesie, MSc

A thesis submitted to
The School of Chemical Engineering
The University of Birmingham

For the degree of
DOCTOR OF PHILOSOPHY

School of Chemical Engineering
The University of Birmingham

October 2017

UNIVERSITY OF
BIRMINGHAM

University of Birmingham Research Archive

e-theses repository

This unpublished thesis/dissertation is copyright of the author and/or third parties. The intellectual property rights of the author or third parties in respect of this work are as defined by The Copyright Designs and Patents Act 1988 or as modified by any successor legislation.

Any use made of information contained in this thesis/dissertation must be in accordance with that legislation and must be properly acknowledged. Further distribution or reproduction in any format is prohibited without the permission of the copyright holder.

Abstract

Aggregation and clustering of asphaltenes have attracted substantial research interest due to their significant impact on the crude oil industry. Despite extensive studies on the molecular structure of natural asphaltene, fundamental knowledge of their aggregation and clustering behaviour is incomplete. It is unclear how the driving forces of association are related to the molecular architecture and the solvent species, which ultimately affect the aggregation mechanism and intermolecular configurations.

In this dissertation, dynamic light scattering (DLS) experiments and molecular dynamics (MD) simulations were carried out to investigate the relation between asphaltene chemical structure and solvent species, to the characteristics of the aggregation mechanism.

The model compounds studied in the present work isolate the driving forces of aggregation by varying the peripheral chain-length and functional groups (triphenylene-cored models), and the planarity of the aromatic core (hexabenzocoronene-cored models), in organic solvents. We started by increasing the chain length around a triphenylene molecule to examine the aggregation potential in toluene and *n*-heptane. The molecular configuration of the aggregates appears to be subject to chemical structure, as the tail groups enforce planar and π -stacking configurations. Amide and carboxylic acid groups induce a degree of polarity to the model compounds that significantly increase the aggregation potential and lead to micron-sized cluster formations. Once clusters are formed, π -stacking appears to drive the molecules to more energetically

favourable arrangements, as dictated by the aromatic core of the molecules. The substitution of toluene with *n*-heptane, appears to increase aggregation potential, as well as facilitate tighter configurations within the aggregates.

Hexabenzocoronene-cored models exhibit structurally selective aggregation and precipitation mechanisms, as the planar molecules are more liable to aggregate and precipitate than the non-planar models due to π -stacking hindrance. The dispersibility of compound in toluene was found strongly dependent on the solid concentration and showed contrasting clustering behaviour. Solvent effects were limited on the non-planar model, while MD simulations show an increased sensitivity on the planar ones.

The motivation behind the development and testing of model polyaromatic compounds lies in the pursuit of isolating the source structural dependence of the compound interactions. This is done by assessing the solute-solute and solute-solvent associations by experimental (DLS) and computational (MD Simulations) approaches, to underpin the structure-function relation dictated by aromatic and/or polar molecules in aromatic or aliphatic solvents.

This dissertation provides insight for the aggregation of model compounds of varying molecular architectures, and sheds light on the intermolecular interactions affected by these variations as well as the solvent species.

Acknowledgements

With all honesty, I would like to take this opportunity to acknowledge the help and support I have received during the past four years.

First and foremost, my deepest gratitude goes to my supervisor Dr Zhenyu J. Zhang. You are a role model for me, both professionally and personally, and I will forever be grateful for all your support, and especially your patience. I always believed you would look good with whiter hair - so I tried my best.

Secondly, I would like to thank Prof. Jan Sefcik and Dr Paul Mulheran for instilling in me the principles of research, and building my confidence, which will be life-long assets for me. I would also like to thank Prof. Joe Wood for greatly broadening my view of science.

A special thanks to Prof. Jon Preece, Greg O'Callaghan, and the whole J.A.P. group for their great help and support both as collaborators as well as friends.

My grateful thanks are extended to the financial support from the EPSRC, and the School of Chemical Engineering, University of Birmingham, UK.

This Ph.D project would not be possible without the support of my loving family (Dorin, Irene and Leontina) and my partner (Silvia), who always believed in me. I hope that by achieving this goal I have been truthful to your faith, and that I am making you all proud.

Last but not least, I would like to thank my friends, both from home and from abroad, with which I have both laughed and cried, but overall thoroughly enjoyed the last 4 years of my life.

The best is yet to come,

Dorin Simionesie

Table of Contents

Abstract	I
Acknowledgements	III
Table of Contents	IV
List of Figures	XI
List of Tables	XX
List of Equations	XXI
List of Abbreviations	XXIII
Chapter 1. Introduction	1
1.1. Motivation	2
1.2. Aims and objectives of the project	4
1.3. Outline of each chapter	5
1.4. Literature review	7
1.4.1. Interactions of colloids	8
1.4.2. Driving forces for asphaltene aggregation	12
1.4.2.1. Van der Waals interactions	12
1.4.2.2. Electrostatic interactions	14
1.4.2.3. Polar interactions	17
1.5. Interactions between natural asphaltenes	17
1.6. Model asphaltene compounds	21
1.7. Summary	29

Chapter 2. Methodology	31
2.1. Dynamic light scattering	32
2.1.1. Theory	32
2.1.3. Literature review of light scattering studies of aggregation	40
2.2. Nuclear magnetic resonance spectroscopy	45
2.2.1. Theory	45
2.2.2. Instrument, experimental and data analysis	49
2.2.3. Literature review of NMR spectroscopy of asphaltenes	51
2.3. Molecular dynamics simulations	54
2.3.1. Theory	54
2.3.2. Model compound molecular structures	63
2.3.3. Practical steps	65
2.3.4. Data Analysis	68
2.3.5. Literature review of molecular dynamics simulations	70
Chapter 3. Intermolecular interaction of triphenylene-cored model compounds in toluene	75
3.1. Introduction	76
3.2. Materials and methodology	80
3.2.1. Materials	80
3.2.2. Methodology	81
3.2.2.1. Dynamic light scattering	81

3.2.2.2. Molecular dynamics simulations	82
3.3. Results	84
3.3.1. Dynamic light scattering of model chemical compounds	84
3.3.1.1. Representative DLS sample set	84
3.3.1.2. Effect of concentration on aggregation in toluene	86
3.3.1.3. Aggregation of model compounds by dynamic light scattering	89
3.3.1.3.1. Effect of chain length on intermolecular interactions in toluene	90
3.3.1.3.2. Effect of functional groups on the intermolecular interactions	92
3.3.1. Molecular dynamics simulations of model compounds	94
3.3.1.1. Radial distribution functions of model compounds solvated by toluene	94
3.3.1.2. Intermolecular distances measured by g_{dist}	98
3.4. Discussion	105
3.4.1. Effect of concentration on aggregation in toluene	105
3.4.2. Effect of chain length on intermolecular interactions in toluene	107
3.4.3. Effect of functional groups on intermolecular interactions in toluene	114
3.5. Conclusions	117

Chapter 4. Effect of <i>n</i> -heptane on the intermolecular interaction between model compounds	120
4.1 Introduction	121
4.2. Materials and methodology	125
4.2.1. Materials	125
4.2.2. Methodology	125
4.2.2.1. Dynamic light scattering	125
4.2.2.2. Molecular dynamics simulations	126
4.3. Results	128
4.3.1. Dynamic light scattering of model compounds	128
4.3.1.1. Effect of chain length on intermolecular interactions in heptol	128
4.3.1.2. Effect of functional groups on intermolecular interactions in heptol	130
4.3.2. Molecular dynamics simulations of model compounds	132
4.3.2.1. Solvent affinity of single molecule model compounds	132
4.3.2.2. Radial distribution functions of model compounds solvated by heptol and <i>n</i> -heptane	137
4.3.2.3. Intermolecular distances measured by <i>g</i> _{dist}	141
4.4. Discussion	148
4.4.1. Effect of chain length on intermolecular interactions in mixed solvent	150

4.4.2. Effect of functional groups on intermolecular interactions in mixed solvent	155
4.5. Conclusions	157
Chapter 5. Effect of planar surface on intermolecular interactions between aromatic model compounds	159
5.1. Introduction	160
5.2. Materials and Methodology	163
5.2.1. Materials	163
5.2.2. Methodology	163
5.2.2.1. Dynamic light scattering	163
5.2.2.2. Chemical analysis of synthesised product	164
5.2.2.3. Molecular dynamics simulations	166
5.3. Results	167
5.3.1. Kinetic, concentration, and solvent effects measured by DLS	168
5.3.1.1. Scattering intensity as a function of concentration	168
5.3.1.2. Kinetics of hydrodynamic size	172
5.3.2. Chemical composition analysis	173
5.3.3. Molecular dynamics simulations	177
5.3.3.1. Radial distribution functions of solute-solvent interactions	177
5.3.3.2. Radial distribution functions of solute-solute interactions	179
5.4. Discussion	183

5.4.1. Clustering of HTBHBC model compound in toluene	183
5.4.1.1. Intermolecular interactions at low concentration	183
5.4.1.2. Intermolecular interaction at high concentration	185
5.4.1.3. Chemical analysis of liquid and solid phases	186
5.4.1.4. Intermolecular interactions in toluene	188
5.4.2. Effect of <i>n</i> -heptane addition	190
5.4.2.1. Light scattering measurements as percentage of <i>n</i> -heptane	191
5.4.2.2. Molecular dynamics simulations in <i>n</i> -heptane	192
5.4.2.3. Intermolecular interactions in <i>n</i> -heptane	194
5.5. Conclusions	195
Chapter 6. Conclusions and future perspectives	197
6.1. Summary	199
6.1.1. Effect of alkoxy group and chain length	199
6.1.2. Effect of amide and carboxylic acid group	201
6.1.3. Effect of planarity on π -stacking	203
6.2. Future perspectives	204
6.2.1. Model compound development	205
6.2.2. Experimental and computational technique development	205
6.2.3. Operational envelope development	206
Chapter 7. References	207
Chapter 8. Appendices	234

8.1. Molecular dynamics simulations additional information	235
8.1.1. Command lines for simulations and data analysis	235
8.1.2. Software operation instructions	238
8.2. Triphenylene-cored model compounds synthesis and quality analysis	239
8.2.1. Synthesis of alkoxy group model compounds	240
8.2.2. Synthesis of functional group model compounds	244
8.3. DOSY NMR spectroscopy of triphenylene-cored model compounds in toluene	246
8.4. HTBHBC one pot synthesis	247

List of Figures

Figure 1.1. Asphaltenes clogging a pipe. Courtesy of A. Pomerantz, Schlumberger [20].	3
Figure 1.2. Models of asphaltene molecular types: (a) “continental” type, and (b) “archipelago” type.....	7
Figure 1.3. Light scattering study of natural asphaltenes aggregation number (N) as a function of time scale τ^* [38]. Flocculation data for <i>n</i> -heptane addition to different asphaltene-toluene solutions. Orange circles represent data for 10 mg/mL asphaltene-toluene solution exhibiting reaction-limited aggregation. Blue squares represent data for 1 mg/mL asphaltene-toluene solution exhibiting diffusion-limited aggregation. Red circles represent data for 5 mg/mL asphaltene-toluene solution exhibiting crossover aggregation kinetics.	9
Figure 1.4. Variation of distance between a dimer formation, for selected solvents [64].	16
Figure 1.5. Scanning tunnelling microscopy images of asphaltene molecular structures.....	21
Figure 1.6. Pyrene-cored model compound proposed for archipelago architecture in asphaltene self-association studies with multiple functional groups (R).	21
Figure 1.7. Hexabenzocoronene-cored model compound proposed for representing continental architecture in asphaltene self-association study with multiple chain lengths (R).	22
Figure 1.8. Representative model compound proposed for continental architecture of asphaltenes with seven aromatic rings and interchangeable heteroatoms (R).	24

Figure 1.9. Violanthrone-78-cored model compound proposed for representing continental architecture of asphaltenes with nine aromatic rings and multiple chain lengths and interchangeable functional groups (R).	25
Figure 1.10. Perylene-cored model compound proposed for representing continental architecture of asphaltenes with seven aromatic rings and interchangeable chain lengths and functional groups (R).	26
Figure 2.1. Schematic diagram of light scattering set-up, measuring the particle sizes of colloidal particles in a suspension and by collecting the scattered light with the photon detector.....	35
Figure 2.2. Example of recorded intensity fluctuations of scattered light over time, for large (red line) and small (black line) particles.	37
Figure 2.3. Example of recorded correlograms for a sample containing particles for which the correlation signal decays earlier for small particles (black line) and later for large ones (red lines).....	38
Figure 2.4. (a) Depiction of signal formation when the magnetic field is applied to the compound. As the nuclei shift between states, the energy difference is recorded as a resonance signal on a spectrum. (b) Schematic diagram of an NMR spectrometer as the magnetic field is applied perpendicular to the axis of the sample tube [165].	46
Figure 2.5. Representation of the positions of chemical shifts in a ¹ H NMR spectrum across the entire chemical shift range [166].	48
Figure 2.6. ¹ H NMR spectra of the HTBHBC 20 mg/mL in deuterated toluene at 168 hours. Spectrum (a) was obtained from the solid deposit and spectrum (b) from the supernatant.	50

Figure 2.7. Schematic representation with periodic boundaries in two dimensions of molecules in a GROMACS MD simulation.....	58
Figure 2.8. Graphical representation of radial distribution functions. The function is applied between the one molecule (black) and a group of molecules (red dots).	60
Figure 2.9. Radial distribution function examples of a parallel and multiple configuration aggregate, over 100 ns simulation time, in organic solvent.....	60
Figure 2.10. g_dist example of (a) a non-aggregating and (b) an aggregating simulation, over 100 ns simulation time in organic solvent. R1 is the molecule with witch all the other intermolecular pairs/distances are recorded.	62
Figure 2.11. VMD snapshot of (a) a single model compound and (b) seven model compounds in a GROMACS generated simulation box prior to solvation.....	66
Figure 2.12. VMD snapshot of a solvated GROMACS simulation box containing seven model compound molecules and 700 toluene molecules.	66
Figure 3.1. Model compound replicating the π -stacking of continental asphaltenes.	78
Figure 3.2. Autocorrelation functions of TPN-C1 model compounds suspended in toluene at a scattering angle of 175°	84
Figure 3.3. Autocorrelation function fitting by Malvern automated software of TPN-C1 model compound suspended in toluene.	85
Figure 3.4. Distribution by (a) intensity and by (b) volume, of the hydrodynamic diameters of TPN-C1-toluene mixture.	85
Figure 3.5. Averaged hydrodynamic diameters of sample TPN-C3 in toluene presented as a function of time at three different concentrations (1, 10 and 20	

mg/mL). Error bars were similar in magnitude to the dimensions of the symbols used in the graph.....	87
Figure 3.6. Averaged hydrodynamic diameters as a function of time for TPN-C10 suspended in toluene at three different concentrations (1, 10 and 20 mg/mL). Error bars were similar in magnitude to the dimensions of the symbols used in the graph.	89
Figure 3.7. Averaged hydrodynamic diameters as a function of time for TPN-C0, TPN-C1, TPN-C3, TPN-C5 and TPN-C10 at 10 mg/mL.....	92
Figure 3.8. Averaged hydrodynamic diameters as a function of time for TPN-C0, TPN-CN, and TPN-CNAcid at 10 mg/mL.....	93
Figure 3.9. Normalised radial distribution functions for TPN-C0, TPN-C1, TPN-C3, TPN-C5, and TPN-C10 model compounds placed in a toluene simulation box over 100 ns.....	95
Figure 3.10. Normalised radial distribution functions for TPN-C0, TPN-CN and TPN-CNAcid model compounds, suspended in toluene, over 100 ns simulation time.....	97
Figure 3.11. Distance between the centres of mass of one model compound molecule with the other six in the simulation over 100 ns simulation time in toluene: (a) TPN-C0; (b) TPN-C1; (c) TPN-C3. The six colours shown in each figure correspond to the distance between each pair of molecules.	99
Figure 3.12. Distance between the centres of mass of one model compound molecule with the other six over 100 ns simulation time in toluene: (a) TPN-C5; (b) TPN-C10. The six colours shown in each figure correspond to the distance between each pair of molecules.	100

Figure 3.13. Distance between the centres of mass of one model compound molecule with the other six in the simulation during the 100 ns simulation in toluene: (a) TPN-C0; (b) TPN-CN; TPN-CNAcid. The six colours shown in each figure correspond to the distance between each pair of molecules.	103
Figure 3.14. Snapshots of MD simulations of seven (a) TPN-C0; (b) TPN-C5; (c) TPN-CNAcid in toluene, showing the interactions between the molecules after 100 ns of simulation time. The toluene molecules are not shown for clarity.	105
Figure 3.15. Averaged hydrodynamic diameters for the model compounds at 10 mg/mL.	108
Figure 3.16. Normalised radial distribution function of seven molecules of TPN-C1, TPN-C3, TPN-C5, TPN-C10, TPN-CN and TPN-CNAcid model compounds, solvated by 700 toluene molecules, over 100 ns simulation time.	109
Figure 4.1. Averaged hydrodynamic diameters as a function of time for TPN-C0, TPN-C1, TPN-C3, TPN-C5 and TPN-C10 at 10 mg/mL,, all suspended in heptol (40% toluene, 60% <i>n</i> -heptane).	129
Figure 4.2. Averaged hydrodynamic diameters as a function of time for TPN-C0, TPN-C1, TPN-C3, TPN-C5 and TPN-C10 at 10 mg/mL, all suspended in heptol (40% toluene, 60% <i>n</i> -heptane).	131
Figure 4.3. Radial distribution functions of TPN-C0, TPN-C1, TPN-C3, TPN-C5 and TPN-C10 model compounds versus solvent, suspended in a heptol simulation box, over 20 ns simulation time.	135
Figure 4.4. Radial distribution functions of TPN-C0, TPN-CN and TPN-CNAcid model compound versus solvent, suspended in a heptol simulation box, over 20 ns simulation time.	136

Figure 4.5. Normalised radial distribution functions for TPN-C0, TPN-C1, TPN-C3, TPN-C5 and TPN-C10 model compounds, placed in (a) heptol and (b) <i>n</i> -heptane simulation box, over 100 ns simulation time.	139
Figure 4.6. Normalised radial distribution functions for TPN-C0, TPN-CN and TPN-CNacid model compounds, placed in (a) a heptol and (b) <i>n</i> -heptane simulation box, over 100 ns simulation time.	140
Figure 4.7. Distance between the centres of mass of one model compound with the other six over 100 ns simulation time: (a) TPN-C0; (b) TPN-C1; (c) TPN-C3 in heptol and (d) TPN-C0; (e) TPN-C1; (f) TPN-C3 in <i>n</i> -heptane. The six colours shown in each figure correspond to the distance between each pair of molecules.	142
Figure 4.8. Distance between the centres of mass of one model compound molecule with the other six over 100 ns simulation time: (a) TPN-C5; (b) TPN-C10 in heptol and (c) TPN-C5; (d) TPN-C10 <i>n</i> -heptane. The six colours shown in each figure correspond to the distance between each pair of molecules.	144
Figure 4.9. Distance between the centres of mass of one model compound molecule with the other six over 100 ns simulation time: (a) TPN-C0; (b) TPN-CN; (c) TPN-CNacid in heptol and (d) TPN-C0; (e) TPN-CN; (f) TPN-CNacid in <i>n</i> -heptane. The six colours shown in each figure correspond to the distance between each pair of molecules.	145
Figure 4.10. Snapshot of MD simulation of seven (a) TPN-C0; (b) TPN-C5; (c) TPN-CNacid model compounds in heptol, and (d) TPN-C0; (e) TPN-C5; (f) TPN-CNacid model compounds in <i>n</i> -heptane, showing the interactions between the	

molecules after 100 ns of simulation time. The solvent molecules are not shown for clarity.....	148
Figure 4.12. Averaged hydrodynamic diameters as a function model compound at 10 mg/mL, all suspended in 40% toluene, 60% <i>n</i> -heptane - heptol.....	149
Figure 4.13. Normalised radial distribution function of seven molecules of TPN-C1, TPN-C3, TPN-C5, TPN-C10, TPN-CN and TPN-CNAcid model compounds, solvated by (a) 350 toluene molecules and 350 <i>n</i> -heptane molecules (heptol), and (b) 700 <i>n</i> -heptane molecules, over 100 ns simulation time.	149
Figure 5.1. Molecular structure of HTBHBC, C ₆₆ H ₆₆ ; Mw = 858.6 g/mol as obtained by the one-pot synthesis established by Rathore and Burns [298].	165
Figure 5.2. Derivative HTBHBC molecule (3D) as hypothesised from the ¹ H NMR spectroscopy and the MALDI-TOF spectroscopy. The excessive amount of <i>tert</i> -butyl leads to an over-reaction that does not allow the carbon bonds to form appropriately. Instead, <i>tert</i> -butyl tails bond to those free positions.	166
Figure 5.3. Normalised scattering intensity of HTBHBC in toluene as a function of time for low concentrations (1-5 mg/mL).....	168
Figure 5.4. Mean normalised scattering intensity of HTBHBC in toluene as a function of time for high concentrations (10–50 mg/mL).....	169
Figure 5.5. Mean normalised scattering intensity acquired at 168 hours as a function of initial concentration. The relation is linear in the low concentration regime but becomes sub-linear as concentration increases.....	170
Figure 5.6. Mean normalised scattering intensity of HTBHBC in toluene after 168 hours, with the addition of <i>n</i> -heptane (80, 60, 40, 20% of toluene volume) as a function of initial concentration.	171

Figure 5.7. Mean hydrodynamic radius of HTBHBC in toluene as a function of time, at high concentrations (10–50 mg/mL).	173
Figure 5.8. ¹ H NMR spectra of the HTBHBC 20 mg/mL in deuterated toluene at 168 hours. Spectrum (a) was obtained from the solid deposit and spectrum (b) from the supernatant.	174
Figure 5.9. MALDI TOF spectra of the HTBHBC (m/z = 858.6) and derivatives: (a) shows the spectrum of precipitate with the major peak belonging to the pure HTBHBC compound; (b) the supernatant shows a variety of peaks that indicate the existence of multiple derivative.....	175
Figure 5.10. Shift in relative integral of peaks at 10.86 ppm and 10.46 ppm, over time as a function of sample purity. Sample set 1 not was not re-suspended while sample set 2, 3 and 4 were re-suspended and measured at 24, 168 and 366 hours, respectively. All samples were kept at room temperature for the entire time interval	176
Figure 5.11. Radial distribution functions of a single HTBHBC and DevHTBHBC model compound versus (a) toluene and (b) <i>n</i> -heptane in simulation boxes of 350 toluene and 350 <i>n</i> -heptane molecules, over 20 ns simulation time.	178
Figure 5.12. Normalised radial distribution functions of HTBHBC and DevHTBHBC model compounds in (a) toluene, (b) heptol, and (c) <i>n</i> -heptane over 10 ns simulation time.....	180
Figure 5.13. Snapshots of MD simulations of seven (a) HTBHBC and (b) DevHTBHBC molecules in toluene, and (c) HTBHBC and (d) DevHTBHBC molecules in <i>n</i> -heptane after 100 ns of simulation time. The solvent molecules are not shown for clarity.....	182

Figure A.1. Depiction of the reaction synthesis into 6a (70%), 6b (30%) and 6c (56% yield).....	241
Figure B.2. Depiction of the reaction synthesis of 3,6,7,10,11-pentapropoxytriphenylen-2-ol (7).....	242
Figure B.3. Depiction of the reaction synthesis of 3,6,7,10,11-pentapropoxytriphenylen-2-ol (7) into 2-(decyloxy)-3,6,7,10,11-pentapropoxytriphenylene (8).....	242
Figure B.4. Depiction of the reaction synthesis of N-octyltriphenylene-2-carboxamide (2).....	244
Figure B.5. Depiction of the reaction synthesis of N-(8-hydroxyoctyl)triphenylene-2-carboxamide (3)	245
Figure B.6. Depiction of the reaction synthesis of 8-(triphenylene-2-carboxamido)octanoic acid (4).....	246
Figure D.7. Depiction of the reaction synthesis of the HPB (raw material) with <i>t</i> -BuCl and FeCl ₃ to obtain the HTBHBC molecule.	248

List of Tables

Table 2.1 Model compound molecular structures along with their chemical details	64
Table 3.1. Triphenylene based chemical compounds.....	81

List of Equations

(1.1)	$V_t = V_a + V_r + V_s$	11
(1.2)	$E = \lambda_{i,j}/H^6$	12
(1.3)	$F = \frac{1}{4\pi\epsilon_0} \times \frac{qQ}{R^2}$	14
(1.4)	$\nabla^2\phi = -\frac{\rho}{\epsilon_0}$	15
(2.1)	$E = hv$	32
(2.2)	$\omega = \pm cq$	33
(2.3)	$q = \frac{4\pi n}{\lambda} \sin(\frac{\theta}{2})$	33
(2.4)	$g_2(\tau) = (e^{-2Dq\tau})$	33
(2.5)	$d_H = \frac{kT}{3\pi\eta D}$	33
(2.6)	$I \propto d^6$	35
(2.7)	$I \propto \frac{1}{\lambda^4}$	35
(2.8)	$\Delta E = \frac{h}{v}$	46
(2.9)	$m_i \frac{\partial^2 r_i}{\partial t^2} = F_i, = 1 \dots N$	56

$$(2.10) \quad F_i = -\frac{\partial v}{\partial r_i} \dots\dots\dots 56$$

$$(2.11) \quad g_{AB} = \frac{\langle \rho_B(r) \rangle}{\langle \rho_B \rangle_{local}} = \frac{1}{\langle \rho_B \rangle_{local}} \frac{1}{N_A} \sum_{i \in A} \sum_{j \in B} \frac{\delta(r_{ij} - r)}{4\pi r^2} \dots\dots\dots 59$$

List of Abbreviations/Symbols

^{13}C	Carbon isotope
^1H	Proton
ACF	Autocorrelation function
AFM	Atomic force microscopy
BlueBEAR	Birmingham environment for academic research
CCC	Critical clustering concentration
CDCl_3	Deuterated chloroform
CMC	Critical micelle concentration
CNAC	Critical nano-aggregate concentration
COM	Centre of mass
COSY	Correlation spectroscopy
D	Translational diffusion coefficient
d	Particle diameter
d_8 -toluene	Deuterated toluene
DevHTBHBC	Hypothesised dominant derivative of HTBHBC
d_H	Hydrodynamic diameter
DLS	Dynamic light scattering
DMSO	Dimethyl sulfoxide
DOSY	Diffusion-ordered spectroscopy
E	Energy of a photon
EIMS	Electron Impact Ionisation Mass Spectrometry
EM	Electromagnetic radiation
EM	Energy minimisation
ES ⁺ MS	Electrospray Mass Spectrometry
F	Total electrostatic force
G(r)	Pair correlation function
GROMACS	Groningen machine for chemical simulations
h	Planck's constant
HMBC	Heteronuclear multiple bond correlation
HSQC	Heteronuclear single quantum coherence
HTBHBC	Hexa- <i>tert</i> -butylhexa- <i>peri</i> -hexabenzocoronene
I	Intensity of scattered light
k	Boltzmann's constant
m	Mass of any atom
MALDI-TOF	Time of flight - matrix assisted laser desorption/ionisation
MD	Molecular dynamics
MS	Mass spectroscopy
n	Refractive index of solvent

N	Number of interacting atoms in the simulation
NMR	Nuclear magnetic resonance
NPT	Number of particles, system pressure and temperature
NVT	Number of particles, system volume and temperature
OPLS-AA	Optimised potential for liquid simulations / all atoms
PAC	Polyaromatic compound
PFGE-SE	Pulsed field gradient spin echo
q	Velocity
q	Propagation vector of density fluctuations
Q	Source charge
r	Position of all atoms in the simulation box
RDF	Radial distribution function
r_{\max}	Maximum possible distance around a particle
SDS	Sodium dodecyl sulfate
SEM	Scanning Electron Microscopy
T	Absolute temperature
TMS	Tetramethylsilane
TPN-C0	$C_{18}H_{12}$
TPN-C1	$C_{24}H_{24}O_6$
TPN-C10	$C_{43}H_{62}O_6$
TPN-C3	$C_{36}H_{48}O_6$
TPN-C5	$C_{48}H_{72}O_6$
TPN-CN	$C_{27}H_{29}NO$
TPN-CNAcid	$C_{27}H_{27}NO_3$
VMD	Visual molecular dynamics
ϵ	Vacuum permittivity
∇	Divergence operator
ϕ	Potential
δ	Chemical shift values
η	Viscosity of the solvent
θ	Scattering angle
λ	Wavelength of light in the medium
v	Speed of light
π	Pi (3.14)
$\rho_B(r)$	Density of type B particles around A
$\rho_{B\text{local}}$	Average density of all particles B
τ	Time decay of the normalised ACF
ω	Frequency shift

Chapter 1. Introduction

Chapter 1

1.1. Motivation

Humankind still has to rely on conventional energy sources for the foreseeable future until sustainable energy sources could take over the role. However, the increase in fuel demand and the diminishing supply of light crude oils force the industry to develop new processes to enhance the production, transport, and refining of heavy crude oils. This is made difficult by the intrinsic properties of the raw crude oil [1]. In the downstream industry, the high viscosity and the potential to foul surfaces make extraction and handling of heavy oils difficult and expensive tasks [2,3]. In the upstream sector, heavy oils are responsible for wettability alterations of mineral surfaces in reservoir formations, as well as their potential to stabilise oil-water emulsions [4,5]. Due to deposition in porous media during extraction steps, severe plugging problems could occur [6]. Furthermore, the increase in size of gas hydrate particles in oil production pipelines could shift the rheological properties which lead to blockage of the lines [7].

One of the major sources of these problems comes from the lack of understanding of one of the heaviest components of crude oil - asphaltenes. They are defined as a solubility class of molecules (soluble in aromatic solvents but insoluble in *n*-alkanes), but are not yet chemically understood [8]. They consist of a core of aromatic rings with various proportions of aliphatic tails, and are speckled with heteroatoms (S, N, O, metals and multiple species of acid functional groups) [9]. The proposed average molecular weight is 750 Da [10-14], and they are regarded as highly polar molecules [3]. Asphaltenes are known to initially form stable nanoaggregates that grow into clusters of various sizes. Due to their strong

Chapter 1

potential to aggregate and precipitate, triggered by various environmental factors, such as solvent quality, concentration, temperature, and pressure, they contribute significantly to the problems faced by the oil industry [2,15]. It is therefore of great industrial and academic interest to investigate the structural and environmental factors that directly influence the aggregation mechanism of asphaltenes.

The lack of understanding of the asphaltene structure-dictates-function relation has motivated the development of synthetic or model compounds to isolate and replicate key structural characteristics of asphaltene behaviour [16-19]. Using model asphaltenes, the links could be established between structural features of the molecules and their aggregation and precipitation, as well as the effect of environmental factors. Once mastered, the operational conditions could be controlled, or additional chemical compounds added, that would prevent the issues causing heavy oil to be so problematic and expensive to work with on an industrial scale.



Figure 1.1. Asphaltenes clogging a pipe. Courtesy of A. Pomerantz, Schlumberger [20].

1.2. Aims and objectives of the project

The complexity and inconsistency of the molecular characteristics make asphaltenes difficult to study due to the intricacies of the structure-function relation. The asphaltene aggregation is driven by van der Waals and electrostatic interactions, and degree of electronegativity, which are heavily dependent on the chemical structure of the molecules, and more specifically the solute-solute and solute-solvent interactions. To further understand the structural and solvent dependence of the asphaltene aggregation mechanism, several model compounds were developed following the “continental” architecture [21]. Seven triphenylene-cored model compounds, with increasing degree of chemical complexity, were synthesised along with a single hexabenzocoronene-cored model compound. The latter is meant to help understand the interaction kinetics of planar and non-planar molecules by forcing an aggregation and sedimentation process, while the former set focuses on the effect of peripheral chain-length, amide or acid functional groups have on the intermolecular interactions.

The system was approached from multiple length scales, as dynamic light scattering was employed to measure the hydrodynamic sizes of the potential aggregates over time (nano-to-micro size range) and molecular dynamics simulations were employed to observe and quantify intermolecular interactions and aggregate configurations. Three NMR spectroscopy methods were applied, including the standard ^1H NMR spectroscopy, to establish the purity of the synthesised compounds, a modified assay method to assess the structurally dependent phase separation of the hexabenzocoronene compound, and diffusion-ordered spectroscopy (DOSY) to support nanoaggregate formation of the

Chapter 1

triphenylene-cored model compounds. The experimental and computational approach of this project is to understand the structure-function relation of key asphaltene characteristics by investigating the aggregation kinetics of these model compounds.

1.3. Outline of each chapter

Chapter 1 (Introduction) of this thesis introduces the main topic and the supporting theory relevant to the study of the aggregation mechanism, such as the attraction and repulsion forces that govern asphaltene interactions. The structure-function relation was emphasised with key model asphaltene chemical features highlighted.

Chapter 2 (Methodology) covers both the theory of the techniques employed in this work, as well as the previous studies of asphaltene where similar techniques were used. Dynamic light scattering (DLS), ^1H NMR spectroscopy, and Molecular dynamics (MD) simulations are the main techniques discussed. Details and characteristics regarding the developed model compounds are also included.

Chapter 3 (Intermolecular interactions of triphenylene-cored model compounds in toluene) and Chapter 4 (Effect of *n*-heptane on the intermolecular interaction between model compounds) investigate the aggregation behaviour of the triphenylene-cored model compounds as a function of structure, solvent, and time. Chapter 3 examined the structure-function relation of the triphenylene cored model compounds in an aromatic solvent (toluene), and established the kinetics and stability of the molecules in toluene. Chapter 4 emphasised the interplay of the solute-solvent relation, as *n*-heptane was introduced in both experimental and

Chapter 1

computational approaches. Additional focus was given to quantify the affinity of each model compound towards solvents, through a novel MD technique. Both chapters are structured as journal articles, each containing a brief literature review, materials and methods, results, discussion, and conclusion, as their publication is soon to follow. Furthermore, DOSY results deriving from a collaboration are mentioned, that complement and support the conclusions of both chapters.

Chapter 5 (Effect of planar surface on intermolecular interactions between aromatic model compounds) focuses on a hexabenzocoronene-cored model compound. The work is to be submitted for peer review under the name “Clustering behaviour of polyaromatic compounds mimicking natural asphaltenes”. The chapter focuses on the synergy between chemical structure and clustering in both toluene and *n*-heptane with the use of DLS, a modified ¹H NMR spectroscopy technique and MD simulations.

Chapter 6 (Conclusions and future work) brings together the conclusions of this thesis in a differently structured view from the individual chapters, to allow the reader a different perspective of the scope and outcome of the results, as they are presented model by model. Future work was also included, with suggestions for the continuation of the project and its applicability to the crude oil industry. Additional information regarding the computational protocol, synthesis and quality analysis of the products can be found in Appendices, while Chapter 7 (References) contains the literature references cited throughout the thesis.

1.4. Literature review

In 1967, a model was proposed to take into consideration the different chemical moieties in asphaltenes, such as polycyclic aromatic hydrocarbons and their stacks, *n*-alkanes, and even petroporphyrins [22]. This model suggests that the behaviour of asphaltenes in organic solvents is similar to that of polar surfactants in aqueous solution, and hence, asphaltenes could be treated and investigated as colloidal particles with a complex structure-function relation [23-29]. With development of more advanced techniques, petrochemical research has advanced to the point where methodologies from fields such as soft matter physics can be employed to investigate and interpret the complex behaviour exhibited by organic systems, such as asphaltenes in crude oil.

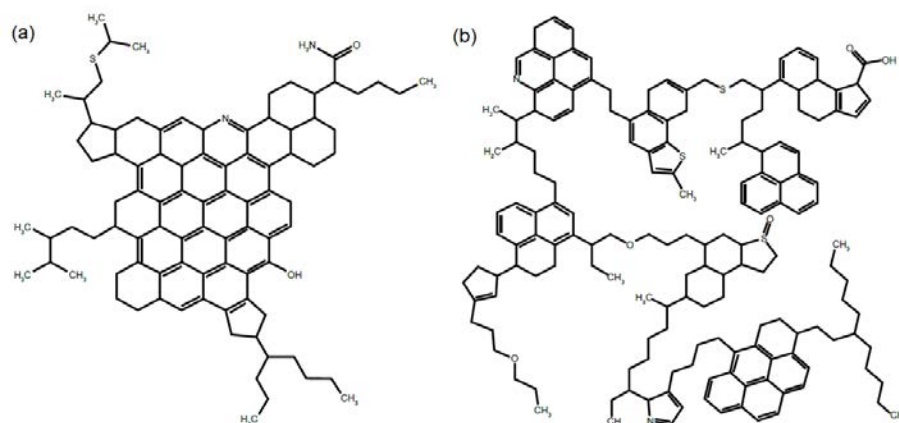


Figure 1.2. Models of asphaltene molecular types: (a) “continental” type, and (b) “archipelago” type.

Despite their initial comparison to polar surfactants, due to their highly polar nature [23], recent investigations confirm that the asphaltene molecular structure is dominated by “continental” architecture rather than “archipelago” (Figure 1.2). This suggests that the majority of asphaltene molecules behave more like liquid crystals, due to their large aromatic surfaces, which could possibly drive both the

Chapter 1

aggregation mechanism, as well as molecular configurations. Some attempts have been made to identify the synergy between experimental results and computational approaches to better understand and identify the driving forces of asphaltene interactions [16,18,19]. Building on current knowledge, this thesis aims to investigate the link between the colloidal and aggregation behaviour measured by dynamic light scattering, and the intermolecular interactions observed by molecular dynamics simulations, in a synergistic approach that focuses on the solute-to-solute interactions as a function of chemical structure and solvent species. However, a basic understanding of the forces and dynamics of the systems involved is required. Since the model compounds developed in this study have chemical structures similar to molecules from other fields such as liquid crystals, and the driving forces of attraction and repulsion are mainly van der Waals, polar, and electrostatic, we consider asphaltenes in organic solvents to be a colloidal system [10].

1.4.1. Interactions of colloids

A colloidal system can be described as a microscopically heterogeneous system, where one component has dimensions in between those of molecules and those of macroscopic particles (in the range of 1 nm to 1 μ m) [30]. Colloidal particles in dispersion are in constant Brownian motion, due to the interplay between the kinetic energy associated with this motion and their stability in the surrounding fluid medium [30,31]. If the collision energy of particles is of the order of a kT , they will be able to overcome the typical repulsive barrier that leads to the stability of charged colloids. The self-assembly that can result allows the molecules to have broad structural diversity as dictated by configurational entropy

[32,33]. A variety of techniques are commonly employed to study colloidal suspensions including dynamic light scattering [33], laser scanning confocal microscopy [34], small angle X-ray scattering [35], and small angle neutron scattering [36]. Aggregation of colloidal particles is governed by the entropic excluded volume interaction, the long-range electrostatic interactions, and short-range van der Waals, as well as the external electromagnetic and gravitational fields [37]. The study of colloids as model atoms/molecules helps to understand complex intermolecular phenomena, such as aggregation, and precipitation. This work focuses primarily on unravelling the aggregation mechanism of asphaltenes as polyaromatic hydrocarbons, and on the structural and environmental factors that de-stabilise the molecules from their colloidal state.

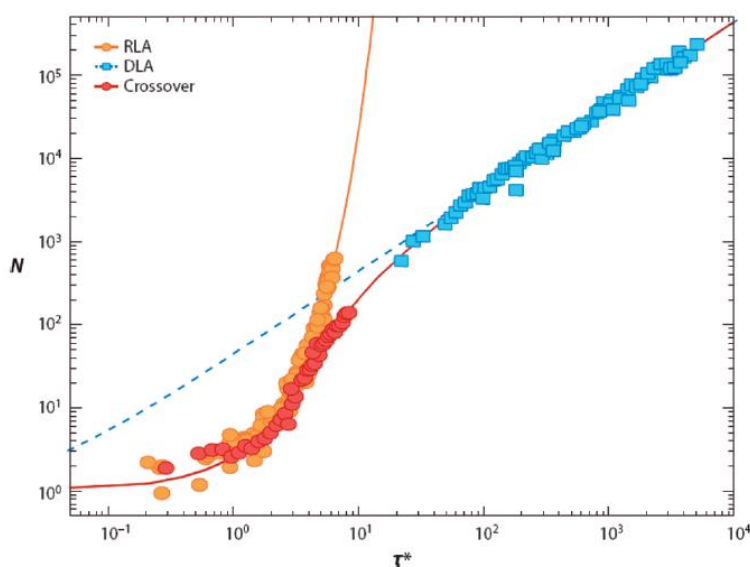


Figure 1.3. Light scattering study of natural asphaltenes aggregation number (N) as a function of time scale τ^* [38]. Flocculation data for n -heptane addition to different asphaltene-toluene solutions. Orange circles represent data for 10 mg/mL asphaltene-toluene solution exhibiting reaction-limited aggregation. Blue squares represent data for 1 mg/mL asphaltene-toluene solution exhibiting diffusion-limited aggregation. Red circles represent data for 5 mg/mL asphaltene-toluene solution exhibiting crossover aggregation kinetics.

Figure 1.3 exemplifies the complexity of asphaltene interactions, as they change aggregation mechanisms depending on the concentration at which an environmental change occurs [38]. The addition of *n*-heptane at any concentration appears to prompt aggregation, however the difference in aggregation mechanisms leads to different floc sizes. These observations were drawn from asphaltene samples originating from the same crude oil source [21]. However, asphaltenes of different origins can be expected to have different molecular characteristics such as varying number of aliphatic and/or functional groups, which significantly impact intermolecular interactions.

To investigate the kinetics of the aggregation mechanisms, the system was divided into fundamental variables that affect the colloidal stability, such as the chemical structure and solvent species, while the temperature and pressure of the system are ambient. Controlling the molecular structure is a crucial part in studying colloidal interaction of model asphaltene molecules, as they alter the interplay between energetics and entropy [39]. The aggregation potential of a colloidal system characterised through the DLVO theory, where when two particles approach one another their ionic atmospheres begin to overlap and a repulsion force is developed. Two forces are considered to affect the stability of a colloidal system: van der Waals and static electrical charges (Coulombic). The sum of the attraction and repulsion potentials yields the total potential energy of the system. DLVO theory applies well for aqueous liquid media. However, this work was performed in organic solvents, as asphaltenes are usually found and studied in. As such, the following equation is used to represent the total potential energy in organic solvent media:

$$V_t = V_a + V_r + V_s \quad (1.1)$$

where V_t is the total potential energy of the system, V_a is the sum of attraction potential (van der Waals forces generated by the molecular structure), V_r is the sum of repulsive potential (electrostatic repulsion) and V_s , the sum of potential energy of the solvent (the molecule is solvophobic or solvophilic) [40-42]. The balance between these potentials determines whether the molecules stay in a colloidal state, form nanoaggregates that remain in a colloidal state or strongly associate until precipitation occurs [43]. When the difference between potentials is small, concentration occupies a greater role as aggregation potential increases proportionally with collision rate. Multiple studies concerning the effect of asphaltene concentration suggest that even at very low concentration, asphaltenes could possibly prefer to form nanoaggregates (2-8 molecules), due to the attraction potential induced by their polyaromatic structures [44]. Increasing concentration, consequently the probability of collisions, leads to the formation of larger clusters or flocs [45]. Shifts in solvent species also occupy a major role, as they can provide a more energetically favourable state for aggregation (V_s), which depends on the solute-solvent interaction. The effect of adding *n*-heptane in an asphaltene-toluene suspension is considered a standard practice in investigating asphaltene aggregation [46]. Toluene, being an aromatic solvent, has a stronger affinity for the aromatic cores of asphaltenes (good solvent), while *n*-heptane, being *n*-alkane, is not attracted to the large aromatic surfaces (poor solvent). Although the attraction potential generated by the chemical structure of the models does not change, the shift in solvent species and solute-solvent interaction can trigger aggregation, as the system strives to achieve equilibrium.

Chapter 1

1.4.2. Driving forces for asphaltene aggregation

To better understand the structure-function relation between the chemical structure and environment, and the aggregation mechanism, both attractive and repulsive driving forces are evaluated.

1.4.2.1. Van der Waals interactions

Van der Waals forces are the result of attraction caused by the correlations in the fluctuating polarisation of electric dipoles of atoms molecules, and they are proportional to the transient shifts of electron density. The resulting forces are permanent, as long as the molecular structure of the molecule does not change. This is due to the electric dipole/multiple moment of the chemical/functional groups that generate a separation in of electric charges. The dynamic attraction between two molecules that is attributed to van der Waals forces mainly comes from the electrostatic interactions between permanent charges, the Debye force, and London dispersion effects, where a rapidly changing dipole of one atom produces an oscillating electric field that acts upon the polarisation of another atom, summarised by:

$$E = \lambda_{ij} / H^6 \quad (1.2)$$

where E is the energy of interaction (similar to V_a), H is the distance between atoms and λ_{ij} is the London constant (atomic number of interaction atoms). If the atomic dipole changes orientation before the field crosses the distance to the neighbouring atom, the attraction potential decreases. This suggests that the interaction energy of two molecules decreases over longer length scales, making

Chapter 1

molecules with a stronger attraction potential more likely to form larger aggregates, as they can attract molecules over increased distances.

In an aromatic ring, the electron density is distributed evenly above and below the plane of the ring (greater electron-density on the face of the ring and far less on the edge) [47], forming π -bonds due to the overlap of atomic p-orbitals (a quadrupole moment with partial negative charge) [48,49]. These electron clouds are the source of attraction between aromatic surfaces that lead to π -stacking. Multiple related interactions are identified throughout aromatic systems such as cation- π [50], anion- π and π -hydrogen [51,52], π -hydrogen bonds [53] or radical- π , the latter of which has received much attention due to the seminal work of Stoddart and co-workers [54,55].

However, the π -stacking of aromatic-cored molecules is influenced by the size of the aromatic surface (number of rings). For example, studies of prototypical aromatic molecules, such as benzene, show that off-set or non-parallel configurations are preferred [56]. By contrast, for larger aromatic molecules, such as hexabenzocoronene, the aggregation potential increases with the hydrogen number (higher polarizability due to broader aromatic surface), which favours π -stacking/parallel configurations [57-60]. A very simplistic definition of a π -stack is two or more aromatic molecules, sitting in a parallel configuration, at a distance of 0.351 nm from each other [61]. The increased electron density on the aromatic surfaces facilitates the formation of π -bonds due to the overlap of atomic p-orbitals [47]. It has been suggested that natural asphaltenes have between 2-8 aromatic rings [9,21], which implies that they contain the aromatic surfaces to facilitate π -stacking. In fact, a multitude of studies consider π -stacking and van der Waals

Chapter 1

attraction forces to be one of the main driving mechanisms for asphaltene aggregation [40,58].

In this project, two sizes of aromatic areas are taken into consideration, as triphenylene (4 rings) and hexabenzocoronene (13 rings) are the cores of model compounds. With hexabenzocoronene-cored model compounds, the investigation focuses exclusively on the π -stacking potential, as the aggregation potential of the model compound was challenged by the planarity of the aromatic surface. By contrast, the study of triphenylene-cored models attempts to underline both the π -stacking capacity as well as the contribution of functional groups and heteroatoms to the aggregation potential, by developing polar model compounds.

1.4.2.2. Electrostatic interactions

The aggregation potential of a suspension of solid particles is not only governed by the strength of short-range forces such as van der Waals, but also by the long-range electrostatic interactions (V_r). The strength/effect of van der Waals interactions between both solute-solute and solute-solvent molecules decreases with increasing distance (see equation 1.2). In a similar manner, electrostatic interactions governed by Coulomb's law are limited by source charge distances:

$$F = \frac{1}{4\pi\epsilon_0} \times \frac{qQ}{R^2} \quad (1.3)$$

where F is the total electrostatic force, ϵ is the vacuum permittivity, q is the test charge, Q is the source charge and R is the distance between two charges. However, Poisson's equation provides a relation between charge potential and

charger density, which makes the electrostatic interactions long range give priority to the solute-solvent interactions.

$$\nabla^2 \phi = -\frac{\rho}{\epsilon_0} \quad (1.4)$$

where ∇ is the divergence operator, ϕ is the potential and ρ charge density [62]. Mathematically this shows why van der Waals interactions can be considered short range, while electrostatic interactions can be considered long range

In aqueous environments, the particles carry surface charges due to the ionisation of surface groups. The distribution of ions changes due to the charged surfaces that disrupt the electro-neutrality of the solution. Coulombic forces drive ions of opposite charge (counter-ions) towards the surface, while ions of similar charge are repelled. This leads to the formation of an electric double layer of ions around a particle. However, the ionic strength is governed by the number of ions made available in the solution; hence the electrostatic interactions between particles in aqueous solutions can be controlled by salinity and pH. The aggregation potential of a suspension depends on the degree of electronegativity around each particle; however, ion solubility is poor in organic solvents and, as a consequence, the electric double layer will not form around molecules. As such, long-range repulsion forces in an organic solvent suspension can be primarily attributed to the solute-solvent relation, which is governed by steric repulsion [63]. To quantify the solvent electrostatic effects between two asphaltene molecules, the distance between a pair of model compounds (dimer) was measured as a function of solvent species (Figure 1.4) [63,64].

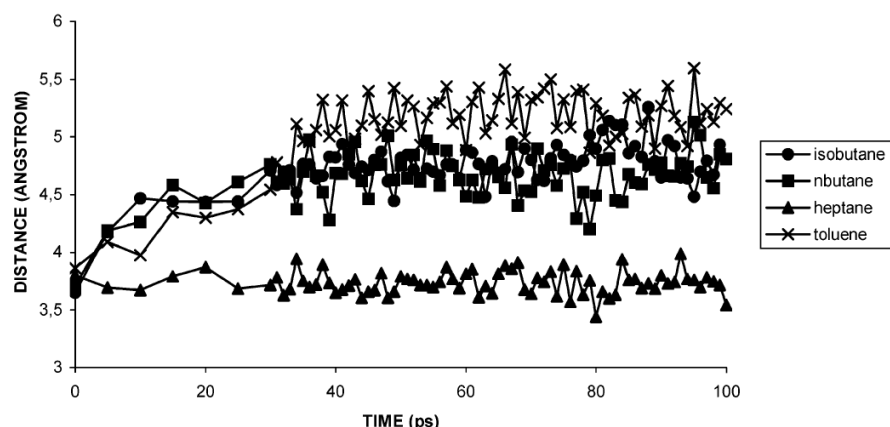


Figure 1.4. Variation of distance between a dimer formation, for selected solvents [65].

The observed change in intermolecular distance of the dimerised molecules, between an aromatic solvent (toluene) and an aliphatic (*n*-heptane) captures the fundamental parameters by which asphaltenes are defined as a solubility class in crude oil. The decreasing distance from toluene to *n*-heptane exhibits how the repulsion towards the *n*-alkane facilitates denser dimers [65].

Another method to assess the solute-solvent relation on the aggregation potential utilises the adsorption of the molecules onto a surface to form a molecular brush. With the change of solvent species, the molecules have the potential to extend away from the solid surface under the effect of the “good solvent” that covers the surface of the molecules [66]. If the solvent molecules form a dense/strong enough layer to overcome the solute-solute van der Waals attraction forces, no aggregation will occur. By contrast, a poor solvent will force the molecules to collapse onto the surface, suggesting a weak solvent-solute attraction, which leads to a greater aggregation potential.

A more appropriate way to discuss the attraction and repulsion forces in this work is to use the analogy between asphaltenes and surfactants drawn by Teh Fu Yen in 1967 [22]. Polar surfactants aggregate in aqueous solvents because their

Chapter 1

chemical structures include a hydrophobic and a hydrophilic component. The hydrophobic component rejects the water molecules and drives the aggregation process, while the hydrophilic component influences the configuration of the aggregates by providing a degree of repulsion towards neighbouring surfactant molecules [67]. In a similar manner, asphaltene aggregation potential is determined as much by the nature of the solvent (solute-solvent interactions, which are solvophobic or solvophilic), as by the chemical structure (solute-solute interactions).

1.4.2.3. Polar interactions

When atoms share electrons equally across a covalent bond, they form non-polar molecules, such as the aromatic ring structures that facilitate π -stacking [68]. However, when two atoms do not share electrons equally across a covalent bond, a dipole is formed, with one atom carrying a slightly positive charge (lower electron density), while the other carries a slightly negative charge (higher electron density). An extreme difference leads to the formation of an ionic bond, while a lesser forms a polar covalent bond. The difference indicates the degree of electronegativity of a molecule [69]. The existence of polar molecules generates attraction towards other polar molecules, similar to magnets attracting each other. The present work introduces model compounds that replicate natural asphaltenes by including amide and carboxylic acid groups, both of which induce different degrees of polarity to the model compounds [70].

1.5. Interactions between natural asphaltenes

It is widely accepted that π -stacking and polarity are the major contributors to asphaltene interactions and consequently precipitation [17,71,72]. Density

Chapter 1

functional theory studies that investigate asphaltene aggregate configuration suggest that the most energetically favourable state is a parallel configuration, rather than any alternatives, such as perpendicular stacking [73-79]. This further supports π -stacking as a major driving force of aggregation, however, it is still unclear whether it is the main driving force [80-83]. Key studies suggested that the π -stacking potential is directly proportional to the size/number of aromatic surface/rings present in the molecule, supporting the principle that structure dictates function [61,84,85]. Asphaltenes, being regarded as polyaromatic compounds, make no exception to this rule; however, asphaltene molecules tend to incorporate heteroatoms (nitrogen, oxygen, sulphur, iron, nickel, vanadium) and acid groups that could be active sites for aggregation [73,86-92]. This has been reported by multiple studies using techniques such as X-ray photoelectron spectroscopy [93-95], NMR spectroscopy [96], infrared spectroscopy [97,98] and UV-visible-near infrared spectroscopy [99]. The presence of these functional groups and heteroatoms can give the molecules a polar aspect. Studies also focus on the asphaltenes behaviour at the oil/water interface, as the polarity of the chemical structure generates attraction towards the aqueous solution, increasing the surface activity [100].

As the solubility of asphaltene is inversely proportional to its polarity, a higher polarity leads to greater aggregation [70]. Polar fraction also contains more metals and chlorine and dissolve slower than lower polarity ones [87]. The primary metallic elements that determine asphaltene polarity are iron, nickel and vanadium [86]. The more complex molecular structures increase the variety of possible molecular arrangements. Parallel configurations are driven by π -stacking, while functional

Chapter 1

groups that provide stronger attraction forces can facilitate non-parallel configurations, or even archipelago-like aggregates (tail-to-tail) [72]. Some debate regarding the intra-aggregate movement exists, as molecules might shift positions within an aggregate, until the lowest energetic state is reached (parallel). It has been observed that aggregation driven primarily by π -stacking occurs spontaneously [101], hence it is safe to consider that aggregation driven by functional groups can generate strong nanoaggregates due to polar attraction; however, π -stacking forces will still attempt to guide molecules into parallel configurations [44,102].

Aggregation of surfactants exhibits a strong relation to concentration, as it takes a certain number of molecules to be present in solution (critical micelle concentration - CMC point) to trigger the aggregation [103]. In a similar manner, asphaltene concentration dependence has been heavily studied, with a generalised CMC being considered to be near 0.1 mg/mL [21,103-105]. Furthermore, the concentration dependent aggregation behaviour could be influenced by the chemical structure of the asphaltene [106]. One study suggests that asphaltenes with low aromaticity do not show a CMC because the major driving force of aggregation is π -stacking [107]. However, the presence of active sites (heteroatoms and acid groups) implies that less energy is required for aggregation to occur, hence nanoaggregates could be formed upon collision of individual molecules [44,102]. The number of collisions increases with concentration, which results in increasing particle sizes [44].

Alternative studies focus on the initial formation of nanoaggregates, arguing that they occur between 0.01 and 0.1 mg/mL [108]. The results suggested that

parts of the asphaltene molecules are more soluble than others; therefore, when clusters are formed, there is a consistent difference between the asphaltenes at the core of the cluster and those on the corona [108]. Joint DLS and MD studies show how variations in the structure of side chains and polarity of functional groups lead to significant variations in molecular association [16,18]. Although the changes in functional groups may not affect the diffusivity of molecules themselves, it has a profound effect on the diffusion coefficient of the aggregates formed, as the strength of intermolecular interactions is directly affected.

Solubilised asphaltene molecules can be treated as colloidal particles, hence their interactions are either long-range electrostatic or short-ranged van der Waals [109]. However, all these forces are subject to the species or quality of the solvent in which asphaltenes are prepared. As crude oil consists of a mixture of saturates, aromatics, resins, and asphaltenes (SARA) in various proportions, it is difficult to deduce the interplay of interactions [46]. Asphaltene characteristics can be observed when prepared in a pure solvent. By tuning the solvent properties (aromatic to aliphatic), the molecular interactions are directly affected, as aromatic solvents hinder the π -stacking of asphaltenes, in comparison to the aliphatic solvents, which favours them [91]. The complex interplay of structure-function-environment makes studying asphaltenes challenging, which generated the need to isolate key parameters in order to understand, predict and discover effective measures to counteract asphaltene behaviours at industrial scales. This led to the development of numerous model asphaltene compounds, the most relevant of which are reviewed below.

1.6. Model asphaltene compounds

Natural asphaltenes are hypothesised to exist in one of two dominant chemical structures, “archipelago” and “continental”. The former is thought to be composed of polyaromatic fractions linked together by aliphatic chains, whilst the latter consists of a single aromatic core surrounded by aliphatic tails and functional groups. High resolution transmission electron microscopy [110] and UV-vis spectroscopy [111] have been employed to assess the number of aromatic rings included in asphaltene structures.

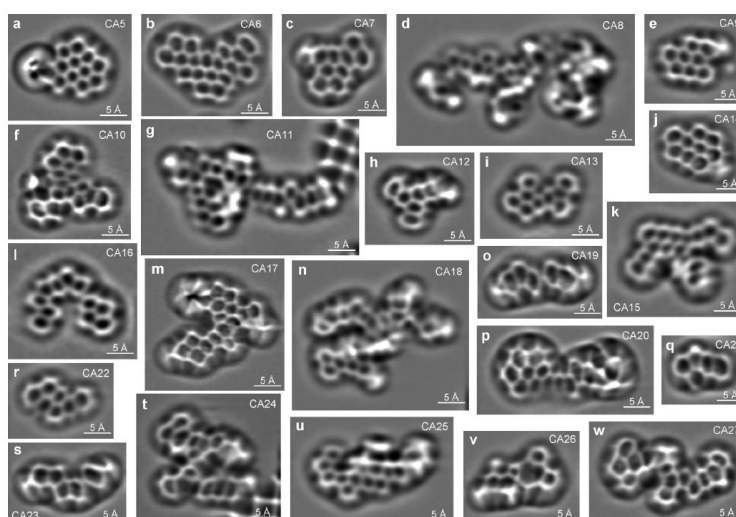


Figure 1.5. Scanning tunnelling microscopy images of asphaltene molecular structures.

Asphaltene molecules have been successfully imaged using atomic force microscopy coupled with scanning tunneling microscopy, Figure 1.5, with its result fully supporting the continental model as the dominant molecular architecture [14].

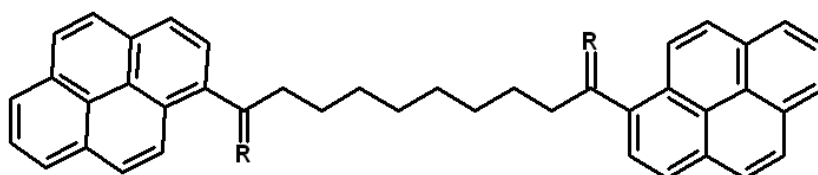


Figure 1.6. Pyrene-cored model compound proposed for archipelago architecture in asphaltene self-association studies with multiple functional groups (R).

In an attempt to investigate both archipelago and continental architectures, model compounds based on either pyrene (4 rings - Figure 1.6) or hexabenzocoronene (13 rings - Figure 1.7) were developed. The pyrene compounds were firstly alkyl bridged (non-polar) and then modified with alcohol and ketone (polar) to mimic archipelago models (Figure 1.6). The non-polar molecules showed no potential to aggregate [19], while the polar ones formed dimers, clearly highlighting the importance of polar groups in any potential natural asphaltene that respect the archipelago arrangement [19].

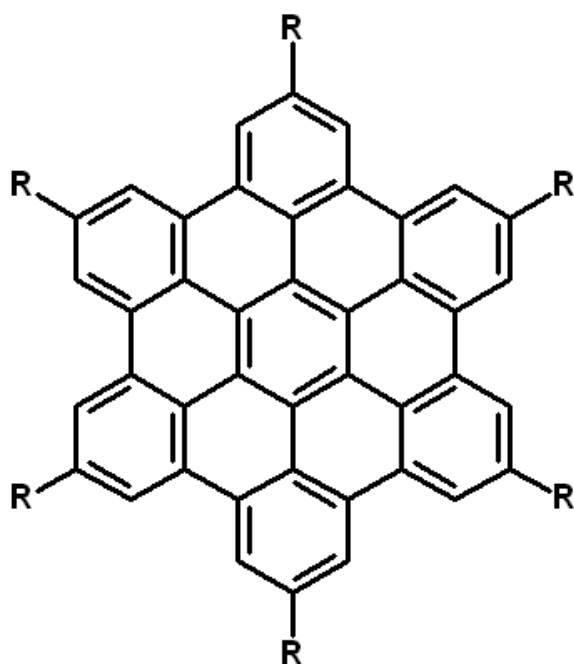


Figure 1.7. Hexabenzocoronene-cored model compound proposed for representing continental architecture in asphaltene self-association study with multiple chain lengths (R).

A hexabenzocoronene model with tail groups surrounding it (C6-HBC), mimicking the continental formation (Figure 1.7), was then investigated, and it was found to form dimers in toluene by π -stacking [112]. The models did however associate into π -stacked columnar formations when the temperature was

increased, highlighting the potential of continental asphaltene models. Following the same logic, another research group utilised the same molecular core, but with *tert*-butyl groups replacing the surrounding tail groups [17]. The study utilised dynamic light scattering measurements to record increasing hydrodynamic diameters, as *n*-heptane was added in the suspension. It was concluded that the model asphaltenes associate into aggregates of up to 500 nm over the course of a few hours.

The comparison of archipelago and continental model asphaltenes was further pursued where a series of chemical structures were investigated [113]. The results were in agreement with the previous work, in that the archipelago models do not allow significant aggregation in organic solvents, in contrast to the continental model.

Fluorescent depolarisation measurements were employed to identify how an average asphaltene model would appear, and the results further support the hypothesis that the majority of asphaltenes follow the continental architecture, with an average molecular weight between 500 and 1000 Da, an aromatic core of 4-9 rings, and aliphatic tails and functional groups on the exterior [73]. It appears that although there might be natural asphaltenes possessing the archipelago structure, the dominant architecture is continental.

Molecular dynamics simulations were employed to develop and test a series of model asphaltene chemical structures presented in Figure 1.8. The interaction potential of the model compounds was investigated in both pure organic solvents (toluene and *n*-heptane), as well as at an oil/water interface.

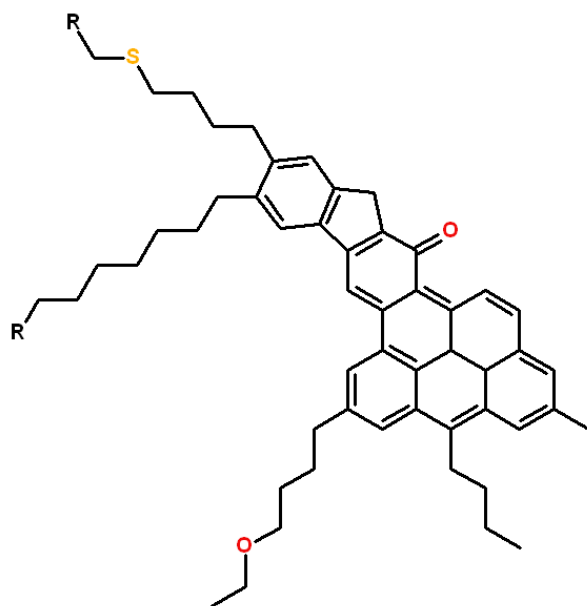


Figure 1.8. Representative model compound proposed for continental architecture of asphaltenes with seven aromatic rings and interchangeable heteroatoms (R).

The study concluded that, despite the aromatic surface (seven rings), the major driving force for self-association and interfacial activity is the functional groups and heteroatoms. This implies that the polarity of the molecule occupies a greater role in aggregation potential than the potential for π -stacking [114,115]. By observing the chemical structure, it can be suggested that the aromatic surface area is extended, rather than centred. This may be a factor in reducing the π -stacking potential in this study, but it is not logical to consider natural asphaltenes as having perfect centro-symmetric aromatic cores. Hence, the model presented in Figure 1.8 might be closer to natural asphaltenes than the alternatives.

Previous studies established that although van der Waals attraction forces between aromatic cores occupy a major role in nanoaggregate formation, various polar and non-polar interactions of the functional groups also influence the initial molecular association, the size of the aggregates, and the stacking configurations [91,116].

A systematic study of the effect of side chains on model asphaltenes (Violanthrone-78 core) in water simulations was performed using a structure presented in Figure 1.9. The side-chains were systematically varied, while the core (9 rings) was kept constant. Due to the study being performed in water, the occurrence of aggregation and the preferred parallel configuration of the model asphaltenes is not surprising. The effect of the side chains was concluded to be nonmonotonic, as short chains can have reduced interference on the π -stacking, therefore not hindering aggregation. Long tail groups, although recognised for hindering π -stacking, can increase aggregation potential by promoting looser configurations [116].

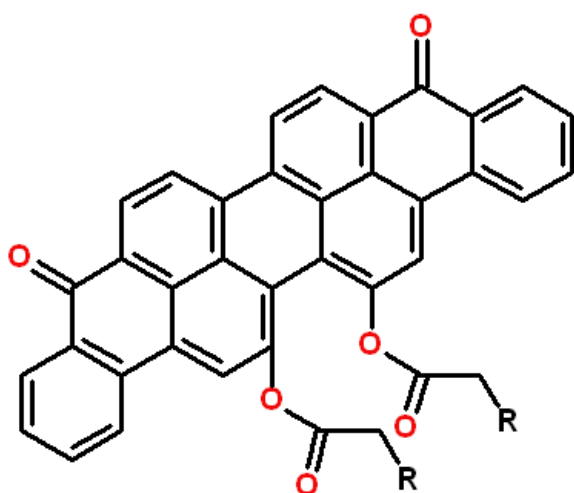


Figure 1.9. Violanthrone-78-cored model compound proposed for representing continental architecture of asphaltenes with nine aromatic rings and multiple chain lengths and interchangeable functional groups (R).

The Violanthrone-78 core structure was further employed to explore the effect of the embedded functional groups [117]. The presence of acid and polar groups in asphaltene tails was found to not only increase the size of the aggregates, but to also increase adsorption to polar surfaces, with the core aligning perpendicularly to the substrate. Asphaltene surface density was reduced

in the absence of the polar groups, as the amount was found to be more sensitive to the presence of functional groups and less to the presence of heteroatoms [118].

The presence of polar groups could possibly act as an aggregation initiator from a fully dispersed state, after which π -stacking takes place, in order to minimise potential energy in the final equilibrium state [119]. It was found that a polarised asphaltene (asphaltene with a polar group) is more likely to aggregate with a non-polarised asphaltene (asphaltene without any polar groups) than two non-polarised asphaltenes [18]. Furthermore, the study concluded that the nanoaggregates formed by asphaltenes with polar groups are more stable, due to the stronger attraction forces generated by the hydrogen bonding. Alternative studies found that tails without any polar functional groups have very little influence over the o/w interface [120]. As more studies emerge on the effect of polar model asphaltene compounds, it is becoming increasingly clear how significant their impact is on asphaltene aggregation.

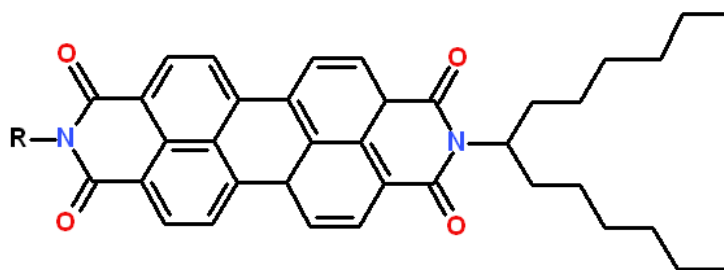


Figure 1.10. Perylene-cored model compound proposed for representing continental architecture of asphaltenes with seven aromatic rings and interchangeable chain lengths and functional groups (R).

The polar aspect is further explored as a different set of model asphaltenes was designed, similar to surfactants, to investigate the characteristics at the

Chapter 1

oil/water interface (Figure 1.10). The models include a fixed hydrophobic part, with a branched alkyl chain attached to a perylene core, and with the opposite side of the molecule occupied, in turn, by one of multiple functional groups. These functional groups included one with an aliphatic head group, and the other three with a terminal carboxylic group and a phenyl or indole groups [16].

The models were assessed with both experimental and computational approaches, to investigate the role functional groups undertake in driving aggregation. Their conclusions underpin the dominant surface activity and the stabilising potential of polar asphaltene models in comparison to non-polar models [100]. This is primarily driven by the attraction of the acid groups with the aqueous solvent due to their hydrogen bonding functionalities [121]. This strong driving force, coupled with the aromatic core of the models, which facilitates π -stacking, leads to the formation of strong, self-organised films at the interface [122]. The model was found to form nanoaggregates of 2-10 molecules per aggregate, and larger clusters of around 30 molecules in the oil phase. The increase in concentration leads to an increase of the large aggregates due to the greater number of molecules available and possible collisions [123]. The smaller aggregates were also found to be more stable in xylene than toluene [123]. Furthermore, when bulk aggregation occurs, interfacial activity is reduced [124]. Overall, by investigating these models, it is implied that the majority of problems occurring at the interface can be attributed to a small, target percentage of asphaltenes with a high degree of polarity [124].

A similar model, a continental asphaltene architecture with two tails on the opposite sides of the core (9 rings), was further investigated to evaluate the effect

of the position a heteroatom (oxygen) on the chemical structure [64]. Although their results were inconclusive, the authors suggest that placing the oxygen on the outside of the ring, rather than at the base of a tail, leads to more compact aggregates.

The solubility of asphaltene aggregates has been investigated as a function of chemical structure, hence two continental models are developed and undergo simulations in a mixture of toluene and *n*-heptane [125]. The study concluded that the solubility decreases with an increase in aggregation number and, in agreement with conventional asphaltene knowledge, the number of aggregates increases with the *n*-heptane percentage. The same method was later applied on a larger number of models with similar conclusions for continental asphaltenes [84].

Multiple asphaltene and resin model chemical structures were developed using molecular mechanics and dynamics calculations and their aggregation potential observed. It was concluded that the model with the greater aromatic surface (greater van der Waals attraction potential), and a lower hydrogen-to-carbon ratio generates a higher stabilisation energy for the aggregates [126]. A molecular simulation geometry optimisation process was employed to generate four model asphaltene structures based on experimental data [127]. The study concluded that the tails occupy a major role in the aggregate configuration, as they might hinder π -stacking and promote alternative arrangements. A broad range of asphaltene models was developed based on different hypothesised structures from reservoirs [128]. Monte Carlo simulations used for simulating systems with many degrees of freedom, such as fluids and disordered materials were employed to assess a total of seven geometrical and energetical parameters. Monte Carlo

Chapter 1

simulations perform analysis by building models of possible results with a substituted range of values, for factors that are inherently uncertain, and changes to different sets of random values from the probability functions [129]. In this case, they conclude that the Hamaker constant, which provides the means to determine the interaction parameter from the van der Waals pair potential, can be utilised as the main representative factor to classify asphaltene and even the additional crude oil compounds by chemical structure. The Hamaker constant ignores the intervening medium between two particles and quantifies their particle-particle pair interactions [130].

1.7. Summary

In this chapter, an overview of current knowledge and previous studies concerning asphaltenes is provided, together with the relevant theoretical background. The major driving forces for asphaltene aggregation are identified based on previous studies from alternative fields. Both the current understanding of asphaltene molecular architecture, as well as the impact of functional groups is reviewed. This core knowledge allowed us to generate model asphaltene compounds, to isolate and replicate key characteristics of the intermolecular interactions. The purpose is to build a link between the structural characteristics of the asphaltene molecule and their impact on aggregation, or simply said the structure-function relation. As such, the majority of studies investigating model asphaltenes appear to reach a set of similar conclusions, on which the model compounds developed in this study were based on:

1. Polar and van der Waals interactions are the major driving forces of asphaltene aggregation;

Chapter 1

2. The polar components are more active in generating aggregation, while the π -stacking generated by the van der Waals attraction impacts the configuration of the formed aggregates;

3. Solute-solvent interactions play a major role as they determine the long range electrostatics. Polar models are less sensitive to solvent than aromatic ones. This is mainly due to the toluene/*n*-heptane pairing, as the former is aromatic and attracted to aromatic-cored asphaltenes, while the latter is aliphatic.

Chapter 2. Methodology

Chapter 2

In the present work, dynamic light scattering (DLS), ^1H nuclear magnetic resonance (NMR) spectroscopy, and molecular dynamics (MD) simulations have been employed to investigate the colloidal characteristics of the synthetic compounds replicating natural asphaltenes.

2.1. Dynamic light scattering

2.1.1. Theory

Dynamic light scattering (DLS) is a technique employed to determine the hydrodynamic diameters of particles or droplets that are prepared in a liquid environment, in the sub-micron region, by absorbing and re-emitting electromagnetic radiation [131]. It is also referred to as photon correlation spectroscopy or quasi-elastic light scattering [132]. A beam of laser light is fired through a liquid sample at the targeted particles. The energy deposited on fixed area by the laser beam during one second is defined as the intensity of the beam (I), and is measured in watts per square meter (W/m^2). That energy is carried in indivisible “masses” called photons. Each photon’s energy is:

$$E = h\nu \quad (2.1)$$

where E is the photons energy, h is Planck’s constant, and ν is the speed of light [133]. The incident photons collide with the suspended particles that come across its pathway. Part of the photon energy is absorbed while part is scattered (secondary radiation) throughout the medium. This occurs as long as the particles have a different polarisability than the medium/solvent. The oscillating dipole moment induced by the electric field of the incident light is related to the direction of polarisation of the incident light, scattering angle, and solution parameters

Chapter 2

[131,133]. According to the Brillouin doublet, the frequency shift (ω) is proportional to the velocity (c) in the medium, and the propagation vector length (q) of the density fluctuations, giving rise to the scattering.

$$\omega = \pm cq \quad (2.2)$$

The propagation vector length is related to the wavelength of light in the medium (λ), and the scattering angle (θ):

$$q = \frac{4\pi n}{\lambda} \sin\left(\frac{\theta}{2}\right) \quad (2.3)$$

As particles in solution are subject to continuous random motion caused by the interactions with solvent particles (Brownian motion), large particles move more slowly than small particles [134]. The speed at which a particle passes through a fixed volume of solvent, delimited by the laser wavelength, is dependent upon the particle size as well as the viscosity of the solvent. This velocity is defined by a property defined as the translational diffusion coefficient (D). The diameter measured by DLS relates directly to how a particle diffuses within a fluid, and is denoted as the hydrodynamic diameter (d_H). The time decay (τ) of the normalised autocorrelation function (ACF), $g_2(\tau)$, is the main output of a light scattering instrument, and is related to the mean diffusivity D of the scattering objects by the following equations:

$$g_2(\tau) = (e^{-2Dq^2\tau}) \quad (2.4)$$

$$d_H = \frac{kT}{3\pi\eta D} \quad (2.5)$$

Chapter 2

where d_H is the hydrodynamic diameter, k is Boltzmann's constant, T is the absolute temperature, and η is the viscosity of the solvent [133,135]. An ACF is defined by the correlation of a signal with a delayed copy of itself as a function of delay. It is a mathematic tool for identifying repeating patterns, in this case, the presence of periodic signals obscured by noise [136]. A number of molecular characteristics, such as surface chemistry, type and number of ions (thickness of the Debye length or electrical double layer), as well as concentration, could affect the diffusivity of any particles within a given solvent. The shape of the particle also influences its translational diffusivity [135], because the hydrodynamic diameter of a non-spherical particle measures the hydrodynamic volume occupied by the particle in solution. However, changes to the shape of the particle, such as aggregation, dissolution, or molecular re-configuration, affect the diffusivity in different ways. For example, increasing the length of a rod-shaped particle will have a more significant impact than changes in width, on the diffusion speed, hence not affecting the d_H [137].

Figure 2.1 shows a graphical representation of a dynamic light scattering set-up. The laser beam enters the sample, scatters off of the particles in suspension, and is registered by a photon detector at an angle respective to the incident beam, but of the users' choice. Usually attached to the photon detector is the autocorrelator that in turn transmits the data output into an external computer. The sample cells are made of glass or quartz.

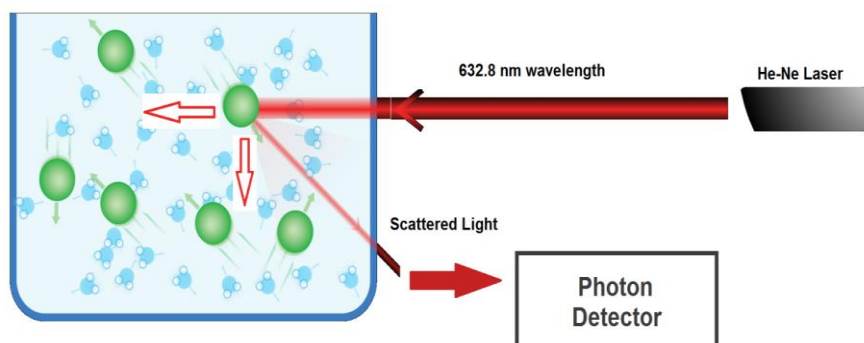


Figure 2.1. Schematic diagram of light scattering set-up, measuring the particle sizes of colloidal particles in a suspension and by collecting the scattered light with the photon detector.

The size of the particles, in comparison to the wavelength of the incident beam (He-Ne Laser $\lambda = 632.8$ nm), is also of significant importance as it determines how the incident beam is scattered. According to Rayleigh scattering theory, small particles (below 50 nm) scatter light isotropically (equal in all directions), due to the oscillating dipole moment induced by the electric field of the incident light beam [133]. The Rayleigh approximation states that:

$$I \propto d^6 \quad (2.6)$$

$$I \propto \frac{1}{\lambda^4} \quad (2.7)$$

where I is intensity of light scattered, d is particle diameter and λ is the laser wavelength. One of the major difficulties in accurately determining the particle size is caused by the degree of polydispersity within a sample, as different sized particles scatter light differently. The d^6 term in equation (2.6) implies that a 50 nm particle scatters 10^6 more light than a 5 nm particle does. This makes particle size distributions misleading, as a solution consisting of 99% 5 nm particles and 1% of

Chapter 2

100 nm particles could potentially yield a particle size distribution that only records the larger particles.

Taking into account the polydispersity of the samples being measured is paramount to understanding and interpreting the results correctly. When the hydrodynamic diameter of the particles are of similar size to the wavelength of the incident laser, a complex function relating intensity with size and angle of detection is required. Mie theory is employed in these circumstances [138] because it facilitates the conversion of the intensity distribution into a volume distribution by utilising the input parameter of the sample refractive index. As a perfectly homogeneous sample does not exist, and some degree of polydispersity is always expected, it has been determined that the signal of the intensity of scattered light is of better quality, at different angles [139]. As the detector needs to be placed where the scattering is optimal, low angles (173°) are preferred for measuring small particles that do not scatter exceedingly, while large angles (15°) are selected for large particles that scatter too much light. By taking measurements of a sample at different angles, information regarding the shape of the particles can be gained, which is called static light scattering (SLS) [99,133,140,141].

2.1.2. Instruments, experiments and data analysis

Dynamic light scattering measures particle size by determining the speed at which particles diffuse through the medium due to Brownian motion. This can be achieved by measuring the rate at which the intensity of the scattered light fluctuates as a function of particle size at a fixed angle. An example of recorded fluctuations in intensity of different sized particles can be seen in Figure 2.2.

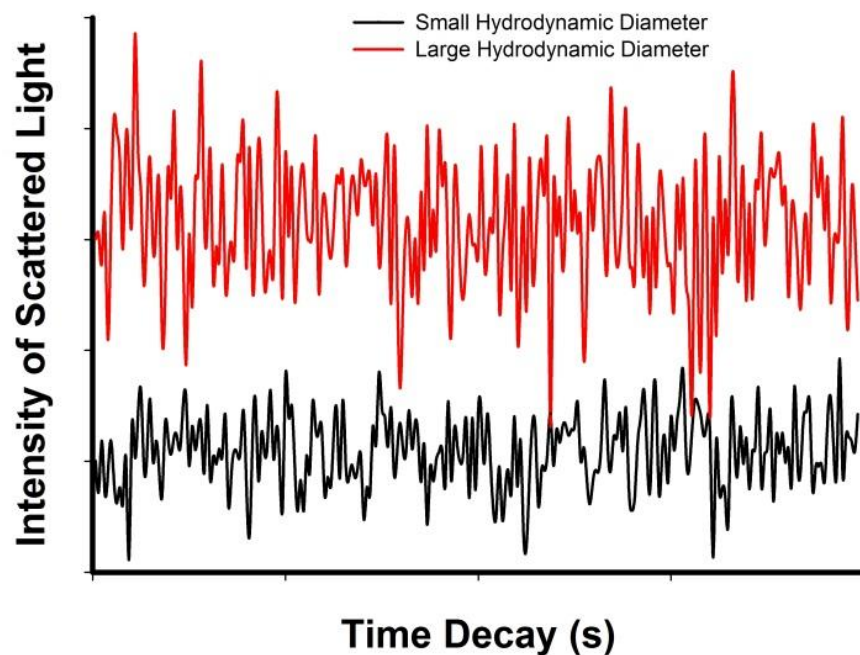


Figure 2.2. Example of recorded intensity fluctuations of scattered light over time, for large (red line) and small (black line) particles.

The correlation over time between two signals depends on particle size, as larger particles will travel slower (larger intensity fluctuations – red line) while smaller particles will travel faster (smaller intensity fluctuations – black line). The size, speed, and fluctuation differences result in faster decay for small particles (earlier τ), and slower decay (later τ) for large particles as shown in Figure 2.3. The mean diffusivity is calculated utilising the intensity ACF data acquired, $g_2(\tau)$, based on equation (2.4). The hydrodynamic diameters are then calculated using the Stokes-Einstein equation (2.5).

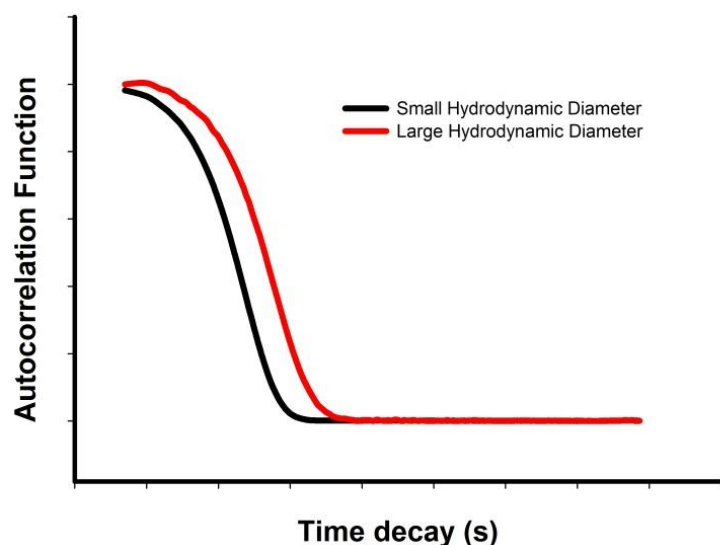


Figure 2.3. Example of recorded correlograms for a sample containing particles for which the correlation signal decays earlier for small particles (black line) and later for large ones (red lines).

DLS measurements of triphenylene-cored model compounds. The dynamic light scattering measurements of the triphenylene-cored model compounds were carried out employing a Zetasizer (Nano Series, Malvern Instruments) with a laser wavelength of $\lambda = 632.8$ nm, on a scattering angle of 173° , with data collected at fixed time intervals (0, 24, 168 hours). Data analysis was performed with the integrated Malvern software. Each datum is an averaged value of three samples, each measured over six repeats. The acquired autocorrelation functions of each sample set were analysed with the software, and only for those meeting the quality criteria, were data recorded to calculate the corresponding hydrodynamic diameters.

Toluene of different grades (99.85%, Extra Dry–AcroSeal; 99+%, extra pure) and PTFE membrane filters (100 nm pore size, Whatman) were purchased from Fisher Scientific (Loughborough, UK). Quartz optical cell (S High Precision Cell –

light path 3x3 mm) was purchased from Hellman Analytics Q, and solvent resistant screw cap vials (7 and 15 mL) were purchased from Sigma Aldrich (Dorset, UK).

DLS measurements of hexabenzocoronene-cored model compounds. The dynamic light scattering of the hexabenzocoronene-cored model compounds were carried out using a compact goniometer system (ALV/CGS-3, ALV-Laser, Germany) in conjunction with a multiple tau digital correlator (ALV/LSE-5004, laser wavelength $\lambda = 632.8$ nm and scattering angle $\theta = 45^\circ$). To examine the stability of HTBHBC and its derivatives as a function of concentration, light scattering measurements were performed in toluene. Both scattered intensity and particle sizes were collected. This approach introduces a robust mechanism to investigate the behaviour of colloidal aggregates in the bulk suspension, especially at low concentrations, where collected scattering signals are not reliable enough to calculate the corresponding mean hydrodynamic radii. However, we note that, at low concentrations, collected autocorrelation functions were not of sufficient quality to be able to fit their initial decay rates reliably and hence, in such cases, averaged scattering intensities provided reliable quantitative information about HTBHBC solutions. The scattering intensity depends on the following factors: number concentration of clusters, size of clusters, and their refractive index contrast with respect to solvent. The scattering intensity will vary proportionally to the concentration of clusters of a given size and structure [131,142,143].

Toluene 99.85%, Extra Dry-AcroSeal, *n*-heptane 99.85%, Extra Dry, PTFE membrane filters (100 nm pore size, Whatman) and DLS optical cells were purchased from Fisher Scientific (Loughborough, UK). Deuterated (d_8) toluene was purchased from Sigma-Aldrich (Dorset, UK), and used as received.

Chapter 2

2.1.3. Literature review of light scattering studies of aggregation

Colloidal particles in suspension are constantly subjected to Brownian motion and the interplay of forces that lead to an energetically stable system. They have significant implication in a wide variety of industrial products ranging from paints, pharmaceuticals, liquid crystals and foods to cosmetics, ceramics, and personal care [134]. By understanding and controlling the shape, average particle size, and surface characteristics of key materials in a suspension the formulation and production steps are impacted [144]. A variety of methods, such as microscopy, electrical sensing, chromatography, and scattering techniques, can be employed to examine the aforementioned physical and chemical properties.

Microscopy techniques offer direct size, shape, and texture measurements as images. However, microscopy usually allows for a fixed part of a sample to be observed, and as the size of the particles reaches nano-scale dimensions, the number of measurements has to increase in order for reliable measurements to be acquired. Advanced microscopy techniques such as scanning electron microscopy (SEM) [145], and atomic force microscopy (AFM) have been developed to observe nanoparticle size distributions [146], however they are still unable to monitor kinetic or dynamic changes in particle characteristics, such as those occurring in colloidal suspensions (aggregation, precipitation, dissolution etc), due to environmental or thermodynamical changes [147]. As such, characterising colloidal particles *in-situ* is of great significance.

Dynamic light scattering is a technique tailored to that purpose, as it provides ensemble averaged estimates of particle sizes in suspension, wide range of measurement techniques for particle characterisation, as well as fast and reliable

Chapter 2

data acquisition [148,149]. The hydrodynamic sizes of nanoparticles, polymers, emulsions, protein or most other types of colloids can be measured [150].

DLS does have its limitations, one of which is the size range of the examined particles cannot be significantly larger than the wavelength of the laser (632.8 nm) [151]. The small end of the spectra is limited by the difference in size between the particles and the solvent utilised to prepare the solution (particle has to be larger than solvent for light to scatter differently), as well as the amount of light the particles scatter [131]. Hence, most DLS instruments are limited to measuring hydrodynamic diameters between 1 and ~ 1000 nm. Some DLS instruments are reported being able to measure particles as big as 10 μm , which is largely sample dependent [152].

A key advantage offered by DLS is its capacity to acquire data *in-situ* in real time, hence the environmental parameters such as temperature and pressure that could influence the colloidal stability of the system can be investigated [144]. Factors that affect the kinetics of the colloidal system, such as variations in concentration, can also be studied by adapted DLS instrumentation [153]. Surfactants subject to critical micelle concentrations (CMC), are often studied as the CMC can be identified by DLS, as well as any other changes over time that the micelles undergo [154]. The study of aggregation in suspensions by light scattering techniques can yield information including not only the size, but also the shape of the scatters by shifting the angle of the photon detector of SLS [155].

More complex experiments, such as unfolding and crystallisation of proteins can be undertaken, which is fundamental to drug design and disease treatments [156,157]. However, conventional DLS and SLS measurements can be

Chapter 2

oversensitive towards unsaturated or supersaturated solutions, because determining the particle size by using the Stokes-Einstein equation is directly related to the diffusivity and scattered light. In these cases, alternative approaches can be employed, where only the intensity of the scattered light is recorded to gain information regarding particle kinetics within a suspension [158].

Light scattering is currently considered as one of the most reliable techniques developed to characterise colloidal systems, and along with all its adjacent methods (DLS, SLS, etc), can be adapted to investigate one of the most complex organic systems in nature, e.g. crude oil. More specifically, this project applies both SLS and DLS to investigate the aggregation of asphaltenes prepared in organic solvents. As is explained in Chapter 1, asphaltenes are soluble in toluene and form a stable colloidal system, but insoluble in *n*-heptane, aggregating and precipitating when it is added. Other than solvent quality, concentration and molecular structure of asphaltenes, other environmental factors, such as temperature and pressure, also occupy a major role in the stability of the system as well as the aggregation process [159]. In this project, dynamic light scattering was employed to observe the hydrodynamic size of asphaltene aggregates as a function of time, concentration, solvent species and molecular structure.

Aggregation of natural asphaltenes has been heavily studied by light scattering techniques. However, as with other experimental techniques, reproducible results are hard to achieve due to the inconsistencies of the chemical structure. Furthermore, when asphaltenes are dispersed in organic solvents, such as toluene, the suspension is either highly opaque (not enough scattered light

Chapter 2

passes through), or at low concentrations, although more transparent, does not scatter enough light.

To overcome the challenges imposed by natural asphaltenes, a special DLS set-up was developed with the capacity to measure particle size, despite the opacity of the system [38]. By using backscattering and corner scattering DLS set-ups, the laser beam is either scattered backwards (reflected), or has the shortest possible path through the opaque suspension (corner scattering), as both the laser source and the detector are placed at the corner/edge of a square sample cell. By recording the backscattering, or reducing the light path through the solution, highly opaque samples can be measured. With these approaches, natural asphaltene particle sizes were measured over a concentration range of 1-10 mg/mL [38,160,161], where sample opacity is a major problem. It is worth mentioning that this is a custom DLS set-up, which might have difficulties in measuring larger particles, due to the limitation in the angles used. However, the investigation managed to identify the kinetics of asphaltene aggregation: into a nucleation stage, where asphaltene molecules aggregate and find an energetically stable state as a colloid at low concentrations; an aggregation stage, where these aggregates form into clusters as a response to change in solvent, pressure or temperature; and a flocculation stage, where flocs with fractal structures are formed, that ultimately precipitate when they become too large to remain in solution.

A number of DLS studies focus on the formation of asphaltene nanoaggregate clusters (100 nm d_H) in toluene suspension at 0.3 mg/mL with the addition of *n*-heptane [17]. Most DLS studies of asphaltenes are very similar,

Chapter 2

relying on the addition of an aliphatic solvent to trigger aggregation, due to the opacity of the suspension when the asphaltene concentration in toluene is near 0.1 mg/mL. At this concentration range, the nanoaggregates could cluster to form large flocs [108].

A number of studies agree with these concentration ranges as asphaltenes are separated into size fractions using centrifugation, and then measured by SLS and DLS to establish the size of the asphaltene nanoaggregates [162]. By centrifugation, asphaltenes are not only separated by size but also by the bonding strength of the formed clusters, allowing DLS and SLS to measure the strongly bonded aggregates, rather than loose flocs. The results obtained vary between d_H of 8 and 80 nm, highlighting the range of sizes in which stable nanoaggregates can exist [162]. A combination of DLS and MD simulation approaches were employed to show how variations in the structure of side chains and polarity of functional groups lead to significant variations in molecular association. Furthermore, by tuning the solvent properties (aromatic to aliphatic), the electrostatic interactions are directly affected, as aromatic solvents hinder π -stacking in comparison to the aliphatic solvents, which favour them [91].

Light scattering can also be utilised to study the effect of temperature on asphaltene aggregation. An increase in hydrodynamic radii of natural asphaltenes was observed when the temperature was reduced from 0 to -10°C , with further reduction of temperature causing sedimentation [159]. This exemplifies the versatility and capacity of light scattering techniques to record the behaviour of complex organic materials, such as asphaltenes, as well as replicating environmental conditions. Solutions to the difficulties caused by asphaltenes in

Chapter 2

the crude oil industry are the main purpose of these studies. DLS investigations are motivated to focus on the effect stabilising compounds such as amphiphilic and polymeric dispersants have on aggregation, because attaching them to asphaltene aggregates can delay their growth [163]. The effect of naphthenic acids on asphaltene aggregation has been monitored by DLS [164]. Natural asphaltene samples with different naphthenic acids were prepared and measured by DLS, after a fixed amount of *n*-heptane was titrated into the samples, to determine the size of the clusters. A correlation was established between the functional groups generated by the different naphthenic acids, size of the aggregates, and the onset of precipitation (precipitation determined by near-infrared spectroscopy) [164].

Across the literature, DLS studies appear to agree that critical concentrations, as well as *n*-heptane addition are triggers for aggregation and precipitation. Furthermore, the studies on natural asphaltenes suggest a very strong structure-function relation, which makes investigating the aggregation mechanism difficult due to the complex chemical architecture.

This project focuses on key model compound chemical structures, with an increasing degree of complexity in terms of molecular geometry and atomic species, to be observed by DLS as a function of time and solvent effect.

2.2. Nuclear magnetic resonance spectroscopy

2.2.1. Theory

Nuclear magnetic resonance (NMR) spectroscopy has been developed as one of the most powerful, analytical, and non-destructive techniques, which yields

Chapter 2

information about structure, dynamics, reaction states, and chemical environment of molecules [165]. NMR spectroscopy measures the interaction of nuclei (instead of outer electrons) with radio-frequency (4-900 MHz) electromagnetic radiation (EM), when being placed in a strong magnetic field. As protons within the nuclei are charged elementary particles with their own magnetic fields and spin quantum number ($\pm \frac{1}{2}$), the orientation is forced upon the spin of the nuclei when exposed to an EM field. When the EM field is de-activated, the spin returns to its original state.

$$\Delta E = \frac{h\nu}{2\pi} \quad (2.8)$$

where ν is the resonance frequency and h is Planck's constant (6.63×10^{-34}). The difference in energy (ΔE) is a linear function of the magnetic field strength; therefore giving characteristic signals that are plotted as a spectrum. Figure 2.4 exemplifies this process:

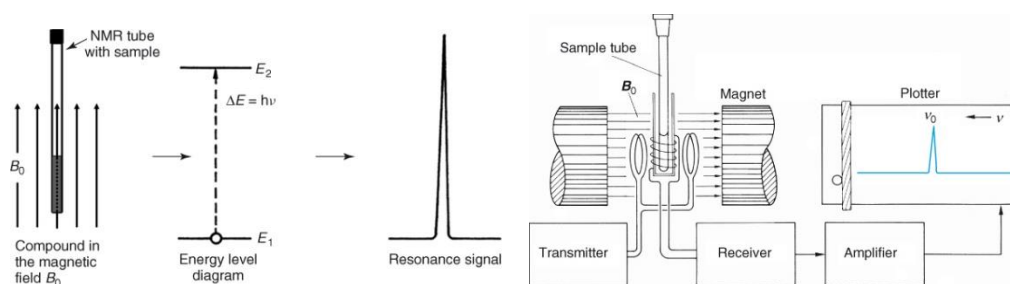


Figure 2.4. (a) Depiction of signal formation when the magnetic field is applied to the compound. As the nuclei shift between states, the energy difference is recorded as a resonance signal on a spectrum. (b) Schematic diagram of an NMR spectrometer as the magnetic field is applied perpendicular to the axis of the sample tube [166].

A spectrum is a graph of intensity plotted against the frequency shift for each atoms signal, acquired by varying or sweeping the magnetic field over a small

Chapter 2

range, while observing the frequency signal of the sample. The orientation of many protons such as ^1H , fluorine nucleus, ^{19}F , nitrogen isotopes, and many others can be affected by the EM radiation, and as the orientation of the spin of the nuclei changes, the spectrum presents said difference. One exception is ^{12}C protons, which have an even mass and even atomic number, hence no magnetic moment. NMR studies with carbon are limited to the stable isotope ^{13}C , that has a natural abundance of 1.1%. Precisely measuring the frequency difference is difficult, even with superconducting magnets, therefore an internal reference standard compound is utilised to generate a sharp signal that provides a constant difference in frequency to the sample signal. The reference signal must originate from the same isotope as the nuclei of interest; hence tetramethylsilane (TMS) is utilised for ^1H and ^{13}C NMR spectroscopy because its signal defines zero on the spectrum. Previously, TMS was mixed with the samples to be examined in the conventional NMR spectrometers, but is kept apart in more recent instruments.

The intensity of each peak is determined by multiplying the height and the half-width of the peak. The intensity of the signals is proportional to the number of protons, while split-peaks suggest that a number of nearby nuclei have magnetic moments. Integrating the area under peaks allows for the analysis of signals to be correlated with number and type of each proton, yielding a downfield to upfield ratio. This ratio, along with knowledge of molecular structures, yields the interpretation of the NMR spectrum.

All nuclei of an isotope possess exactly the same magnetogyric ratio, but they may be found at different positions in the spectrum, depending on the nature of the solvent, as well as the surrounding temperature. The number of electrons

Chapter 2

surrounding a nucleus determines the level of shielding, which is inversely proportional to the resonance frequency. In turn, the resonance frequency shifts the peak further to the right of the NMR spectrum. As an example, carbon-carbon triple bonds and aromatic rings yield a pronounced anisotropic-induced magnetic field, hence acetylenic hydrogen is unusually shielded while aromatic carbon is usually de-shielded. Figure 2.5 provides a breakdown of the NMR spectrum and establishes where to expect the peaks of different molecular structures to appear [167].

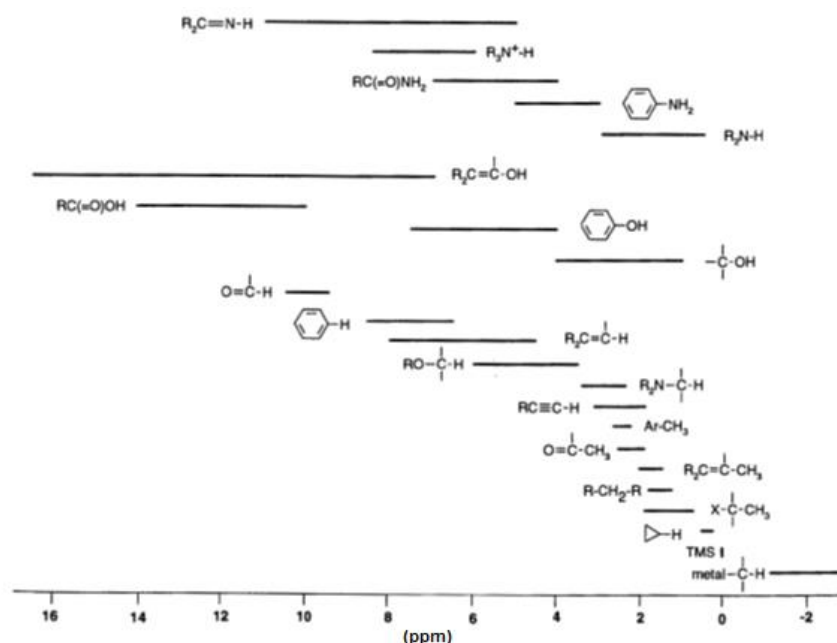


Figure 2.5. Representation of the positions of chemical shifts in a ^1H NMR spectrum across the entire chemical shift range [167].

The application of NMR to the various problems of inorganic, organic and physical chemistry is complemented by an increasing variety of experimental techniques such as diffusion ordered spectroscopy (DOSY), and pulsed field gradient-spin echo (PFG-SE) [168], that make NMR spectroscopy a highly utilised and versatile technique, with great impact on any chemical related industry.

Chapter 2

2.2.2. Instrument, experimental and data analysis

NMR spectroscopy was employed in two parts of this project. Standard ^1H and ^{13}C NMR spectroscopy were employed for assessing the quality of the synthesised compounds, and a modified assay data analysis method was developed to record changes over time in the purity of the HTBHBC molecule. All experiments were performed on the same equipment, a Bruker Avance III and 5 mm PABBO probe head with a sweeping frequency of 300 MHz. The initial data processing was done with a Topspin software v 2.1. ^{13}C NMR spectra were recorded using a Bruker Avance IV and proton-carbon dual plus probe head. The sweeping frequency was 100 MHz and the data was processed using Topspin software v 2.1. Chemical shifts are reported as δ values relative to CDCl_3 at $\delta_{\text{c}} = 77.4$ ppm. All samples for standard ^1H NMR spectroscopy were prepared with deuterated chloroform (CDCl_3), with the exception of TPN-CNacid model compound, which was dissolved in dimethyl sulfoxide (DMSO). The HTBHBC samples for the modified assay were prepared in deuterated toluene. The spectra were plotted and analysed using MestReNova software v 6.0.2.

Utilising the standard ^1H NMR spectroscopy, it was determined that the HTBHBC suspensions contained a significant percentage of impurities, which impact the aggregation and precipitation processes. A quantitative way of determining the presence of impurities in a sample was developed by modifying the NMR assay technique.

Modified assay method. Upon the assumption that all the impurities in a sample can be detected by ^1H NMR, the strength (assay) of the sample can be determined by identifying and integrating the corresponding peaks. The assay is usually

quantified by comparing the integrated peaks of a sample against those of a standard weighed into the sample [169-171]. However, introducing references could potentially cause complication with the interpretation of the results.

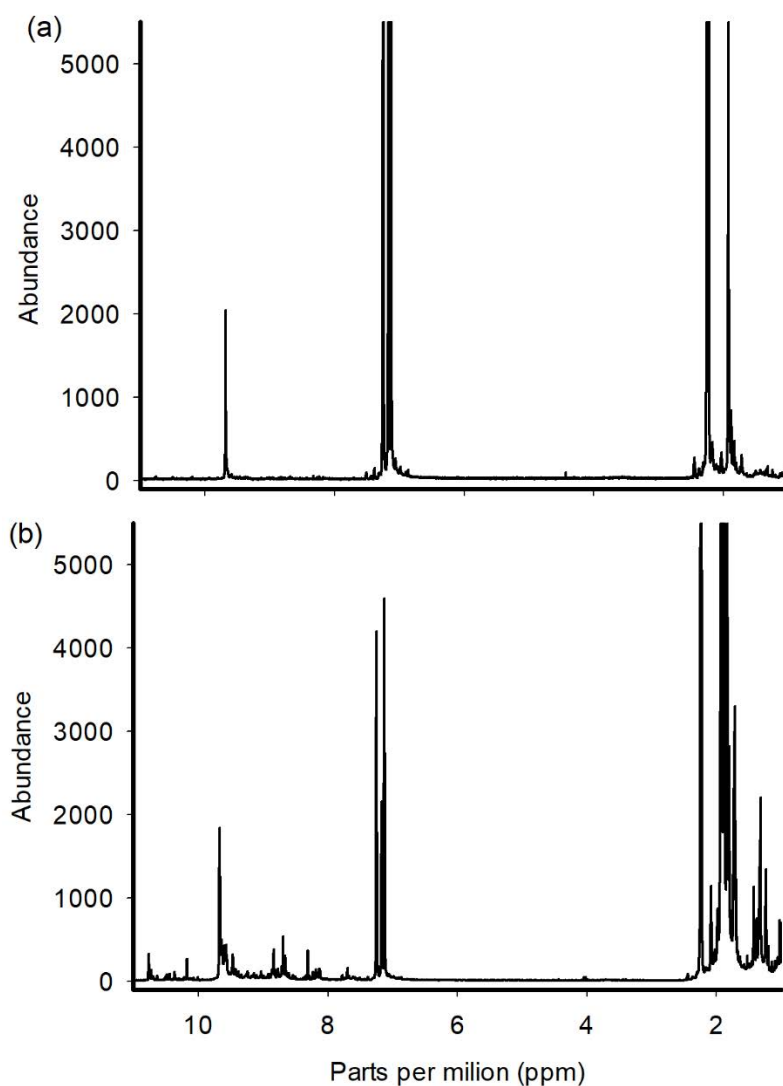


Figure 2.6. ^1H NMR spectra of the HTBHBC 20 mg/mL in deuterated toluene at 168 hours. Spectrum (a) was obtained from the solid deposit and spectrum (b) from the supernatant.

Instead of including any assay sample in the solutions, the peak corresponding to the aromatic protons of HTBHBC at 9.76 ppm was used as reference so that the molar ratio between HTBHBC and its derivative can be examined (Figure 2.6). The areas under the peaks (10.86 ppm and 10.46 ppm -

Chapter 2

Figure 2.6b) were integrated and normalised against that under the reference peak. Solvent peak at 2.36 ppm was also integrated for each measurement to account for the concentration change as a result of solvent evaporation. Of the 12 HTBHBC samples (20 mg/mL in d_8 -toluene), 3 were randomly examined by ^1H NMR spectroscopy at each time interval (1, 24, 168, 336 hours), the supernatant was extracted and the solid deposit was dissolved in d_8 -toluene and re-measured (Figure 2.6). The method relies on the reduction of the intensity of the peaks as the concentration of particular compounds decrease over time due to a sedimentation process.

The relative integral of each peak was summed up for each sample and plotted as a function of time. This allows examination of shifts in percentages of purity, within solutions, over measurement time.

2.2.3. Literature review of NMR spectroscopy studies of asphaltenes

Early asphaltene NMR studies took a very direct approach, by precipitating the asphaltenes from crude oil using aliphatic solvents, and characterising with ^1H and ^{13}C NMR spectroscopy, in an attempt to establish an averaged molecular weight and hypothetical structure [172]. In one particular study, ^{13}C NMR spectroscopy was used to observe the difference between asphaltenes obtained through slightly different precipitation methods (temperature variations and reflux), highlighting how broad asphaltene molecular structures are as a solubility class [172-174]. These early attempts were successful only in drawing conclusions valid for single samples, or very limited environmental factors.

Chapter 2

The complex chemical structure of natural asphaltenes could invalidate such standard approaches. However ^1H and ^{13}C NMR spectroscopy have been crucial tools in investigating the molecular structure of complex polycyclic aromatic hydrocarbons (PAH) in petroleum or coal due to their impact on the fuel and carbon industry [175]. By developing an effective method of data acquisition based on the carbon skeleton of each component, distinctions can be made between the bi-aryl linkages, methylene bridges and naphthenic rings [175]. This approach allows for a structure-function relation to be established, since the chemical architecture of the molecules are identified and linked to the behaviour of the crude oil. The coal industry also benefits from advancing ^1H NMR spectroscopy by isolating tetra- and penta-cyclic aromatic hydrocarbons of Victorian Brown coal and analysing them, further validating the existing knowledge regarding the chemical structures [176]. The possibility of streamlining NMR spectroscopy coupled with liquid chromatography was also investigated to achieve a continuous and quantitative analysis of PAH mixtures [177].

More recently, advanced NMR techniques have been employed to investigate the molecular structure of asphaltene, concluding that the most probable number of fused rings in the core of the asphaltene is between 4 and 10 [178]. ^1H and ^{13}C NMR spectroscopy can provide reliable structural information such as aromatic carbon fraction, averaged numbers of carbons per alkane side chains, as well as averaged percent of substitution of aromatic carbons [179-181]. By accurately assessing the differences in molecular structure of asphaltenes of different origins, or different separation methods, a correlation relating molecular structure to colloidal characteristics can be drawn [178].

Chapter 2

NMR spectroscopy was used to establish a cut-off between bridgehead carbon and peripheral carbon, and suggested that only a small fraction of bridgehead carbon is present in asphaltenes, which confirms that the asphaltene cores only have a small number of aromatic rings [9]. Studies coupling NMR spectroscopy with a number of techniques such as X-ray photoelectron spectroscopy concluded that the diameter of single asphaltene molecule is between 1 and 2 nm, and further support the average molecular weight of asphaltenes between 500 – 1000 amu, reported in the Yen-Mullins model compound [9]. These studies are of significant importance, as the separation of carbon types, present in the chemical structure allow for insight into the aggregation process, as a structure-function relation may emerge [9,73,85,182].

NMR spectroscopy forms the basis for a multitude of techniques meeting the requirements of different research applications [183]. Pulsed field gradient spin echo (PFG-SE) is one of the methods to investigate colloidal mixtures, as each molecular species will yield different chemical shifts for each chemical group of each molecule [168]. By observing the echo attenuation of these peaks, the diffusion coefficient for different chemical species can be measured simultaneously [37]. These experiments allow for monitoring the kinetics of a colloidal system in real time. Aggregation or sedimentation can be monitored as a function of diffusion coefficient, yielding information about dynamic colloidal systems. An investigation applied similar NMR diffusion techniques to study the diffusion behaviour of SDS (sodium dodecyl sulfate) as a function of concentration [184]. The study yielded insight into the adsorption and desorption of SDS to a pigment, added in solution, as a function of concentration. More specifically this

Chapter 2

approach allows the user to follow a particular chemical species' in a multi-component colloidal suspension [184].

The NMR spectroscopy studies referenced above, focus on investigating the molecular structure of natural asphaltenes, through a variety of approaches. In this project NMR spectroscopy was used for two purposes. The first was to establish the purity of the model compounds, by standard $^1\text{H}/^{13}\text{C}$ NMR spectroscopy, while the modified assay method uses the ^1H NMR spectroscopy to characterise the quantitative behaviour generated by the aggregation of HTBHBC and its derivatives as explained above.

2.3. Molecular dynamics simulations

2.3.1. Theory

To understand the influence of chemical structure on the aggregation characteristics of polyaromatic compounds, GRONingen MAchine for Chemical Simulations (GROMACS) v4.6.5 suite was employed to generate a molecular dynamics simulations and energy minimisation. These are two of the main techniques used in computational chemistry that can help model dynamics of large complex molecular aggregates. The goal is to generate molecular models that help describe complex chemical systems in terms of a realistic atomic model, to understand and predict macroscopic properties. Macroscopic properties are ensemble averages over a representative statistical ensemble of molecular systems either in equilibrium or in non-equilibrium. Thermodynamic systems at equilibrium imply that no net macroscopic flow of matter or energy is occurring i.e. simultaneous thermal, mechanical, chemical and radiative equilibria. By contrast,

Chapter 2

thermodynamic systems in non-equilibrium exhibit net macroscopic flows of matter and/or energy, which makes generating the ensemble averages and analysis of dynamic events more complicated, as they require the calculation of forces [185]. While other computational approaches, such as Monte Carlo, may be simpler than molecular dynamics, as they do not require the competition of forces, they do not yield significantly better statistics in a given amount of computation time. By performing molecular dynamics (MD) simulations and energy minimisation (which removes kinetic energy from a system), it is possible to understand and predict macroscopic properties based on detailed knowledge on the atomic scale [186].

Diverse molecular dynamics simulation packages are available, each with their unique features and advantages, such as GROMACS, AMBER and NAMD. To facilitate results validation and reproduction, the majority of the packages support cross-platform force fields and trajectory file formats.

The GROMACS software is in the public domain and distributed along with source code and documentation under the GNU General Public License 2.1. [187]. It is a versatile molecular dynamics simulation package designed to be utilised for investigating biochemical molecules such as proteins and lipids in aqueous environments . However due to its capacity to swiftly calculate non-bonded interactions, it is also heavily used for simulating non-biological systems such as polymers and polyaromatic hydrocarbons [114,115,188,189]. The main advantages of GROMACS lie in its simplicity and compatibility with standard personal computers, with limited processing power, as its authors report the performance to be 3 to 10 times better than other MD programs [190], compared

to NAMD, who performs better on high-end parallel computers [191]. GROMACS also boasts a lack of scripting necessity, as the software is actually a suit of small command-line programs, each with a simple set of options. This applies for building, running and analysing the simulations, which allows users to quickly master and adapt GROMACS to their project necessities. Not having a force field of its own, GROMACS is compatible with GROMOS96, OPLS-AA and ENCAD. Various coupling methods for temperature and pressure controls are also possible, allowing fine control over the thermodynamic parameters [186]. The MD simulations solve the classical equations of motion numerically for a system of N interacting atoms as the equations below:

$$m_i \frac{\partial^2 r_i}{\partial t^2} = F_i, = 1 \dots N \quad (2.9)$$

where r is the position of all atoms in the system, v is the velocity of all atoms in the systems, and F and m are the force on any atom respectively the mass of that atom. These forces are negative derivatives of the potential function $v(r_1, r_2 \dots r_N)$:

$$F_i = - \frac{\partial U}{\partial r_i} \quad (2.10)$$

The equations are solved step-by-step, so that the positions are recorded periodically in an output file. Taking into consideration the temperature and pressure of the system, the coordinates, as a function of time, represent the trajectories of the atoms. The software first allows for primary adjustments, after which the macroscopic properties, averaging over equilibrium trajectory, are calculated.

Potential Functions. The systems trajectories are guided by three different categories of potential functions: Non-bonded, Bonded and Restraints.

- Non-bonded potentials: the computation depends on the presence of the neighbours present and listed by a specific radius. These neighbour lists automatically exclude any bonded atoms inside such a range.
- Bonded potentials: depending on predefined parameters for covalent bonds, angles, and also proper and improper dihedrals.
- Restraints: depend on a fixed list, but also introduce information regarding positions, angles, dihedrals and distances.

Force Fields. For the potential function calculations to occur, the parameters and possible interactions have to be defined by a force field. The development and application of the force field is consistent and directly related to the molecule species employed in the system of interest [186]. The OPLS/AA (optimised potential for liquid simulations / All Atoms) force field was applied due to its precision in representing properties such as enthalpy of vaporisation and density, which is ideal for aromatic compounds [192]. Correct representation of such properties gives confidence in the description of non-bonded interactions including hydrogen bonding and in the size of molecules. By comparing such properties to well-understood fluid properties, the MD simulations can be validated. The OPLS/AA has also been employed in a number of asphaltene related simulations [189,193,194]. The force field parameters utilised in these simulations were validated through preliminary MD simulations for an organic solvent (toluene), at averaged pressure and temperature conditions. The standard methodology used

to calculate the enthalpy of vaporisation and density agrees with experimental data as shown in a previous study performed within this group and one other [195,196].

Periodic Boundary Conditions. The systems built with GROMACS can be defined by their shape, size, number, and types of molecules, and the coordinates, and velocities of all atoms. The geometries of these systems are usually of rectangular boxes with periodic boundary conditions. It can be described as a box thoroughly surrounded by copies of itself [197], as represented in Figure 2.7. This implies that a molecule would reappear in the opposite side of the neighbouring copy when it crosses the edge of one simulation box, as shown in Figure 2.7. The replication of bulk properties in small systems such as those commonly applied in MD simulations could be achieved when periodic boundaries were applied on the simulation box.

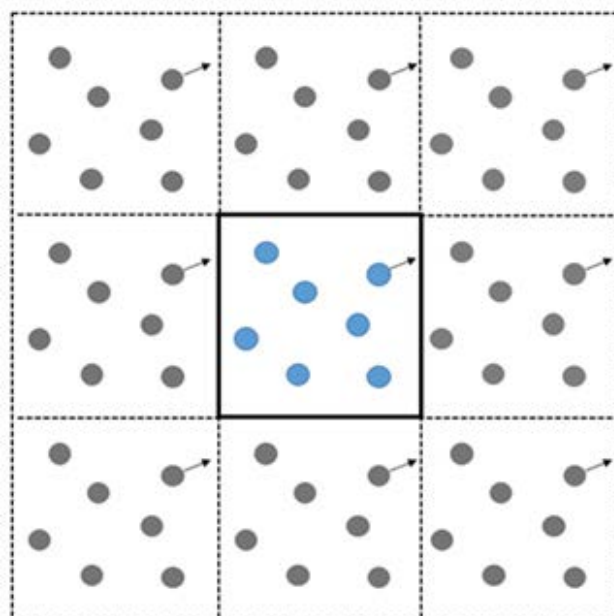


Figure 2.7. Schematic representation with periodic boundaries in two dimensions of molecules in a GROMACS MD simulation.

Radial Distribution Functions. Radial distribution functions (RDFs), also known as pair correlation functions ($g_{ab}(r)$), are widely applied to characterise the properties of a simulated system in terms of the randomness of their structure. Equation (2.11) shows how RDF distributions correlate density of particles to radial distances:

$$g_{AB} = \frac{\langle \rho_B(r) \rangle}{\langle \rho_B \rangle_{local}} = \frac{1}{\langle \rho_B \rangle_{local}} \frac{1}{N_A} \sum_{i \in A} \sum_{j \in B} \frac{\delta(r_{ij} - r)}{4\pi r^2} \quad (2.11)$$

where $\rho_B(r)$ is the density of type B particles around A within a radial distance r , and $\rho_B/local$ is the average density of all particles B in relation to the maximum possible distance (r_{max}) around particles type A . Usually, r_{max} is given as the half of the cell box length [185,198].

Figure 2.8 illustrates the regular radial distribution function for a liquid system. As the radius of interaction increases, a potential for a uniform distribution is observed ($G(r)$ converging to 1). The positions and intensities of the distribution peaks provide the averaged distance between the molecules. RDFs are regularly employed to characterise systems that aggregate, including information with regard to the potential configurations of such aggregates.

Figure 2.9 is a representative set of RDFs of aggregated molecules. The average distance distribution between the molecules can help to interpret the nature of the aggregate molecular configuration. In this example the parallel configuration is considered to be related to π -stacking, as the molecules used exhibited a large aromatic core.

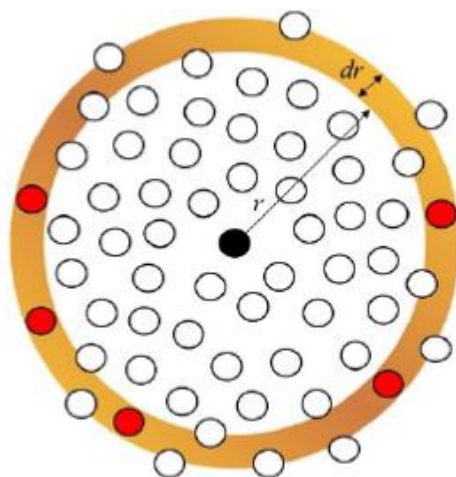


Figure 2.8. Graphical representation of radial distribution functions. The function is applied between the one molecule (black) and a group of molecules (red dots).

Previous experimental studies conclude that average π -stacking distance between the centre of mass (COM) of molecules is ~ 0.35 nm [61], which makes the example aggregate in Figure 2.9 (dark red) a good fit for parallel configuration. If molecules within an aggregate did not associate in an orderly fashion, the COM-COM distances will be displayed as a broader distribution (Figure 2.9 yellow - multiple-configurations).

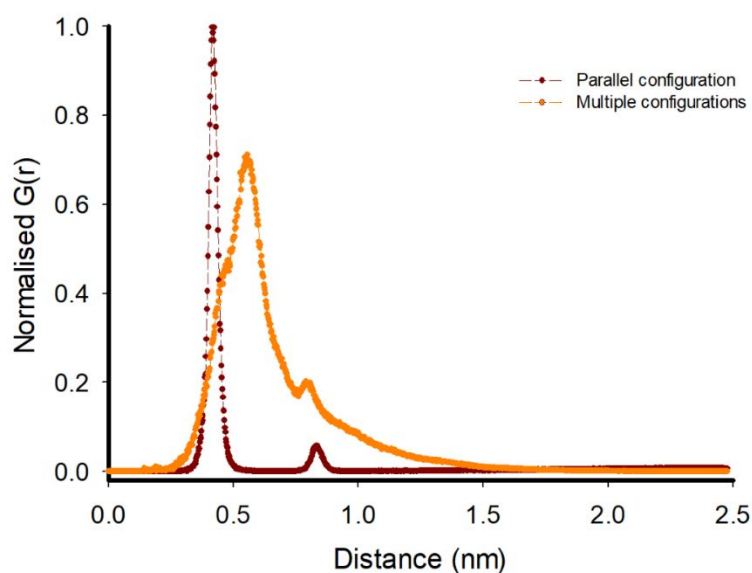


Figure 2.9. Radial distribution function examples of a parallel and multiple configuration aggregate, over 100 ns simulation time, in organic solvent.

g_dist. The `g_dist` function is one of the analytical tools provided by GROMACS to quantify the obtained data from simulations. It calculates the distance between the centres of mass of selected atoms as a function of the simulation time. The total distance and its x-, y-, and z- components are extracted as a function of the simulation time. For example, this tool helps quantify the aggregation or interaction between two molecules during a simulation. Figure 2.10 shows how the distances between (a) non-aggregating and (b) aggregation simulation can be displayed by `g_dist`. In Figure 2.10a, the seven molecules are in a colloidal state, only random collisions occurring at distances below 1 nm. Figure 2.10b displays a group of seven molecules that aggregate after ~ 10 ns simulation time into one cluster. Information about the configurations can also be extracted as the distance between the COMs is displayed. It is important to note that while the RDF collects data for distances between all possible pairs of selected molecules, and displays a distribution, `g_dist` presents the distance one pair at a time. In Figure 2.10 only the distance between one molecule (R1) and the other six (R2-R7) is presented.

By linking the videos with RDF's and `g_dist`, quantitative observation regarding the behaviour of target molecules may be made. Both tools are heavily used in asphaltene MD studies, which are mentioned in the literature review subsection (2.3.5) of this chapter.

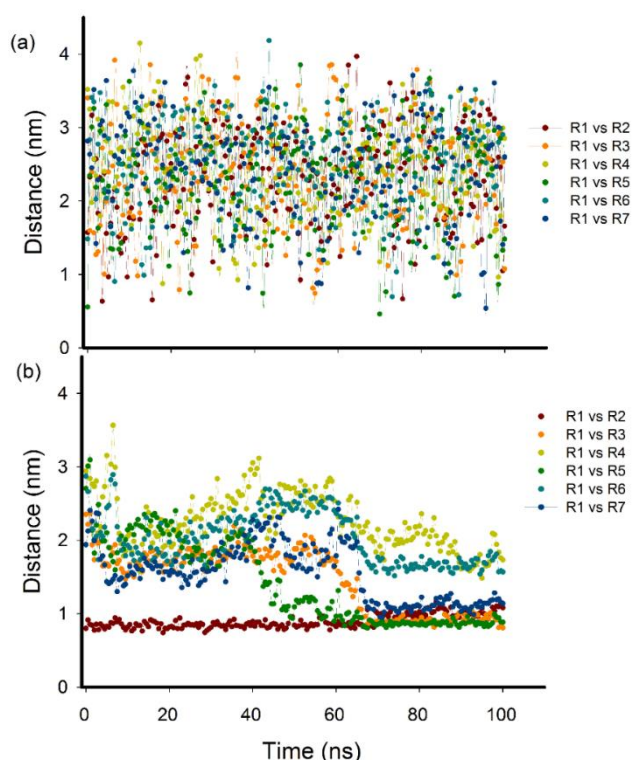


Figure 2.10. g_dist example of (a) a non-aggregating and (b) an aggregating simulation, over 100 ns simulation time in organic solvent. R1 is the molecule with which all the other intermolecular pairs/distances are recorded.

Visual Molecular Dynamics (VMD). VMD is a molecular visualisation program utilised for viewing, animating, and analysing simulation boxes using 3D graphics and built in scripting. For this project, VMD v 1.9.3. was employed to visually observe the MD simulations, as well as convert the data into picture frames for sharing purposes [199]. Windows Movie Maker is then applied to convert the frames into short movies.

Molecular Model Compound Building. Model compounds were custom built and designed for MD simulations to understand the structure effect on the aggregation mechanism. The first step of building a model compound employs the Accelrys Draw package v4.2 from BIOVIA (San Diego, USA) to connect the atoms to their correct positions in the molecular structure [200]. The output is then translated to 3D model compounds according to the force field parameterisation. The MKTOP

application is employed to generate the appropriate OPLS topologies for the model molecules and their solvents, with the exception of partial charges [201,202]. These are manually assigned to individual atoms by linking them to the OPLS/AA library in the same manner as the referenced research group [203]. The assignment of the charge distribution throughout the molecule should result in a total neutral charge, as well as be in line with current organic chemistry principles, e.g. heteroatoms that draw charge from aromatic structures.

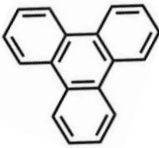
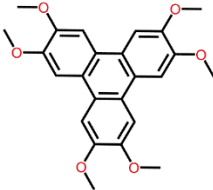
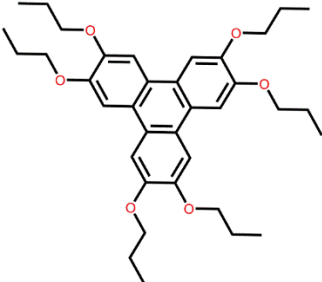
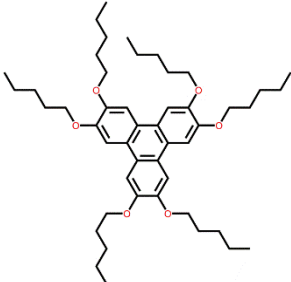
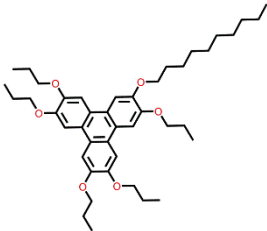
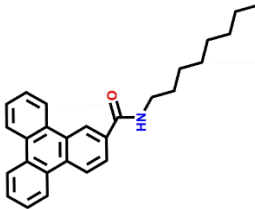
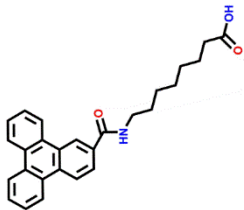
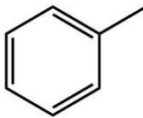
Solvent Affinity Simulations. A secondary set of simulation boxes was built following the same method described above. However, only one model compound molecule at a time is placed in a constructed solvent box that contains 350 toluene and 350 *n*-heptane molecules. RDFs are applied between the single molecule and all the molecules of each solvent species, which allows the model compound affinity towards either the aromatic or the *n*-alkane solvent to be established, by quantifying the density of solvent molecules around the model molecule. RDF data sets were then plotted, with the height and width of the peaks indicating the degree of affinity between the molecule and the solvent species. As the density of the solvent becomes uniform in all directions (see Figure 2.8), the distributions lead to 1 $G(r)$ after 2-3 nm distance relative to the model compound molecule.

2.3.2. Model compound molecular structures

The chemical structure of the model compounds developed in this project are presented in Table 2.1 below, along with additional compound information such as chemical formula, exact mass, mass divided by charge, and elemental analysis.

Chapter 2

Table 2.1 Model compound molecular structures along with their chemical details

				
	TPN-C0		TPN-C1	
MW (Da)	228.26	MW (Da)	408.45	
Chemical Formula	C ₁₈ H ₁₂	Chemical Formula	C ₂₄ H ₂₄ O ₆	
Exact Mass	228.09	Exact Mass	408.16	
m/z	228.09 (100.0%), 229.10 (19.5%), 230.10 (1.8%)	m/z	408.16 (100.0%), 409.16 (26.0%), 410.16 (2.7%), 410.16 (1.2%)	
EA	C, 94.70; H, 5.30	EA	C, 70.58; H, 5.92; O, 23.50	
				
	TPN-C3		TPN-C5	
MW (Da)	576.77	MW (Da)	745.1	
Chemical Formula	C ₃₈ H ₄₈ O ₆	Chemical Formula	C ₄₈ H ₇₂ O ₆	
Exact Mass	576.35	Exact Mass	744.53	
m/z	576.35 (100.0%), 577.35 (38.9%), 578.35 (4.7%), 578.35 (2.7%), 578.35 (1.2%)	m/z	744.53 (100.0%), 745.54 (51.9%), 746.54 (13.2%), 747.54 (1.4%), 746.54 (1.2%)	
EA	C, 74.97; H, 8.39; O, 16.64	EA	C, 77.38; H, 9.74; O, 12.88	
				
	TPN-C10		TPN-CN	
MW (Da)	674.96	MW (Da)	383.54	
Chemical Formula	C ₄₃ H ₆₂ O ₆	Chemical Formula	C ₂₇ H ₂₈ NO	
Exact Mass	674.45	Exact Mass	383.54	
m/z	674.45 (100.0%), 675.46 (46.5%), 676.46 (10.6%), 676.46 (1.2%)	m/z	383.22 (100.0%), 384.23 (29.2%), 385.23 (2.7%), 385.23 (1.4%)	
EA	C, 76.52; H, 9.26; O, 14.22	EA	C, 84.55; H, 7.62; N, 3.65; O, 4.17	
				
	TPN-CNacid	Toluene	Heptane	
MW (Da)	413.52	MW (Da)	92.14	100.21
Chemical Formula	C ₂₇ H ₂₇ NO ₃	Chemical Formula	C ₇ H ₈	C ₇ H ₁₆
Exact Mass	413.52	Exact Mass	92.06	100.13
m/z	413.20 (100.0%), 414.20 (29.2%), 415.21 (2.7%), 415.21 (1.4%)	m/z	92.06 (100.0%), 93.07 (7.6%)	100.13 (100.0%), 101.13 (7.6%)
EA	C, 78.42; H, 6.58; N, 3.39; O, 11.61	EA	C, 91.25; H, 8.75	C, 83.90; H, 16.10

Chapter 2

2.3.3. Practical steps

Building GROMACS simulation boxes and running the simulations requires several key files and preliminary steps.

- The *.mdp* files that define the parameters of the thermodynamic process, as well as the periodic boundary conditions.
- The *.pdb* files that define the topology of the molecules in use
- The *.itp* files that define the characteristics of the molecule such as charges, bond lengths and angles.

A simulation box (~5 nm) with seven model compounds was built with the molecules placed at equal distances from each other, to minimise the interactions during the preliminary steps and to ensure a consistent start for all simulations (command lines included in Appendices A. The simulation box can be visualised using VMD as shown below.

After a simulation box is generated and solvated (with specified solvent), energy minimization is performed to ensure a stable initial configuration. Equilibration steps (1000) of 100 ps were then performed to prepare the simulation for trajectory production. The Berendsen algorithm was adopted to relax the system to 298 K and 1 atm pressure. Once steady fluctuations reached the average volume, the 100 ns simulations were performed with an integration time of 2 fs, a cut-off of 1.0 nm used for van der Waals interaction and periodic boundary conditions [204]. The OPLS/AA force field used for these simulations is a result of both the Lennard-Jones potentials, which approximates the interaction between a pair of neutral atoms or molecules, and the electrostatic contributions

according to the electrostatic value of each atom, following the work of a previous publication [196].

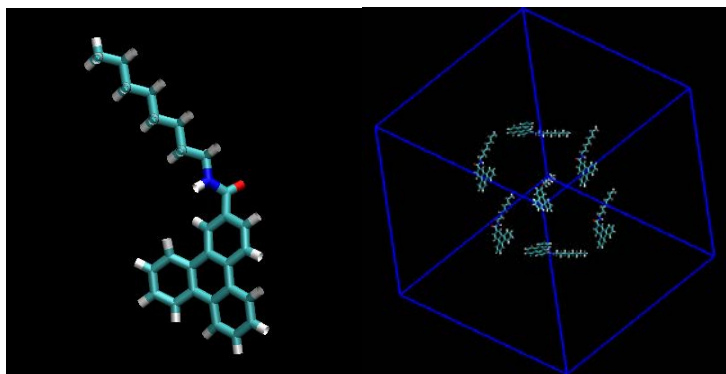


Figure 2.11. VMD snapshot of (a) a single model compound and (b) seven model compounds in a GROMACS generated simulation box prior to solvation.

The number of asphaltene molecules chosen was seven, as it allows asphaltene/solvent concentration be within experimental limits [193]. The simulation box was solvated with toluene, *n*-heptane or heptol (a mixture of 50% toluene and 50% *n*-heptane) (command lines included in Appendices A). Individual molecules could be selected and viewed using VMD, whilst all the others could be made invisible (Figure 2.11).

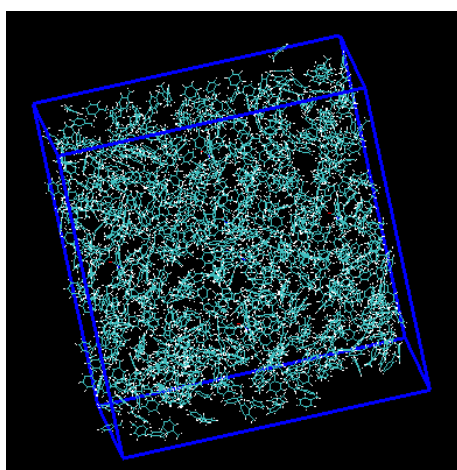


Figure 2.12. VMD snapshot of a solvated GROMACS simulation box containing seven model compound molecules and 700 toluene molecules.

Chapter 2

The generation of the simulated system (loading the simulation box with solute and solvent molecules) yields a non-equilibrium system with the molecules in a non-equilibrium state, as intermolecular distances, volume and pressure are unrealistic and unstable. As such, a MD simulation would crash, because the forces between the molecules would not be realistic (not at thermodynamic equilibrium) due to the purely geometrical loading (insertion) of the molecules in an unconstrained simulation box. To allow the thermodynamic parameters of the system to reach equilibrium, several steps were performed to ensure the energy minimization (EM step), volume (NVT step) and pressure (NPT step) are stable. Command lines are included in Appendices A.

The EM step ensures the removal of kinetic energy from the system, which leads to uniform intermolecular distances between molecules in the box. The EM algorithm stops when a user specified number of steps (1000) are performed, that calculate the new positions of the molecules in the box. This minimization or uniformization of energy allows for the elimination of energy flow, which in turn leads to thermodynamic equilibrium [205].

The NVT step which stands for “constant number, constant volume, constant temperature’ is used to enforce a constant temperature in the simulated system. The Berendsen thermostat (employed in this work for the temperature control) is an algorithm that mimics weak coupling with first order kinetics to an external (imaginary) “heat bath”. The effect of the algorithm is that a deviation of the system temperature is slowly corrected, with increasing accuracy proportional to allotted time [206].

Chapter 2

In a similar manner to the temperature equilibration (NVT), the NPT step uses an external (imaginary) “pressure bath”. The Berendsen algorithm is again employed as it scale the coordinats and box vectors every step, which has the effect of a first order kinetic relaxation of the pressure towards given reference pressure [207].

The molecular dynamics simulations could be run after all the steps above were completed successfully, with the system having achieved thermodynamic equilibrium. The equilibrium is considered to be achieved when the energy from EM, temperature from NVT and pressure from NPT are constant and in the case of the last two parameters is consistent with the imaginary “bath” set values (298 K and 1 bar). Usually, a short (4 ns) simulation is performed when examining a new system or molecule to ensure the behaviour of the molecule is realistic, after which a full length simulation (100 ns) can be carried out. The simulations were performed, subject to availability, on one of two different computer set-ups: a High Performance Computer at the University of Strathclyde and the BlueBEAR (Birmingham Environment for Academic Research) computer cluster at the University of Birmingham.

2.3.4. Data Analysis

To interpret and understand the MD simulation results, several tools were employed:

1. VMD – the software was employed to generate, edit and view in a 3D graphical model the obtained simulations. Although this approach is by far the

Chapter 2

most appealing, as an observer can see the molecules within the solvent environment, the conclusions drawn are of a subjective nature. Software processing steps in Appendices A.

2. RDF – included in the GROMACS tool package RDF functions, were plotted to quantitatively depict the average distance between the model molecules. This allows for a statistical average distance between selected molecule species to be calculated as a function of the density of local interactions divided by the density average of the whole simulation box. For each solvent type used (toluene, heptol and *n*-heptane), the RDF distributions were normalised by the highest datum per solvent type. This was done for the RDF data acquired from the simulations with seven model compound molecules in order to allow the distributions to be compared from model to model.

The RDF tools were deployed to record the distances between the COM of a single model compound molecule and all of the solvent molecules of either toluene or *n*-heptane in the same simulation box, at 20 ns. The plotted RDFs show the intermolecular interactions between the model molecules and all the solvent molecules, one species at a time. The purpose is to quantify the degree of affinity each model compound has towards aromatic or *n*-alkane solvents, or the difference in the average distance between the COM of the model compound molecule and the COM of either toluene or *n*-heptane molecules. All the RDFs tend to unity, as the solvent molecules are not influenced by the presence of the model molecule after a certain distance is exceeded, which results in a uniform density.

3. `g_dist` – distance as a function of time is plotted for all the simulations. The `g_dist` tool is utilised to plot the distance between the one model molecule paired with all the other (6) model molecules. Based on the obtained data, the interaction and aggregation of the model molecules can be quantified as a function of time, as well as observations on the resulting configurations can be made.

By coupling the three analysis techniques, a comprehensive overview of the model compounds characteristics can be generated. The VMD allows for a visual interpretation of systems, whilst the RDF and `g_dist` function yield the quantitative interpretation of the interactions, as well as insight regarding how the aggregation occurs for each model compound.

2.3.5. Literature review–MD simulations of asphaltenes using GROMACS package

The advantages that MD simulations offer lie in the capacity of rigorous and meticulous consideration of discrete particle trajectories, collisions, and configurations that contribute to the precise representation of the particle system at different length scales. While experimental techniques, such as microscopy and light scattering reach conclusions based on the characteristics of the bulk colloidal systems, MD simulations investigate the intermolecular interactions by replicating not only the molecular structures, but also, to a certain extent, the environments in which the experiments are performed [208]. Furthermore, MD simulations deconstruct the macroscopic systems into individual contributing forces and variables, allowing the user to isolate the individual contributions towards the systems characteristics [209]. Molecular dynamics simulate the particle system as

Chapter 2

a set of Newtonian mechanics equations of motion, considering forces such as inter-particle interactions, diffusive forces, osmotic pressure and external forces.

The real target of MD simulations is to predict macroscopic properties such as energy, pressure, and heat capacity, from molecular properties such as atomic positions and velocities. By focusing on time dependent statistical mechanics a bridge between macro and molecular size systems can be established [210].

MD simulations are often limited by the available processing power; hence, large colloidal systems that come close to replicating the size of experimental scales are not widely available until computer processing power increases significantly. Therefore, MD simulations are more adequate to analyse a target molecule or a smaller system that represents a colloidal suspension. As an idealised system, macroscopic behavioural patterns such as intermolecular or liquid-solids interactions can be simulated. The behaviour of single entities, such as proteins, and their complex adsorption to solid surfaces can be exemplified by computational approaches [211]. Even though these methods are far from being able to completely replicate experimental results, the potential computational methods compensate for physical constraints, such as diffraction limit in optical methods that experimental approaches have [212]. Depending on the target of the research, a variety of MD software packs are available [209].

GROMACS simulations have been employed to study complex organic systems such as crude oil, with an increasing number of possible individual components, which are usually challenging for experimental approaches [16,213]. GROMACS simulations offer the possibility of generating key molecular model

Chapter 2

compounds, isolating variables, such as solvent quality, temperature, pressure, and observing the structure-function relation. MD studies that focus on the interactions of asphaltene models within a crude oil system or at the oil/water interface have been published, and as expected, they conclude that the chemical structures undertake a significant role in the aggregation mechanisms [214]. The systematic increase of side-chain length attached to model asphaltenes proved that the effect was nonmonotonic, as short chains can have reduced interference on the π -stacking, therefore not hindering aggregation. Long tail groups, although recognised for hindering π -stacking, can increase aggregation potential by promoting looser configurations [116]. Other studies embedded functional and acid groups into model compounds to increase the polarity of the model compounds, and monitor their interactions, configurations, binding sites, solvent and temperature dependency [114,115].

With the aid of GROMACS tools (RDF, g_dist), the presence of acid and polar groups in asphaltene tails was found to increase the size of the aggregates, due to an increase in polarity [117,118]. Heteroatoms across the chemical structure were found to influence the intermolecular interactions to the point where an excess can even prevent aggregation [215].

Asphaltene model compound design in GROMACS was taken one step further by generating the chemical structure of the model PACs based directly on the results of chemical analysis experiments, such as ^1H NMR spectroscopy, elemental analysis, and vapour pressure osmometry [193]. This leads to the development of model compound molecular structures closer to their natural counterparts.

Chapter 2

Formation of asphaltene nanoaggregates was studied as a function of solvent and concluded that nanoaggregation occurs regardless of solvent species, however a higher value for the free dimerization energy is required to dissolve nanoaggregates in *n*-heptane, which implies stronger intermolecular attraction due to solvophobic effects [194]. A number of GROMACS simulation studies agree with the Yen-Mullins model, as a significantly higher number of different asphaltene molecules prepared with *n*-heptane, aggregate in the three theorised stages: nanoaggregate, cluster, floc [189].

Further calculations of the free energy of dimerisation of the asphaltene molecules by other techniques, such as umbrella sampling (pulling dimers apart) help support the idea that the aromatic cores are the major driving force of asphaltene association [189]. The magnitude of the attraction is not only dependent on the number of aromatic rings, but also on the polarity induced by heteroatoms located within the core [189]. MD simulations were also employed in an attempt to eliminate the solvation effects as a factor in asphaltene aggregate configuration. In the absence of any solvent, the interaction of 100 model molecules was observed as the temperature was gradually varied from 25 to 300 °C [216]. The study conducted over this temperature range concluded that the rate at which the specific volume of asphaltenes increases with temperature is directly related to the length of the aliphatic chains (longer chains faster increase in specific volume with increasing temperature). Furthermore the glass transition temperature increases with the number of aromatic rings present in the core [216].

All the mentioned simulation studies mainly highlight the impact of the asphaltene chemical structure on the thermodynamic properties of their

Chapter 2

aggregation mechanism. This project employs the GROMACS software package to observe how changing the complexity of the chemical structure affects the asphaltene aggregation in an organic solvent suspension.

Chapter 3. Intermolecular interaction of triphenylene-cored model compounds in toluene

Chapter 3

3.1. Introduction

The molecular structure of natural asphaltene is predominantly composed of a core of aromatic rings surrounded by peripheral *n*-alkane chains, as suggested by previous studies [9,11-14,21,103,217,218]. The complex molecular structures along with functional groups cause asphaltenes to aggregate and precipitate when triggered by various environmental factors such as temperature, solvent quality, and concentration [3]. Asphaltenes follow a complex aggregation mechanism driven by polar and van der Waals interactions, which in turn are dictated by the molecular structure of the asphaltenes [1]. Previous attempts to investigate the relation between molecular structure, colloidal stability, and the driving forces of asphaltene aggregation concluded inconsistent mechanisms by which asphaltene molecules associate and aggregate because of the complex chemical nature of samples employed.

To isolate the effect of the aforementioned factors on the aggregation characteristics of asphaltene, model compounds with controlled chemical structures have been developed over the past decade [16,17,72]. Such model compounds can be categorised into two general groups, namely “archipelago” and “continental”. The “continental” class of asphaltenes is formed by a dominant aromatic core surrounded by alkyl side chains, while the “archipelago” class consists of aromatic and cyclo-alkyl groups linked together with alkyl carbon bridges [114,219].

Recent computational investigations of the “archipelago” [72] and “continental” [116] suggest that the polyaromatic rings of both archipelago and continental model asphaltenes associate into nanoaggregates in toluene due to

the presence of aromatic cores that favour π -stacking [114-116]. Asphaltene models with increased number of aromatic rings present in the core, such as hexabenzocoronene, show stronger aggregation behaviour due to the larger surface available for π -stacking interactions [112], which confirms a “continental” model would be suitable in replicating the π -stacking behaviour of natural asphaltenes. Previous studies on the self-association of small core models such as pyrene and alkyl bridged dipylene, representative of archipelago models, concluded that polar groups such as functional groups, play a major role in the formation of aggregates larger than a dimer [19]. This is primarily due to the polar charges these moieties possess, leading to strong polar and hydrogen bond interactions, as suggested by another study [122]. It confirms that the presence of key atoms or functional groups in the structure of polyaromatic compounds (PAC) has an equal or even greater influence than the size of the aromatic area available for π -stacking in promoting the aggregation of asphaltenes.

The effects of side group and chain length on the size and number of aggregates in both organic solvent and at the oil-water interface have been examined previously by incorporating a fixed hydrophobic part with branched alkyl chains with the polyaromatic core [38,121,122,160]. Research performed in the field of liquid crystals suggests that the presence and length of the side chains could possibly limit the potential stacking configurations to aromatic ring plane/core on aromatic ring/core (π -stacking interactions), as represented in Figure 3.1. The length of the chains also influences the interaction between formed aggregates or columns, as they determine the distance at which they are located from each other [220].

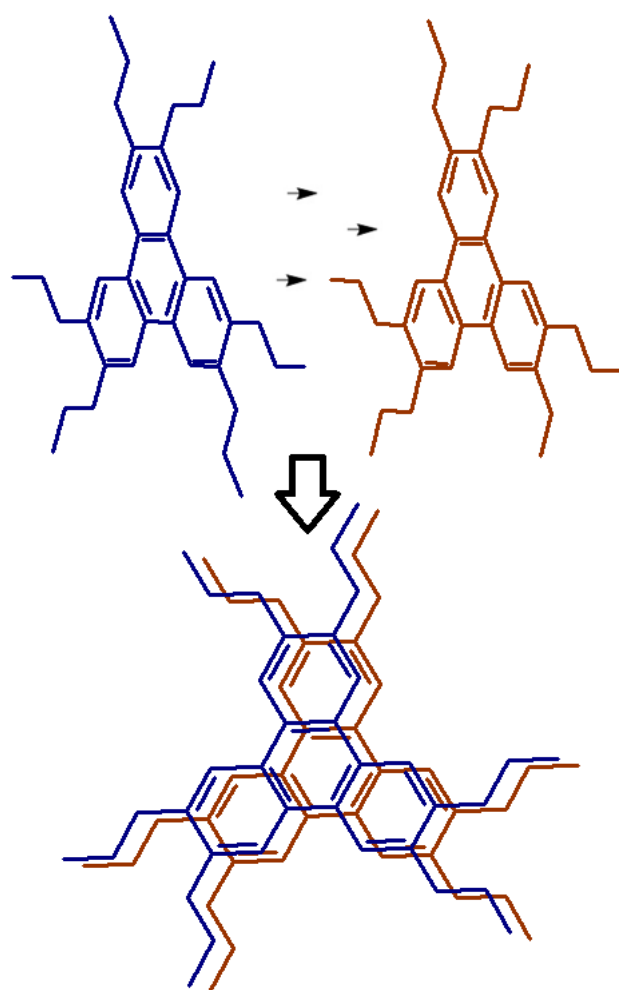


Figure 3.1. Model compound replicating the π -stacking of continental asphaltenes.

A range of molecular structures that fit the description of the “continental” model have been developed for liquid crystal applications [221]. Most of them are discotic molecules (aromatic core) which prefer to stack on top of each other forming columns, surrounded by heteroatoms and other moieties [222]. The majority of discotic liquid crystals form columnar meso-phases driven by the strong π -stacking interactions between their aromatic cores, with an approximated separation of 0.35 nm between the cores [223]. The properties of four symmetrically fused aromatic rings named “triphenylene” has been investigated

for decades and is the core structure for over 500 discotic liquid crystal [150,224]. Due to its exceptionally high charge carrier mobility, triphenylene was recognised as a suitable core element for discotic liquid crystals and has been employed as a starting structure for a variety of compounds [225].

Polyaromatic compounds have been developed for a wide range of applications such as harvesting arrays [226,227], organic thin film transistors [228,229], laser dyes [230], and organic solar cells [231], all of which harness the π -stacking and aggregation potential of triphenylene. Aromatic molecules such as triphenylene are a typical example of core molecule to which various lengths and species of side chains can be easily attached [232]. They exhibit liquid crystallinity at room temperature, and good solubility in organic solvents as well as being receptive to synthesising derivative compounds [233]. Furthermore, the obtained liquid crystals self-assemble into stacks, and therefore avoid charge trapping and recombination [233-235]. The stacking potential generates various physical properties, such as one-dimensional charge and energy migration [236], electroluminescence, ferroelectric switching [237], alignment and self-assembling behaviour in suspension, and on surfaces [232,236,237].

Due to its π -stacking capability and its broad potential for synthesising a variety of controlled chemical structures, triphenylene can be regarded as a strong core-element candidate for model asphaltene with continental molecular architecture. Asphaltene aggregation is considered to be mostly driven by π -stacking, and the attraction generated by functional groups [17,22,81]. As such, triphenylene was selected as the core molecule for synthesising model asphaltene

Chapter 3

compounds, to decipher the relation between the chemical structure of PACs and the corresponding self-association in an organic solvent environment.

Motivated by the large scale industrial problems caused by asphaltenes, this chapter focuses on the development of a series of “continental” model compounds replicating natural counterparts. A combination of experimental and computational approaches has been developed to investigate the solution dynamics of triphenylene based model compounds across multiple length scales as a function of concentration and time, while dispersed in toluene. Dynamic light scattering measurements were carried out to underpin the effect of concentration for two asphaltene model compounds and then the kinetics of all other compounds. Diffusion-ordered spectroscopy was employed as a complementary technique to DLS to identify the formation of nanoaggregates (dimers, trimers, or tetramers) as a function of concentration. Molecular Dynamics simulations were used to examine the aggregation and stabilisation mechanism, which also reveals the preferential interaction of the molecules as they reach equilibrium in more energetically favourable states.

3.2. Materials and methodology

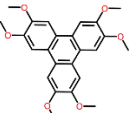
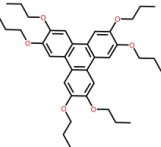
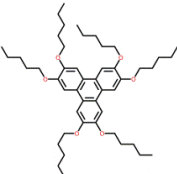
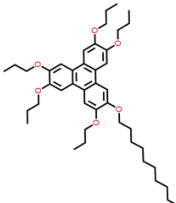
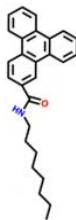
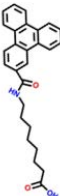
3.2.1. Materials

A series of model compounds were designed to investigate the individual effect of chain length and functional groups on the overall aggregation process. All triphenylene-based model compounds examined in the present work were synthesised by the group members of Professor Jon Preece in the School of Chemistry, University of Birmingham, UK. The model chemical structures are

Chapter 3

presented above in Table 3.1. Details concerning the chemical synthesis procedures are described in Appendices B.

Table 3.1. Triphenylene based chemical compounds

						
TPN-C0	TPN-C1	TPN-C3	TPN-C5	TPN-C10	TPN-CN	TPN-CNAcid

3.2.2. Methodology

3.2.2.1. Dynamic light scattering

Throughout the experimental work all samples and solvents were kept at constant room temperature ($22 \pm 0.5^\circ\text{C}$), ambient pressure, and with minimal exposure to visible light. All glassware was thoroughly washed with toluene and dried under nitrogen flow. Prior to suspending the compounds for DLS measurements, the toluene was filtered three times with PTFE filters (100 nm pore size). The synthesised compounds were mixed with toluene to reach target concentrations, of which 1 mL was loaded in quartz optical cell.

Toluene of different grades (99.85%, Extra Dry–AcroSeal; 99+ %, extra pure) and PTFE membrane filters (100 nm pore size, Whatman) were purchased from Fisher Scientific (Loughborough, UK). Quartz optical cell (S High Precision Cell –

light path 3x3 mm) was purchased from Hellman Analytics Q, and solvent resistant screw cap vials (7 and 15 mL) were purchased from Sigma Aldrich (Dorset, UK).

DLS measurements were carried out using a Zetasizer (Nano Series, Malvern) with a laser wavelength of $\lambda = 632.8$ nm, and scattering angle of 173° , with data collected at fixed time intervals (0, 24, 168 hours). Data analysis was performed with the integrated Malvern software. Each datum is an averaged value of three samples each measured over six repeats. The acquired ACFs of each sample set were analysed with the software, and only those meeting the quality criteria were recorded to calculate corresponding hydrodynamic diameters. TPN-C3 and TPN-C10 were measured at different concentrations (1, 10, and 20 mg/mL), while all the other model compounds (TPN-C0, TPN-C1, TPN-C5, TPN-CN and TPN-CNAcid) were measured at a constant concentration (10 mg/mL).

3.2.2.2. Molecular dynamics simulations

Molecular dynamics simulations were carried out using a GROMACS 4.6.5 software package that had been previously used to investigate asphaltene aggregation and intermolecular interactions, [18,116,185]. OPLS/AA force field was chosen as it has been tested with polyaromatic molecules previously [192], and has been proven to be reliable in examining PACs [193,194].

After a simulation box is generated and solvated, energy minimization is performed to ensure a stable initial configuration. Equilibration steps (1000) of 100 ps were then performed to prepare the simulation for trajectory production. The Berendsen algorithm was adopted to relax the system to 298 K and 1 atm

Chapter 3

pressure. Once steady fluctuations reached the average volume, the 100 ns simulations were performed with an integration time of 2 fs, a cut-off of 1.0 nm used for van der Waals interaction and periodic boundary conditions [204]. More detailed explanations regarding the software package and force field used are discussed in the Methodology chapter, while simulation command lines are included in Appendix A. Seven different asphaltene model compounds were constructed utilising the protocols established in previous studies, as described in Chapter 2. Initially, seven identical molecules of one model compound were placed in a toluene simulation box (700 toluene molecules) at equidistant positions. Once the equilibration steps were completed, the simulation was run for 100 ns during which the effect of the alkyl chain length and functional groups on molecular aggregation were examined.

The simulations were analysed using three methods: visual observations using a dedicated software - visual molecular dynamics (VMD), radial distribution functions (RDF) and the “g_dist” GROMACS function. VMD is a video software employed to visualise the simulation boxes, selectively observe molecules, and obtain snapshots of the video frames. RDFs were applied to quantify the average distance between the COM of selected molecules into distributions of $G(r)$ as a function of distance. The positions and intensities of the distribution peaks obtained, yield information about the average distance between the molecules. RDFs indicate the occurrence of aggregation events and quantify the interactions between molecules. The data obtained is normalised by the highest datum of the entire set to allow for a better comparison and presentation of the data. The g_dist function was used to examine the number of aggregation events by showing the

Chapter 3

distance of pairs formed between one molecule and the other six counterparts in the simulation box over the 100 ns simulation in toluene.

3.3. Results

3.3.1. Dynamic light scattering of model chemical compounds

3.3.1.1. Representative DLS sample set

An autocorrelation function (ACF) is defined as the correlation of a signal with a delayed copy of itself as a function of time [136]. Three ACF measurements of TPN-C1, prepared with toluene (concentration = 10 mg/mL), in the optical cell, at a scattering angle of 175° are presented in Figure 3.2 as an example of the data selection process.

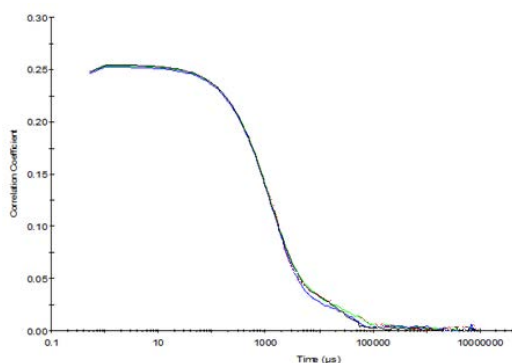


Figure 3.2. Autocorrelation functions of TPN-C1 model compounds suspended in toluene.

The ACF curves (blue, green, black) showed consistent sample characteristics, with a smooth decay from 300 to 3000 µs, indicating a uniform particle size distribution.

Acquired ACF data were fitted by the integrated software, as presented in Figure 3.3 to obtain corresponding diffusion coefficients, which were used to calculate the hydrodynamic diameter, based on the Stokes-Einstein equation

(2.5). The distribution of hydrodynamic diameters could be plotted by intensity and by volume (Figure 3.4).

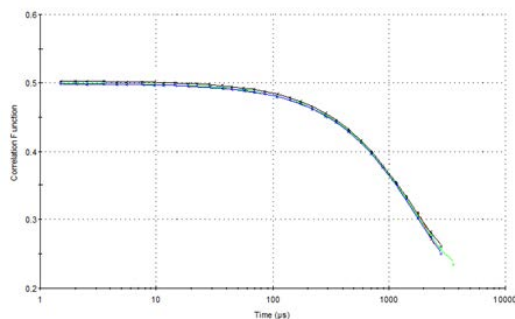


Figure 3.3. Autocorrelation function fitting by Malvern automated software of TPN-C1 model compound suspended in toluene.

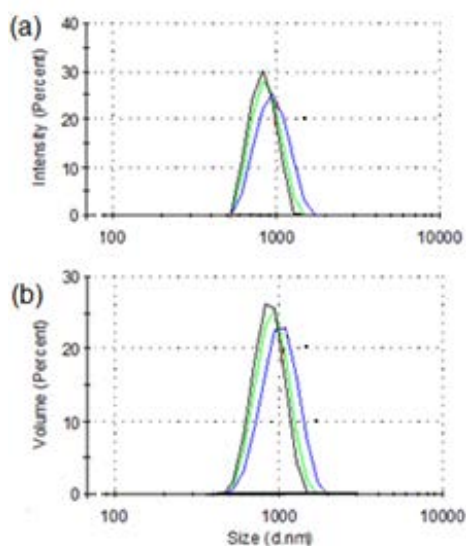


Figure 3.4. Distribution by (a) intensity and by (b) volume, of the hydrodynamic diameters of TPN-C1-toluene mixture.

Figure 3.4a presents the distribution of hydrodynamic diameters by intensity, which were weighted by the intensity of scattered light corresponding to each particle size fraction. For biological or polymeric samples, the intensity distribution can be misleading as it is proportional to the square of the molecular weight, which implies that particles of large size have significant influence on the averaged values than small ones do [142].

Based on Mie theory [138], the intensity distribution can be converted to a volume distribution (Figure 3.4b) that describes the relative fraction of each individual component in the mixture, depending on their mass or volume rather than scattering intensity [138]. However, volume distributions assume that all particles are spherical; hence they output the hydrodynamic diameter of the particles.

From the data presented in Figure 3.4, it can be concluded that the TPN-C1 molecules aggregate into clusters of around 1000 nm in hydrodynamic diameter, which is confirmed by the consistency between the distributions of both volume and intensity. The hydrodynamic diameters presented in the rest of this chapter are the average of the volume distributions (three measurements of each sample). DLS measurements record the hydrodynamic volumes particles/molecules occupy in solution. As such, if planar molecules such as the model compounds investigated in this study π -stack, the difference in hydrodynamic volume of the aggregate is not detectable by DLS until the length of the stack is longer than the width of the core model compound molecule. This can lead to uncertainty in measurements as it is very difficult to determine the difference between a single molecule and nanoaggregate formation (dimer, trimer, and tetramer) solely by relying on DLS measurements.

3.3.1.2. Effect of concentration on aggregation in toluene

Previous studies suggest that the concentration of natural asphaltenes has a significant influence on their aggregation despite inconsistent threshold for aggregation being reported, especially when comparing natural asphaltene to model compounds. It was identified that natural asphaltenes tend to aggregate at

~0.3 mg/mL or above, whilst the model asphaltene aggregation was recorded above 5 mg/mL [17,21,162]. The hydrodynamic diameters of representative models (TPN-C3 and TPN-C10) were measured as a function of concentration at multiple time intervals, across a range of concentrations (1, 10, and 20 mg/mL in toluene), and are shown in Figure 3.5 and 3.6.

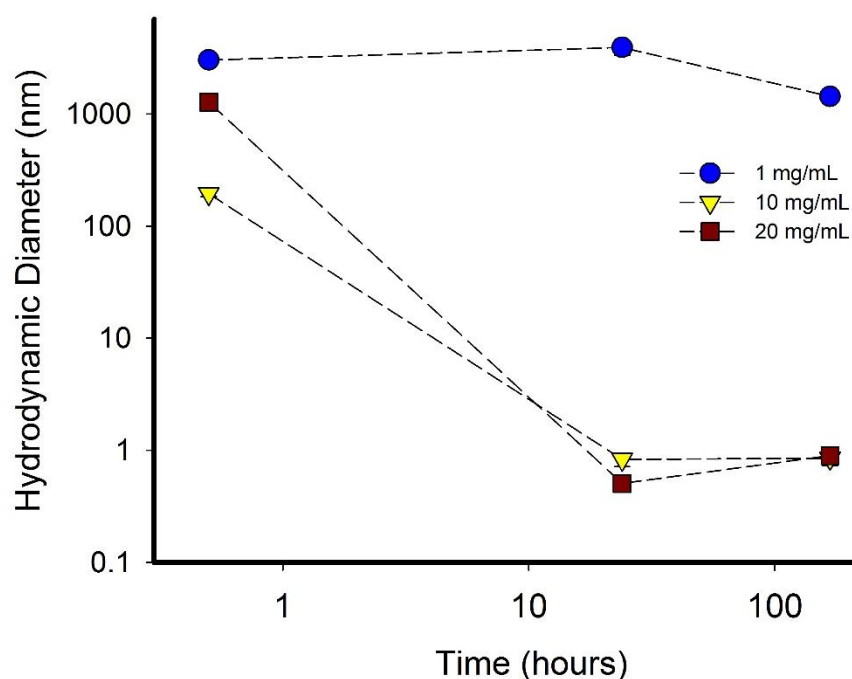


Figure 3.5. Averaged hydrodynamic diameters of sample TPN-C3 in toluene presented as a function of time at three different concentrations (1, 10 and 20 mg/mL). Error bars were similar in magnitude to the dimensions of the symbols used in the graph.

For TPN-C3, the initial particle sizes are over 500 nm without any particular correlation with the concentration, as shown in Figure 3.5. For the lowest concentration (1 mg/mL), the size remains constant throughout the measurement period (168 hours), whilst the averaged size reduces substantially to ~ 1 nm after the first 24 hours for the suspensions of 10 and 20 mg/mL. Some degree of turbidity was observed immediately after introducing TPN-C3 to toluene with high target concentrations (10 and 20 mg/mL), which was not found with 1 mg/mL

Chapter 3

suspension. Within 24 hours, the initial powder compound was completely dissolved in the toluene.

The first measurements of the 10 and 20 mg/mL concentrations yielded large and erratic particle sizes. However, if left to settle for a few minutes, the sizes decreased and stabilised to ~ 1 nm. It is probable that some degree of precipitation occurred at 10 mg/mL, although it was not visible, but the quality and consistency of the measurements significantly increased after settling. At 20 mg/mL, precipitation was visible and the initial particle size was significantly larger. However, it decreased to ~ 1 nm after 24 hours, in a similar manner to the sample at 10 mg/mL, only at a slower rate. The sediment of the 20 mg/mL sample, observed at the bottom of the optical cell, suggests the saturation limit of the solvent reached for the TPN-C3.

Light scattering measurements were then carried out with TPN-C10 suspensions, and the acquired hydrodynamic diameter is presented as a function of target concentration and time in Figure 3.6. Unlike what was observed with TPN-C3, which possesses a large particle size initially, the measured hydrodynamic diameter for TPN-C10 upon being suspended in toluene is ~ 1 nm, which suggests a complete and instantaneous solvation of the TPN-C10 by the toluene. It is worth noting that the particle size remains constant throughout the measurement window, indicating that the model compounds are stable with no aggregation occurring between them. The results also show that light scattering is a suitable technique in studying the solution dynamics of PACs despite that some caution is necessary when interpreting the acquired data.

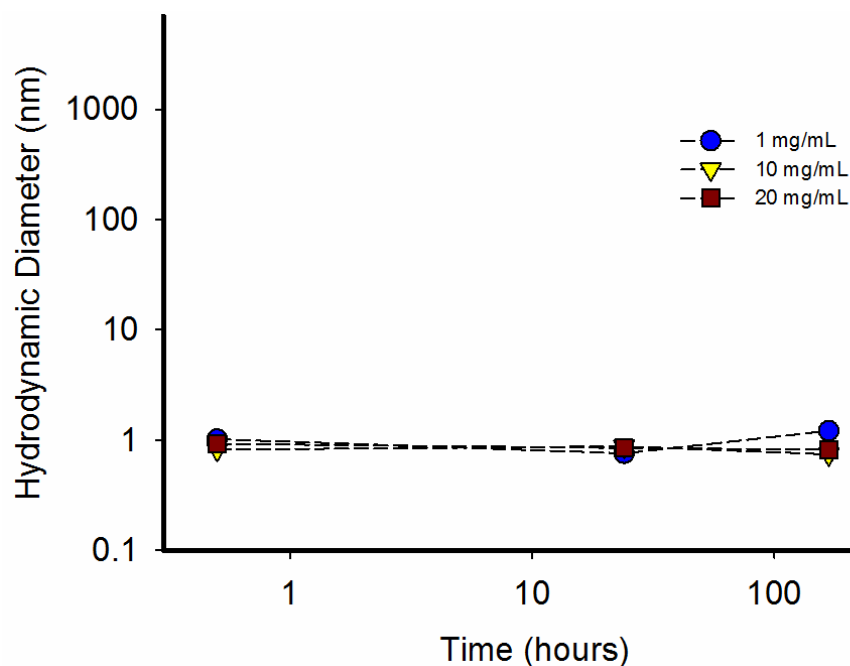


Figure 3.6. Averaged hydrodynamic diameters as a function of time for TPN-C10 suspended in toluene at three different concentrations (1, 10 and 20 mg/mL). Error bars were similar in magnitude to the dimensions of the symbols used in the graph.

3.3.1.3. Aggregation of model compounds by dynamic light scattering

To investigate the influence of chemical structure, specifically the length of the alkyl branches and functional groups, on the aggregation and stability of polyaromatic molecules in toluene, the seven model compounds developed could be categorised in two groups. TPN-C0 (triphenylene) was included in both groups as a benchmark because it is the core structure for all of the compounds examined in the present work. The first group is focused on the effect of the presence and length of the alkyl chains on the aggregation mechanisms of the model compounds, while the second group investigates the impact of an amide and a carboxylic acid group.

During the synthesis, two alkoxy groups were introduced on each of the three external aromatic rings of triphenylene (TPN-C0). The products possessing centrosymmetric structures are named as TPN-C1, TPN-C3, and TPN-C5

according to the number of carbon atoms in the alkyl branch (1, 3 and 5). One of the six branches of TPN-C3 was extended to 10 carbons, so called TPN-C10. To examine the impact of functional groups, an alkyl chain (9 carbons) with an amide group were added to the triphenylene core and named TPN-CN for the nitrogen in the amide group. To the tail-end of the TPN-CN, a carboxylic acid group is added and the model compound TPN-CNacid named.

3.3.1.3.1. Effect of chain length on intermolecular interactions in toluene

The hydrodynamic diameters of aggregates in toluene were measured as a function of time for the following model compounds: TPN-C0, TPN-C1, TPN-C3, TPN-C5, and TPN-C10, to underpin the influence of chain length on the intermolecular interactions between such model compounds. The ACFs were collected from three samples per compound, with each sample being measured six times. The previous section described the concentration dependence of two model compounds, and highlighted different solubility between the model compounds. TPN-C10 was dissolved and achieved particle stability in solution instantly, however TPN-C3 required more time with increasing concentration. As such, 10 mg/mL was chosen as the default concentration for all model compounds as it allows for stability to be achieved within minutes while at the same time, sufficient molecules exist in solution to scatter enough light for DLS measurements and to potentially aggregate. The averaged hydrodynamic diameters acquired, with corresponding standard errors, are presented in Figure 3.7. The data reveal not only the effect of the peripheral aliphatic chain length on the preference of aggregation, but also the corresponding kinetics.

Chapter 3

After mixing the PACs with toluene, it was found that visible aggregates were immediately formed for some of the compounds, but not others. As the benchmark, the aromatic core without any side chains (TPN-C0) dispersed completely in toluene, resulting in an initial hydrodynamic diameter of 0.7 nm, which remains constant throughout. As a contrast, PACs with extended alkyl branches tend to form significantly large particles upon being introduced into toluene – the aggregates formed by TPN-C1, TPN-C3, and TPN-C5 are all above 100 nm in diameter. It is worth noting that TPN-C10 has a similar average diameter to that of TPN-C0 despite the presence of one alkyl tail.

Data collected at 24 hours shows a significant reduction in size for TPN-C3 and TPN-C5, with a similar size for TPN-C0 and TPN-C10. Not only does this suggest that there is dissolution during the 24 hours, but also that the PACs are well dissolved by the end of the process. However, TPN-C1, the model compound with shortest branch, does not dissolve fully, despite that the size is reduced to approximately 700 nm.

After 168 hours, it appears that the four PACs that were fully dispersed at 24 hours remain at a similar size (~ 1 nm), which indicates that these compounds are in a stable configuration after the dissolution. It is likely that the presence of alkyl branches brings in steric hindrance to hamper the formation of aggregates once they are fully dissolved. Such an effect is reduced to minimum with TPN-C1 that has an averaged size of ~ 1100 nm after 168 hours.

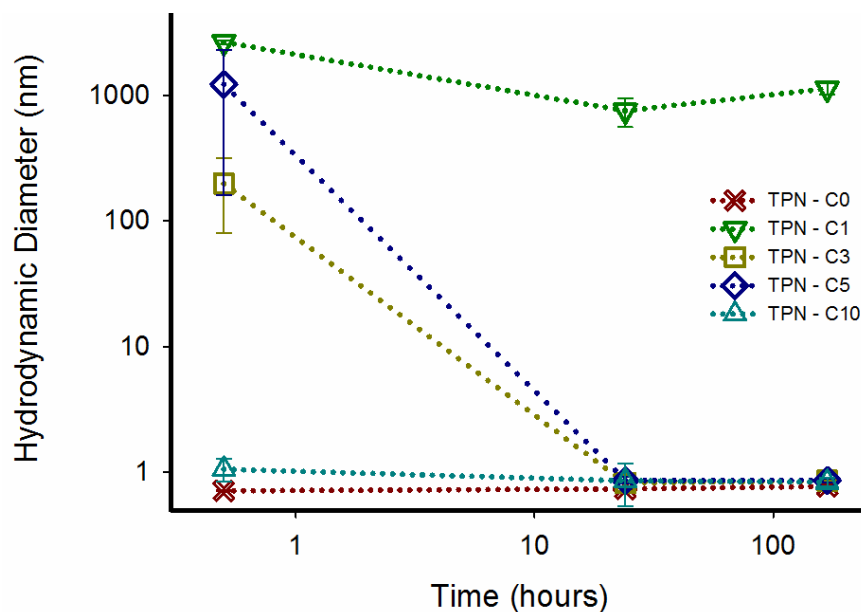


Figure 3.7. Averaged hydrodynamic diameters as a function of time for TPN-C0, TPN-C1, TPN-C3, TPN-C5 and TPN-C10 at 10 mg/mL.

3.3.1.3.2. Effect of functional groups on the intermolecular interactions

By incorporating an amide group (TPN-CN) or a carboxylic acid group (TPN-CNacid) to an alkyl branch attached to the triphenylene core, large clusters were observed immediately upon being mixed with toluene. Figure 3.8 compares the hydrodynamic diameters of the model compounds with functional groups (TPN-CN, TPN-CNacid) to the benchmark (TPN-C0), as a function of time. The one without any alkyl branch, as noted in the previous section, remains dispersed throughout the measurement period with size less than 1 nm.

Similar to the ones carrying alkyl branches, TPN-CN and TPN-CNacid form large aggregates whose sizes are ~ 774 nm and ~ 378 nm respectively, once they are dispersed in toluene. After 24 hours, the size of TPN-CNacid particles was reduced to nearly half of the initial value, which could be due to the dissolution, whilst the size of the TPN-CN particles remains constant (~399 nm). The

hydrodynamic diameters of both TPN–CNAcid and TPN-CN increase to 3012 nm and 794 nm respectively after 168 hours. This suggests that the presence of functional groups in asphaltene model molecular structure increased the aggregation potential of the chemical structure and overcame the repulsion barrier set by the aromatic solvent. It was assumed that these size variations occurred due to continuous re-configurations of the existing clusters. Previous studies of non-centrosymmetric model compounds with polar moieties recorded initial aggregation driven by functional groups [15,118,122]. Furthermore, the studies suggested that π -stacking can occur, and participate, in intra-aggregate reconfiguration, after initial aggregates are formed. This would explain the large aggregates with varying cluster sizes recorded by DLS in this study.

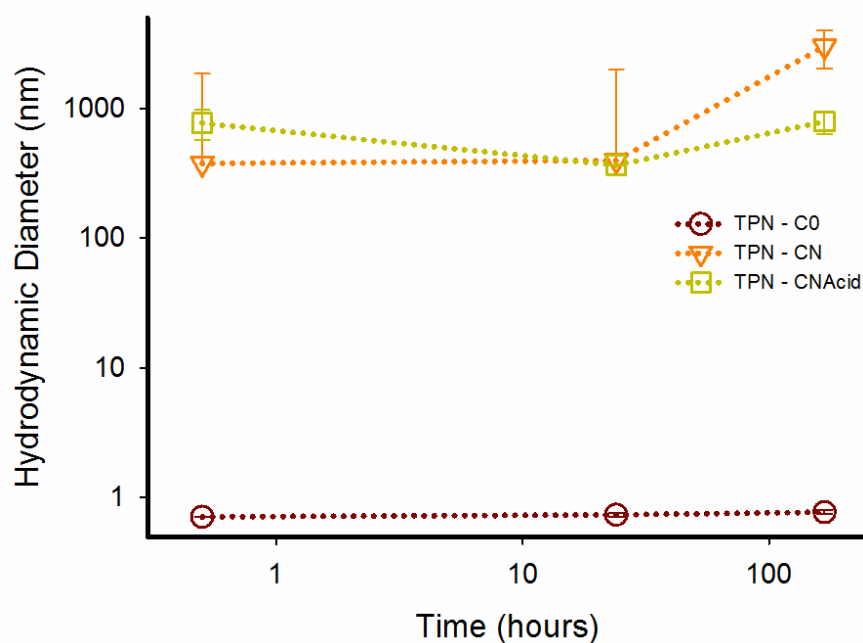


Figure 3.8. Averaged hydrodynamic diameters as a function of time for TPN-CO, TPN-CN, and TPN-CNAcid at 10 mg/mL.

Chapter 3

3.3.1. Molecular dynamics simulations of model compounds

3.3.1.1. Radial distribution functions of model compounds solvated by toluene

The radial distribution function (RDF) is one of the most commonly employed approaches to analyse molecular interactions and characteristics in GROMACS MD simulations. They quantify the average distance between the centres of mass of selected molecules into distributions of $G(r)$ as a function of distance. After running simulation where seven molecules of each model compound were placed in a toluene simulation box, RDF plots were then generated from each simulation. The height and width of the peaks presented in the RDF are related to the molecules interacting, the occurrence of aggregation events, as well as the aggregate configuration in toluene, by relating the known chemical distances, such as 0.351 for π -stacking of aromatic molecules, to recorded RDF data. Previous studies utilise RDF data to assess packing distances and configurations of asphaltene model compounds as a function of solvent species [238]. The RDF data results were normalised by the value of the highest datum of all model compounds and presented in two groups accordingly.

Figure 3.9 shows the RDF of the compounds with different tail groups placed in a toluene simulation box. The height of the peaks (intensity of $G(r)$) indicates the density of the interaction between the model compounds, while the position of the peak marks intermolecular distances.

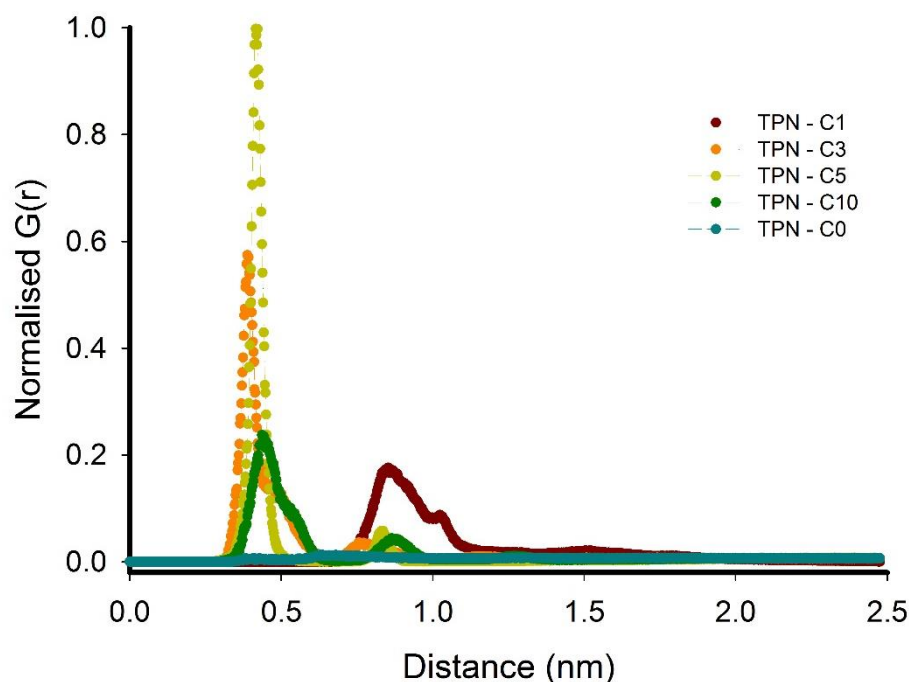


Figure 3.9. Normalised radial distribution functions for TPN-C0, TPN-C1, TPN-C3, TPN-C5, and TPN-C10 model compounds placed in a toluene simulation box over 100 ns.

A narrow peak indicates a consistent distance between molecules, which can be associated with specific configurations, such as 0.35 nm is the average distance between two π -stacked aromatic molecules [61]. A broad peak (multiple distances) suggests that particles have associated/aggregated but are positioned at multiple distances apart [185].

The RDF of TPN-C0 model molecules do not exhibit interactions other than collisions resulting from Brownian motion. As such, no bell-peak forms, only a slight increase, as the RDF shifts due to the uniform density distribution. Broad peaks such as are exhibited by TPN-C1 indicate the existence of aggregation, but across a large distance (0.7 and 1.1 nm). The resulting aggregates present a variety of configurations, which can be associated with the large hydrodynamic sizes recorded by the DLS.

TPN-C3 and TPN-C5 both exhibit tall and narrow peaks at a distance matching parallel configurations, which implies that the main aggregate conformation can be attributed to π -stacking [112]. So far, increasing the chain length around the aromatic core appears to impose parallel conformation upon the aggregates, a behaviour similar to liquid crystals [223]. TPN-C10 displays a broader distribution but with its highest point close to the same π -stacking distance. This suggests that the increase of one chain facilitates the formation of other configurations, but not necessarily limited to core-on-core, but tail-to-core as well.

Overall, the increasing chain length has a marked effect on limiting the interactions to parallel configurations, until non-centrosymmetric molecules allow for alternatives, but still driven by π -stacking. The limiting factor of the model compounds can be associated with the DLS data, that show large aggregates corresponding to the position indicated in the distributions.

As suggested by the light scattering results, the nature of aggregation changes significantly upon incorporation of amide or carboxylic acid groups to the model compounds. Figure 3.10 shows the normalised RDFs of the two model compounds with amide or carboxylic acid groups placed in toluene simulation box. TPN-C0 data is included to highlight the influence of the chemical functional groups on the intermolecular interactions and distances.

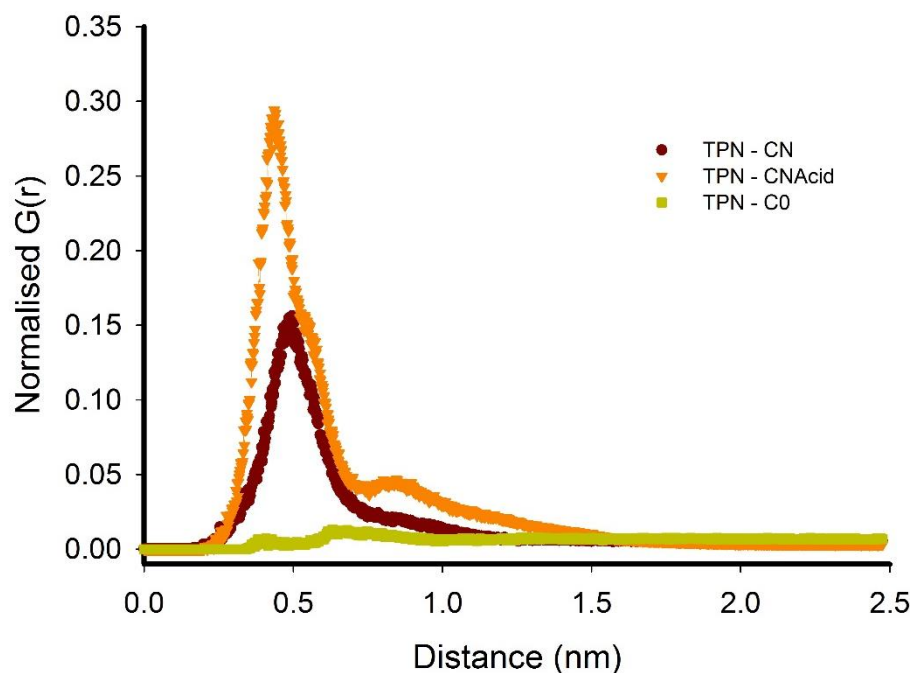


Figure 3.10. Normalised radial distribution functions for TPN-C0, TPN-CN and TPN-CNacid model compounds, suspended in toluene, over 100 ns simulation time.

The RDF curve of TPN-CN shows a broad peak between 0.3 nm and 0.7 nm, with a slow decay from 0.7 nm to 1.2 nm, which suggests the formation of aggregates in toluene with broad conformational freedom. The polarity of the model compound overtakes the π -stacking, which allows the non-centrosymmetric molecules to associate due to their polarity rather than the size of the aromatic surface [118]. This is reflected in the large sizes recorded by DLS measurements. However the continental architecture of the model compound tends towards the more energetically favourable planar configurations [72], as shown by the position of the main peak.

The TPN-CNacid model compound exhibits a peak between 0.3 nm and 0.7 nm, with a distinctive height, and a secondary peak (0.7 nm to 1.6 nm) on its decay at 0.8 nm, indicating a similar but stronger behaviour to TPN-CN. The addition of the acid group at the tail-end increases the polarity of the model compound, which

in turn increase the aggregation potential. Again, the continental architecture of the model compound re-configures the aggregates towards planar arrangements, as was noted in previous studies [121,122].

Overall, the polar aspect of the model compounds not only increases aggregation potential, as demonstrated by the large aggregates measured by DLS and previous studies [16], but also broadens molecular configurations.

3.3.1.2. Intermolecular distances measured by g_dist

For any of the simulations carried out, the distance between one individual model compound molecule and the other six in the same simulation box, could be extracted and presented as a function of simulation time by utilising the GROMACS g_dist function. The g_dist function for all seven model compounds are shown in Figure 3.11, Figure 3.12, and Figure 3.13. The six curves shown in each figure correspond to the distance between each pair, which reveals the intermolecular distances and the preference for aggregation. The dimension of the simulation box is fixed as 5 nm (± 0.3 nm) in each direction, which constrains the distance between each pair of molecules to be less than that. Formation of aggregates driven by π -stacking shows a characteristic distance of 0.3-0.5 nm [61]. Once a stable aggregate is formed (dimer, trimer, tetramer), the corresponding plot is reduced and remains constant. In the cases of large aggregates where more than two molecules are involved, multiple stabilised g_dist plots could be observed – the number of parallel, consecutive plots shows how many molecules stack together.

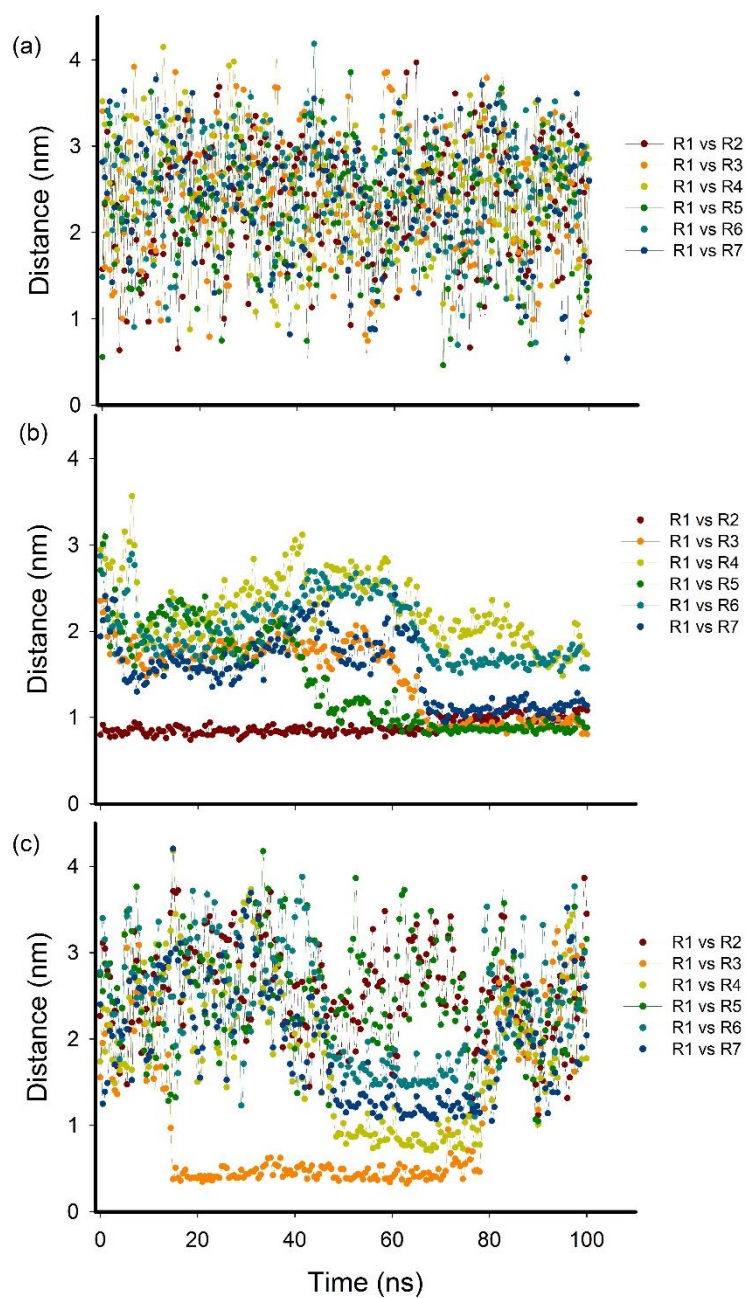


Figure 3.11. Distance between the centres of mass of one model compound molecule (R1) with the other six (Rn) in the simulation over 100 ns simulation time in toluene: (a) TPN-C0; (b) TPN-C1; (c) TPN-C3. The six colours shown in each figure correspond to the distance between each pair of molecules.

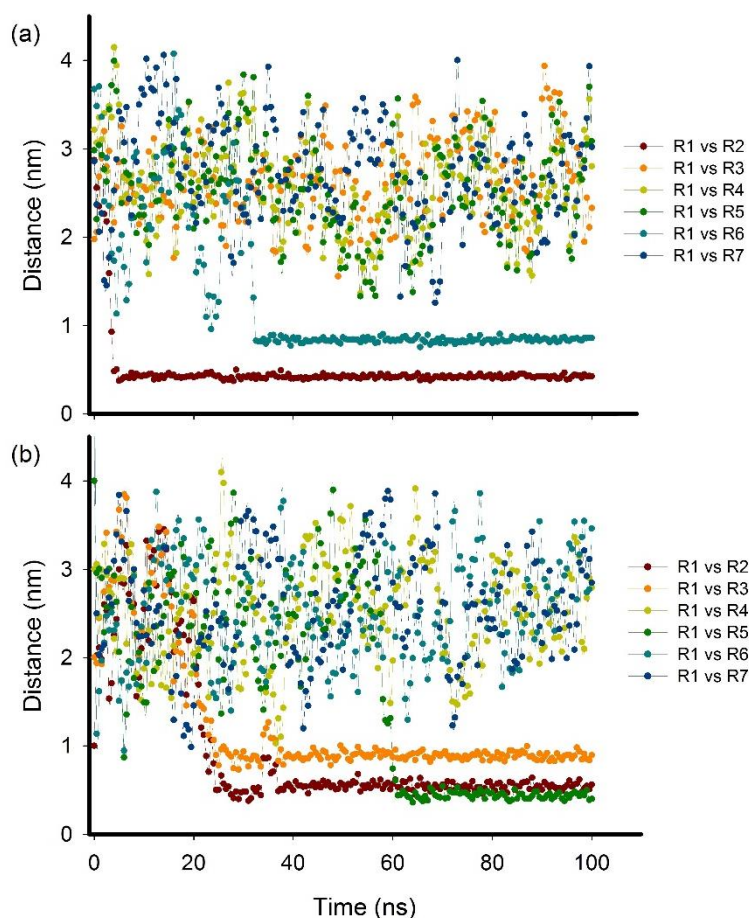


Figure 3.12. Distance between the centres of mass of one model compound molecule (R1) with the other six (Rn) over 100 ns simulation time in toluene: (a) TPN-C5; (b) TPN-C10. The six colours shown in each figure correspond to the distance between each pair of molecules.

Figure 3.11a shows the g_dist plots of TPN-C0 molecules as they randomly collide over the 100 ns simulation period with distances registered between 0.5 and 4 nm, which is expected for a freely diffusive system that follows Brownian motion. This is consistent with the light scattering result of TPN-C0 which is fully dissolved in toluene with no aggregation for a prolonged measurement window. As for TPN-C1 (Figure 3.11b), one pair of molecules forms a dimer of non-parallel configuration, that remains a constant distance for the entire simulation time. Other pairs of molecules are kept at a distance ~ 2 nm before some participate in the aggregation. Overall, the characteristics of g_dist plots of TPN-C1 behaviour

suggest the existence of multiple aggregation configurations, as the peripheral alkyl chains were too short to force any limitations on the assembly. This is also in agreement with the light scattering result, which shows a strong tendency for TPN-C1 to aggregate.

As shown in Figure 3.11c, although the TPN-C3 molecules appear to be dispersed at the initial stage of the simulation, one dimer is formed at ~ 20 ns, with another three pairs of molecules associated with the cluster at around 50 ns. However, the formed tetramer, indicated by four parallel g_{dist} plots, dissolved at 80 ns. In agreement with the DLS data, the TPN-C3's aggregation number, after stabilisation, is limited to nanoaggregate sizes. Liquid crystal literature suggests the size of the aggregates varies depending on solvophobicity [239]. TPN-C3 tends to associate into larger aggregates by π -stacking, but dissolves once the aggregate size exceeds an energetically favourable state. A similar pattern of aggregation behaviour has been recognised with TPN-C5, with one dimer being formed at the start of the simulation and another molecule associating with the stack at around 37 ns (Figure 3.12a). Despite being surrounded by aromatic solvent molecules, and the long peripheral chains possibly limiting the assembly to π -stacking, TPN-C3 and TPN-C5 show the preference to aggregate in π -stacking configurations because of their large aromatic surface and their size limitation to nanoaggregates as was recorded by DLS.

Figure 3.12b show the distance over time of the TPN-C10 molecules. The formation of a trimer occurred at approximately 25 ns (dark red and orange) with another molecule associating with the stack at 60 ns (green). This captured the aggregation that occurred due to π -stacking interactions, although at a lower

magnitude than the TPN-C3 and TPN-C5 model compounds. This could possibly be due to the long tail group added to this model compound, which is known to impede aggregation [116,220]. The behaviour is reflected in the DLS measurements, which captured nanoaggregates of ~ 1 nm. Unlike TPN-C3 and TPN-C5 that required more than 24 hours to dissolve, TPN-C10 dissolves immediately after solvation. This behaviour can be solely attributed to the increase of one side-chain. The extending of the tail destabilises the column association that TPN-C3 and TPN-C5 follow, making TPN-C10 more soluble in toluene, less disposed to aggregate, but still allowing parallel configurations in the nanoaggregates to occur.

Figure 3.13a (g_{dist} of TPN-C0) is again introduced as a standard for a fully dissolved model compound. Figure 3.13b shows the assembly of several TPN-CN dimers for short periods of time. At 30 ns a trimer was formed, but it dissolved at 45 ns. The predisposition of TPN-CN to form unstable aggregates is reflected in the error bars of the DLS data. The distances recorded by MD simulations suggests that TPN-CN molecules aggregate into loose configurations.

The TPN-CNacid (Figure 3.13c) showed the highest number of associations. A dimer was formed at the start of the simulation (dark red), trimer at 15 ns (green), and tetramer 20 ns (yellow). At 40 and 50 ns two more molecules associated with the existing cluster (orange at 40 ns and yellow at 50 ns) for a short period of time. The varying distances (blue and green) suggest a continuous re-assembly throughout the cluster as would be expected of the model compound with the most polar functional groups.

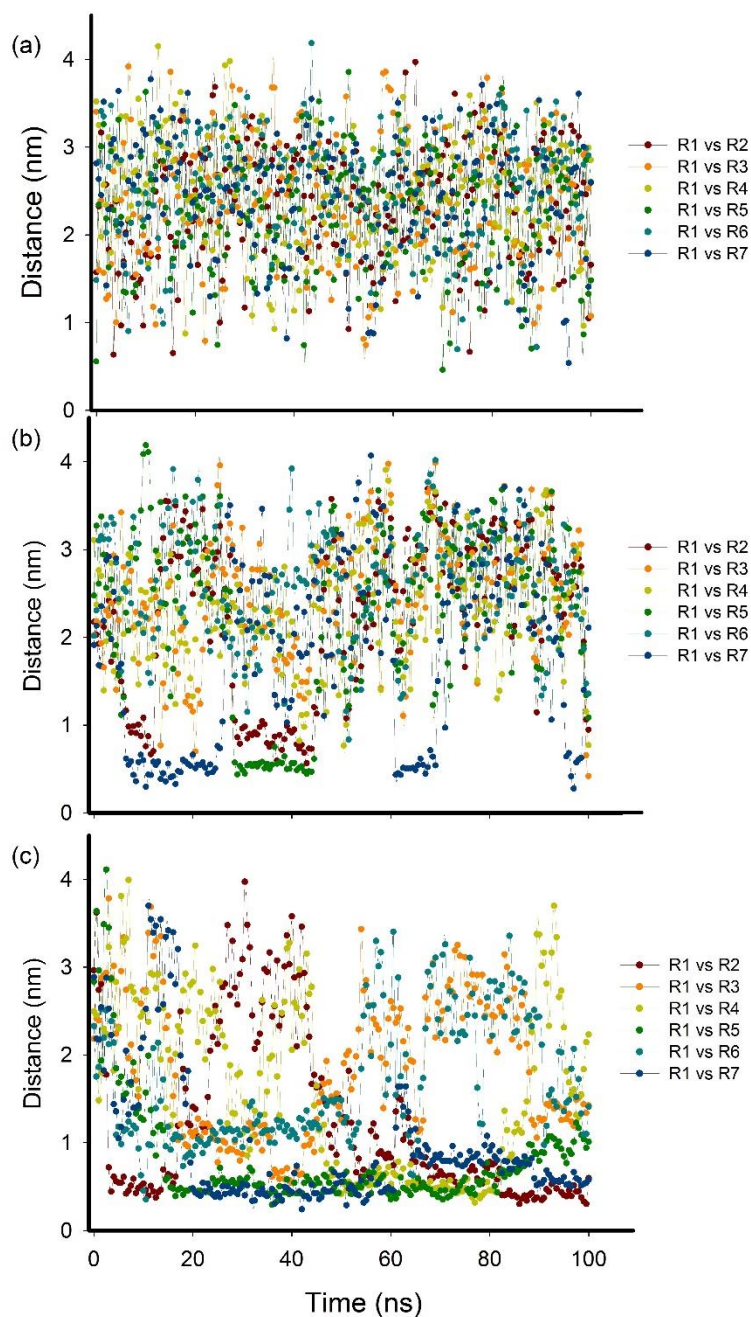


Figure 3.13. Distance between the centres of mass of one model compound molecule with the other six in the simulation during the 100 ns simulation in toluene: (a) TPN-C0; (b) TPN-CN; TPN-CNAcid. The six colours shown in each figure correspond to the distance between each pair of molecules.

These chemical groups induce the polarity to the model compound that in turn significantly increases the aggregation potential, as also seen by DLS data. Furthermore, the polar nature of the model compound drives initial aggregation to form clusters with multiple configurations. However, other studies suggest that π -

Chapter 3

stacking contributions can be seen over time [4,18]. The g_dist data supports this as distances between 0.3 and 1.2 nm are recorded, which indicate multiple, including parallel, configurations.

Representative snapshots of the simulations of three of the seven model compounds are presented in this chapter in order to allow for a visual component to complement the numerical and plotted data presented so far. The snapshots were chosen from among the final frames of the simulation time and represent a subjective manner of observing the characteristics and interactions of the model compounds as a function of chemical structure. TPN-C0 (Figure 3.14a) was chosen, not only because it is the core model compound, but also because it is the only model compound that does not aggregate in toluene. In fact, the model compound operates as expected of a colloidal suspension, with random collisions occurring throughout the observation time. In the snapshot of TPN-C5 (Figure 3.14b), dimers can be seen, as is consistent with the RDF and the g_dist data. The π -stacking configuration of the dimers can also be observed, as the peripheral alkyl chains restrict the number of possible configurations. This is consistent with other molecular dynamics simulation studies of “continental” asphaltene model compounds [193]. The snapshot of TPN-CNacid (Figure 3.14c) shows how the molecules prefer to aggregate into a larger, less dense cluster, as expected from both the RDF, g_dist and DLS data. The configuration does not appear to be limited to π -stacking, as the carboxylic acid and amide groups favour both head-to-tail and head-to-head configurations.

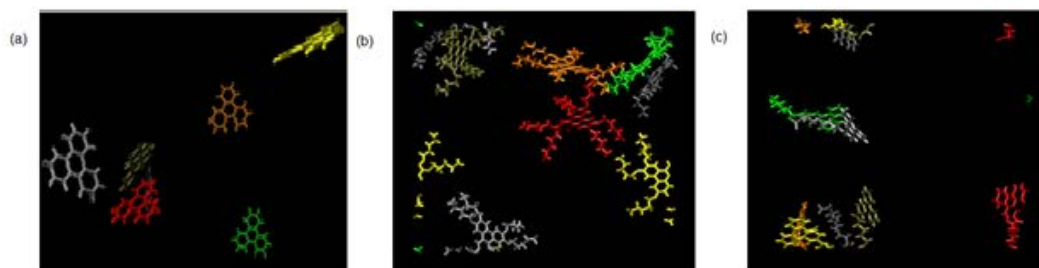


Figure 3.14. Snapshots of MD simulations of seven (a) TPN-C0; (b) TPN-C5; (c) TPN-CNAcid in toluene, showing the interactions between the molecules after 100 ns of simulation time. The toluene molecules are not shown for clarity.

3.4. Discussion

3.4.1. Effect of concentration on aggregation in toluene

The concentration of natural asphaltenes in crude oil has been identified as a major factor to influence the stability of the crudes as well as the aggregation mechanisms of asphaltenes [240]. However, it is very challenging to isolate the specific intermolecular interactions and associate them with the effects of asphaltene concentration, due to the myriad of chemical structures possessed by natural asphaltene. The hydrodynamic diameter results acquired from the model compounds (TPN-C3 and TPN-C10) dispersed in toluene would help to clarify the concentration dependence of asphaltene-like compounds and the corresponding equilibrium kinetics. Although discotic liquid crystals based on triphenylene have been reported to have concentration dependent properties, such as conductivity, which is linearly dependent to the number of carriers, the size and stability of nanoaggregates in organic solvents such as toluene has not been studied [241].

Three concentrations of the two models compounds (TPN-C3 and TPN-C10) were investigated and are represented in Figure 3.5 and Figure 3.6. The inconsistency with particle sizes of TPN-C3 at 1 mg/mL is probably due to the poor quality of scattering during the measurement. With concentrations as low as 1

Chapter 3

mg/mL, there are scattering units to scatter the light beam – the instrument tends to over-compensate if the detected intensity is too weak, resulting in unrealistic particle sizes. At 10 mg/mL, DLS is capable of recording the hydrodynamic diameters of the aggregates around 1 nm in size, suspended in toluene. Visible precipitation was observed for TPN-C3 suspended in toluene at 20 mg/mL, indicating the presence of an excessive amount of precipitate that probably does not influence the size of the aggregates once stability is reached (after 24 hours). Overall, TPN-C3 does not seem to have a clear concentration dependence because it appears to reach a stable state (1 nm), after 24 hours, for concentrations of 10 mg/mL and above.

By contrast, different types of correlation between solubility and molecular structure were observed for TPN-C10, which dissolves completely in toluene (1 nm) and requires very little time to reach the equilibrium for any of the 3 concentrations examined. Comparison between TPN-C3 and TPN-C10 (same structure but with a 10 carbon alkyl chain) suggests that the length and structure of the PACs have a significant role in determining solubility in toluene.

Because light scattering techniques can only measure the hydrodynamic diameter, whereas the model compounds examined in the present work possess a planar molecular structure, which facilitates π -stacking, it was very difficult to differentiate between single molecules (complete diffusivity) and nanoaggregates that grow in aggregation number but not in hydrodynamic diameter. As such, DOSY experiments were performed for the TPN-C3 and TPN-C10 model compounds. The diffusion coefficients indicated that the molecules formed stable

nanoaggregates (3-5 molecules/aggregate) in toluene, suggesting that a stabilised state of the TPN-C3 and TPN-C10 models in solution was achieved.

Natural asphaltenes are often compared to surfactants [22], and as such are thought to have concentration-dependent aggregation behaviour in toluene [103]. Unlike the myriad of chemical structures that impact the concentration dependence in natural asphaltenes, this project employs well known structures and succeeds in isolating the structure-function relation, as the addition of a long tail (TPN-C10) appears to negate the concentration dependence by increasing solubility and produces stable nanoaggregates (~ 1 nm) at all tested concentrations. According to DOSY measurements, TPN-C3 exhibits a similar behaviour, but at 1 mg/mL, there is insufficient scattering for DLS measurements, while at 20 mg/mL solid deposits were observed. This led us to choose 10 mg/mL as the nominal concentration for this study. At 10 mg/mL TPN-C3 requires more time to reach a stable state (1 nm nanoaggregates), a behaviour attributed to either a slow dissolution of the solid powder in toluene, or the formation of large unstable columns that later break down into smaller stacks, as was observed in previous studies of PACs in toluene [109,112]. By coupling the DOSY and DLS data, we can conclude that concentration did not play a significant role in the aggregation of the model compounds in this work, once the suspension has stabilised.

3.4.2. Effect of chain length on intermolecular interactions in toluene

Previous studies concerning liquid crystals suggest that the length of alkyl chains surrounding the triphenylene core could have the following two roles: stabilising the formed discotic liquid crystal columns, and determining the distance

between the columns [221]. Furthermore, functional groups were often added to these chains to facilitate specific reactions or to influence the self-association process of these molecules. When employed as model compounds in replicating the behaviour of natural asphaltenes, the focus is on the intermolecular association as a function of chemical structure and solvent, as well as the kinetics of aggregate formation.

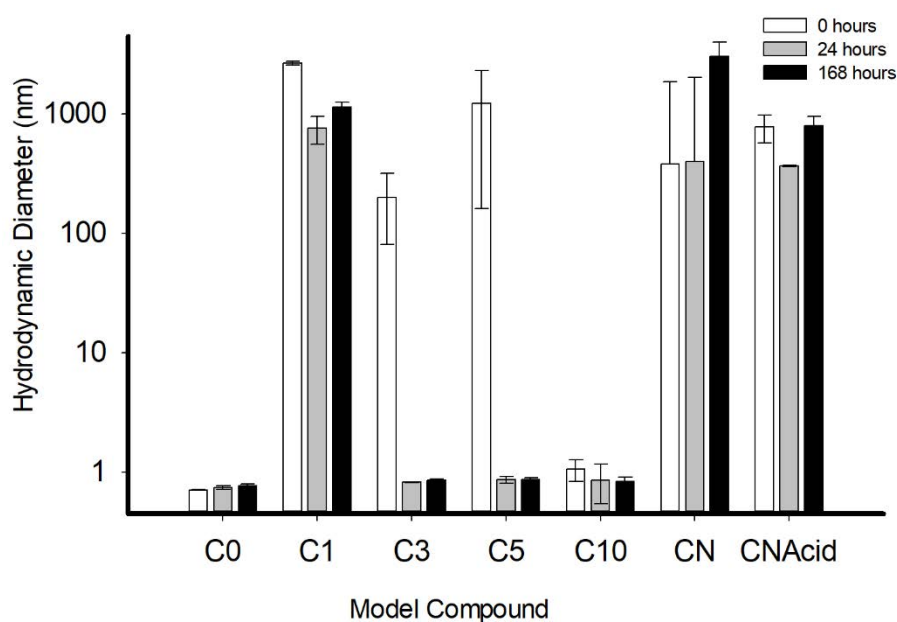


Figure 3.15. Averaged hydrodynamic diameters for the model compounds at 10 mg/mL.

The benchmark model compound used, TPN-C0, does not appear to aggregate when suspended in toluene. Despite it being composed of four fused aromatic rings, generating an open aromatic surface, the triphenylene was found to be fully dissolved without any preference for self-association when dissolved in toluene – no particles above 1 nm were observed in the DLS experiments.

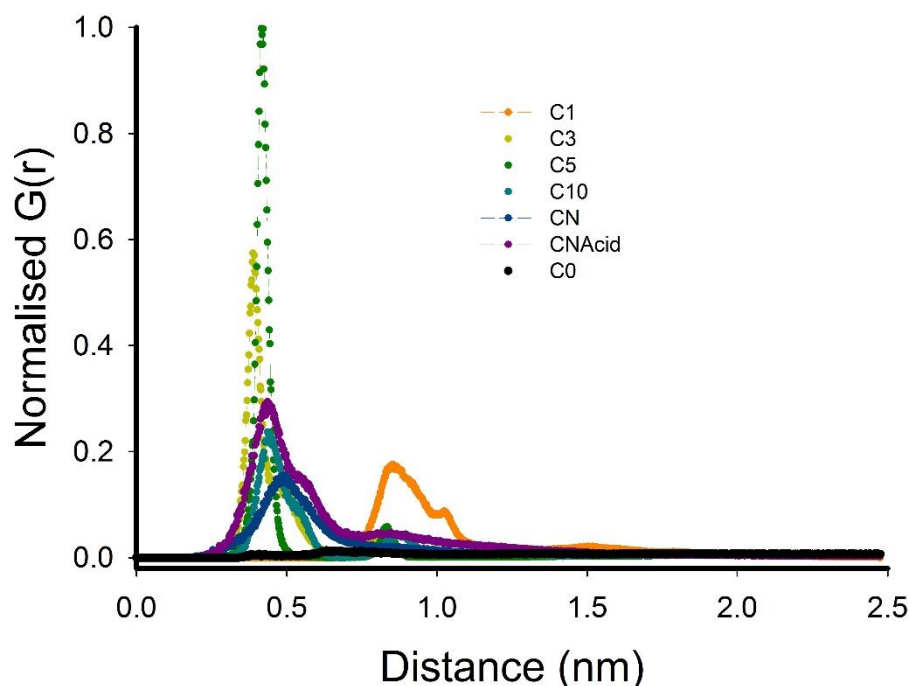


Figure 3.16. Normalised radial distribution function of seven molecules of TPN-C1, TPN-C3, TPN-C5, TPN-C10, TPN-CN and TPN-CNAcid model compounds, solvated by 700 toluene molecules, over 100 ns simulation time.

The MD simulation results, including both RDF and g_dist measurements (Figure 3.9 and Figure 3.11a), also suggest that no notable intermolecular interaction was recorded, other than collisions due to Brownian motion, as can be observed in the Figure 3.14 snapshot of the simulation box. The lack of any tails and oxygen atoms resulted in no molecular associations occurring when prepared with toluene. Other studies that investigated increased aromatic ring surfaces, such as coronene, have observed π -stacking in a variety of solvents [242]. This suggests that just four fused aromatic rings might not generate enough attraction to completely overcome the toluene repulsion barrier.

Although previous studies indicate that an increased aromatic surface facilitates stronger electron clouds, the van der Waals forces generated attract both solvent and solute molecules [47]. As toluene is an aromatic solvent, it makes

sense that the solute-solvent attraction is stronger than the solute-solute attraction, which hinders any aggregation from occurring. Previous studies that investigate asphaltene models with aromatic cores in toluene recorded only dimer formation [19,112]. Further investigations that utilised model asphaltene compounds with even larger aromatic cores (7 rings) than triphenylene concluded that in both toluene and *n*-heptane, the greater contributors to the driving force for self-association and interfacial activity are the functional groups. This implies that the polarity of the molecule plays a greater role in aggregation potential than the potential for π -stacking [114,115]. This suggests that model compounds that lack chemical structures with a larger aromatic surface or any functional groups, such as TPN-C0, are highly unlikely to aggregate in toluene.

Light scattering results of TPN-C1 suggest the presence of large aggregates (above 1000 nm) over a prolonged period of time, which is consistent with literature where the oxygen atoms on the exterior produce negative charge that increase the polarity of the molecular structure. [232,243]. The polar components generate enough attraction to overcome the solvophilic nature of the aromatic cores in toluene, and increase the aggregation potential. The particle sizes recorded by DLS suggest that these clusters initially increased in size (2653 nm – highest recorded) and then decreased over time as they re-configure into stable clusters of around 1000 nm hydrodynamic diameter. The RDF plotted in Figure 3.9 shows that TPN-C1 molecules aggregate throughout the 100 ns simulation. However, the width of the peak (0.7-1.2 nm) indicates multiple aggregation configurations as the nominal distance for parallel stacking is 0.35 nm [61]. The data suggests that the planar molecules are aggregated but at different angles

(parallel to perpendicular), which explains the increased/broad distance range. This is also supported by the g_dist function result shown in Figure 3.11b where small distances (0.7-1.2 nm) between multiple pairs of molecules over longer periods of time can be observed, indicating the formation of large clusters. It is probable that even though the aromatic core could promote π -stacking interactions between the molecules, the alkyl chains (with one carbon) are too short to force any restraints on the configuration of the formed aggregates. Therefore, the resulting clusters could aggregate with multiple possible configurations, in parallel (π -stacking) and perpendicular (T -stacking) arrangements. Previous studies of prototypical aromatic molecules, such as benzene, conclude that off-set configurations are preferred [56,68], due to the distribution of the electron density.

On large aromatic molecules, electron density is distributed evenly above and below the plane of the rings, [47], forming π -bonds due to the overlap of atomic p-orbitals (a quadrupole moment with partial negative charge) [48,49]. These electron clouds are the source of attraction between aromatic surfaces that lead to π -stacking. While for smaller aromatic surfaces, the magnitude of the calculated attraction decreases with the hydrogen number, which decreases the potential for π -stacking/parallel configurations [57-60]. In the case of TPN-C1, four rings comprise the aromatic surface, and oxygen atoms border the molecule, which generates high polarity that attracts both aromatic solvent (triphenylene core) and solutes (oxygen and triphenylene core). This makes π -stacking of the solutes less energetically favourable [58,59], further supporting the existence of multiple configurations present in the large aggregates that cluster in toluene.

Both TPN-C3 and TPN-C5 have been studied previously as discotic liquid crystals [221]. The solvent species and temperature have been known to impact the size of the π -stacked columns. Light scattering data shows that TPN-C3 and TPN-C5 molecules form large aggregates immediately, once being introduced into toluene, but dissolved to 1 nm sized particles after the first 24 hours and stay stable afterwards. DOSY data of TPN-C3 suggests that it tends to form nanoaggregates of 3-5 molecules in toluene in a similar manner to natural asphaltenes forming nanoaggregates [103]. The limited size of the aggregates is mainly attributed to the aromatic nature of the solvent [63,66], and the length of the side-chains that enforce a parallel configuration [116]. As such, the column-like nanoaggregates cannot exceed a certain size. Given the similarity between their molecular structures and solution characteristics, it is safe to assume that the TPN-C5 model compound is subject to the same limitations as TPN-C3. The MD simulations performed suggest that both model compounds have a high potential for π -stacking, as implied by the narrow but high RDF peaks (0.3–0.5 nm) observed in Figure 3.16.

The g_dist function plots presented in Figure 3.11c show that a large column of TPN-C3 molecules is assembled at 50 ns, but dissolved at 80 ns. For TPN-C5, Figure 3.12a initially shows a stable dimer, that further grows into a trimer at 35 ns and remained in that state throughout the simulation time. Snapshots in Figure 3.14b show the existence of the dimers/trimers and the parallel configuration of the nanoaggregates. In discotic liquid crystal studies, the columnar phases are engineered by controlling the space-filling components, which enforce parallel configurations and fixed inter-columnar distances [244,245]. Natural asphaltenes

Chapter 3

contain random numbers and lengths of side-chains, which vary the nanoaggregate interactions, but the side-chains, if long enough, limit the aggregates by imposing parallel configurations. This is observed in the contrast between TPN-C1 and TPN-C3 and TPN-C5. The latter can be considered good “continental” model asphaltene compounds, as they form kinetically stable nanoaggregates, due to π -stacking, that have a constant size after 24 hours when suspended in toluene.

TPN-C10 was found to have an increased solubility in toluene than the other model compounds examined in the present study, as its hydrodynamic diameter is around 1 nm throughout the measurement (see Figure 3.15). Given that the only difference between TPN-C10 and TPN-C3 model compound is the additional long alkyl tail, it is highly likely that the increase in solubility observed was due to this modification in the chemical structure. Longer side-chains are known to hinder/limit aggregation [116], which might explain the difference in the stabilisation time between the model compounds. However, the TPN-C10 molecules could form nanoaggregates consisting 3-5 molecule, as suggested by the DOSY result. This is further supported by MD simulations, where a tetramer was observed at 60 ns (Figure 3.12b). The broad RDF peak between 0.3 and 0.6 nm in Figure 3.16, confirms that π -stacking is the main driving mechanism for nanoaggregate formation, with the possible molecular configurations still parallel (π -stacking at 0.35 nm [61]). The broader distribution can be attributed to the shifted COM of TPN-C10 due to its non-centro-symmetric molecular structure, which increases the intermolecular distance. Investigations of asymmetric compounds suggest that long chains could hinder the aggregation of PACs and

limit the size to which the nanoaggregates could form [104,105]. Other studies further support this statement by removing long side chains from model compounds, which allows the molecules to achieve a more energetically favourable state as better ordered/more densely packed nanoaggregates [246].

According to the literature, aliphatic side chains increase the stability of asphaltene nanoaggregates [247]. This is very similar to the model compounds studied in this work where the systematic increase in size of chains (TPN-C1/C3/C5/C10) decreased the aggregation potential but increased the stability of the nanoaggregates. The configurational limitations imposed by the aliphatic side-chains increase in proportion to their length (TPN-C1 to TPN-C3/C3), as parallel configurations become the most energetically favourable. Longer chains (TPN-C10) further impact the intermolecular interactions, as the limitations imposed increase the solubility by decreasing the aggregation potential. Overall, the aromatic solvent (toluene) imposes a size limitation to the aggregates when they can only π -stack. The size is no longer limited in the absence of enforced configuration – side-chains are too short to impose π -stacking (TPN-C1).

3.4.3. Effect of functional groups on intermolecular interactions in toluene

Investigation of TPN-CN and TPN-CNAcid could systematically examine the effect of an amide group and a carboxylic acid group on the aggregation mechanisms of model compounds under the influence of different solvents. A range of heteroatoms such as N, S, and metals can be found in asphaltenes, significantly influencing the interaction and aggregation between asphaltene molecules [248]. Along with acid groups, these functional moieties increase the polarity of molecules, which occupy a vital role in the strength and stability of

aggregates, as well as greatly impact the roles asphaltenes undertake at the oil/water interface [91,241,249]. The use of TPN-CN and TPN-CN_{Acid} attempts to replicate some of the effects. Acid groups have previously been attached to triphenylene with the purpose of controlling the properties (such as thermal stability) of the structures formed, and were proved to enhance the intermolecular interactions, by increasing the polarity of the compounds [250].

The hydrodynamic diameters of TPN-CN and TPN-CN_{Acid} shown in Figure 3.15 suggest that both compounds associate into large aggregates in the toluene suspension immediately after mixing. After the initial 24 hours, their sizes change slightly, but appears to increase until 168 hours. This indicates that both model compounds aggregate into large and unstable clusters for an extended period of time, which is different to the other compounds examined that do not have such a high degree of polarity. The RDF peaks of the TPN-CN and TPN-CN_{Acid} model compounds in Figure 3.16 were not very high, but cover a broad distance range (0.3 – 1.3 nm), suggesting that the formed clusters have multiple configurations and a lower packing density than TPN-C3 and TPN-C5. The VMD movies of the simulation suggest that although clustering did occur, it appears to be driven by the presence of the functional groups rather than the aromatic core, as both head-to-tail and head-to-head stacking was observed. The snapshot in Figure 3.14 failed to describe the dynamics by which these complex aggregates formed, as it only captured one frame of a dynamic process. However, it does capture the existence of multiple aggregates.

By comparison, TPN-C0 (the core model molecule) does not show any sign of aggregation, which indicates that the main driving forces behind the aggregation

of TPN-CN and TPN-CN_{Acid} is the presence of the amide and/or the carboxylic acid functional groups, rather than the π -stacking between the aromatic cores. As such, far larger clusters could form and remain in solution than the π -stacking driven model compounds (TPN-C3, TPN-C5 and TPN-C10), as shown by the DLS measurements. A higher RDF peak could be observed for the TPN-CN_{Acid} at the π -stacking distance, implying stronger, more compact aggregates; however, the broadness of the peaks suggest more configurational freedom than the TPN-CN model compound. Figure 3.13c shows that over time clusters form, but the dissolution was far less than in the TPN-CN model. This implies that the carboxylic acid group increased the aggregation potential of the model compound.

The simulation video not only showed the formation of clusters, but also how the acid group acted as an attraction site for other acid groups, as well as the triphenylene core. The increase in the number of active aggregation sites (functional groups) per molecule increases the aggregation potential as was concluded by a number of studies [86-92]. However, density functional theory studies that investigated asphaltene aggregate configurations concluded that parallel configurations are the most energetically favourable state for natural asphaltenes [73-79], which suggests that although larger aggregates are formed, they have an inclination to continuously re-assemble into more stable configurations. According to previous studies, this re-assembly is driven by the weaker van der Waals forces generated by the aromatic rings, which prefer parallel configurations [121,122].

3.5. Conclusions

A combination of experimental and computational approaches were deployed to systematically investigate the effect of chemical structure of PACs on their aggregation behaviour in toluene as a function of concentration and time. As such, seven model compounds were evaluated by measuring their hydrodynamic sizes over a 168 hour interval using DLS measurements, and their intermolecular interactions were evaluated utilising MD simulations. The behaviour of the model compounds employed to investigate the chain length effect concluded that the major impact they have is on the configuration of aggregates. The limitations imposed by the structure impact the aggregation potential, as short chains allow any configuration (1000 nm aggregates – TPN-C1), and long chains limit the aggregates to parallel configurations (1nm aggregates – TPN-C3/C5/10). Furthermore, the absence of alkoxy groups highlights the limitations of van der Waals attraction in a solvent (toluene) of similar nature to the model molecule (TPN-C0), as no aggregation was observed.

Consistent with literature, low polarity continental model compounds form nanoaggregates of limited size in toluene [251]. It was found that the side-chains of model compounds (TPN-C3, TPN-C5, and TPN-C10) could have a major role in stabilising nanoaggregates because they limit the potential configurations in which the asphaltenes could self-associate by π -stacking. Stability was reached as the nanoaggregates formed in parallel configurations of 3-5 molecules, similar to [21]. The affinity of the toluene with the model compound due to its aromatic structures prevents the formation of large columns and hinders their aggregation completely in the absence of alkoxy side-groups (TPN-C0). The non-

Chapter 3

centrosymmetric molecules (TPN-C10) showed a stronger and faster solubility in toluene; however, the hydrodynamic diameters of the stable nanoaggregates were still around 1 nm. This highlights the effect of longer side-chains (TPN-C10) on the solubility of the model compounds.

As shown by the MD simulations, a shorter chain (TPN-C1) did not hinder aggregation and allowed for clustering to occur, but in more loose configurations such as perpendicular stacking. This leads to the formation of larger (above 1000 nm) clusters. In this case, the affinity towards toluene was overcome by the self-association potential of the chemical structure.

The addition of functional groups to the core structure appears to increase the aggregation potential, yielding very large clusters, as shown by the DLS measurements. The increase in polarity generated a greater aggregation potential, as TPN-CN_{Acid} (most polar) yields larger aggregates than TPN-CN, and both are larger than TPN-C10 aggregates. The resulting clusters did not exhibit ordered configurations, similar to liquid crystals (TPN-C3 and TPN-C3C5), however, they appear to have a higher aggregation potential, as was concluded in other studies that investigated similar asphaltene model molecules [16]. The aggregate size limit was increased due to the high polarity of the models that generate stronger attraction forces than the aromatic surface, and the absence of long side-chains surrounding the core prevented any configurational limitations.

This chapter investigated the relationship between chemical structure and aggregation of model compounds in toluene. Natural asphaltene studies show that, although asphaltenes are well solvated by toluene, they could form

Chapter 3

nanoaggregates under certain conditions [108,252] when the intermolecular forces are strong enough to overcome the solute-solvent interactions. The model compounds in this study help to understand how even a small change in chemical structure (TPN-C1 to TPN-C3) can significantly impact the aggregation mechanism. The increase in chain length around the triphenylene core (TPN-C3 and TPN-C5) imposes ordered configurations (π -stacking) upon the nanoaggregates, while the non-symmetry of a model compound increased solvation potential. The addition of functional groups (TPN-CN and TPN-CNAcid) leads to the formation of larger, unorganised clusters, that are loosely packed and in a continuous re-configuration, as the attraction between the aromatic surfaces was greatly overcome by the new chemical groups (amide and acid). This chapter underpins the intermolecular interactions involved in natural asphaltene aggregation and could help to develop strategies to counter the clustering of natural asphaltenes.

**Chapter 4. Effect of *n*-heptane on the intermolecular interaction
between model compounds**

Chapter 4

4.1 Introduction

Asphaltenes are defined as the heaviest fraction of crude oil that precipitate in *n*-alkane solvents, such as *n*-heptane, and are soluble in aromatic solvents, such as toluene [46]. Due to their sensitivity towards environmental and thermodynamic fluctuations, asphaltenes can precipitate when changes in temperature, pressure, or solvent quality occur [253,254]. These changes can happen at any point during oil production, transportation, or processing, which result in obstructions of the pipeline and production facilities, reduction of storage capacity, fouling on equipment surface, and catalyst deactivation [255,256]. Both upstream and downstream processes involve variations in temperature, which can lead to shorter precipitation onset times [257]. Studies suggest that an increase in temperature (above 289.85°C) leads to a dissolution of asphaltene clusters, and the fractal-like association returns upon lowering the temperature back to ambient [159]. Effects of pressure on asphaltene aggregation are far less studied, and it is generally accepted that although pressure variations lead to subtle structural changes, the mechanism by which these occur is still unclear due to the complex interplay of molecular interactions [258].

Effects of solvent have been studied extensively, with emphasis on the effect of *n*-alkanes on precipitation of asphaltenes. This is due to a common practice, known as blending [259,260] in the crude oil industry which is typically performed by combining heavier oils with lighter crudes to improve properties such as viscosity or distillation yield [261]. The blending of two or more crudes where a broad range of *n*-alkanes are included leads to the destabilisation of the asphaltene fractals and hence the onset of precipitation, due to the impact that

different *n*-alkane chain lengths have on asphaltenes [259]. The carbon number of the *n*-alkanes was found to be inversely proportional to the precipitation effect caused to the asphaltenes [262]. This phenomenon is ascribed to the entropy of mixing molecules of different sizes, as concluded by different asphaltene phase behaviour studies that rely on Flory-Huggins theory [263-266]. Alkanes directly impact the kinetic behaviour of asphaltenes, as the different molecular lengths of the *n*-alkane chains change the viscosity. Increased viscosity is expected to impact aggregation rates and implicitly the aggregation time. However, due to the decreasing yield of the precipitated asphaltenes with increasing chain length, it has been suggested that the interactions and the aggregation tendencies of asphaltenes might vary between different *n*-alkanes. This is supported by an extensive study that investigated seven *n*-alkane chain lengths, and discovered a non-monotonic variation between the increase in viscosity, as a function of chain length, and the aggregation rate of asphaltenes [267].

The influence of a wide range of solvents, both aromatic and *n*-alkane, on asphaltene behaviour was studied [268] and *n*-alkanes were found to cause asphaltenes to precipitate, while aromatic solvents, such as toluene, allow asphaltenes to diffuse and maintain a stable, colloidal state [251]. The solubility and stability of asphaltenes in aromatic solvents is still heavily debated [10]. Different degrees of interaction energy were recorded between asphaltenes and aromatic solvents, such as quinoline and tetralin, by differential scanning calorimetry and microcalorimetry [269]. It was found that asphaltenes interact more strongly with quinoline; however, the study did not have an explanation as to why this was so [269].

According to their definition, asphaltenes are polyaromatic compounds that tend to aggregate and precipitate in *n*-alkanes, which makes them insoluble in species such as *n*-heptane [85,270]. Understanding and controlling the solubility of natural asphaltenes has proven to be a challenging task, due to the diverse chemical structures that natural asphaltenes can have as well as the wide range of solvent species that influence the solute-solute interactions. The aggregation rate of asphaltene is under the influence of two factors: the frequency of the collisions and the strength of interactions between molecules. The strength of these interactions depends upon the degree of attraction and repulsion forces of chemical structures in solution. Attraction forces could be van der Waals, polar interactions, hydrogen bonding, and metal coordination [80,271-273]. Literature suggests that repulsion forces are of steric origin, and are caused by the alkyl chains that surround the aromatic cores of “continental” asphaltene molecules [116]. This summarises the chemical structure dependency of solute-solute interactions.

Equally, the solute-solvent relation plays a major role. In an aromatic solvent, such as toluene, the repulsion forces overcome the attraction forces, and asphaltene molecules or nanoaggregates remain in a colloidal state due a stronger affinity towards toluene than they would towards other asphaltenes - a lower aggregation potential [84,248,268]. This is likely related to the aromatic nature of the toluene, which is attracted to the aromatic surface of “continental” asphaltenes [47]. However, when an *n*-alkane solvent is added, the effectiveness of repulsion forces increases because of the breakdown of the steric layers, resulting in asphaltene self-association [66]. Asphaltenes, when suspended in an aromatic

solvent, are generally regarded as solid nano-sized colloidal particles [103,251,274-276]. When the asphaltene concentration is increased, the number of potential interactions increases, resulting in asphaltene nanoparticles or clusters [103]. With *n*-alkanes, the aggregation potential is also increased, as the aromatic surface does not attract the solvent, and π -stacking interactions between the aromatic cores are preferred.

Asphaltene precipitation could also be influenced by the presence of *n*-heptane [277], as an increased amount of *n*-alkane usually implies greater aggregation potential. These structural changes directly affect the potential and rate of aggregation when *n*-alkane solvents are added. This was investigated by measuring the increase in particle size as a function of increasing *n*-heptane volume with DLS [17]. Furthermore, by focusing on the effect of asphaltene concentrations on aggregation in toluene solutions with *n*-heptane addition, two mechanisms were identified [10,160]. At concentrations below a critical micelle concentration, the aggregation process occurs through diffusion-limited aggregation, while above the critical micelle concentration, reaction limited aggregation dominates. The studies attributed this shift in aggregation path to the structure of the nanoparticles, or more specifically the change from nanoaggregates to clusters [10]. Other studies investigated the diffusivity of asphaltenes at various concentrations, and found that it is no longer constant, but instead was strongly related to the concentration [238,278-281].

The effect of concentration of model compounds in this work has been examined by DOSY NMR and DLS experiments in Chapter 3. It has been concluded that triphenylene-cored model compounds were able to overcome the

Chapter 4

repulsive forces in toluene due to structural preferences, at 10 mg/mL; however, the nanoaggregate size is different for each model in toluene.

In this chapter, *n*-heptane, the most common *n*-alkane solvent utilised for asphaltene precipitation, was added in both experimental and computational investigations. DLS measurements were used to monitor the hydrodynamic sizes over an extended period of time (168 hours), while MD simulations were used to investigate the intermolecular interactions. Both approaches focus on the impact *n*-heptane has on the model compound-toluene suspensions in the hope of correlating the solute-solute interactions with the solute-solvent relation.

4.2. Materials and methodology

4.2.1. Materials

Heptane 99.85%, Extra Dry, was purchased from Fisher Scientific (Loughborough, UK) and used to prepare the suspensions. All other materials and solutions used are the same as in Chapter 3. Table 3.1 shows the chemical structures of the model compounds and their acronyms.

4.2.2. Methodology

4.2.2.1. Dynamic light scattering

Similar to the previous chapter, all samples and solvents were kept at constant room temperature ($22 \pm 0.5^\circ\text{C}$), at ambient pressure, and with minimal exposure to visible light. All glassware was thoroughly washed with toluene and dried under nitrogen flow. Prior to mixing the model compounds in solvent for DLS measurements, PTFE filters (100 nm pore size) were used three times to filter the

Chapter 4

toluene and *n*-heptane. The model compounds were initially prepared with toluene, and only after 24 hours of stabilisation time was *n*-heptane added at 4 parts toluene to 6 parts *n*-heptane ratio (heptol), to obtain a final concentration of 10 mg/mL (solute to solvent mixture). Immediately after *n*-heptane addition, the samples measurements were carried out employing a Zetasizer (Nano Series, Malvern) with a laser wavelength of $\lambda = 632.8$ nm, and a scattering angle of 173° , with data collected at fixed time intervals (0, 24, 168 hours). Data analysis was performed with the integrated Malvern software. Each datum is an averaged value of three samples, each measured over six repeats. The acquired autocorrelation functions (ACFs) of each sample set were analysed with the software, and only for those meeting the quality criteria, was data recorded to calculate the corresponding hydrodynamic diameters. Data selection for quality criteria is described in detail in Chapter 3.

4.2.2.2. Molecular dynamics simulations

Molecular dynamics simulations carried out in this chapter employed a GROMACS 4.6.5. software package and the OPLS/AA force field as described in Chapter 2. Equilibration steps (1000) of 100 ps were then performed to prepare the simulation for trajectory production. The Berendsen algorithm was adopted to relax the system to 298 K and 1 atm pressure. Once steady fluctuations reached the average volume, the simulations were performed with an integration time of 2 fs, a cut-off of 1.0 nm used for van der Waals interaction and periodic boundary conditions [204]. Initially, seven identical molecules of one model compound were placed in an *n*-heptane simulation box (700 *n*-heptane molecules) and in a 50% toluene, 50% *n*-heptane simulation box (350 toluene molecules, 350 *n*-heptane

Chapter 4

molecules – heptol). The molecules were placed at equidistant positions, the simulations run for 100 ns, during which the effect of the alkyl chain length and functional groups on molecular aggregation was examined.

The simulations were analysed using three methods: visual molecular dynamics (VMD), radial distribution functions (RDF) and the “g_dist” GROMACS function. VMD is a video software employed to visualise the simulation boxes, selectively observe molecules, and obtain snapshots of the video frames. RDFs were applied to quantify the average distance between the centre of mass (COM) of selected molecules into distributions of $G(r)$ as a function of distance. The positions and intensities of the distribution peaks obtained, yield information about the average distance between the molecules. RDFs investigate the occurrence of aggregation events and quantify the interactions between molecules. The data obtained is normalised by the highest datum of the entire set to allow for a better comparison and presentation of the data.

A secondary set of simulation boxes was built using the same software package and force field. However, only one model molecule was placed in a heptol simulation box of 700 solvent molecules (350 *n*-heptane and 350 toluene). RDF analysis ensued between the model compounds and, in turn, each solvent species. The purpose of this analysis was to determine the affinity each asphaltene model compound had towards either aromatic or *n*-alkane solvent.

Chapter 4

4.3. Results

4.3.1. Dynamic light scattering of model compounds

The solution kinetics of model compounds, with different chemical structures, in toluene was investigated by dynamic light scattering Chapter 3. By increasing the number of carbons in the alkyl chains surrounding the triphenylene core of the model compounds, some stable nanoaggregates of 3-5 molecules were observed with a hydrodynamic diameter of around 1 nm (TPN-C3, TPN-C5 and TPN-C10). The presence of functional groups allowed the model compounds to overcome the solvent effect induced by toluene to form large (1000 nm) clusters, as suggested by DLS and MD simulations.

This chapter aims to investigate the solution kinetics of the triphenylene based model compounds as a function of chain length and chemical group with the presence of 60% *n*-heptane, at a final concentration of 10 mg/mL, to understand the impact of *n*-alkane solvents on the aggregation process and molecular interactions.

4.3.1.1. Effect of chain length on intermolecular interactions in heptol

The hydrodynamic diameters of aggregates in heptol were measured as a function of time for the following model compounds: TPN-C0, TPN-C1, TPN-C3, TPN-C5 and TPN-C10. The ACFs were collected from three samples per model, each sample being measured six times. The averaged hydrodynamic diameters acquired, with corresponding standard errors, are presented in Figure 4.1.

After dissolving the model compounds in toluene, the solutions were left for 24 hours, prior to the addition of *n*-heptane, after which DLS measurements were

carried out at 0, 24 and 168 hour time intervals. It was found that, after *n*-heptane addition, TPN-C0, the unaltered triphenylene, possesses a hydrodynamic diameter below 1 nm with no observable change over 168 hours. This suggests that the addition of *n*-heptane does not prompt the aggregation of the TPN-C0 model compound, in contrast to what would be expected from natural asphaltenes. It appears that not enough *n*-heptane was added to overcome the solvophilic effect of the toluene that is generated by aromatic core attraction, as aromatic molecules are expected to aggregate in *n*-alkane solvents [282].

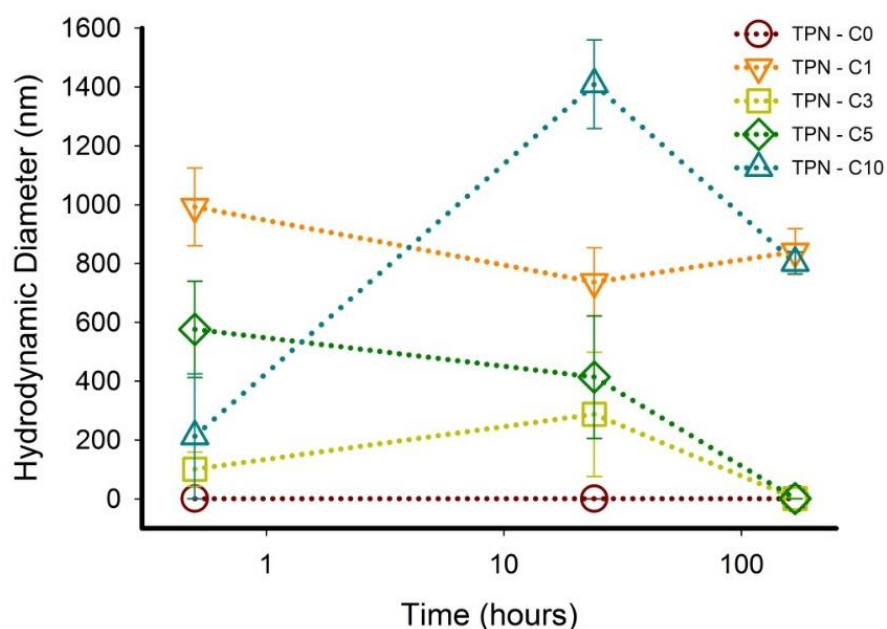


Figure 4.1. Averaged hydrodynamic diameters as a function of time for TPN-C0, TPN-C1, TPN-C3, TPN-C5 and TPN-C10 at 10 mg/mL, all suspended in heptol (40% toluene, 60% *n*-heptane).

In contrast, the model compounds with alkyl branches tend to form significantly larger aggregates upon the addition of *n*-heptane, and exhibit different aggregation kinetics from that observed in toluene. TPN-C10 displayed a notable variation in hydrodynamic size over time - a large increase in the first 24 hours, after which the clusters appear to dissolve and stabilise into smaller

aggregates (~ 800 nm). Similar to their behaviour in toluene, TPN-C3 and TPN-C5 aggregate initially to form structures of 100 nm and 600 nm respectively, after which they slowly dissolved into nanoaggregates of 1 nm size. The addition of *n*-heptane appears to have slowed the dissolution of the larger aggregates. In contrast to the behaviour in pure toluene, these model compounds tend to stabilise between 24 and 168 hours. DLS measurements of the TPN-C1 in heptol exhibit slightly smaller hydrodynamic sizes than in toluene. It is possible that the clusters start to precipitate when the size is above 1000 nm, which is supported by the observation that no larger particles are recorded by DLS with the addition of *n*-heptane. The collected data reveals the effect that peripheral *n*-alkane chain length have on the preference for aggregation, as well as the corresponding kinetics.

Overall, the model compounds exhibit different degrees of sensitivity towards the addition of *n*-heptane. The chain length effect is marked by the slower dissolution of TPN-C3 and TPN-C5, as well as the significant aggregation brought by the addition of one long side-chain (TPN-C10).

4.3.1.2. Effect of functional groups on intermolecular interactions in heptol

Upon the addition of *n*-heptane to the toluene-compound mixture, it was found that the effect of *n*-alkane on the stability and the aggregation of polyaromatic compounds is dependent on the chemical structure of the PAC. Figure 4.2 compares the hydrodynamic diameters of the model compounds with functional groups (TPN-CN, TPN-CNAcid), with the core triphenylene (TPN-C0) in the heptol solvent mixture.

Similar to the ones carrying alkyl branches, TPN-CN and TPN-CNAcid form large aggregates whose sizes are ~ 500-700 nm and 1400 nm respectively in the first 24 hours. An increase in the size of the standard error must be noted and is attributed to the precipitation that occurs with the addition of *n*-heptane. After 168 hours, TPN-CNAcid exhibits a significant decrease in particle size (~ 300 nm), while TPN-CN continues to increase to above 1000 nm, where the instrumental limitation decreases the accuracy of the results – DLS cannot accurately measure particles significantly larger than the wavelength of the laser. As TPN-CNAcid is considered of higher polarity than TPN-CN, the difference between the model compounds at 168 hours might be related to the precipitation of the clusters, as previous studies suggest that natural asphaltene of different origins exhibit different precipitation characteristics [85,248,263,268].

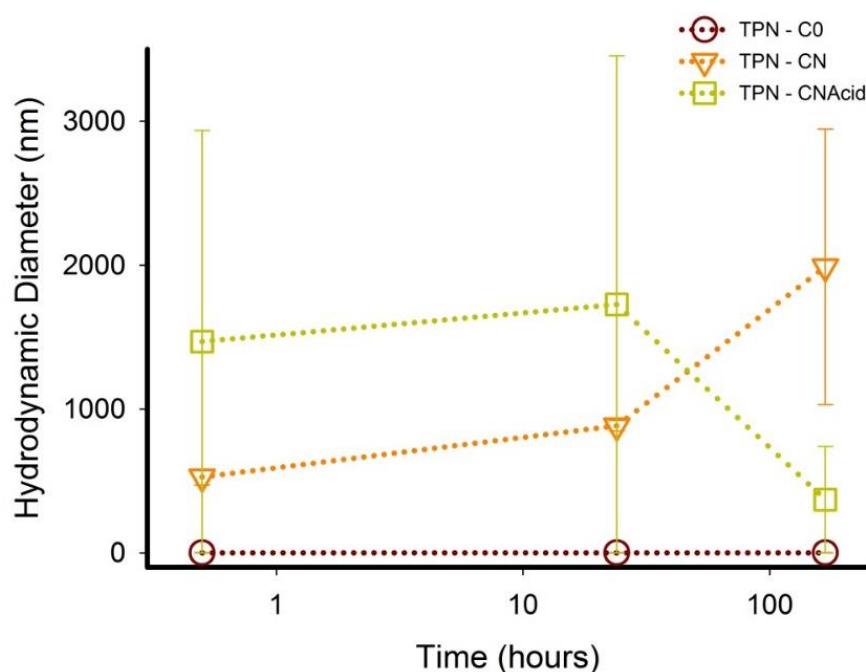


Figure 4.2. Averaged hydrodynamic diameters as a function of time for TPN-C0, TPN-C1, TPN-C3, TPN-C5 and TPN-C10 at 10 mg/mL, all suspended in heptol (40% toluene, 60% *n*-heptane).

The variation in particle size of the TPN-CN implies a complex aggregation mechanism that does not show a uniform size distribution, even after 168 hours, as multiple sizes are indicated by the large standard errors. While DLS can only measure the hydrodynamic diameters of the particles, it cannot yield any insight as to how or why such an unstable clustering mechanism is occurring. However, the impact of adding polar functional groups and generating non-centrosymmetric model compounds significantly increases the complexity of the intermolecular interactions, which leads to a more intricate aggregation mechanism. The presence of the amide and acid group on model compounds in a mixture of both aromatic and *n*-alkane solvent increases the similarity between the natural asphaltenes and the systems (model compounds and solvents) investigated in this study to a natural asphaltene system.

4.3.2. Molecular dynamics simulations of model compounds

4.3.2.1. Solvent affinity of single molecule model compounds

Previous studies concerning natural asphaltenes have focused on asphaltene – asphaltene interactions rather than asphaltene – solvent interactions [283]. Therefore, the affinity between natural asphaltene molecules and their solvent is investigated here to provide information regarding the strength of attraction between the solute and each solvent species. The radial distribution function (RDF) is one of the most commonly employed approaches to analyse molecular interactions and characteristics in GROMACS MD simulations. They quantify the average distance between the COM of selected molecules into distributions of $G(r)$ (density of local interactions divided by the density average of the whole simulation box) as a function of distance.

To investigate the solute-solvent interaction, the RDF tools were deployed to record the distances between the COM of a single model compound molecule and all of the solvent molecules of either toluene or *n*-heptane in the same simulation box, at 20 ns. The plotted RDFs show the intermolecular interactions between the model molecules and all the solvent molecules, one species at a time. The purpose is to quantify the degree of affinity each model compound has towards aromatic or *n*-alkane solvents, or the difference in the average distance between the COM of the model compound molecule and the COM of either toluene or *n*-heptane molecules. All the RDFs tend to unity, as the solvent molecules are not influenced by the presence of the model molecule after a certain distance is exceeded, which results in a uniform density. This length is relative to each model. The analysis method is very similar to that presented in a previous study [284], where a model for molecular hydrogen is interacting with aliphatic and aromatic hydrocarbons and the COM distances are recorded.

Radial distribution functions were generated and recorded (Figure 4.3a) between a single TPN-C0 molecule and the two species of solvent molecules present in the simulation box (350 molecules of each solvent). The RDF records the average distance between the COM of the model compound molecule and the COMs of all molecules belonging to one of the solvents. Both solvent RDFs will always reach unity on $G(r)$ because after 1.5-2 nm the model molecules do not affect the solvent molecules, so a uniform density distribution is achieved. The difference in affinity is determined by the height and width of the peaks until the model molecule stops influencing solvent molecules. For TPN-C0, the *n*-heptane shows a faster/steeper increase, with a spike at 0.4 nm, while the toluene shows

a slower increase, with multiple spikes at 0.6-0.7 nm. This implies that the TPN-C0 model compound probably possess a marginally higher degree of affinity towards the *n*-heptane rather than the toluene. However, such an indication is inconsistent with the DLS results suggesting TPN-C0 does not present different degrees of solvophobicity towards either solvent species – they do not aggregate in either solvent. This is very likely due to the limited number of aromatic rings of triphenylene, which does not generate enough attraction to overcome the solvent interactions.

TPN-C1 shows the strongest affinity towards toluene of all the model compounds (Figure 4.3b), while only a small peak at 0.5 nm, and then a gradual slope towards $G(r) = 1$ was recorded against *n*-heptane. This is very likely due to the COM of the TPN-C1 molecule being very close to the COM of toluene, whilst the *n*-heptane molecule is not able to come closer to the aromatic core. The lack of long side-chains might also play a role in the absence of affinity towards *n*-heptane. In a similar manner this behaviour is observed in the other model compounds (TPN-C3, TPN-C5 and TPN-C10 - Figure 4.3c, d, e), however, the increase in chain length both facilitates the shorter *n*-heptane distances to the COM, while at the same time repels the toluene. This is due to the structural similarity that allows more *n*-heptane chains to be closer to the molecules as well as around it. By contrast, the side-chains of the molecule repel the toluene molecules, which reduces the average density of the aromatic solvent around the model molecule and limits the solute-aromatic solvent interaction to only the aromatic area of the model compound.

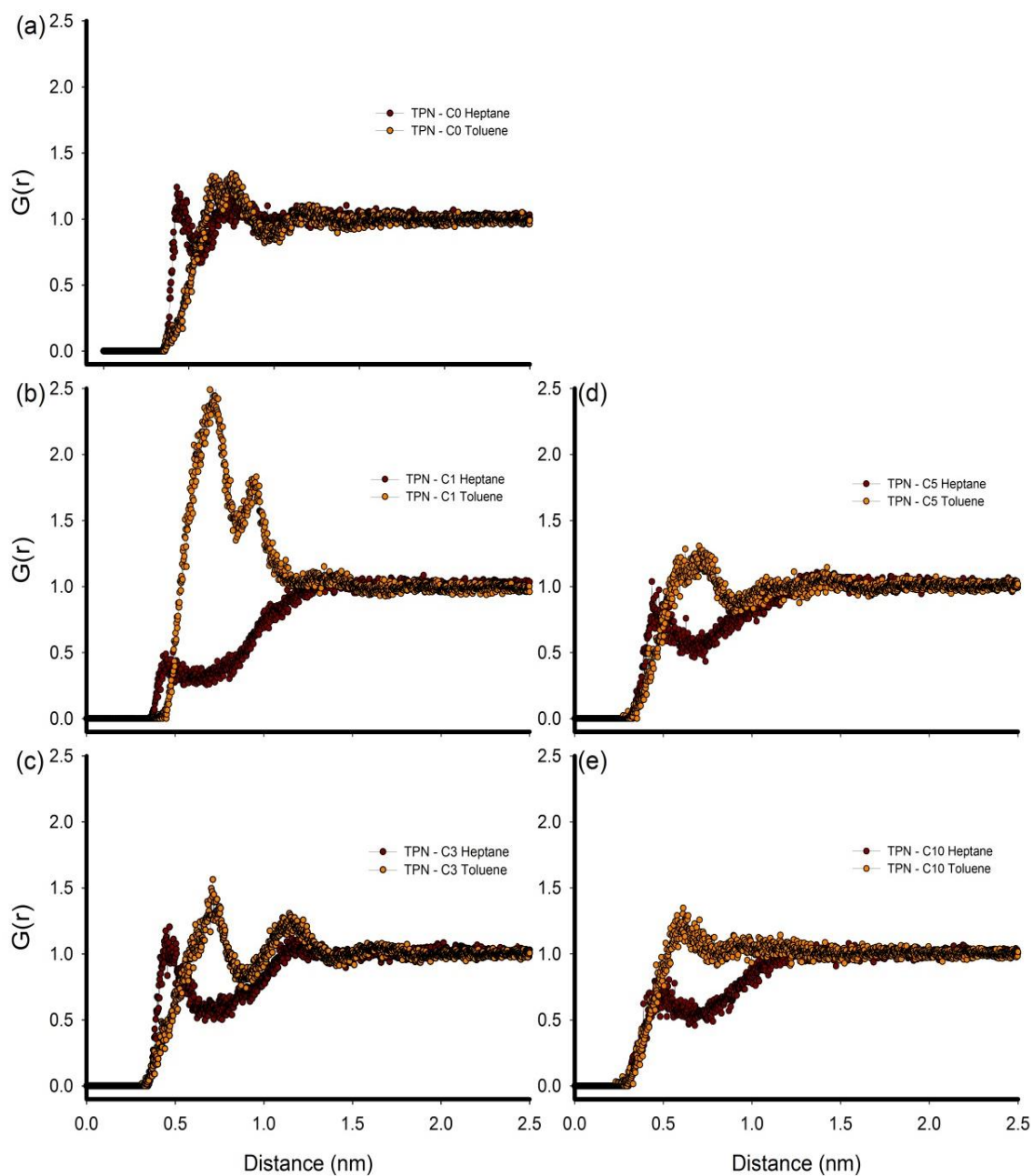


Figure 4.3. Radial distribution functions of TPN-C0, TPN-C1, TPN-C3, TPN-C5 and TPN-C10 model compounds versus solvent, suspended in a heptol simulation box, over 20 ns simulation time.

This behaviour is reflected in the solute-solute interactions in toluene (Chapter 3), where for example TPN-C3 and TPN-C5 only aggregate by π -stacking due to the configurational limitations imposed by the molecular structure, resulting in limited size nanoaggregates as recorded by DLS.

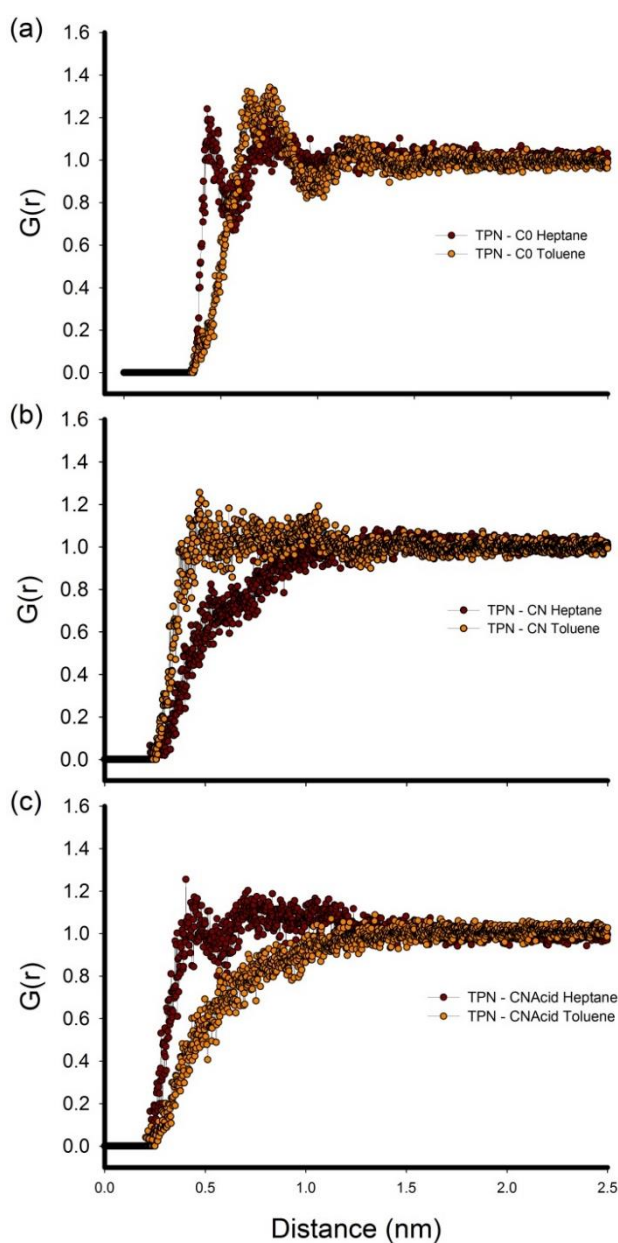


Figure 4.4. Radial distribution functions of TPN-C0, TPN-CN and TPN-CNacid model compound versus solvent, suspended in a heptol simulation box, over 20 ns simulation time.

Figure 4.4 shows the affinity of the polar compounds towards different solvent species. Figure 4.4a (TPN–C0) also serves as a visual comparison with the previous model compounds seen in Figure 4.3. The TPN–CN and TPN–CNAcid display weak differences between the toluene and *n*-heptane, the only significant remark being that toluene is the dominant peak for TPN–CN while the opposite is true for TPN–CNAcid, where the *n*-heptane peak is higher. This is very likely due to the presence of the functional groups, which decrease the effect of solvent on the structure due to a significantly higher polarity than the solvents [285]. Both solvents employed in this study are of low polar nature by comparison to the amide and/or acid group incorporated in the TPN–CN/CNAcid molecular structures. While the aromatic versus *n*-alkane interplay does generate a difference due to the aromatic core of the model compounds and the lack of side-chains, the overall effect of the solvents is surpassed by the higher polar nature of the model compounds. This is reflected in the DLS results as the polarised model compounds were found to aggregate in both aromatic and *n*-alkane solvent.

4.3.2.2. Radial distribution functions of model compounds solvated by heptol and *n*-heptane

To evaluate the effect of *n*-heptane addition on the solute-solute interactions as a function of increasing alkyl chain length, simulations were carried out in a toluene/*n*-heptane (heptol) simulation box (Figure 4.5a), and in a box filled with 100% *n*-heptane (Figure 4.5b).

Normalised radial distribution functions quantify the interaction of the TPN–C0, TPN–C1, TPN–C3, TPN–C5 and TPN–C10. TPN–C0 does not register any significant peaks at any distance throughout the simulations, indicating no change

in behaviour or interactions in either solvent mixture. This behaviour is in agreement with the DLS measurements, which recorded no aggregation between the triphenylene molecules. TPN-C1, known to aggregate in toluene (DLS and MD), exhibits multiple peaks with increased magnitude and reduced width over a broad distribution, as the remaining toluene is completely replaced with *n*-heptane in Figure 4.5b. This can be interpreted as a change in the packing configuration of TPN-C1 (from loose to compact) when excessive amounts of *n*-heptane is present. The shift in the solute-solute RDF distributions indicate that the TPN-C1 model compounds are forced into tighter configurations due the solvophobicity between TPN-C1 and *n*-heptane. This is consistent with the solvent affinity simulation that shows a greater affinity towards toluene, and with the DLS data, that shows a decrease in particle size as *n*-heptane is added.

As the alkyl chain length increases, the configurational limitations imposed by the planar molecular architecture, similar to what was observed in toluene, cause TPN-C3, TPN-C5 and TPN-C10 to aggregate in parallel configurations. The DLS measurements in heptol suggests that TPN-C3 and TPN-C5 take more time to form small nanoaggregates, and TPN-C10 forms significantly larger clusters than was recorded in toluene, in Chapter 3. The temporary existence of larger aggregates or other configurations for TPN-C3 and TPN-C5 is reflected in the secondary peaks (0.6-0.8 nm) exhibited in Figure 4.5, that further increase from heptol (a) to *n*-heptane (b). This along with the increase in width of the TPN-C10 distribution suggests that the rise in percentage of *n*-heptane generates more interactions between the models with longer chains. This is likely due to the affinity between the side chains and the *n*-alkane solvent, as was also identified in the solute-solvent simulations in Figure 4.3.

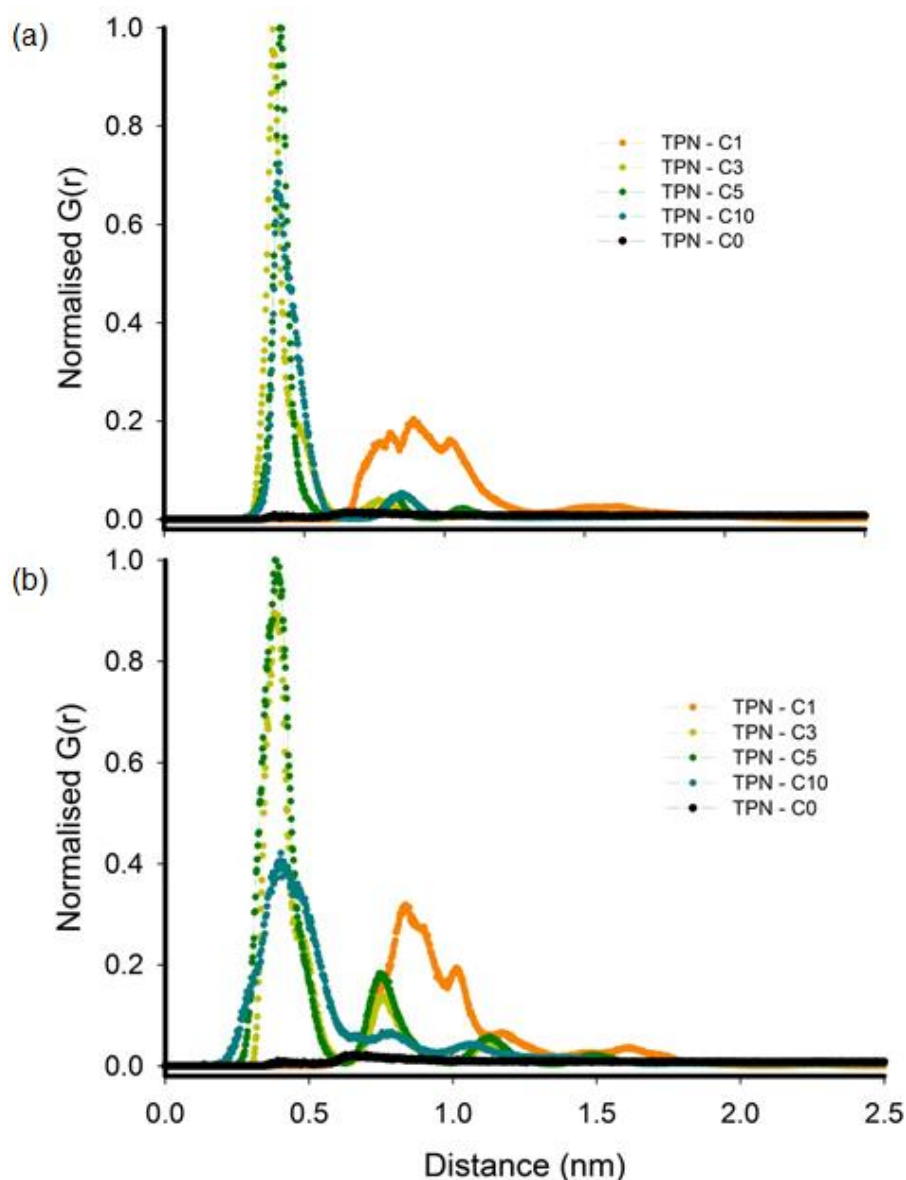


Figure 4.5. Normalised radial distribution functions for TPN-C0, TPN-C1, TPN-C3, TPN-C5 and TPN-C10 model compounds, placed in a (a) heptol and (b) *n*-heptane simulation box, over 100 ns simulation time.

Suggested by the light scattering results, the nature of aggregation changes significantly upon incorporation of functional groups to the model compounds, as well as the shift in solvent species. Figure 4.6 shows the normalised radial distribution functions for the model compounds with different chemical groups solvated by (a) heptol and (b) *n*-heptane, with TPN-C0 included as a benchmark. The broad distribution of the RDF peaks suggests that TPN-CN and TPN-CNacid can aggregate

in a variety of configurations. The major peak at the key π -stacking distance (0.3-0.4 nm) implies that parallel stacking is the most preferred state. However, the increased width and magnitude of the peaks with the increasing presence of *n*-heptane suggest a rise in aggregation potential that is related to the percentage of *n*-heptane in the solvent.

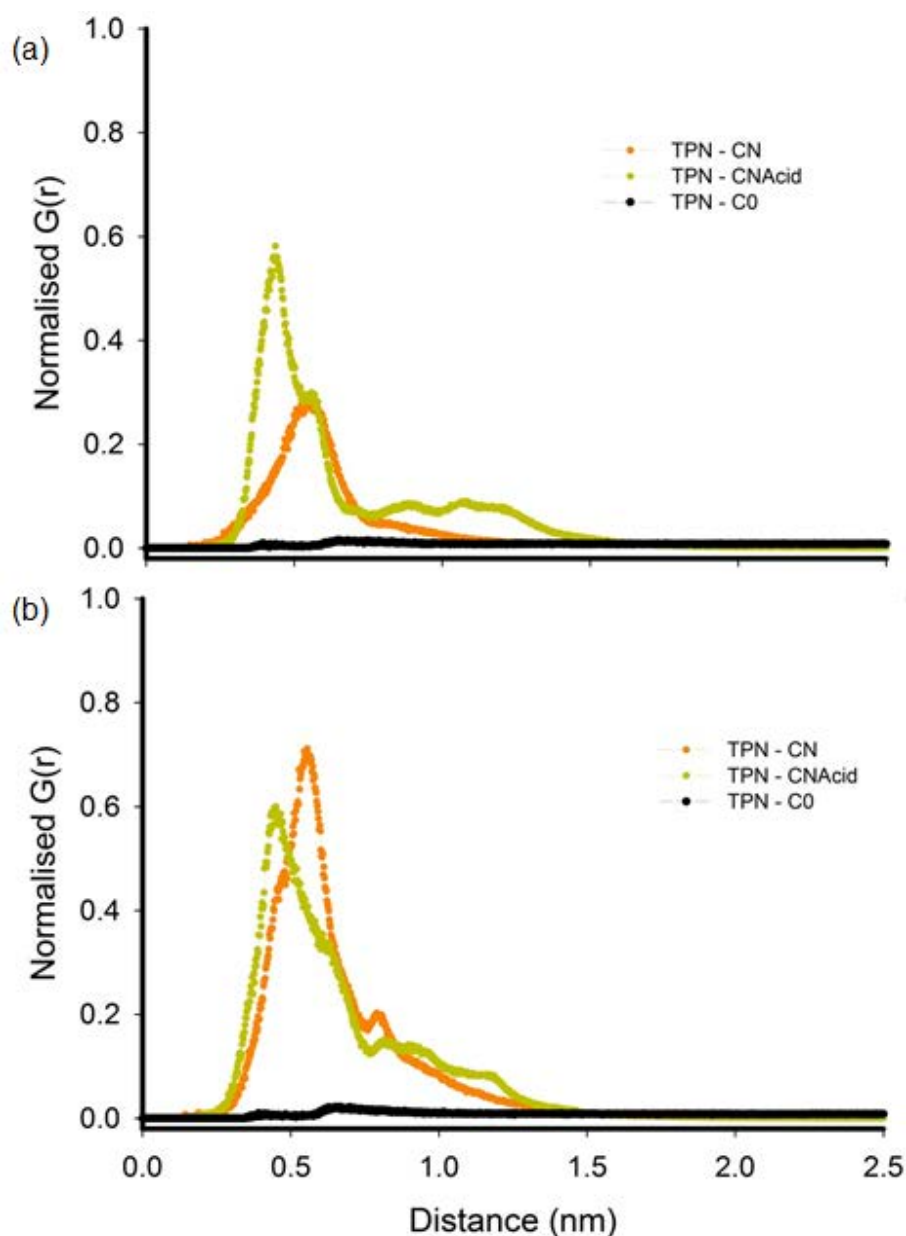


Figure 4.6. Normalised radial distribution functions for TPN-C0, TPN-CN and TPN-CNacid model compounds, placed in (a) a heptol and (b) *n*-heptane simulation box, over 100 ns simulation time.

Furthermore, TPN-CN displays a notable increase in aggregation (higher peak) from heptol to *n*-heptane, which might be attributed to the chemical nature of the functional groups. The acid might not be as responsive to the solvent shift as the amide group [286], but its presence increases the polarity of the model compound, which leads to TPN-CNacid being less sensitive to the solvent shift than TPN-CN.

4.3.2.3. Intermolecular distances measured by g_dist

For all the solute-solute simulations carried out (seven model compound molecules in 700 solvent molecules), the distance between one individual model compound and the other six in the same simulation box could be extracted and presented as a function of simulation time by implementing the g_dist function. The g_dist results of all seven model compounds are shown in Figure 4.7 and Figure 4.8. The six plots shown in each figure correspond to the distance between each pair, which reveals the intermolecular distances and the preference for interaction/collision/aggregation. The dimensions of the simulation box is fixed at 5 nm (± 0.3 nm) in each direction, which constrains the distance between each pair of molecules to be similar to or less than that. Formation of aggregates driven by π -stacking interaction shows a characteristic distance of 0.3-0.5 nm [61]. Once a stable aggregate is formed (dimer, trimer, tetramer), the corresponding plot is reduced and remains constant. In the cases of large aggregates where more than two molecules are involved, multiple stabilised g_dist plots could be observed – the number of parallel, consecutive plots show how many molecules stack together.

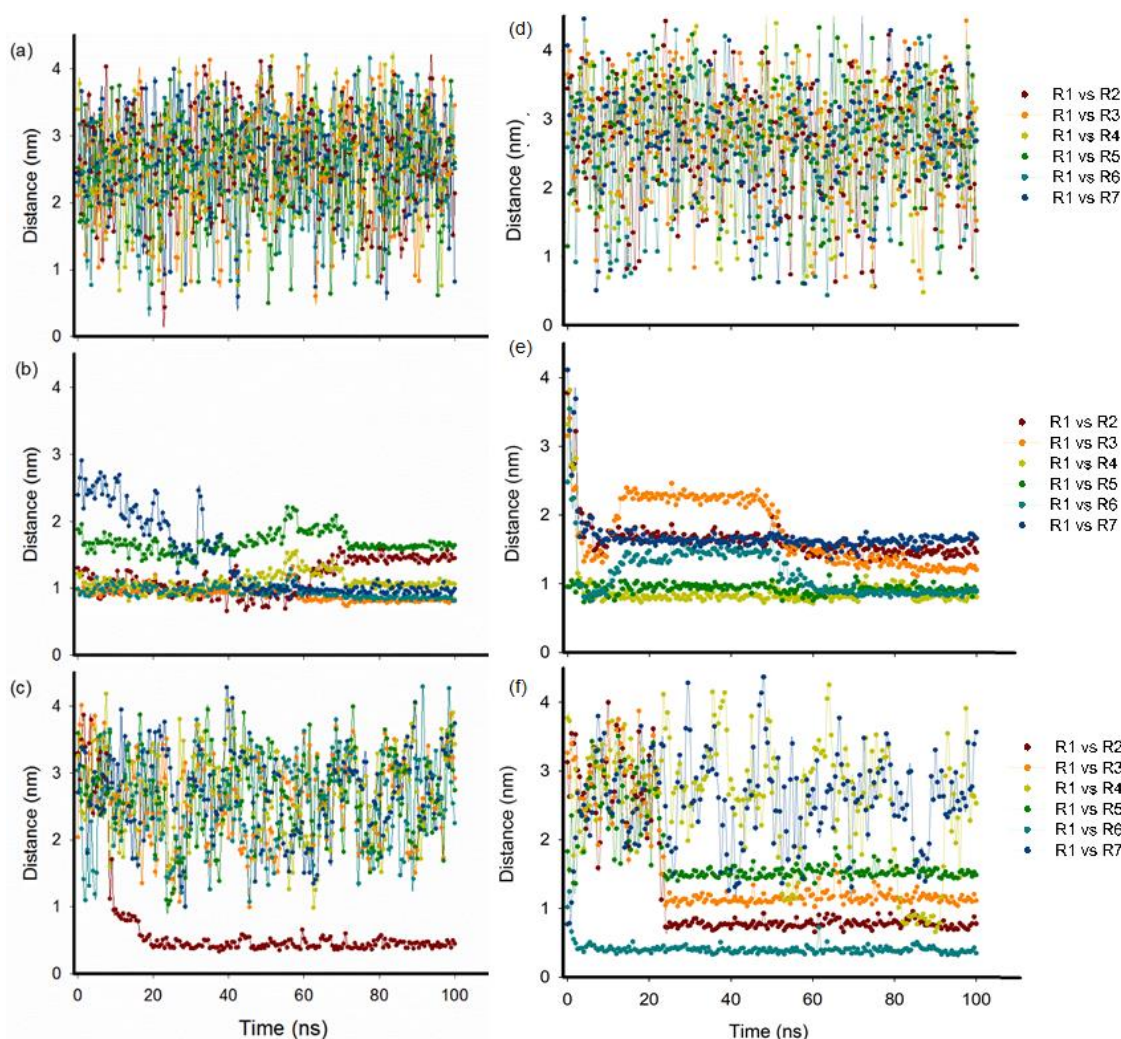


Figure 4.7. Distance between the centres of mass of one model compound molecule (R1) with the other six (R_n) over 100 ns simulation time: (a) TPN-C0; (b) TPN-C1; (c) TPN-C3 in heptol and (d) TPN-C0; (e) TPN-C1; (f) TPN-C3 in *n*-heptane. The six colours shown in each figure correspond to the distance between each pair of molecules.

Figure 4.7a and d show the g_dist plots of the TPN-C0 molecules in heptol and *n*-heptane respectively, as they were allowed to randomly collide over the 100 ns simulation period with distances registered between 0.5 and 4 nm. There is no sign of aggregation as the distance between each pair of molecules changes as a function of time, which is expected for a freely diffusive system that follows Brownian motion. This is consistent with the light scattering result of TPN-C0 that is completely dispersed in both heptol (Figure 4.7a), and *n*-heptane (Figure 4.7d), with no aggregation for a prolonged measurement window. By contrast, most of

the TPN-C1 molecules in Figure 4.7b and e remain at a shorter distance from each other (~ 1 nm), indicating the existence of multiple aggregation configurations, as the peripheral alkyl chains were too short to force any limitations on the assembly. This is also in agreement with the light scattering result which shows a strong tendency for TPN-C1 to aggregate. It can be speculated that the distances recorded in *n*-heptane are smaller, suggesting a tighter configuration as the *n*-heptane percentage increases.

In contrast to TPN-C1, the solvent shift impact is thought to be stronger on the TPN-C3 model compound, as can be observed in Figure 4.7. Only a dimer is observed in heptol, while in *n*-heptane, a tetramer forms at ~ 25 ns and remains stable for the remainder of the simulation. The *g*_dist data agrees with the DLS results in that the aggregation potential increases as a function of aliphatic solvent percentage, as well as, the hypothesised configuration being confirmed – parallel stacking into column-like nanoaggregates, as would be expected of discotic liquid crystals [232].

The results show that the solvent species can increase the aggregation potential, but cannot overcome the association limitations imposed by the molecular architecture. It is important to keep in mind that the *g*_dist datasets show the distances between the pairs formed by one molecule with all six others, but not all of the possible pairings in the simulation box. As such, the datasets should not be taken as recording the total number of aggregation events. The increasing side-chain length from TPN-C3 to TPN-C5 and TPN-C10 yields similar effects observed in Figure 4.8 (a and b to c and d). With the increase in *n*-heptane percentage, an increase in the number of stable/stacked nanoaggregates is observed.

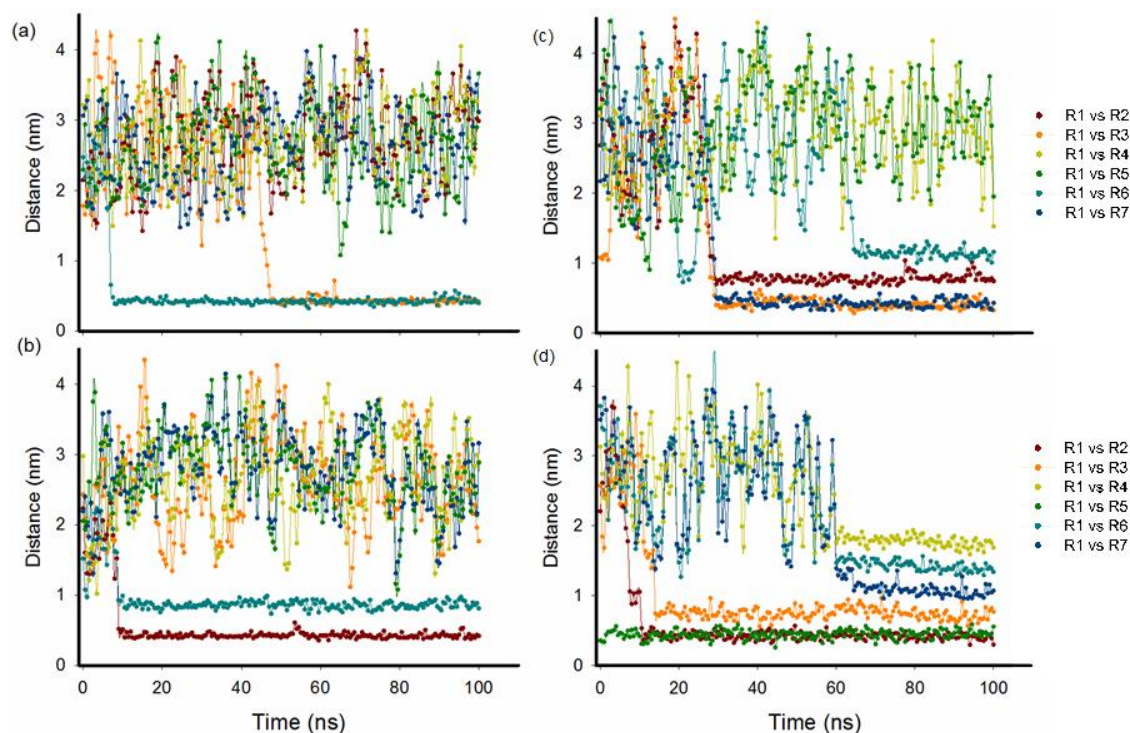


Figure 4.8. Distance between the centres of mass of one model compound molecule (R1) with the other six (Rn) over 100 ns simulation time: (a) TPN-C5; (b) TPN-C10 in heptol and (c) TPN-C5; (d) TPN-C10 *n*-heptane. The six colours shown in each figure correspond to the distance between each pair of molecules.

This effect is more profound with the TPN-C10, as all the molecules are associated in *n*-heptane. Similarly to TPN-C3, TPN-C10 forms dimer-trimer aggregates in the heptol that maintains their pairing for an extended period of simulation time. However, when all the toluene is replaced with *n*-heptane, the molecules appear to form large column-like aggregates. The distance between the aggregated molecules appears to consistently equal π -stacking distances [61], which matches the liquid-crystal behaviour expected of these planar molecules when the solvent facilitates aggregation.

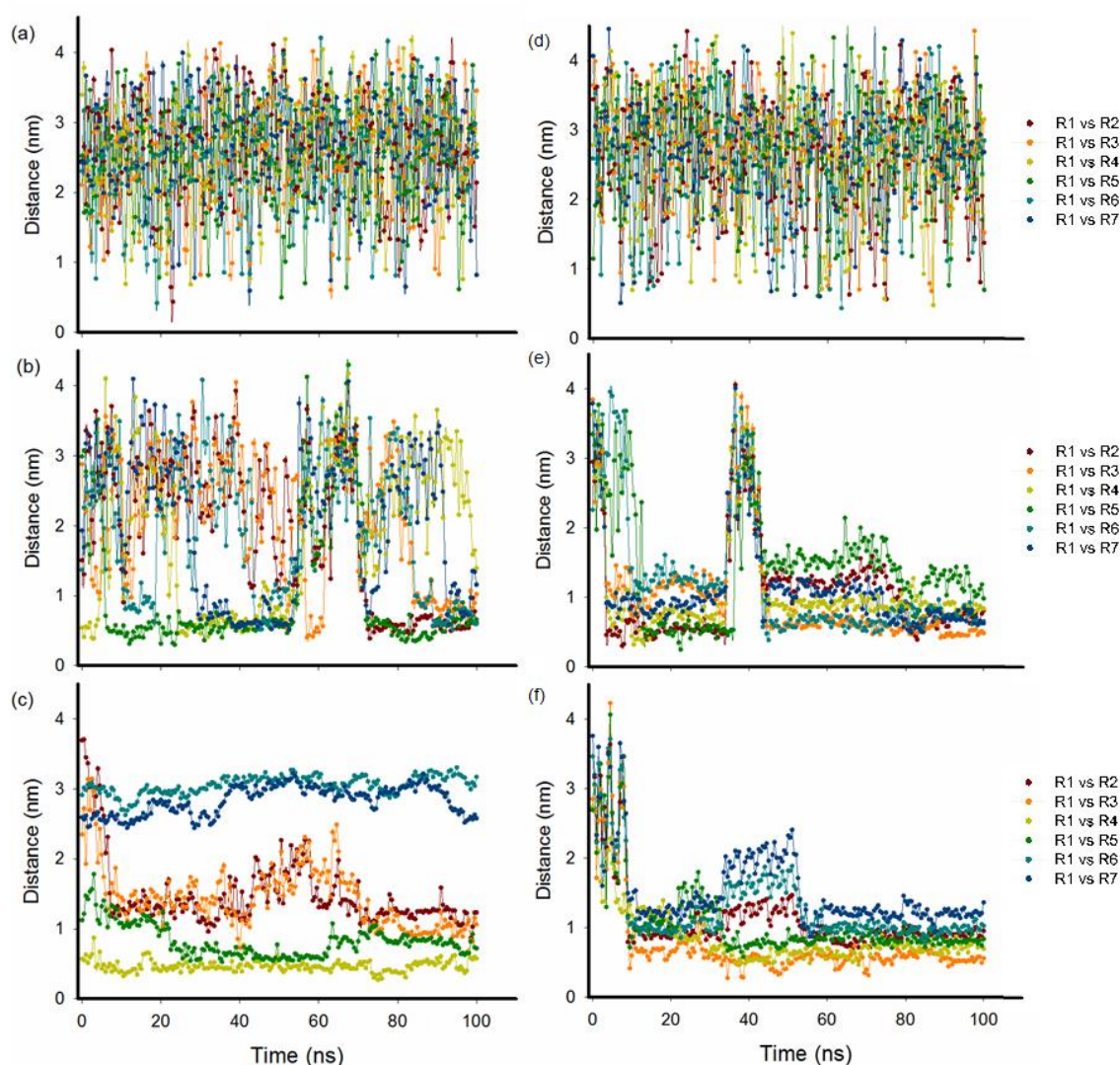


Figure 4.9. Distance between the centres of mass of one model compound molecule (R1) with the other six (Rn) over 100 ns simulation time: (a) TPN-C0; (b) TPN-CN; (c) TPN-CNacid in heptol and (d) TPN-C0; (e) TPN-CN; (f) TPN-CNacid in *n*-heptane. The six colours shown in each figure correspond to the distance between each pair of molecules.

Figure 4.9 displays the distance over time of TPN-C0, TPN-CN and TPN-CNacid in heptol (a, b, c) and *n*-heptane (d, e, f), with TPN-C0 added as a benchmark for the model compounds with embedded functional groups. TPN-CN in heptol exhibits a dynamic aggregation and dissolution process over the 100 ns simulation time, as dimers, trimers and tetramers are found to continuously form and separate. Such characteristics are consistent with the DLS results, where

TPN-CN exhibits large standard errors throughout the recorded hydrodynamic sizes. This indicates that the heptol mixture significantly increases the aggregation of TPN-CN. When toluene was completely replaced, TPN-CN appears to completely cluster into a large aggregate, further highlighting its sensitivity towards *n*-heptane.

TPN-CNAcid (Figure 4.9c) exhibits a far less dynamic behaviour in heptol, as only one dimer remains at constant π -stacking distance throughout the simulation time, while the remaining aggregation events appear to occur across a broader distance (~ 0.6 - 1.2 nm). Again, this is consistent with DLS results that suggest the occurrence of aggregation, but without increasing over time, in contrast to TPN-CN. When completely solvated by *n*-heptane, TPN-CNAcid clusters into a single large aggregate that strives to achieve the most energetically favourable state. As such, small distances are recorded (under 1 nm) that suggest a preference for parallel configurations.

This is further supported by the distribution recorded in the RDF measurements. Representative snapshots of the simulations of three of the seven model compounds are presented in this chapter in order to allow for a visual component to the numerical and plotted data presented so far. The snapshots were chosen from among the final frames of the simulation time and represent a subjective manner of observing the characteristics and interactions of the model compounds as a function of chemical structure.

TPN-C0 (Figure 4.10a) was chosen not only because it is the core model compound but also because it does not aggregate, regardless of solvent species (aromatic or *n*-alkane). In fact, the model compound operates as expected of a colloidal suspension, with random collisions occurring through the observation time. By contrast, dimers, trimers and tetramers can be found in the snapshots of TPN-C5 (Figure 4.10b and e), which is consistent with the RDF and *g*_dist data presented in this section. The restrictions imposed by the peripheral alkyl chains continue to restrict the number of available configurations and hence promote the π -stacking-driven aggregation. This does not seem to change with regard to solvent species; in fact the addition of *n*-heptane appears to increase the aggregation potential, as is concluded by studies of both natural and model asphaltene [16,17,91,116].

The snapshots of TPN-CNAcid (Figure 4.10c and f) show how the molecules prefer to cluster into larger aggregates, with multiple configurations. The snapshots do not manage to capture the shift from heptol to *n*-heptane in the same quantitative way that *g*_dist and RDFs do, as it is only a static and qualitative view of the simulation. It is, however, worth noting that the tail groups are entangled in the aggregates as much as the aromatic core, which is due to the high polarity induced by the carboxylic acid group and amide groups.

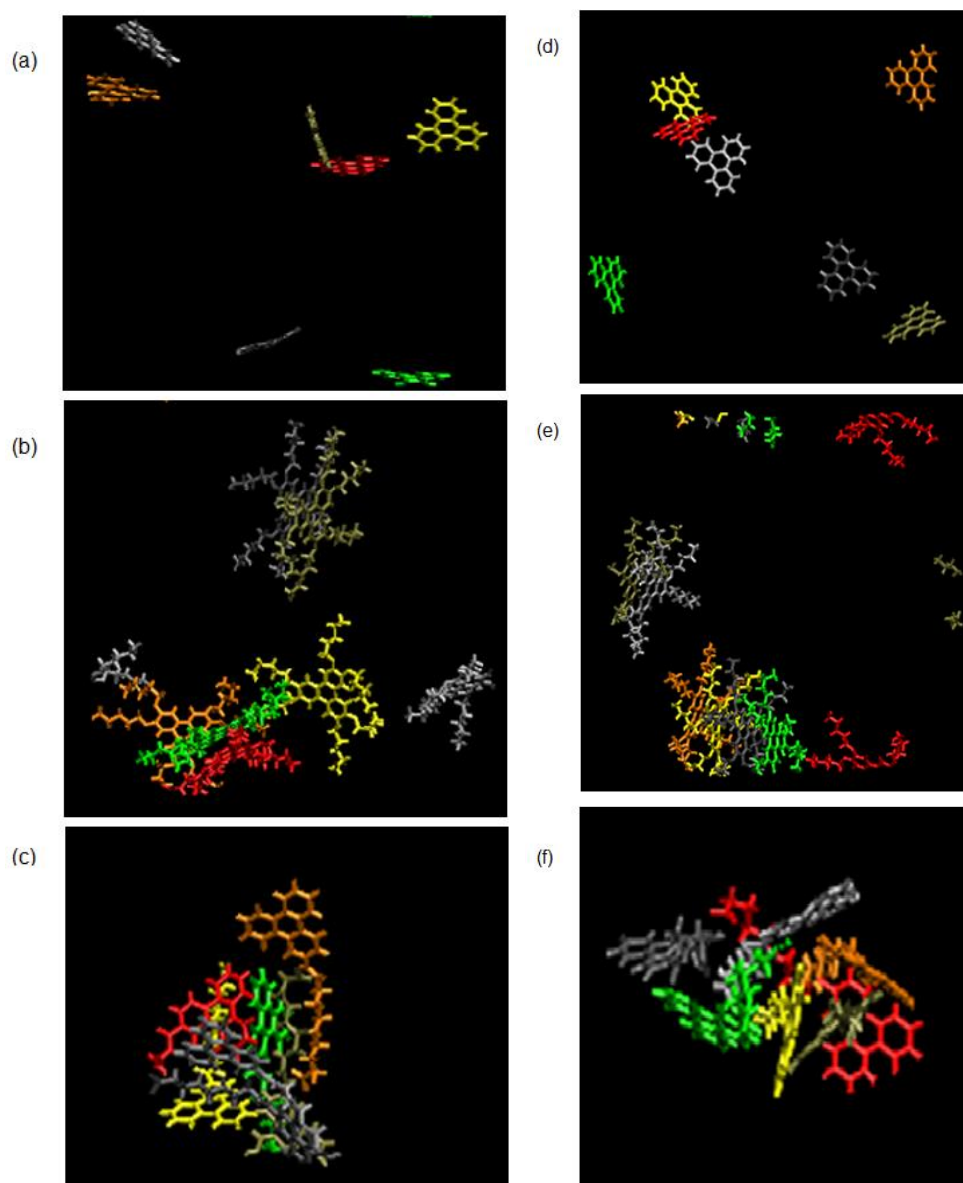


Figure 4.10. Snapshot of MD simulation of seven (a) TPN-C0; (b) TPN-C5; (c) TPN-CNacid model compounds in heptol, and (d) TPN-C0; (e) TPN-C5; (f) TPN-CNacid model compounds in *n*-heptane, showing the interactions between the molecules after 100 ns of simulation time. The solvent molecules are not shown for clarity.

4.4. Discussion

To improve the data clarity for discussion, the hydrodynamic diameters (Figure 4.11) and the RDFs (Figure 4.12) of all seven model compounds in heptol and pure *n*-heptane are presented in two comprehensive figures.

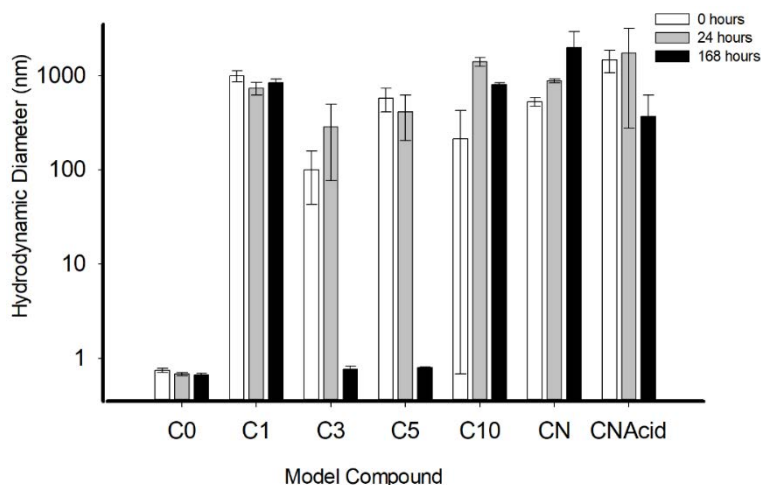


Figure 4.11. Averaged hydrodynamic diameters as a function model compound at 10 mg/mL, all suspended in 40% toluene, 60% *n*-heptane - heptol.

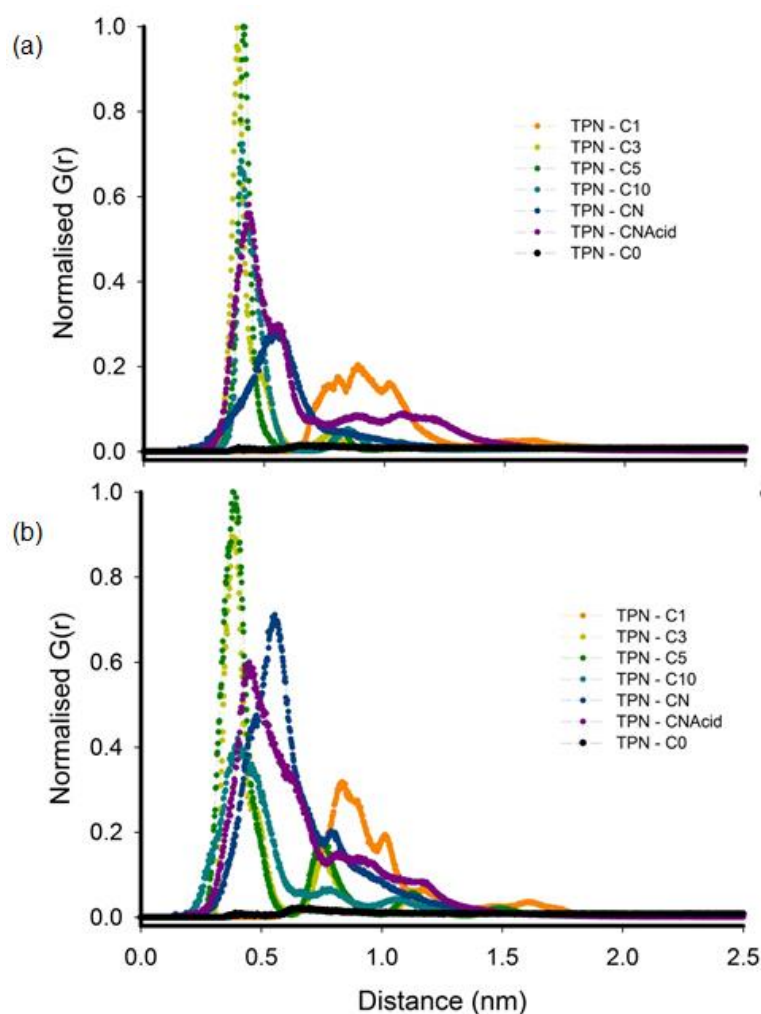


Figure 4.12. Normalised radial distribution function of seven molecules of TPN-C1, TPN-C3, TPN-C5, TPN-C10, TPN-CN and TPN-CNAcid model compounds, solvated by (a) 350 toluene molecules and 350 *n*-heptane molecules (heptol), and (b) 700 *n*-heptane molecules, over 100 ns simulation time.

4.4.1. Effect of chain length on intermolecular interactions in mixed solvent

Previous studies concerning liquid crystals suggest that the length of the alkyl chains surrounding the triphenylene core has the following two roles: stabilising the formed discotic liquid crystal columns and determining the distance between the formed columns [221]. Chemical groups embedded in these chains could facilitate specific reactions or impact the self-association process of these molecules [287]. With the relation between the chemical structure and the aggregation mechanisms of the model compounds in toluene being discussed in the previous chapter, attention is directed towards the effect of solvent species (*n*-alkane) on the intermolecular interactions. As such, in the DLS samples, 60% of the toluene was replaced with *n*-heptane, while in MD simulations 50% and then 100% of the toluene was replaced with *n*-heptane.

Most asphaltene literature considers that *n*-alkane solvent effects are exhibited when more than 50% of the solvent volume is *n*-heptane [103,240,268], which is why the DLS experiments were performed at 60/40 *n*-heptane/toluene ratio. While the MD simulations 50/50 ratio was kept in order to match the results between the solvent affinity (1 model compound molecule in 700 solvent molecules) and solute-solute (7 model compound molecules in 700 solvent molecules). This section discusses the effect of solvent quality on the model compounds as a function of the chain length. In both experiment and simulation, TPN-C0 was used as a benchmark, as it does not appear to aggregate when suspended in either aromatic or aliphatic solvent. The affinity of TPN-C0 as recorded in the RDF graphs in Figure 4.3a, suggests that the molecule has a slight preference towards the toluene rather than *n*-heptane. This is probably

because both toluene and triphenylene are of aromatic nature and the greater electron density is exhibited by the aromatic surface of molecules which facilitates π -bonds [47]. However, in comparison to other model compounds [112], both solute and solvent molecules have a reduced aromatic surface and a limited attraction strength over distance, as determined by the energy of interaction equation (1.1).

The hydrodynamic diameters determined by DLS (Figure 4.11) as a function of time for the TPN-C0, suggest that the presence of 60% *n*-heptane is not enough to overcome the solute-solvent attraction towards toluene and to facilitate aggregation due to the reduced aromatic surface of triphenylene. Additional MD simulations that test the TPN-C0 in both mix solvent (heptol) and pure *n*-heptane suggest that the triphenylene molecules do not aggregate in either solvent. RDF data (Figure 4.12) show no interactions while the *g_dist* (Figure 4.7) captures the occurrence of collisions due to Brownian motion. Previous studies debate whether π -stacking is the main driving mechanism of natural asphaltenes [80-83], however, the general consensus appears to be that this is dependent on the size/number of the aromatic rings [61,84,85], a fact which is reflected by TPN-C0 with its reduce number of aromatic rings (4 rings).

For the TPN-C1 model compound, the addition of *n*-heptane in the DLS experiments (Figure 4.11) yielded slightly smaller hydrodynamic diameters than in pure toluene. Literature suggests that the addition of the alkoxy groups surrounding the triphenylene core facilitates the aggregation between the molecules [232,243]. However, smaller clusters were obtained by DLS upon the addition of *n*-heptane, which is inconsistent with what is expected from natural

asphaltene [46]. The solvent affinity simulations (Figure 4.3) suggest a far greater attraction towards toluene than *n*-heptane for TPN-C1, which is logical due to the aromatic core and the size of the model compound that facilitated reduced COM-COM distances. However, it is the RDF (Figure 4.12) and *g*_dist (Figure 4.7) data that provide an explanation for the smaller than expected sizes. It appears that the nanoaggregates exhibit denser/tighter configurations as more *n*-heptane is added, which explains the small particle size, as denser aggregates would precipitate before looser ones. This is due to the solvophobic nature of the model compounds, as is reflected in previous solubility studies of natural asphaltenes [84,248,268].

The simulation data suggests that there is very little π -stacking occurring between the TPN-C1 molecules, other random configurations being preferred due to the short side-chains. Loose aggregates form and break apart, which is not unfamiliar for triphenylene derivatives in *n*-alkane solvents [288]. This implies that the cluster formation is partially driven by the core, while the aliphatic side-chains are not long enough to impose any stacking configuration that would limit the size of the aggregates and stabilise the molecular self-association. Overall, incorporating alkoxy groups with triphenylene improves the aggregation potential of the model compounds [243]. The addition of *n*-heptane could result in an increase in the packing density of the aggregates, while loose, non-parallel configurations are energetically acceptable in toluene [66,289].

Both TPN-C3 and TPN-C5 model compounds shows less sensitivity between aromatic and *n*-alkane solvents in Figure 4.3c and Figure 4.3d than TPN-C1; however, it is worth noting the width of the toluene peak at 0.6-0.7 nm,

which suggests that the toluene molecules are closer to the COM of the model molecules than the *n*-heptane molecules.

This implies that the change in solvent species might increase the aggregation potential. The hydrodynamic diameters recorded by DLS in heptol support this, as they show the existence of large TPN-C3 and TPN-C5 clusters in the initial heptol mixture (Figure 4.11). However, the recorded hydrodynamic diameters decrease over the 168 hour measurement period until they achieve similar sizes to those observed in pure toluene. This dissolution effect is attributed to the configurational limitations of the molecular structures that do not favour the stability of larger aggregates. The RDF data for both the heptol (Figure 4.12a) and the pure *n*-heptane (Figure 4.13b) show a clear preference towards π -stacking, when the intermolecular distance is between 0.3 and 0.5 nm [61], which is also observed in the snapshots (Figure 4.10) of TPN-C5 simulation. Once toluene is completely replaced with *n*-heptane, the *g*_dist records a significant increase in the degree of aggregation, suggesting that most of the TPN-C5 molecules in the simulation aggregate into large columns of parallel orientation. This behaviour highlights the strength of the electrostatic forces attributed to the solvent species [63,66], as parallel configured clusters result from model compound aggregation. This implies that as long as the alkyl tail-groups are long enough to limit the associations to π -stacking/parallel configurations, the nature of the solvent has a limited impact on the aggregation mechanism of centrosymmetric molecular structures with a triphenylene core [232,290]. The solvent plays a minor role in π -stacking, but a slightly larger impact is observed for the

longer range interactions, suggesting that the presence of more *n*-alkanes influences the model behaviour.

TPN-C10 exhibits similar characteristics to that of TPN-C3 and TPN-C5, despite that they aggregate into far large clusters and stay stable for extended periods of time, according to DLS (Figure 4.11). Although the MD simulations do not show a striking contrast between TPN-C10, TPN-C3 and TPN-C5, the increase in aggregate hydrodynamic size obtained by DLS is solely attributed to the increase in length of a side-chain, as it is the only difference between TPN-C3 and TPN-C10. The *g*_dist data suggest that planar configurations are still dominant within the aggregates, as previous studies have shown that longer tails limit potential configurations [116]. Similarly, natural asphaltenes exhibit a broad distribution of side-chain lengths, and the molecules are shown to heavily aggregate with the addition of *n*-heptane [9,10,21]. This implies that non-centrosymmetric molecular structures with longer side-chain lengths increase the affinity towards solvent species, as would be expected of a model compound that replicates asphaltenes (soluble in toluene and insoluble in *n*-heptane).

The sensitivity of the model compounds regarding the shift from aromatic to *n*-alkane solvents has been proven to increase with side-chain length, however, the solvophobic effects that impact aggregate configuration and packing density appear to be influenced by the aromatic core of the molecule (triphenylene) as much as the length of the side chains (TPN-C1, TPN-C3, TPN-C5, and TPN-C10).

4.4.2. Effect of functional groups on intermolecular interactions in mixed solvent

In Chapter 3, the impact of amide (TPN-CN) and acid groups (TPN-CNAcid) on the asphaltene aggregation mechanism in toluene has been discussed, suggesting that the highly polar characteristics added to the molecules could significantly increase aggregation potential. This potential is further increased when aliphatic solvents are added, as triphenylene cored compounds with functionalised terminal groups are usually suspended in aliphatic solvents such as chloroform or dichloromethane, to facilitate aggregation for applications in other fields [291].

The solvent affinity simulations (Figure 4.4) results suggest that neither TPN-CN nor TPN-CNAcid model compounds exhibits an excessively strong attraction or repulsion towards either toluene or *n*-heptane. This might occur because the degree of polarity induced by the functional groups far exceeds that of either solvent utilised [69]. DLS measurements (Figure 4.11) suggest the presence of large aggregates for both model compounds (TPN-CN and TPN-CNAcid), with a notable difference between their behaviour. TPN-CN aggregates appear to increase in size over time, while TPN-CNAcid aggregates dissolved over the same time interval. This contrast in behaviour is consistent with the *g_dist* data in heptol showing that TPN-CN molecules undertake a highly dynamic association and separation process throughout the simulation time, whilst TPN-CNAcid shows a lower degree of intermolecular interactions over time. This may be attributed to the additional carboxylic acid group that generates stronger bonding forces between the aggregates, which reduces the chances of dissolution. When the toluene is completely replaced by *n*-heptane, both model

compounds appear to aggregate and form closely packed aggregates, of which TPN-CNacid exhibits more dense configurations (Figure 4.9). The decreased hydrodynamic size of TPN-CNacid could be attributed to the formation of higher density aggregates that precipitate more readily than TPN-CN.

The RDFs in Figure 4.12 display a significant change from the heptol to the pure *n*-heptane simulations. The TPN-CN data has a significant increase in both height and width, suggesting that the increased presence of *n*-heptane molecules facilitates greater interaction between the model compound molecules, as would be observed in natural asphaltene [103]. The major configuration present is thought to be parallel, as per the RDFs, although others are certainly possible as the width is broad enough to include non-parallel positions [61].

By contrast, the TPN-CNacid model RDFs do not show a significant difference occurring due to a shift in solvent species. The snapshot images (Figure 4.10c and d) show that the TPN-CNacid form a large cluster; however, π -stacking is not the major driving mechanism, and when the standard errors in the DLS data are taken into consideration (Figure 4.9), the clusters can be considered unstable. This supports the hypothesis that acid groups play a major role in asphaltene aggregation, not only because they facilitate aggregation, but also because they lead to significantly different configurations, which in turn alter the macroscopic properties and behaviour. Previous studies reach similar conclusions, as model asphaltenes with acid functional groups aggregate at oil/water interfaces; the aromatic cores drive a reconfiguration process that seems to align the molecules in parallel configurations [4,16,121]. The described process is regarded as energetically favourable because the polar attraction is

far stronger, and hence a greater driver of aggregation in the initial stages, than the electron clouds present on aromatic surface [48,49]. However, once aggregated, the π -stacking forces drive the re-configuration of the aggregates into the most energetically favourable configurations, which are parallel, due to the aromatic cores of the molecules [223].

4.5. Conclusions

The combination of experimental and computational approaches developed to systematically investigate the effect of chemical structure of model asphaltene compounds on aggregation was advanced further by exploring the impact of solvent. The seven model compounds were evaluated by measuring their hydrodynamic diameters over 168 hours in a 40% toluene/ 60% *n*-heptane mixture using DLS measurements, and their intermolecular interactions were examined utilising MD simulations. The behaviour of the model compounds employed to investigate the chain length effect as a function of solvent species suggests that the major impact they have is on the configuration of aggregates. The different degrees of solvophobicity exhibited by the model compounds is observed as the increase in chain length leads to tighter configurations as toluene is replaced with *n*-heptane, while the asymmetric model compound (TPN-C10) shows a greater aggregation potential as larger clusters remain stable in solution. The aggregation behaviour of TPN-C1 proves that π -stacking is not enough to form stable aggregates, whilst the presence of *n*-heptane could cause them to re-configure into tighter clusters. The formation of nanoaggregates from the TPN-C3 and TPN-C5 models occurs in a similar manner in *n*-heptane as it does in toluene, with the surrounding alkyl chains imposing a π -stacking configuration,

although a slower dissolution of the initial large clusters was recorded by DLS measurements, which makes sense, as *n*-heptane is known to facilitate larger aggregates for TPN-C3, TPN-C5 and TPN-C10.

The incorporation of an amide (TPN-CN) and acid group (TPN-CNAcid) appears to disrupt any π -stacking from initial occurrence, which leads to the formation of large and unstable clusters. Furthermore, the cluster configurations observed from the MD simulations show tail-to-head and head-to-head formations, and along with the MD analysis, imply that the major driving force of aggregation lies in the functional groups, rather than the aromatic cores. According to DLS data, TPN-CN appears to be more *n*-heptane responsive, as larger particle sizes are observed. The clusters formed by TPN-CNAcid model compound appeared to be more unstable with the addition of *n*-heptane; however, the MD simulations suggest that the cluster configurations are tighter, as is expected due to the insolubility in *n*-heptane. After the aggregates are formed, the tendency towards energetically favourable configurations is thought to be driven by π -stacking forces, as the molecules appear to strive towards parallel alignments.

The structure-function relationship has been explored as a function of solvent species for seven model compounds, and it can be concluded that polar attractions overtake van der Waals associations, but are far less sensitive to solvent species. Natural asphaltenes exhibit more complex structures than those investigated, however, although this study has succeeded in isolating key structural characteristics that affect the aggregation mechanism.

**Chapter 5. Effect of planar surface on intermolecular interactions
between aromatic model compounds**

Chapter 5

5.1. Introduction

Asphaltenes, consisting of multiple aromatic rings and various proportions of aliphatic chains, comprise the heaviest fraction of crude oil [10]. As a solubility group, they are broadly defined as soluble in aromatic solvents, such as toluene and xylene, but insoluble in *n*-alkanes, such as *n*-heptane and pentane [8]. It is generally accepted that asphaltene molecules predominantly possess a single aromatic core with peripheral *n*-alkanes, as described by the “continental” model compounds, and their most probable molecular weight is around 750 Da [11-14,21]. With the highly polar and complex molecular structures, asphaltenes occupy a vital role in determining the viscosity of crude oil, which consequently influences different aspects of flow assurance [3].

To elucidate the specific influence of chemical structures on the aggregation process of asphaltenes, one of the approaches is to develop model polyaromatic compounds with well-controlled structure, replicating that of natural asphaltene [16]. The developed chemicals can then be utilised as model compounds studied by both experimental and computational approaches to establish how molecular structures determine aggregation characteristics [16]. This path has been explored in Chapters 3 and 4 with seven triphenylene-cored model compounds that exhibit increasing alkyl chain lengths, an amide, and a carboxylic acid group. However, this chapter aims to isolate the model compound aggregation to that achieved solely by π -stacking interactions. In the previous studies where pyrene was employed as the core for model compounds, it was reported, based on ^1H NMR spectroscopy and steady-state fluorescence, that dimers formed in toluene, however, the interactions are considered to be weak π -stacking due to the small

aromatic surface exposed by the pyrene [72]. Further studies on pyrene-based archipelago models concluded that polar groups occupy a major role in the self-association of aggregates larger than a dimer [19]. This suggests that in the absence of a large aromatic core, π -stacking interactions are limited. Hence, model compounds with increased aromatic cores are taken into consideration, and as such one of the most common found throughout literature studies are those based on hexabenzocoronene (HBC). A multitude of studies highlights the potential of hexabenzocoronene-cored structures to self-associate and yield novel electrical and optical properties [220,292,293]. The core of the compound (13 condensed aromatic rings) gives strong association in solution based on π -stacking association [68]. One study investigates the effect of different tails groups (including *tert*-butyl) on the molecular interactions in polar and non-polar solvents [294]. The study concludes that the interaction of aggregates can be tailored by varying the steric repulsion provided by the side-groups, and that the aggregation potential of all derivatives increased in the presence of a polar solvent, due to solvophobic effects.

Studies utilised hexabenzocoronene as a core for supramolecular assembly investigations [80,242,295], with a general conclusion that both π -stacking and cluster to cluster interaction are influenced by the molecular structure more than any other factor. One study involving pure hexabenzocoronene and 21 solvents (most successful at solvation being halogenated aromatic and amide based), concluded that even in the best solvents, a considerable concentration dependent aggregation effect was observed [296].

To further understand the structural dependence of the asphaltene aggregation mechanism, a planar model compound, hexa-*tert*-butylhexa-*peri*-hexabenzocoronene (HTBHBC) and its non-planar derivatives were developed for the present chapter. Following previous work [17], HTBHBC is recognised to aggregate upon the addition of *n*-heptane, however, concentration-triggered aggregation is more structurally dependent. In one study, HTBHBC was found to not self-associate in 1,1,2,2-tetrachloroethane-*d*₂, unlike the alternative model compounds with long *n*-alkane chains surrounding the core, due to the steric repulsion facilitated by the short side-groups. The impact of HTBHBC concentration was not investigated; however, the previous model compounds had various degrees of sensitivity towards concentration variations [297]. The conclusions suggest that although HTBHBC might have the potential to aggregate in specific environmental conditions (solvent, concentration), it does not necessarily do so in all circumstances.

This work aims to determine how the planarity of a model compound influences the kinetics of aggregation in toluene, as well as the impact of *n*-alkane solvent (*n*-heptane) on the stabilised supernatant. Previous studies have utilised HTBHBC as a model asphaltene compound and have shown that aggregation and formation of clusters (200-500 nm hydrodynamic radius) can ensue with the addition of *n*-heptane [17]. A previous computational simulation study from the authors group suggests that any modification to the structure of HTBHBC could result in different aggregation pathway [196], which highlights the structure-dictates-function relation. This chapter initially focuses on the time and concentration dependence of HTBHBC and derivatives prepared with toluene, by

Chapter 5

using DLS, ^1H NMR spectroscopy, and MD simulations, after which different percentages of *n*-heptane were added and the outcome recorded.

5.2. Materials and Methodology

5.2.1. Materials

Toluene 99.85%, Extra Dry-AcroSeal, *n*-heptane 99.85%, Extra Dry, PTFE membrane filters (100 nm pore size, Whatman) and DLS optical cells were purchased from Fisher Scientific (Loughborough, UK). Deuterated (d_8) toluene was purchased from Sigma-Aldrich (Dorset, UK), and used as received. The HTBHBC was synthesised following Rathore and Burns one pot synthesis [298]. One significant modification to the referenced synthesis involved adding excess *tert*-butyl chloride to increase the reactivity of the HBC. The process description can be found in Appendix B.

5.2.2. Methodology

5.2.2.1. Dynamic light scattering

DLS measurements were made using a compact goniometer system (ALV/CGS-3, ALV-Laser, Germany) in conjunction with a multiple tau digital correlator (ALV/LSE-5004, laser wavelength $\lambda = 632.8$ nm and scattering angle $\theta = 45^\circ$). The optical cell, washed with toluene and dried with nitrogen, was placed in an immersion liquid (toluene bath) to reduce spurious scattering and improve temperature control. All experiments were performed at room temperature ($22 \pm 0.5^\circ\text{C}$) and ambient pressure. Toluene was filtered three times using PTFE filters (pore size 100 nm) before the HTBHBC powder was added at concentrations 1, 2, 3, 4, 5, 10, 15, 20, 30, 40, and 50 mg/mL. All samples were kept at room

temperature without any further agitation prior to measurements. Time-averaged scattering intensities and autocorrelation functions were acquired for each sample at four different times (0, 24, 168, and 336 hours). At every time, 100 readings were collected during a 30 minute period. After 168 hours, the supernatant was extracted and mixed with triple filtered *n*-heptane in 20%, 40%, 60% and 80% percent ratios relative to toluene. The samples were re-measured following the same protocol. Scattering intensity data was normalised with respect to the incident beam intensity, and background scattering from toluene was subtracted. The mean diffusivity, D , was calculated based on the intensity autocorrelation function acquired $g_2(\tau)$, based on the Stokes-Einstein equation (2.5).

5.2.2.2. Chemical analysis of synthesised product

^1H NMR spectroscopy (Bruker AVANCE III equipped with a 5 mm PABBO probe head) was utilised to quantify the purity of the HTBHBC powder dissolved in d_8 -toluene. Sweeping frequency was 300 MHz, and chemical shifts were reported as δ values relative to CDCl_3 .

In a conventional ^1H NMR assay spectroscopy, a well characterised compound is introduced in the sample as reference. The modified-assay approach used in this work avoids contaminating the sample with a foreign compound by considering an internal standard that corresponds to the aromatic protons of HTBHBC at 9.7620 ppm.

The area under the reference peak (HTBHBC) was integrated and set to unity and the variations in the remaining peaks (10.86 ppm and 10.46 ppm) were compared to it. Solvent peaks were also integrated at 2.36 ppm in each

measurement to account for the concentration change as a result of solvent evaporation. Of the 12 HTBHBC samples (20 mg/mL in d_8 -toluene), three were examined by ^1H NMR at each time (1, 24, 168, 336 hours), the supernatant extracted and the solid deposit dissolved in d_8 -toluene.

A Micromass liquid chromatography time-of-flight (TOF) (Waters - MALDI micron MX) with electrospray ionisation and a CH_3OH mobile phase was employed to examine the chemical composition of the dried solid deposit and supernatant at 168 hours. Ion detection was performed using a dual micro channel plate detector assembly and data was acquired using a 4.0 GHz time-to-digital converter. All data was processed by the MassLynx software system. The results are meant to complement the ^1H NMR spectra, to highlight the difference between the supernatant and solid deposit, as well as help identify the dominant derivative chemical structure. From the ^1H NMR spectroscopy and the MALDI–TOF chromatography, the pure HTBHBC compound was found (Figure 5.1) and the chemical structure of the dominant derivative compound Figure 5.2:

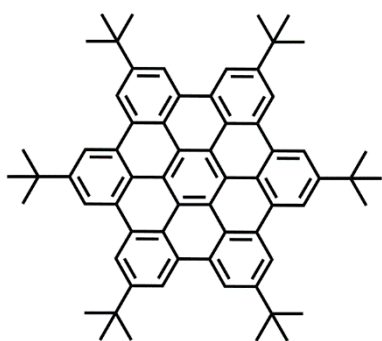


Figure 5.1. Molecular structure of HTBHBC, $\text{C}_{66}\text{H}_{66}$; Mw = 858.6 g/mol as obtained by the one-pot synthesis established by Rathore and Burns [298].

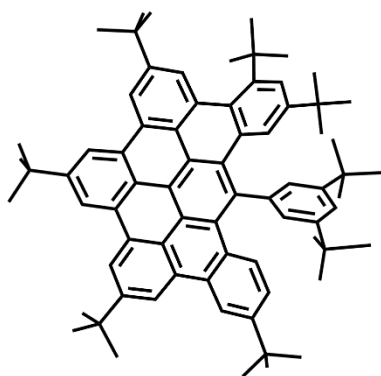


Figure 5.2. Derivative HTBHBC molecule (3D) as hypothesised from the ^1H NMR spectroscopy and the MALDI-TOF spectroscopy. The excessive amount of *tert*-butyl leads to an over-reaction that does not allow the carbon bonds to form appropriately. Instead, *tert*-butyl tails bond to those free positions.

5.2.2.3. Molecular dynamics simulations

Molecular dynamics simulations in this chapter were performed with the GROMACS 4.6.5 software package and the OPLS/AA force field following the same procedure described in previous chapters. Two model compounds were built with the protocol described in Chapter 2, one replicating the chemical structure of the HTBHBC compound (Figure 5.1) and the additional, labelled “DevHTBHBC” Figure 5.2, was built based on the most likely derivative chemical structure as concluded from the ^1H NMR spectroscopy and MALDI-TOF results.

After a simulation box is generated and solvated, energy minimization is performed to ensure a stable initial configuration. Equilibration steps (1000) of 100 ps were then performed to prepare the simulation for trajectory production. The Berendsen algorithm was adopted to relax the system to 298 K and 1 atm pressure. Once steady fluctuations reached the average volume, the 100 ns simulations were performed with an integration time of 2 fs, a cut-off of 1.0 nm used for van der Waals interaction and periodic boundary conditions [204].

Chapter 5

To investigate the solute-solute interactions, seven molecules of the same chemical structure were placed in toluene and *n*-heptane (700 toluene or *n*-heptane molecules) and in 50% toluene – 50% *n*-heptane simulation box (350 toluene molecules - 350 *n*-heptane molecules). RDFs were employed to underpin the average distance between selected molecules, and VMD was employed to extract snapshots of the simulation.

To investigate the solute-solvent interactions, a secondary set of simulation boxes were built using the same software package and force field. However, only one model compound molecule was placed in a simulation box of 700 solvent molecules (350 *n*-heptane and 350 toluene). RDFs were employed to establish the averaged distance between the selected molecule and each solvent species during the simulation, which reveals the magnitude of affinity of each model molecule towards each solvent.

5.3. Results

This chapter employs a synergistic approach by combining experimental and molecular dynamics simulations to understand the complex interplay of the structure-function relation. The experimental approach consisted of DLS and ¹H NMR spectroscopy. The results recorded (scattering intensity or hydrodynamic size) by DLS are divided by concentration (below or above 5 mg/mL) and by solvent species (toluene or different percentages of *n*-heptane added). The ¹H NMR spectroscopy was employed to assess the quality of the compounds and to quantify the difference between the chemical structures found in the solid deposit and the supernatant. Molecular dynamics simulations were employed to assess solvent affinity of the two model compounds (one molecule in solvent simulation

box), and the molecule to molecule interaction (seven model compounds in solvent simulation boxes).

5.3.1. Kinetic, concentration, and solvent effects measured by DLS

To examine the clustering of HTBHBC and its derivatives as a function of concentration, light scattering measurements were initially performed in toluene. Both time-averaged scattering intensity (static light scattering) and autocorrelation function (dynamic light scattering) were recorded and presented in separate sub-chapters below.

5.3.1.1. Scattering intensity as a function of concentration

The initial scattering intensity (at 0 minutes) in the low concentration regime was found to increase as a function of concentration in toluene. Consequently, a prolonged period was required for the scattering intensity to stabilise for samples with increased concentration.

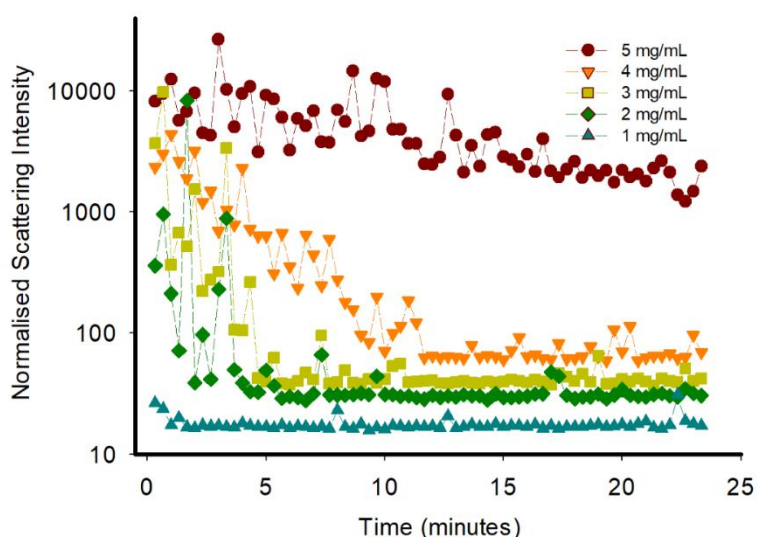


Figure 5.3. Normalised scattering intensity of HTBHBC in toluene as a function of time for low concentrations (1-5 mg/mL).

At 2, 3 and 4 mg/mL the samples required 5, 7 and 10 minutes to stabilise, while at 5 mg/mL, more than 25 minutes were needed. Although no visible precipitation was observed, the decrease in scattering intensity during the stabilisation process could be attributed to restructuring of initially formed clusters, gradual dispersion of loosely aggregated assemblies into smaller colloidal scale entities, or sedimentation of larger clusters.

To further explore the effect of concentration on the clustering of the model compounds prepared, samples with concentration between 10 and 50 mg/mL were examined by light scattering. After introducing HTBHBC into toluene, undissolved solids remained, which sediment readily.

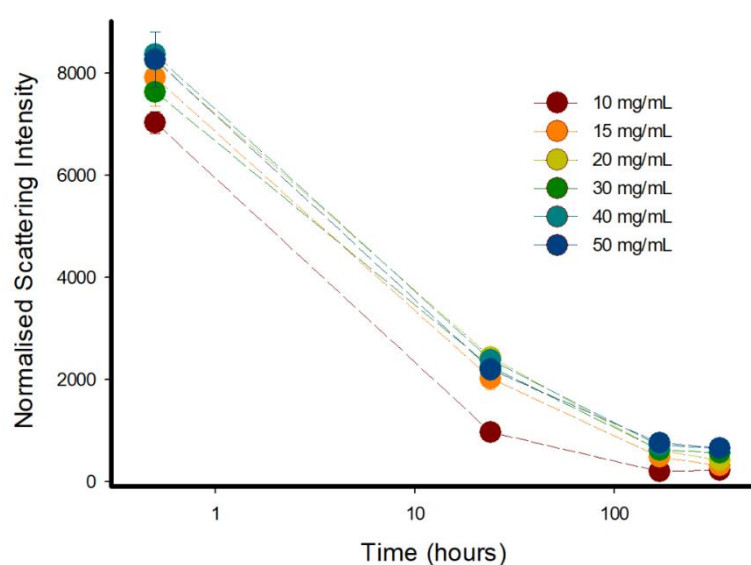


Figure 5.4. Mean normalised scattering intensity of HTBHBC in toluene as a function of time for high concentrations (10–50 mg/mL).

Figure 5.4 presents the measured scattering intensity over an extended period of time (up to 336 hours) for samples at high concentrations. The time-averaged scattering intensity acquired within the first hour for all samples examined was similar to that obtained for the 5 mg/mL sample. Furthermore, the variation between the initial intensity values acquired from different concentrations

was not as significant as in the low concentration regime. Within the first 24 hours, there is a significant reduction in scattering intensity. This can be attributed to restructuring of initially formed clusters, gradual dispersion of loosely aggregated assemblies into smaller colloidal scale entities, or sedimentation of larger clusters. The scattering intensity continues to decrease beyond 24 hours, albeit at a slower pace, until it remains relatively constant after about 336 hours, suggesting that the clustering reached an equilibrium configuration [108].

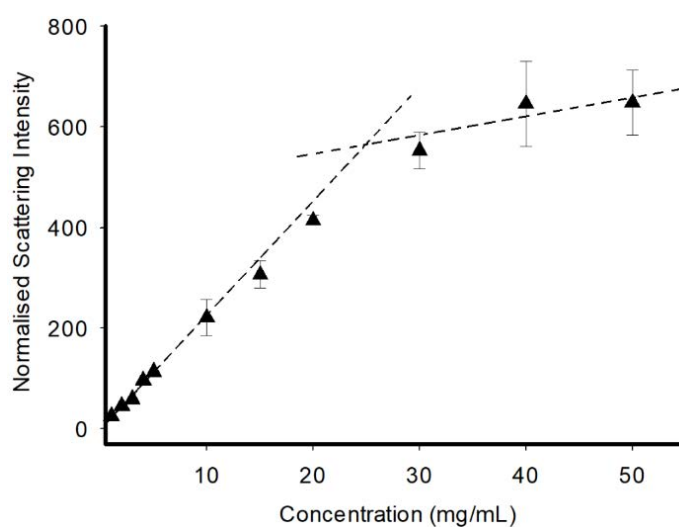


Figure 5.5. Mean normalised scattering intensity acquired at 168 hours as a function of initial concentration. The relation is linear in the low concentration regime but becomes sub-linear as concentration increases.

To verify the correlation between scattering intensity and initial concentration values, Figure 5.5 was plotted, with data acquired after the systems reached equilibrium (168 hours). The scattering intensity can be seen to increase as a function of initial concentration starting from 1 mg/mL to 50 mg/mL, as a higher number of particles are present in solution. This indicates that, after the system achieved a stable state, the number of particles present in solution was still proportional to the initial concentration.

To validate the correlation between scattering intensity and the addition of different volumes of *n*-heptane, acquired after each system had reached equilibrium (168h), the scattering intensity was collected and plotted in Figure 5.6. The normalised scattering intensity is presented as a function of initial concentration, with each data-line indicating a different percentage of *n*-heptane dilution. For example the 100 V% toluene data set is the product prepared with toluene for 168 hours. The 80 V% toluene is the same initial concentration of product in toluene, but with 20% of the initial solvent volume added as *n*-heptane.

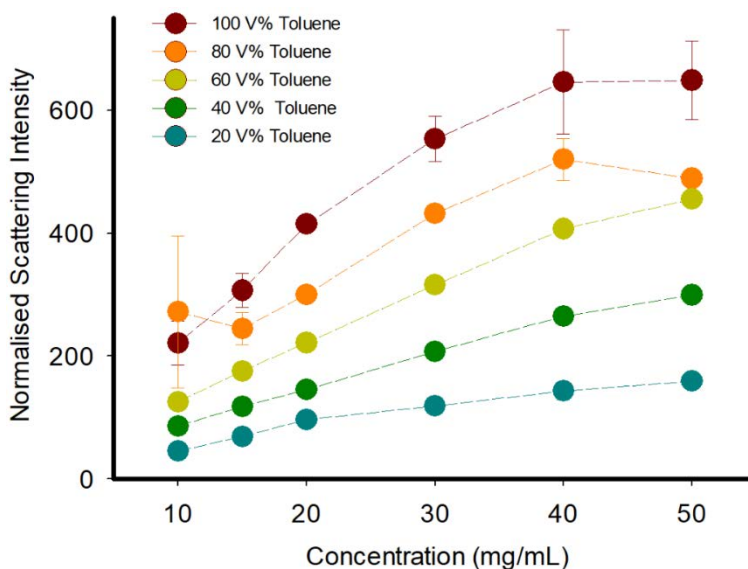


Figure 5.6. Mean normalised scattering intensity of HTBHBC in toluene after 168 hours, with the addition of *n*-heptane (80, 60, 40, 20% of toluene volume) as a function of initial concentration.

The scattering intensity of each point decreased proportional to its degree/percentage of dilution with *n*-heptane, which implies that the addition of *n*-heptane did not have any impact on the stabilised suspension, other than diluting the solution.

5.3.1.2. Kinetics of hydrodynamic size

Based on the autocorrelation functions from light scattering measurements, hydrodynamic radii of the HTBHBC clusters were calculated and presented as a function of initial concentration in Figure 5.7. The radius of the HTBHBC aggregates was found to be around 1000 nm and was not dependent on the initial concentration. The radii of the HTBHBC clusters remained constant, whilst the scattering intensity reduced significantly during the same period, as shown in Figure 5.4. This supports the rationale suggested above, that this is a restructuring process of initially formed clusters. However, it does not suggest any gradual dispersion of loosely aggregated assemblies into smaller colloidal scale entities, or sedimentation of larger clusters, because either explanation would result in decreasing mean hydrodynamic radius within the first 24 hours. After 168 hours, the radii of clusters were about half of those measured at 24 hours, and these values are similar to those reported previously for HTBHBC in toluene - *n*-heptane mixtures [17]. We note that no reliable correlation function could be acquired for samples at 10, 15, and 20 mg/mL after 24 hours, even though the intensity was similar to that acquired in the remaining samples.

To understand the dominant driving forces promoting the aggregation of HTBHBC and derivatives in toluene, ¹H NMR spectroscopy and MALDI-TOF measurements were carried out to identify the exact chemical nature of both the compounds that were in the liquid phase and those in solid deposits.

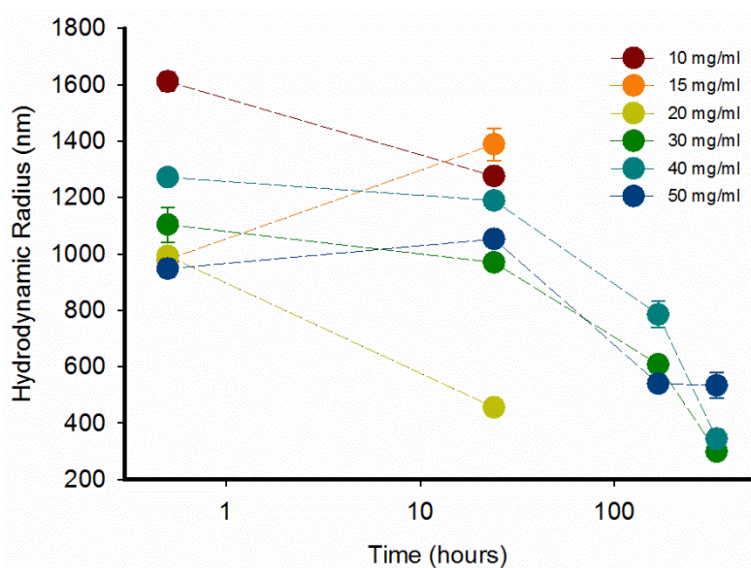


Figure 5.7. Mean hydrodynamic radius of HTBHBC in toluene as a function of time, at high concentrations (10–50 mg/mL).

5.3.2. Chemical composition analysis

HTBHBC (Figure 5.1) dissolved in d^8 -toluene (20 mg/mL), was examined by ^1H NMR spectroscopy at the same times as in light scattering experiments. At 24, 168 and 336 hours, the solid was separated from the supernatant, and dissolved in d^8 -toluene, before both suspensions were examined by ^1H NMR spectroscopy. Figure 2.6a displays the spectrum corresponding to the solid deposit while Figure 2.6b displays the spectrum of the supernatant at 168 hours.

In the spectra presented, the peak at 9.7 ppm corresponds to the aromatic rings of coronene, the double peaks at 7.2 ppm and the peaks between 2 and 3 ppm were respectively attributed to CH and CH_3 groups of toluene, while peaks below 2 ppm correspond to CH_3 groups of the HTBHBC. The minor peaks observed between 8 and 10 ppm were attributed to alternative types of aromatics, which indicate the presence of derivatives, in addition to the desired product.

This is attributed to the excessive amount of *tert*-butyl chloride added to the one-pot synthesis, altering the reaction kinetics, which results in a fraction of derivatives with extra *tert*-butyl functional groups surrounding the aromatic core. The reaction product was a mixture of HTBHBC and its derivatives, containing symmetric and asymmetric model compounds.

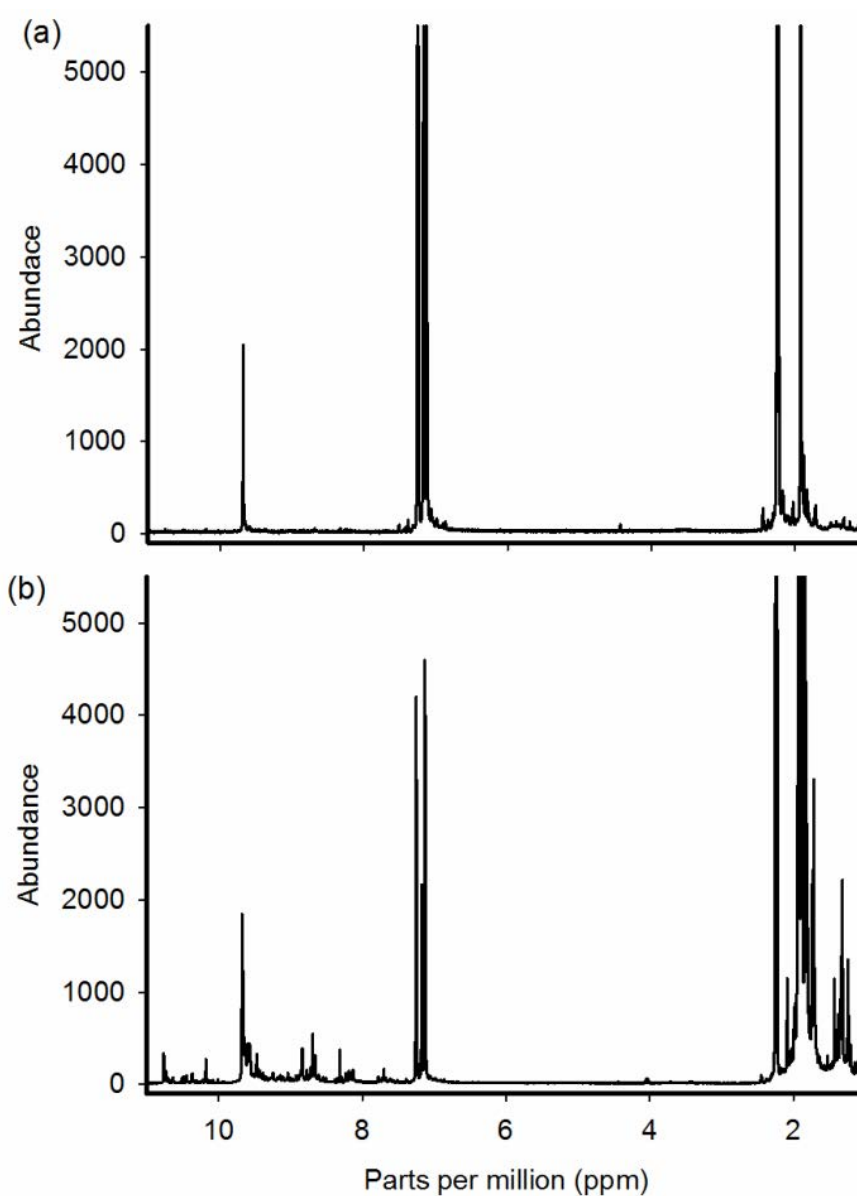


Figure 5.8. ¹H NMR spectra of the HTBHBC 20 mg/mL in deuterated toluene at 168 hours. Spectrum (a) was obtained from the solid deposit and spectrum (b) from the supernatant.

The supernatant and precipitate were further examined by MALDI-TOF. Mass spectra (MS) acquired from solid deposit (a) and supernatant (b) are presented in Figure 5.9. The supernatant MALDI-TOF spectrum confirmed the presence of the derivative compounds in addition to HTBHBC ($m/z = 858.6$).

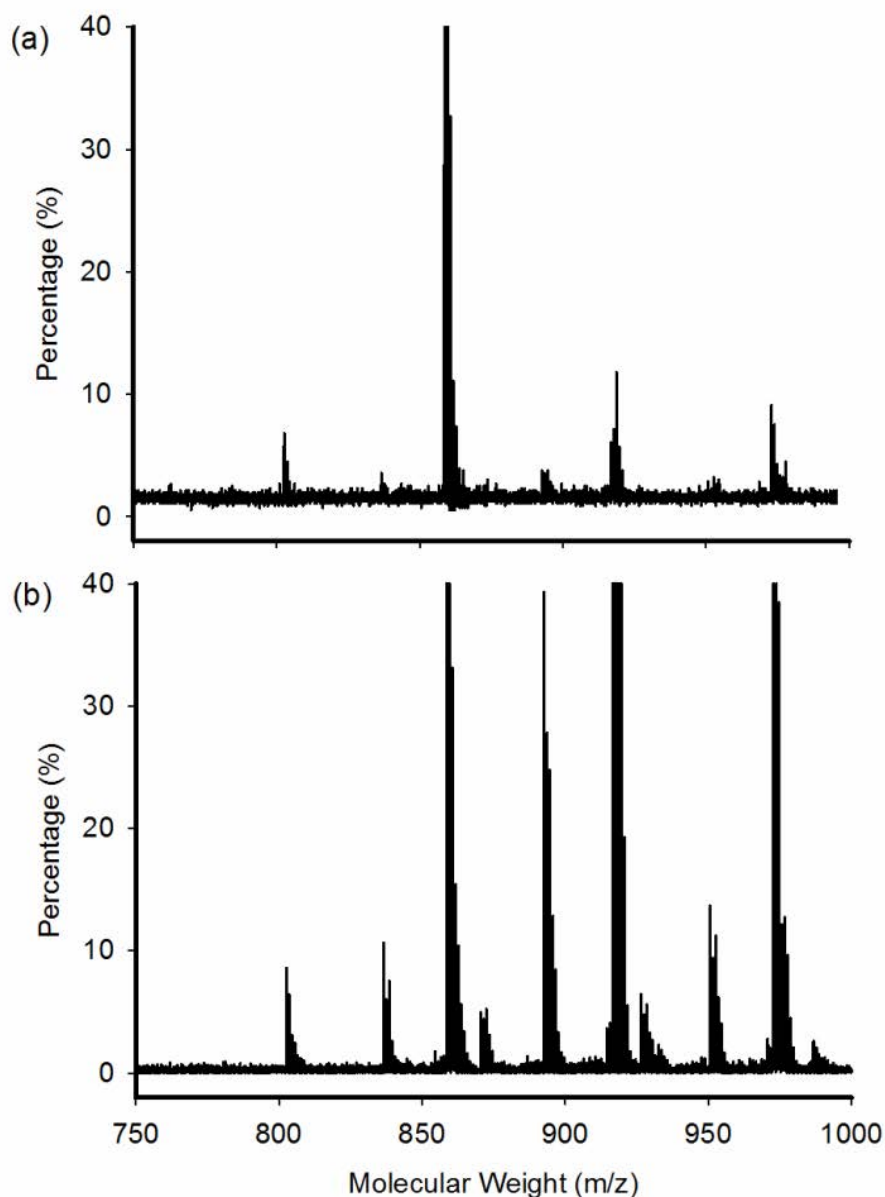


Figure 5.9. MALDI TOF spectra of the HTBHBC ($m/z = 858.6$) and derivatives: (a) shows the spectrum of precipitate with the major peak belonging to the pure HTBHBC compound; (b) the supernatant shows a variety of peaks that indicate the existence of multiple derivative

Evidence observed in the supernatant indicate that the derivatives prefer to remain in solution. However, only one major peak that corresponds to HTBHBC was found in the solid deposit spectrum, suggesting that the majority of the solid is composed of pure HTBHBC.

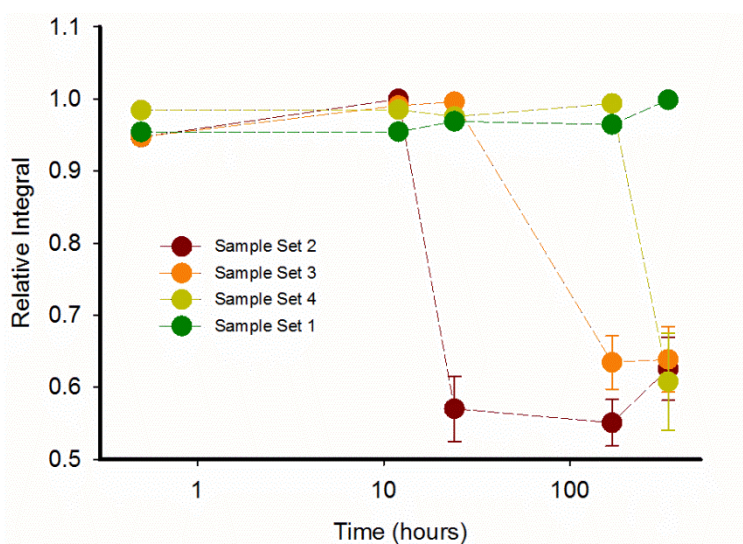


Figure 5.10. Shift in relative integral of peaks at 10.86 ppm and 10.46 ppm, over time as a function of sample purity. Sample set 1 not was not re-suspended while sample set 2, 3 and 4 were re-suspended and measured at 24, 168 and 366 hours, respectively. All samples were kept at room temperature for the entire time interval

Due to the difference in chemical structure between the molecules in suspension and the precipitate, a more thorough investigation was performed to understand the effect chemical structures have on the stability of the system over a prolonged time interval. Following the same time steps as the light scattering measurements in Figure 5.4, ^1H NMR spectra were acquired at the same times using the approach described in the experimental section. Figure 5.10 quantifies the changes in areas under peaks at 10.86 ppm and 10.46 ppm as the solid deposit separated from the liquid supernatant and re-dissolved. Sample set 1 was not re-suspended, hence it does not decrease in relation to the relative integral throughout the experimental time. For sets 2, 3 and 4, the solid deposit was re-

suspended at 24, 168 and 336 hours respectively, showing a clear decrease in the relative integral. As the relative integral was obtained from the impurity peaks, the decrease observed in sample set 2, 3 and 4 indicate a decrease in the amount of impurities. In Figure 5.10, a purification of the original product occurs, when concentration forces the precipitation of the pure compound (HTBHBC), while the impurities (DevHTBHBC) remain in solution. As HTBHBC is known to aggregate in a variety of conditions due to its large, planar surface area. By facilitating π -stacking and forming large aggregates, it is far more likely that it is the species precipitating [17]. Sample set 2 shows the lowest decrease (re-suspended solid deposit), while Sample sets 3 and 4 are slightly higher. This implies that the more time the initial samples are left un-separated (supernatant from precipitate), the more DevHTBHBC contributes to the sediments.

5.3.3. Molecular dynamics simulations

Molecular dynamics simulations were performed to further understand the association potential of HTBHBC and DevHTBHBC as well as underpin the effect of solvent species. The solute-solvent interactions of one model molecule (either HTBHBC and DevHTBHBC) were quantified by using radial distribution functions. Then the solute-solute interactions were investigated with the simulations that contain seven model compound molecules in a 50/50 toluene/*n*-heptane and a *n*-heptane simulation box.

5.3.3.1. Radial distribution functions of solute-solvent interactions

The intermolecular interactions of each model molecule (HTBHBC and DevHTBHBC) placed in a 50/50 toluene/ *n*-heptane simulation box for 100 ns were quantified using RDFs. These display the density of the two solvent species

around the model compound as a distance distribution, which allows for the interpretation of solute-solvent interaction or the affinity of a molecule to each solvent species.

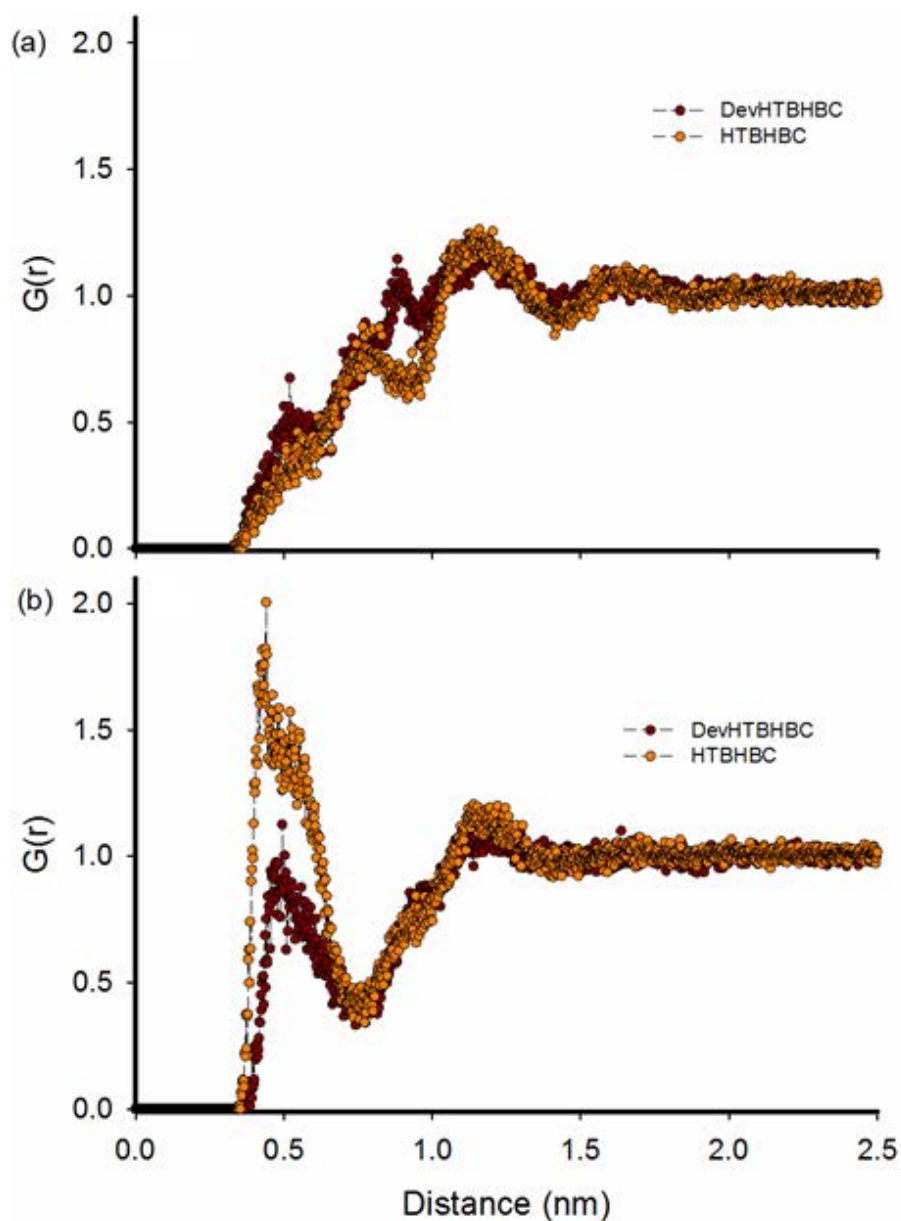


Figure 5.11. Radial distribution functions of a single HTBHBC and DevHTBHBC model compound versus (a) toluene and (b) *n*-heptane in simulation boxes of 350 toluene and 350 *n*-heptane molecules, over 20 ns simulation time.

The RDFs presented in Figure 5.11 quantify the solvation strength of toluene and *n*-heptane relative to the planarity of the chemical structure of the

model compound (HTBHBC DevHTBHBC). In Figure 5.11a the two slightly greater peaks of DevHTBHBC, at 0.5 and 0.8 nm, suggest a marginally stronger attraction towards toluene than the HTBHBC, however, both chemical structures have a similar degree of affinity towards toluene molecules. By contrast to its behaviour in toluene, HTBHBC shows a higher affinity towards *n*-heptane (Figure 5.11b - peak at 0.5) suggesting a greater affinity of *n*-heptane for the larger aromatic surface presented by the planar HTBHBC. The higher affinity of HTBHBC towards *n*-heptane might be reflected in the COM-COM distances, as more *n*-heptane COMs can come closer to the HTBHBC COM than toluene COM. This is also suggested by the difference in the slopes of the distributions. While in toluene, the height of the peaks are gradual until they achieve nominal density, in *n*-heptane, the peak intensity increases above nominal, decreases below, and only after does it reach nominal, which might explain why the solute-solvent interactions favour the *n*-alkane solvent, as opposed to the aromatic.

5.3.3.2. Radial distribution functions of solute-solute interactions

To assess the association capacity of each model compound in different solvent species, MD simulations with seven molecules were performed in the three solvent simulation boxes. Figure 5.12 shows the RDFs of HTBHBC versus DevHTBHBC in a toluene simulation box (a), a heptol box (b), and a *n*-heptane box (c).

In the toluene simulation boxes, both molecular species exhibited a limited degree of interaction between themselves. This is expected due to aromatic core of the molecule being highly solvophilic towards aromatic solvents, generating a strong electrostatic repulsion (Stern layer) [66].

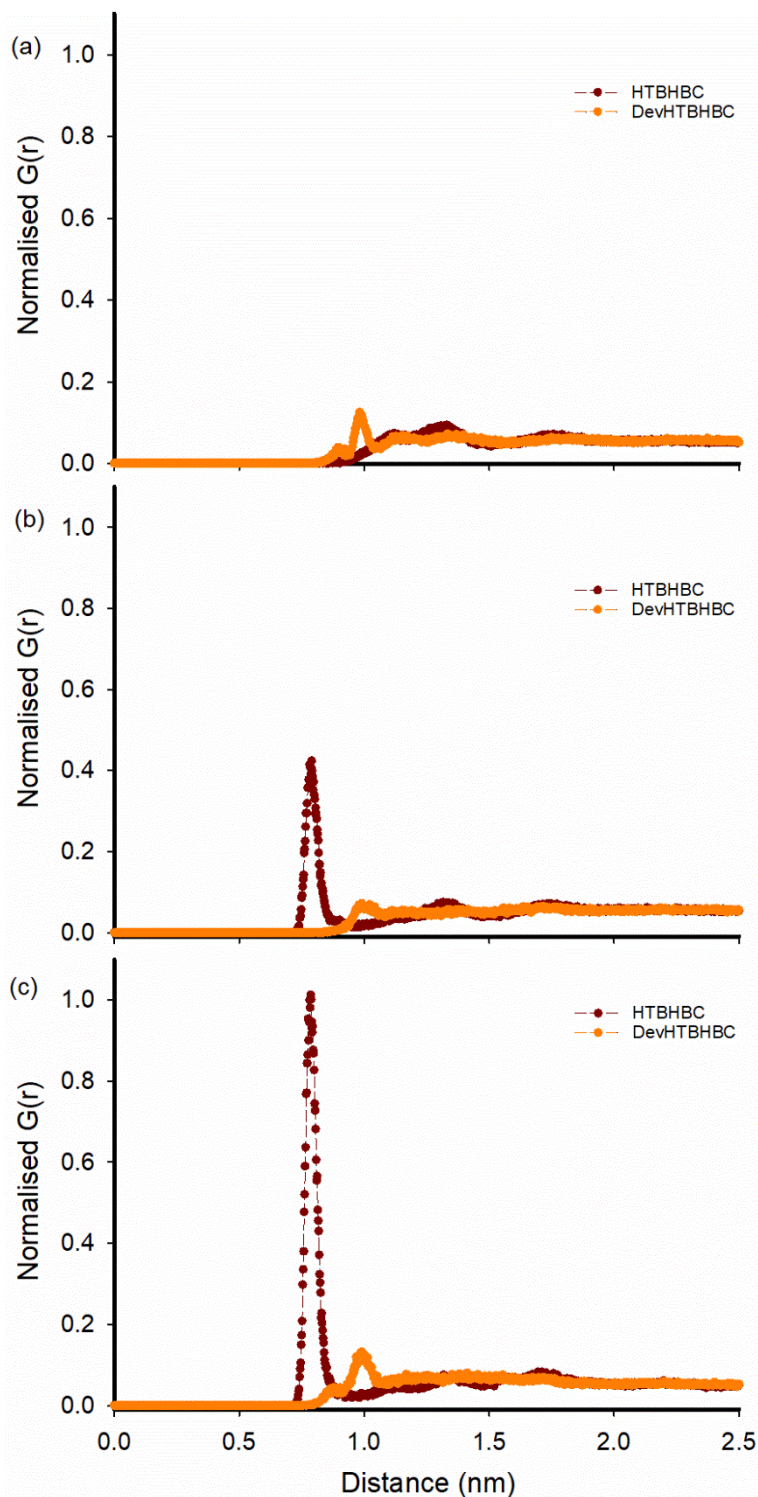


Figure 5.12. Normalised radial distribution functions of HTBHBC and DevHTBHBC model compounds in (a) toluene, (b) heptol, and (c) *n*-heptane over 100 ns simulation time.

The DevHTBHBC showed a small peak at 1.0 nm, which can be associated with the shifted COM (from planar in HTBHBC to non-planar DevHTBHBC) that

allows the interactions to appear closer than they physically are. In the heptol simulation boxes, the DevHTBHBC shows a small peak at 1.0 nm (similar to Figure 5.12a, while HTBHBC displayed an increased peak at 0.7-0.8 nm, which could be associated with molecular interactions, although they are above π -stacking distances. As expected from previous studies the addition of *n*-heptane facilitates the interaction of HTBHBC [17].

In the *n*-heptane simulation boxes (Figure 5.12c) the DevHTBHBC exhibits the same small peak at 1.0 nm, while HTBHBC displays the highest peak in the RDF dataset at 0.7-0.8 nm. The increasing interaction peak of HTBHBC from Figure 5.12a to c implies that the rise in *n*-heptane percentage increased HTBHBC aggregation potential. Although the distance is not associated with what is accepted as π -stacking interactions (0.35 nm) [61], the result does match previous literature [17] where HTBHBC aggregates under the influence of *n*-heptane, while DevHTBHBC appears to not react to the change in solvent species. This lack of interaction is associated with the non-planar nature of the molecule. To corroborate the quantitative results obtained from RDFs, VMD was employed to obtain snapshot images of the simulation boxes after 100 ns of simulation time. It is important to note that in this work, snapshots are regarded as fundamentally subjective results, and are not used as reliant discussion elements, in contrast to other groups [193].

The distance between the HTBHBC molecules was seen to decrease in the *n*-heptane simulation box (Figure 5.13 c and d), rather than with toluene (Figure 5.13a and b).

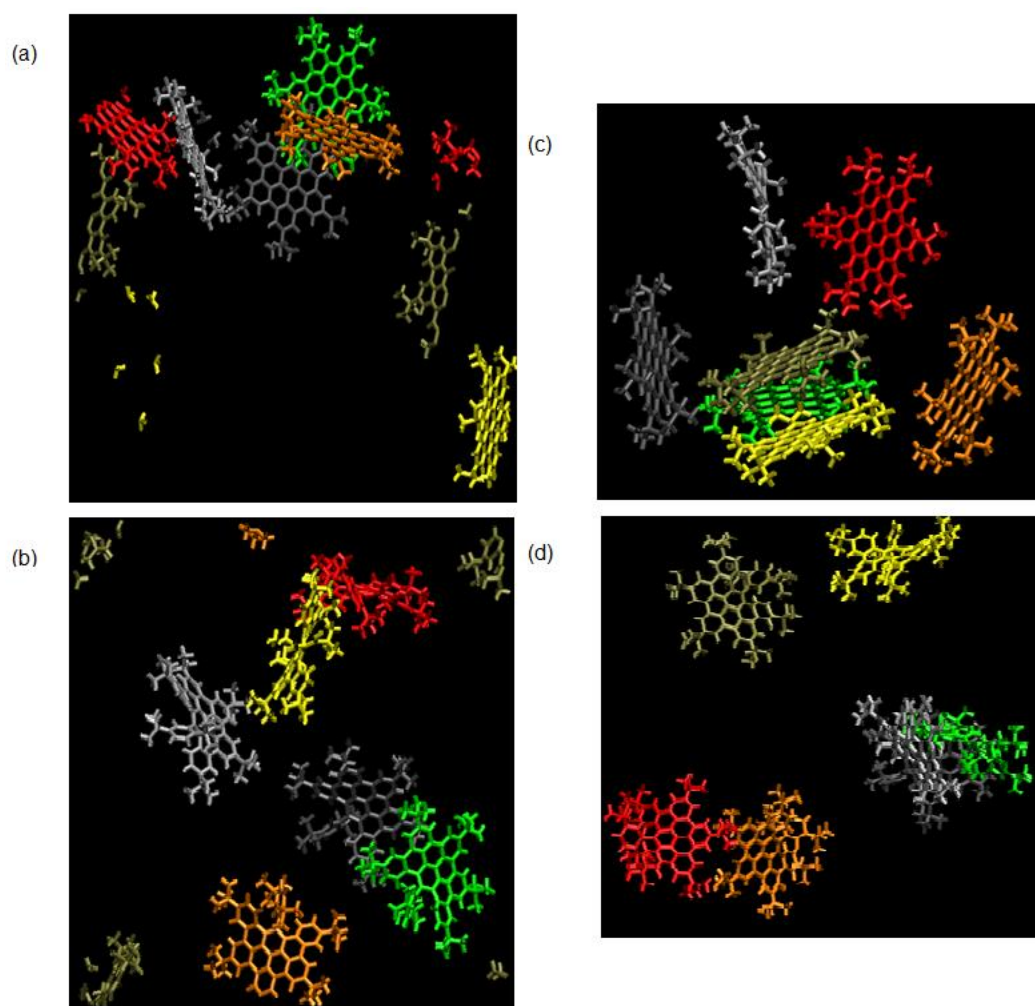


Figure 5.13. Snapshots of MD simulations of seven (a) HTBHBC and (b) DevHTBHBC molecules in toluene, and (c) HTBHBC and (d) DevHTBHBC molecules in *n*-heptane after 100 ns of simulation time. The solvent molecules are not shown for clarity.

As suggested by the RDFs, *n*-heptane appears to facilitate tighter configurations of HTBHBC molecules than toluene, while by contrast, the degree of interaction of DevHTBHBC molecules appears to be indifferent to the solvent (Figure 5.13b and d).

5.4. Discussion

5.4.1. Clustering of HTBHBC model compound in toluene

5.4.1.1. Intermolecular interactions at low concentration

Previous chapters of this dissertation focus primarily on the effects chain length and functional groups have on intermolecular interactions, with the attraction forces being generated by a combination of van der Waals (aromatic surface), π - π interactions, polarity (functional groups) or electrostatics (shift in solvent species). This chapter employed a model compound with a large aromatic surface (HTBHBC), and proceeded to assess the effects of concentration and solvent species on that compound and its non-planar derivatives.

The concentration of natural asphaltenes in solution has been heavily studied throughout the literature. Previous studies suggested two possible molecular arrangements that asphaltenes might adopt. Nanoaggregates are reported to form at low concentrations (at the critical nanoaggregate concentration, CNAC \sim 0.1 mg/mL), and clusters at high concentrations, the so-called critical cluster concentration (CCC - 1-10 mg/mL) [21,299]. In the present work, the scattering intensity at low concentrations (1–5 mg/mL) in toluene was presented in Figure 5.3 and it was found that the acquired intensity remains approximately constant with time at the lowest concentration (1 mg/mL). This indicates that HTBHBC and its derivatives were readily reaching equilibrium in toluene. The result is consistent with literature on natural asphaltenes where cluster sizes are stable at low concentrations [251]. It is worth noting that sizes and concentrations of natural asphaltene aggregates reported in the literature are

sample dependent and variable [1,24,26,251]. A previous aggregation study that compared natural asphaltenes to the HTBHBC compound performed measurements at 0.3 mg/mL (natural asphaltenes) and 5 mg/mL (HTBHBC). The very low natural asphaltene concentration is due to the opacity of the mixture that prevents the acquisition of scattered light through more concentrated solution, as well as the significant increase in the aggregation potential of the natural asphaltenes (diverse chemical species present, including functional groups) [17].

The initial scattering intensity in Figure 5.3 was found to increase over two orders of magnitude with increasing concentration of HTBHBC powder in toluene from 1 to 5 mg/mL, indicating that large clusters were present upon first introduction into toluene. Subsequently, an increasingly long period was required for the intensity to stabilise for samples with increased concentration. For example, it took 5 minutes for the 2 mg/mL sample to equilibrate, but nearly 24 hours for the 5 mg/mL sample. As no visible solid deposits were observed, the decrease in scattering intensity during the stabilisation process can be attributed to restructuring of initially formed clusters, gradual dispersion of loosely aggregated assemblies into smaller colloidal scale entities, or sedimentation of larger clusters.

Previous studies suggest two possible molecular arrangements that asphaltenes might adopt. Asphaltenes form nanoaggregates at lower concentrations (~ 0.1 mg/mL), but form clusters at higher concentrations (1-10 mg/mL), above the CCC [21,299]. In the present work, the initial scattering intensity became greater with the increased concentration of HTBHBC (from 1 to 5 mg/mL). It is probable that both HTBHBC and its derivatives were driven to self-associate and form aggregates as the concentration increases, which is in

agreement with a previous work where the same compound was found to start aggregating with the addition of *n*-heptane at 5 mg/mL [17]. A similar concentration range (0.1–10 mg/mL) was reported with natural asphaltenes which was used to investigate asphaltene aggregation kinetics with samples of different origins, observing the shift between diffusion-limited and reaction-limited aggregation as a function of concentration [300].

5.4.1.2. Intermolecular interactions at high concentration

The scattering intensity and hydrodynamic radii of the model compounds were measured for higher concentrations (10, 15, 20, 30, 40, 50 mg/mL) over 336 hours. Starting with 10 mg/mL, solid deposits initially resulting from undissolved powder were observed after mixing with toluene. The initial scattering intensity and particle size was high, and after the first 24 hours a significant reduction in scattering intensity was recorded in the scattering intensity (Figure 5.4). This is considered to occur as a result of sedimentation during which oversized agglomerates are no longer present in the measurement volume (pathway of the laser). After 168 hours, without the oversized agglomerates, the further reduction in scattering intensity could be attributed to either a decrease in concentration, a reduced size of aggregates as the result of dissolution, or a synergistic effect of both. The intensity remained relatively constant after 168 hours, suggesting that the colloidal suspension reached equilibrium with consistent particle size and concentration [108,299].

The particle size data in Figure 5.7 suggests that: (i) reduction in the number of aggregates presented in the suspension is the major contribution to the significantly decreased scattering intensity for the first 24 hours; (ii) the measured

radii represent the maximum sizes of the HTBHBC aggregates in toluene – larger clusters would precipitate; (iii) a continuous aggregation and precipitation process occurs during the first 168 hours, after which the scattering intensity stabilises and the particle sizes gradually continue to decrease. After 168 hours, the radii of HTBHBC aggregates were found to be half the value of those measured at 24 hours, the values being in agreement with previous studies in which HTBHBC was promoted to aggregate upon addition of *n*-heptane [17].

For the samples at 10, 15, 20 mg/mL that had hydrodynamic radii with unreliable ACFs, it is suggested that the model compounds were either completely dissolved or precipitated after 24 hours. Because the ratio between HTBHBC (symmetric structure with planar configuration) and the derivatives (asymmetric structure with non-planar configuration) remains the same for all samples examined, and the planar are more likely to aggregate due to π -stacking, we hypothesise that the aggregation and dissolution observed were generated by the various chemical structures of the model compounds [242,294,301].

5.4.1.3. Chemical analysis of liquid and solid phases

In previous studies where pyrene-based model systems were developed, it was observed by ^1H NMR spectroscopy and steady-state fluorescence spectroscopy that dimers formed in toluene, even though the interactions are considered to be weak π -stacking due to the small aromatic surface exposed by the pyrene [72]. A number of studies utilised model compounds with increased aromatic surfaces to facilitate stronger π -stacking, such as the model compounds utilised in this chapter [302]. A previous computational simulation study from this

group suggests that modifications to the structure of HTBHBC could result in different aggregation pathways [196].

To underpin the structural dependence of the aggregation mechanism to the characteristics of the model compounds, ^1H NMR spectroscopy and MALDI-TOF measurements were carried out to identify the exact chemical nature of both the compounds that were in the liquid phase, and those in solid deposits.

Figure 2.6a shows the ^1H NMR spectrum of the dissolved solid deposit after the initial solution has reached apparent stability (168 hours). In the spectrum presented, the peak at 9-10 ppm corresponds to the aromatic ring, the peaks at 7 ppm and 2-3 ppm correspond to the CH and respectively CH_3 in toluene, while peaks below 2 ppm correspond to alternative CH_3 groups. In Figure 2.6a, the major peaks correspond to the solvent and the symmetrical HTBHBC molecule. Compared to the spectrum of the initial suspension (0 hours) in Figure 2.6b, multiple smaller peaks are no longer present in Figure 2.6a, which suggests the absence of non-symmetrical chemical structures, hence a HTBHBC compound with increased purity.

At the beginning of the experiment, it was found that HTBHBC was the dominant peak although alternative aromatic species were present, suggesting a mixture of the pure compound and derivatives or impurities. Over time, as sample stability was reached, as suggested by the scattering intensity data in Figure 5.3, the spectrum of the re-suspended solid deposit was generated and a significant decrease in the peaks that correspond to derivative aromatic species was observed (Figure 2.6a). This analysis implies that the suspension separates

according to molecular structure, with the pure compound aggregating and precipitating out of solution, while the impurities remain in solution.

The ^1H NMR spectroscopy results were echoed by MALDI-TOF analysis of the solid deposit and the supernatant at 168 hours. Based on ^1H NMR and mass spectrometry results, it was then possible to predict the chemical structures of the derivatives that co-exist with HTBHBC in solution. The proposed structure is shown in Figure 5.2, which is believed to be one of the dominant derivatives. When an excessive amount of *tert*-butyl chloride was utilised during the synthesis, the resulting product was no longer of a symmetrical chemical structure. Consequently, the presence of such by-products can be expected to influence clustering behaviour.

The separation of the species by precipitation is expected due to the higher π -stacking potential between the planar HTBHBC molecules rather than the non-planar DevHTBHBC. HTBHBC is expected to aggregate in a variety of conditions due to its large, planar surface area. By facilitating π -stacking and forming large aggregates, it is far more likely that it is the one aggregating and precipitating.

5.4.1.4. Intermolecular interactions in toluene

The potential of HTBHBC to aggregate and precipitate allows for an explanation of the DLS data. The planar HTBHBC molecules appear to be the first to aggregate and precipitate at higher concentrations, while the non-planar derivatives, although clustered, stay in solution for longer as they cannot reach a large enough size to precipitate, hence they re-configure or dissolve into smaller, more stable, aggregates as suggested by the decreasing hydrodynamic radii in

Chapter 5

Figure 5.7. The ^1H NMR spectroscopy approach (Figure 5.10) expresses the difference in the chemical compounds between the supernatant and the solid deposit by the shift in the relative integral over time and sample. Sample set 1 shows the relative integral of the initial mixture (20 mg/mL HTBHBC in toluene) over the 336 hours, during which the phase separation occurs, with no significant variation in the relative integral. This implies that the number of peaks associated with impurities (DevHTBHBC – non-planar structures) does not change.

For Sample sets 2, 3 and 4, the solid deposit was mixed with d_8 -toluene, and the relative integral values exhibited a significant decrease due to the reduction of the number and height of the peaks, which correlates to the amount of derivative product. This along with the difference observed in the ^1H NMR spectra (Figure 2.6), suggests a clear dominance of the HTBHBC molecules in the solid deposit, while the supernatant is mostly composed of non-planar derivatives (DevHTBHBC). The aggregation triggered by concentration of the planar molecules leads to their precipitation. At 10 and 20 mg/mL, as less planar molecules are in solution, the precipitation decreases the concentration to a point where particle sizes can no longer be measured, in a similar manner to what occurred at low concentrations (1 -5 mg/mL). At higher concentrations, although the planar molecules precipitate, large aggregates/clusters remain in solution. However, as the number of non-planar molecules (DevHTBHBC) increases proportionately with increasing initial concentration, the scattering intensity of the supernatant becomes proportional to the concentration.

To understand the clustering kinetics after reaching equilibrium, the scattering intensity values at 168 hours are presented as a function of initial

concentration in Figure 5.5. The gradual increase in the scattering intensity as a function of the initial concentration can be observed for all toluene samples (1–50 mg/ml) examined in Figure 5.6. Such correlations, combined with the decreasing particle size, imply that the number of particles in toluene after 168 hours was relatively stable, but the remaining aggregates were reconfiguring into more energetically favourable states. If the solution was saturated (maximum possible amount of solid material), the trend line would have plateaued at the onset of precipitation/sedimentation. This would have implied that the solubility limit of HTBHBC in toluene had been reached, and a fixed amount of HTBHBC would remain in solution (after precipitation), regardless of the initial concentration, as suggested by the trend lines in Figure 5.5. This is not the case, as the scattering intensity continues to increase as a function of concentration even after sedimentation occurs (10 mg/mL). Coupled with the ^1H NMR results, it can be concluded that above a critical concentration, planar molecules (HTBHBC) readily precipitate, due to their molecular structure that favours aggregation (π -stacking), while non-planar derivatives (DevHTBHBC) are more likely to remain in solution, as smaller aggregates, that attempt to re-associate into more energetically favourable configurations.

5.4.2. Effect of *n*-heptane addition

Throughout asphaltene literature (including both model and natural compounds), the addition of an *n*-alkane solvent in various proportions is considered the main trigger for aggregation and concentration [10,14,17,21,105]. As such, in this chapter, the addition of *n*-heptane has been investigated with DLS as a function of initial compound concentration and *n*-heptane percentage. MD

simulations have been employed to investigate the compound solute-solvent and solute-solute interactions by radial distribution functions.

5.4.2.1. Light scattering measurements as a function of *n*-heptane concentration

All samples prepared for DLS measurements were left to stabilise (168 hours) prior to *n*-heptane addition. According to the previous section that focused on the model compound kinetics in toluene, most of the planar molecules, capable of aggregation have precipitated, leaving the non-planar (DevHTBHBC) to dominate the supernatant, in which *n*-heptane, in various volume-ratios, was added..

The DLS measurements in Figure 5.6 were made following the same protocols as with toluene, which allowed the inclusion of the data points from toluene in Figure 5.6 (i.e. 100 V%). With all samples prepared in the same manner, *n*-heptane was added in different volumes (20% volume increments) to individual samples

Natural asphaltenes and similar model compound, when suspended in an aromatic solvent (toluene), are known to aggregate upon the addition of aliphatic solvents (*n*-heptane) due to the change in solute-solvent interactions [17]. Contrary to the behaviour of natural asphaltenes and other model compounds, the addition of *n*-heptane does not seem to trigger aggregation as no significant change in the scattering intensity is observed in Figure 5.6. Although precipitation did occur before the addition of *n*-heptane, hydrodynamic sizes were recorded of aggregates suspended in toluene (Figure 5.7). However, the potential of recording sizes was limited to higher concentration, and changed over time as seen in Figure

5.7. More precisely, higher concentrations allow hydrodynamic sizes to be measured over longer periods. If these samples were diluted, the reduction in scattering bodies would prevent accurate measurements, as occurred in Figure 5.7. This suggests that the addition of *n*-heptane is a dilution, as leaving the samples more time decreased the data acquisition capacity, as a function of concentration, so does the dilution by *n*-heptane.

This lack of response to *n*-heptane addition could be attributed to the chemical structures of the molecules that remain suspended after 168 hours in toluene. The hypothesized derivative (Dev HTBHBC) suggests a reduced aromatic surface of the solute, which reduces the aggregation potential. The systematic decrease in mean scattering intensity acquired by DLS in Figure 5.6, suggests that the addition of *n*-heptane diluted the stabilised suspension, without changing the aggregation potential or intermolecular interactions.

5.4.2.2. Molecular dynamics simulations in *n*-heptane

Molecular dynamics simulations were employed to complement the experimental approach and to exemplify the different characteristics of the planar HTBHBC vs the non-planar DevHTBHBC.

The solvent affinity simulation data (Figure 5.11) suggests that aromatic molecules (toluene) solvate both planar and non-planar model compounds to a similar extent (Figure 5.11a). Literature suggests that large aromatic molecules have an affinity for aromatic solvents due to the electron density of the aromatic surface [47], which decreases the aggregation potential in aromatic solvents. By contrast, aliphatic solvents facilitate aggregation due to the lack of attraction

between aromatic surfaces and aliphatic solvents. This implies that HTBHBC should have a greater affinity towards toluene than *n*-heptane. However, the solute-solvent RDFs in Figure 5.11b show a greater affinity between the HTBHBC and *n*-heptane than between HTBHBC and toluene. It is possible that more of the *n*-heptane COMs are closer to the HTBHBC COMs than toluene COMs. This explains the higher affinity RDF (Figure 5.11b), as a problem of geometrical possibilities and not of intermolecular attraction. The solvent affinity simulations, although generate some confusion due to their counter-intuitive results, although they identify one key conclusion, that HTBHBC and DevHTBHBC display similar affinity towards toluene, while towards *n*-heptane, the larger aromatic surface of HTBHBC favours reduced COM-COM distances due to their large aromatic surface.

The solute-solute interactions are quantified by the RDF data in Figure 5.12, where the changes generated by the addition of *n*-heptane can be observed as a function of chemical architecture. In toluene (Figure 5.12a), a small degree of interaction was found for both the model compounds. The small peak displayed by DevHTBHBC in all simulation boxes occurs due to the shifted COM of the molecule from its position in HTBHBC (on the aromatic surface) to a slightly elevated position (above the *tert*-butyl chains plain of influence), which facilitates contact between molecules.

Throughout the rest of the MD simulations (Figure 5.12b and c), *n*-heptane does not appear to influence the interactions between the DevHTBHBC model molecules. This is in accordance with the DLS experiments, and as such leads to the conclusion that the non-planar or non- π -stacking molecular structures are far

less susceptible to solvent species than molecules with a predisposition towards π -stacking. *n*-Heptane appears to have a greater effect on the planar HTBHBC, than on the non-planar DevHTBHBC. According to the increase in the RDF peaks observed in Figure 5.12 from toluene (a) to heptol (b) and then to *n*-heptane (c), the more *n*-heptane is added, the greater is the interaction potential between the HTBHBC molecules. As the RDF peaks of HTBHBC are similar in width to those observed in a number of model compounds that π -stack (Chapters 3 and 4) such as TPN-C3 and TPN-C5, it is believed that parallel, π -stacking configuration occurs. The snapshots further suggest this configuration to be possible (Figure 5.13). However, the distance at which the peak is set (0.7-0.9 nm) does not fit with what is accepted as π -stacking distances (0.35 nm) [61]. A previous investigation lead by this group [196] suggests that even if π -stacking interaction causes the aggregation, they are not strong enough to overcome the structural repulsion set by the *tert*-butyl tails in simulations.

5.4.2.3. Intermolecular interactions in *n*-heptane

In both experiment and simulation, a significant difference was noted between the planar and non-planar molecules. The planar HTBHBC did not readily aggregate and precipitate in toluene until above a critical concentration, when the supernatant is dominated by derivative structures, while the solid deposit is comprised mostly of HTBHBC. *n*-Heptane was added only after stability was achieved (168 hours after toluene), and as such the *n*-alkane solvent did not appear to impact the non-planar derivatives left in solution after HTBHBC precipitates. The MD simulations do not indicate a shift in interaction potential of DevHTBHBC with *n*-heptane addition corroborate this.

The MD simulations aid in quantifying the impact of solvent changes as a function of chemical structure, as they highlight how the planar HTBHBC has a higher aggregation potential with increase in *n*-heptane percentage. By contrast, DevHTBHBC exhibits no increased interaction as a function of *n*-heptane percentage, nor is it affected by the aliphatic component in the DLS experiments, even at 80% *n*-heptane volume.

5.5. Conclusions

In the present work, experimental approaches were employed to investigate the molecular interactions and corresponding aggregation of HTBHBC and its derivatives as a function of concentration. It was observed that, in toluene at low concentrations, the scattering intensity stabilises with no visible precipitation, suggesting both the fully reacted compound and its derivatives are well solvated in this concentration range, which is not high enough to trigger aggregation. The intensity over the first time interval takes more time to stabilise as the concentration is increased from 1 to 5 mg/mL. Due to the reduced scattering, hydrodynamic size measurements were not possible at these low concentrations. However, the decreasing scattering intensity over time as a function of concentration suggests that the existing aggregates are changing their structural configuration. The CNAC is believed to be above 1 mg/mL where the intensity is constant from the start. By the decrease in scattering intensity, it appears conclude that the clusters strive towards a more stable configuration at times proportional to the initial concentrations.

At concentrations above 10 mg/mL, precipitation occurs and the scattering intensity decreases at increasing with time until it stabilises after 168 hours. The

hydrodynamic radii continue to decrease as the clusters left in solution try to achieve equilibrium. However, the scattering intensity after 168 hours shows a direct relation to the concentration. Further analyses using MALDI TOF mass spectrometry and ^1H NMR spectroscopy lend credence to the DLS data as they support differences between the behaviour of HTBHBC and its derivatives.

The behaviour of model compound systems composed of HTBHBC and its derivatives was rigorously investigated as a function of time and concentration with the conclusion that each compound, upon suspension in toluene, forms clusters that reach stability at different time intervals. At higher concentrations, the driving forces of aggregation facilitate the aggregation and precipitation of HTBHBC due to its planar structure, while its non-planar derivatives remain in solution, only to slowly reconfigure into smaller, more energetically favourable aggregates. Experimentally the addition of *n*-heptane did not affect the supernatant because the derivative HTBHBC molecules, which, as the MD simulations proved, do not exhibit an increase in aggregation potential as a function of solvent shift, dominate it. However, the MD simulations did highlight the HTBHBC intermolecular interactions as the addition of *n*-heptane increased the aggregation potential, in agreement with previous literature studies [17].

Chapter 6. Conclusions and future perspectives

Chapter 6

6.1. General summary

An investigation combining both experimental and computational approaches was performed to study the aggregation mechanisms of model polyaromatic compounds replicating natural asphaltenes in organic solvents. Through these studies, the effects of hydrocarbon chain lengths and the presence of amide and carboxylic acid groups on the aggregation of model asphaltenes were investigated as a function of concentration, time, and solvent type. Eight model compounds of different chemical structures were developed based on the asphaltene continental molecular architecture. Their solubility, molecular interactions, and aggregation potential were evaluated by dynamic light scattering (in pure toluene and 40/60 toluene/*n*-heptane) and molecular dynamics simulations (in pure toluene, 50/50 toluene/*n*-heptane, and pure *n*-heptane). It was concluded that the polarity of the model compounds drives the aggregation mechanism, while π -stacking plays a greater role in influencing the configuration within the formed aggregates. The aromatic cores were found to have a significant impact on the degree of solvophobicity for each model compound molecule. Finally, the consequences of altering the planar aromatic surface on aggregation are presented for the HTBHBC model compound and its identified non-planar derivative (DevHTBHBC). The methodology and techniques employed are discussed in Chapter 2. The triphenylene cored model compounds are discussed in Chapters 3 and Chapter 4, separated by solvent species, while the HTBHBC model itself is discussed in Chapter 5.

Chapter 6

6.1.1. Effect of alkoxy group and chain length

By developing a series of model compounds from the same aromatic core, it was possible to systematically examine the effect of side chains on the aggregation mechanism. It was found that chain length could directly interfere with the intermolecular interactions and configurations of the formed aggregates by limiting the aggregation pathways of molecules, which is consistent with previous studies [244,245]. It was found that the aromatic core, TPN-C0, does not aggregate while being dispersed in either toluene or *n*-heptane. The DLS data does not show any hydrodynamic size greater than 1 nm, while MD simulations did not reveal any specific interactions between molecules, other than collisions facilitated by Brownian motion. The intermolecular attraction between TPN-C0 molecules was not strong enough to overcome the interactions between the model compounds molecules and the solvent molecules [47,57]. Consequently, TPN-C0 does not aggregate in either solvent. By contrast, TPN-C1 formed large aggregates ($\geq 1\mu\text{m}$) in both solvents, and MD simulations showed a high aggregation potential with multiple molecular configurations (parallel and perpendicular). The uniform distribution of the alkoxy groups surrounding TPN-C1 enable a centro-symmetric molecular structure, which leads to an increased aggregation potential, generating large clusters, regardless of solvent species. The main difference observed as a function of solvent comes from the MD simulations, where the distance between the molecules in an aggregate was found to be reduced.

The high degree of electronegativity induced by the oxygen atoms generates a strong attraction between the TPN-C1 molecules, which greatly overcomes the

barriers set by the solvent [85], and leads to aggregation. DLS and MD results lead to the conclusion that although initial aggregation occurred due to the presence of the oxygen atoms, the aromatic core has the potential to reconfigure the aggregate towards parallel stacking that is more energetically favourable [76]. This two-step process of initial aggregation and later reconfiguration due to π -stacking has been previously observed with other model PACs at the oil/water interface [121,122]. It can be concluded that the incorporation of alkoxy and methyl groups to triphenylene could significantly increase the potential for aggregation, with large but disordered clusters formed in both solvents, and closely packed configurations in *n*-heptane.

By increasing the length of the surrounding chains of TPN-C1, model compounds with almost liquid crystalline appearance were obtained. According to DLS and DOSY experiments, TPN-C3 and TPN-C5 could form clusters initially, but then dissolve into nanoaggregates (1 nm) of 2-4 π -stacked molecules over time (faster in aromatic solvent than in *n*-alkane). Both MD simulations and the light scattering experiments agree, suggesting that parallel stacking is the predominant configuration. In a similar manner to TPN-C1, the attraction forces were generated by the aromatic core as well as the alkoxy groups surrounding it. However, the longer tail groups surrounding the core enforce parallel configurations, as the aliphatic side-chains provide steric repulsion, which enforce parallel configurations. The size of the stable aggregates were similar between TPN-C3 and TPN-C5, as was previously observed by a study with the same approach but a different core [112].

According to the DLS and DOSY data, the addition of the tail (TPN-C10) appears to have drastically increased the solubility of the molecule in toluene, as it immediately formed nanoaggregates, while at the same time increased its solvophobicity towards *n*-heptane. The MD data revealed the main configuration to be parallel due to π -stacking; however, TPN-C10 exhibited a significant solvent dependence, as the simulations in *n*-heptane showed an increased degree of aggregation. The addition of the tail appears to impact the intermolecular interactions and reduce the potential energy required

The interplay of attraction and repulsion forces is significantly influenced by the molecular architecture of the solutes [57,58]. The effect of alkoxy groups and chain length makes no exception, as it can increase the attraction forces, limit the aggregation configuration and change the solvophobicity of the molecule. The model compounds evaluated so far isolate and highlight these effects and their impact on the aggregation mechanism.

6.1.2. Effect of amide and carboxylic acid group

The second group of key structural features isolated and investigated in this study is the impact of functional group, namely an amide and a carboxylic acid group, on the aggregation characteristics of the model compounds. This underpins the aggregation pathway of natural asphaltenes. TPN-CN, which consists of an amide group attached to a triphenylene-cored structure, exhibited a significantly increased aggregation potential than previous (non-polar) models. The addition of a carboxylic acid group (TPN-CNAcid) produced similar results. The DLS data show large and unstable clusters in toluene, and even larger clusters in *n*-heptane, with significantly increased error bars, signalling even instable particles present in

the suspension. The MD data displayed the main intermolecular distance to be between 0.4 and 1.1 nm, which suggests that multiple configurations are possible, while no archipelago-like aggregates were identified.

The aggregates formed by TPN-CN/CNAcid appear to be stacked either head-to-head (π -stacked) or head-to-tail, which causes the broader peak in the RDF of TPN-C3 and TPN-C5. As the amide and acid groups both generate significant attraction, due to the increase in polarity produced by the functional groups [58,124], large but unorganised clusters are formed. Both DLS and MD results show that solvent species significantly increased the aggregation potential, as not only larger clusters, but also a reduced intermolecular distance within the aggregates (g_{dist}) was measured. This could potentially be linked to the behaviour seen in TPN-C10, as both TPN-CN and TPN-CNAcid have one long tail group. The aromatic core of the model compounds are more attracted to toluene (aromatic) than *n*-heptane, which suggests that reconfiguration of the molecules after aggregates are formed, might be stronger in an aliphatic solvent than an aromatic one.

It is highly likely that the polarity, induced by their functional groups, of TPN-CN and TPN-CNAcid is the main driving force of aggregation, as reported with other model PACs with complex acid groups [118,124]. The contributions brought by these model compounds consist of comparing their identified behaviours, interaction mechanisms, and aggregation potential. They can be compared not only to the other PACs studied here, but to previous asphaltene models found in the literature [16,116]. The addition of the functional groups that induced a polar aspect to the molecules drove the aggregation mechanism to form larger clusters

than centro-symmetric, less polar model compounds. Furthermore, the π -stacking potential is not to be neglected, as it appears to have a greater role in the re-configuration of the aggregates, rather than the initial aggregation.

6.1.3. Effect of planarity on π -stacking

In Chapter 5, several experimental and computational approaches were employed to investigate the molecular interactions and corresponding aggregation of the planar HTBHBC and its non-planar derivatives (DevHTBHBC), suspended in toluene and *n*-heptane, as a function of concentration and time. DLS in toluene measured a decreasing intensity over time as a function of concentration (1 to 5 mg/mL), suggesting that existing aggregates are shifting their structural configuration. As no precipitation was observed, both the fully reacted compound and its derivatives were considered well solvated in this concentration range. Precipitation occurred above 10 mg/mL, when the scattering intensity decreases at far larger time intervals, until it stabilises after 168 hours. At the same time, the hydrodynamic radii continue to decrease as the clusters left in solution try to achieve equilibrium. At these high concentrations, the most likely molecules to form large enough aggregates to precipitate are the ones with the most planar surface (HTBHBC), while those with non-planar architecture remain in solution. This structural separation mechanism was proven by ^1H NMR spectroscopy. The DevHTBHBC clusters that remained in solution, dissolve and reconfigure, into more energetically favourable states. *n*-Heptane was added after 168 hours with no observable impact according to DLS measurements.

MD simulations support the experimental data by highlighting the lower solvophobicity towards *n*-heptane of the DevHTBHBC as opposed to HTBHBC,

which explains the differences between our study and previous literature [17]. The simulations further exposed the higher potential for aggregation of the planar compound as more *n*-heptane was added. Although the peak does not fall on ideal π -stacking distance (0.3-04 nm) [223], the leanness of the peak coupled with the MD snapshots, suggests that a parallel configuration dominates the HTBHBC aggregates. The increase distance is attributed to the *tert*-butyl tail groups, preventing the molecules from fully π -stacking.

A selective aggregation mechanism is identified, as the planar, pure HTBHBC molecules cluster and precipitate, while the non-planar derivatives remain suspended in solution. At concentrations above 5 mg/mL, the pure HTBHBC molecules overcome the steric repulsion barrier set by the solvent, as such potential is suggested by the simulations, and start to aggregate until the cluster sizes are large enough to precipitate. The non-planar derivatives remain in suspension, as their non-planar structure hinders staking interactions, regardless of concentration or solvent. The selective aggregation mechanisms explored in this work depicts the impact of the chemical structure on concentration induced aggregation of model asphaltene compounds.

6.2. Future perspectives

The development of PACs model compounds can lead to a significant understanding of the structure-function relation that can benefit not only the asphaltene knowledge, but also other fields such as liquid crystals, pharmacy, and food research. By investigating the interactions of idealised molecules both in organic and aqueous solvents, great steps can be made towards identifying key structural features that lead to financial and operational progress. However, within

the scope of the project, the following perspectives are suggested for future consideration:

6.2.1. Model compound development

The seven triphenylene-cored models have proven to be potent model compounds due to their simplicity, which allows for the structure-function relation to be identified and quantified. As such, it would be beneficial to add other functional groups, to replace the carboxylic acid group, or amide, with sulphur or other acid groups [73]. The last step would be the addition of metal atoms, which would complete the systematic exploration of the currently identified classes of atoms present in natural asphaltenes [10].

Further effort can be directed towards the study of solvent effects. A systematic experimental study of the impact of *n*-alkane solvent chain length on natural asphaltenes was completed, and concluded that different chain lengths impact the aggregation and precipitation rates [267]. Changing the solvent in both experimental and computational approaches of this project would yield valuable insight into the interplay of the structure-function relation.

6.2.2. Experimental and computational technique development

The quantification of the intermolecular interactions is key to identifying the driving forces of aggregation. A previous study from this group employed pulling simulations to generate energy profiles for model compound dimers through the umbrella sampling technique [196]. The same approach could be employed to assess the strength of interaction, not only between solute-solute, but also

between solute and solvent. This would better quantify the molecular interplay occurring both before and after aggregation ensues.

6.2.3. Operational envelope development

It is important not to lose sight of the purpose of this project, which is to aid the industry in solving asphaltene related issues. The potential of this work lies in the development of an operational envelope that could be used to test chemical counter-measures, such as de-emulsifiers, to the problems caused by asphaltenes.

Once key asphaltene models are established, and thoroughly evaluated, counter-measures could be actively tested against these known standards, and the effects thoroughly quantified, in a cheap and accessible manner. By unravelling the asphaltene enigma to the industry, a significant impact can be made on the global economy, which is still crude oil dependent.

References

References

1. Barré, L., et al., *Relation between nanoscale structure of asphaltene aggregates and their macroscopic solution properties*. Oil Gas Sci. Technol., 2009. **64**(5): p. 617-628.
2. Chaisoontornyotin, W., et al., *Combined asphaltene aggregation and deposition investigation*. Energy Fuels, 2016. **30**(3): p. 1979-1986.
3. Hammami, A. and J. Ratulowski, *Precipitation and deposition of asphaltenes in production systems: a flow assurance overview*, in *Asphaltenes, heavy oils, and petroleomics*. 2007, Springer: New York, NY. p. 617-660.
4. Hemmingsen, P.V., et al., *Emulsions of heavy crude oils. I: Influence of viscosity, temperature, and dilution*. J. Dispersion Sci. Technol., 2005. **26**(5): p. 615-627.
5. Jestin, J., et al., *A small angle neutron scattering study of the adsorbed asphaltene layer in water-in-hydrocarbon emulsions: structural description related to stability*. Langmuir, 2007. **23**(21): p. 10471-10478.
6. Nabzar, L. and M. Aguiléra, *The colloidal approach. A promising route for asphaltene deposition modelling*. Oil Gas Sci. Technol., 2008. **63**(1): p. 21-35.
7. Sinquin, A., T. Palermo, and Y. Peysson, *Rheological and flow properties of gas hydrate suspensions*. Oil Gas Sci. Technol., 2004. **59**(1): p. 41-57.
8. Subirana, M. and E.Y. Sheu, *Asphaltenes: fundamentals and applications*. 2013, 223 Spring Street, New York, NY 10013, USA: Springer Science & Business Media.
9. Groenzin, H. and O.C. Mullins, *Asphaltene molecular size and structure*. J. Phys. Chem. A, 1999. **103**(50): p. 11237-11245.
10. Mullins, O.C., et al., *Asphaltenes, heavy oils, and petroleomics*. 2007, 223 Spring Street, New York, NY 10013, USA: Springer Science & Business Media.
11. Sabbah, H., et al., *Evidence for island structures as the dominant architecture of asphaltenes*. Energy Fuels, 2011. **25**(4): p. 1597-1604.

References

12. Andrews, A.B., et al., *Diffusivity of asphaltene molecules by fluorescence correlation spectroscopy*. J. Phys. Chem. A, 2006. **110**(26): p. 8093-8097.
13. Lisitza, N.V., et al., *Study of asphaltene nanoaggregation by nuclear magnetic resonance (NMR)*. Energy Fuels, 2009. **23**(3): p. 1189-1193.
14. Schuler, B., et al., *Unraveling the molecular structures of asphaltenes by atomic force microscopy*. J. Am. Chem. Soc., 2015. **137**(31): p. 9870-9876.
15. Wang, X., et al., *Interactions of Polyaromatic Compounds. Part 2: Flocculation Probed by Dynamic Light Scattering and Molecular Dynamics Simulation*. Energy Fuels, 2017 31 (9), pp 9201–9212.
16. Sjöblom, J., S. Simon, and Z. Xu, *Model molecules mimicking asphaltenes*. Adv. Colloid Interface Sci., 2015. **218**: p. 1-16.
17. Breure, B., et al., *Modeling asphaltene aggregation with a single compound*. Energy Fuels, 2012. **27**(1): p. 172-176.
18. Jian, C., *Molecular Dynamics Investigation on the Aggregation of Polyaromatic Compounds in Water and Organic Solvents*, in *Department of Mechanical Engineering 2015*, University of Alberta: Alberta, Canada.
19. Akbarzadeh, K., et al., *Association behavior of pyrene compounds as models for asphaltenes*. Energy Fuels, 2005. **19**(4): p. 1268-1271.
20. Abdel-Raouf, M.E.-S., *Crude Oil Emulsions: Composition Stability and Characterization*. 2012: InTech. Croatia: 2012 183-204
21. Mullins, O.C., et al., *Advances in asphaltene science and the Yen–Mullins model*. Energy Fuels, 2012. **26**(7): p. 3986-4003.
22. Dickie, J.P. and T.F. Yen, *Macrostructures of the asphaltic fractions by various instrumental methods*. Anal. Chem., 1967. **39**(14): p. 1847-1852.
23. Yen, T.F., J.G. Erdman, and S.S. Pollack, *Investigation of the structure of petroleum asphaltenes by X-ray diffraction*. Anal. Chem., 1961. **33**(11): p. 1587-1594.
24. Sheu, E.Y. and D.A. Storm, *Colloidal properties of asphaltenes in organic solvents*, in *Asphaltenes*, O.M. EY Sheu, Editor. 1995, Springer: New York: Plenum. p. 1-52.
25. Wiehe, I. and K. Liang, *Asphaltenes, resins, and other petroleum macromolecules*. Fluid Phase Equilib., 1996. **117**(1): p. 201-210.

References

26. Barré, L., S. Simon, and T. Palermo, *Solution properties of asphaltenes*. Langmuir, 2008. **24**(8): p. 3709-3717.
27. Fenistein, D. and L. Barre, *Experimental measurement of the mass distribution of petroleum asphaltene aggregates using ultracentrifugation and small-angle X-ray scattering*. Fuel, 2001. **80**(2): p. 283-287.
28. Gawrys, K.L. and P.K. Kilpatrick, *Asphaltenic aggregates are polydisperse oblate cylinders*. J. Colloid Interface Sci., 2005. **288**(2): p. 325-334.
29. Gawrys, K.L., G.A. Blankenship, and P.K. Kilpatrick, *Solvent entrainment in and flocculation of asphaltenic aggregates probed by small-angle neutron scattering*. Langmuir, 2006. **22**(10): p. 4487-4497.
30. Perrin, J., *Nobel Lectures on Physics 1922–1941*. World Dcientific, Singapore, 1998.
31. Russel, W.B., D.A. Saville, and W.R. Schowalter, *Colloidal dispersions*. 1989: Cambridge university press.
32. Sood, A.K., *Structural ordering in colloidal suspensions*. Solid State Phys., 1991. **45**: p. 1-73.
33. Poon, W. and P. Pusey, *Phase transition of spherical colloids*, in *Observation, prediction and simulation of phase transitions in complex fluids*. 1995, Springer. p. 3-51.
34. Van Blaaderen, A. and P. Wiltzius, *Real-space structure of colloidal hard-sphere glasses*. Science, 1995. **207**: p. 1177-1177.
35. Sirota, E., et al., *Complete phase diagram of a charged colloidal system: A synchrotron x-ray scattering study*. Phys. Rev. Lett., 1989. **62**(13): p. 1524.
36. Chen, L., et al., *Rheological and microstructural transitions in colloidal crystals*. Langmuir, 1994. **10**(8): p. 2817-2829.
37. Palit, S., *Pulsed field gradient NMR study of colloids*, in *Department of Physics and Physical Oceanography*. 2007, Memorial University of Newfoundland: St. John's, Newfoundland, Canada.
38. Burya, Y.G., et al., *Light-scattering study of petroleum asphaltene aggregation*. Appl. Opt., 2001. **40**(24): p. 4028-4035.

References

39. Churaev, N. and V. Sobolev, *Prediction of contact angles on the basis of the Frumkin-Derjaguin approach*. Adv. Colloid Interface Sci., 1995. **61**: p. 1-16.
40. Cubberley, M.S. and B.L. Iverson, *¹H NMR investigation of solvent effects in aromatic stacking interactions*. J. Am. Chem. Soc., 2001. **123**(31): p. 7560-7563.
41. Meyer, E.A., R.K. Castellano, and F. Diederich, *Interactions with aromatic rings in chemical and biological recognition*. Angew. Chem., Int. Ed. Engl., 2003. **42**(11): p. 1210-1250.
42. Cozzi, F., et al., *Polar Interactions between Stacked π Systems in Fluorinated 1, 8-Diarylnaphthalenes: Importance of Quadrupole Moments in Molecular Recognition*. Angew. Chem., Int. Ed. Engl., 1995. **34**(9): p. 1019-1020.
43. Israelachvili, J.N., *Intermolecular and surface forces*. 2015, Santa Barbara, California, USA: Academic press.
44. Zhang, L., et al., *Molecular weight and aggregation of heavy petroleum fractions measured by vapor pressure osmometry and a hindered stepwise aggregation model*. Energy Fuels, 2014. **28**(10): p. 6179-6187.
45. Kovalchuk, N. and V. Starov, *Aggregation in colloidal suspensions: Effect of colloidal forces and hydrodynamic interactions*. Adv. Colloid Interface Sci., 2012. **179**: p. 99-106.
46. Mullins, O.C., *The asphaltenes*. Annual Review of Analytical Chemistry, 2011. **4**: p. 393-418.
47. Waters, M.L., *Aromatic interactions in model systems*. Curr. Opin. Chem. Biol., 2002. **6**(6): p. 736-741.
48. Chakrabarti, P. and R. Bhattacharyya, *Geometry of nonbonded interactions involving planar groups in proteins*. Prog. Biophys. Mol. Biol., 2007. **95**(1): p. 83-137.
49. McGaughey, G.B., M. Gagné, and A.K. Rappé, *π -Stacking interactions alive and well in proteins*. J. Biol. Chem., 1998. **273**(25): p. 15458-15463.
50. Dougherty, D.A., *Cation- π interactions in chemistry and biology: a new view of benzene, Phe, Tyr, and Trp*. Science, 1996. **271**(5246): p. 163.

References

51. Guha, S., et al., *Electronically regulated thermally and light-gated electron transfer from anions to naphthalenediimides*. J. Am. Chem. Soc., 2011. **133**(39): p. 15256-15259.
52. Guha, S. and S. Saha, *Fluoride ion sensing by an anion- π interaction*. J. Am. Chem. Soc., 2010. **132**(50): p. 17674-17677.
53. Gierszal, K.P., et al., *π -Hydrogen bonding in liquid water*. J. Phys. Chem. Lett., 2011. **2**(22): p. 2930-2933.
54. Coskun, A., et al., *Mechanically stabilized tetrathiafulvalene radical dimers*. J. Am. Chem. Soc., 2011. **133**(12): p. 4538-4547.
55. Spruell, J.M., et al., *Highly stable tetrathiafulvalene radical dimers in [3] catenanes*. Nat. Chem., 2010. **2**(10): p. 870-879.
56. Sinnokrot, M.O. and C.D. Sherrill, *High-accuracy quantum mechanical studies of π - π interactions in benzene dimers*. J. Phys. Chem. A, 2006. **110**(37): p. 10656-10668.
57. Marsili, S., et al., *Thermodynamics of stacking interactions in proteins*. Phys. Chem. Chem. Phys., 2008. **10**(19): p. 2673-2685.
58. Björk, J., et al., *Adsorption of aromatic and anti-aromatic systems on graphene through π - π stacking*. J. Phys. Chem. Lett., 2010. **1**(23): p. 3407-3412.
59. Grimme, S., C. Mück-Lichtenfeld, and J. Antony, *Noncovalent interactions between graphene sheets and in multishell (hyper) fullerenes*. J. Phys. Chem. C, 2007. **111**(30): p. 11199-11207.
60. Zhao, Y. and D.G. Truhlar, *A prototype for graphene material simulation: structures and interaction potentials of coronene dimers*. J. Phys. Chem. C, 2008. **112**(11): p. 4061-4067.
61. Moreira da Costa, L., et al., *Computational study of the effect of dispersion interactions on the thermochemistry of aggregation of fused polycyclic aromatic hydrocarbons as model asphaltene compounds in solution*. J. Phys. Chem. A, 2014. **118**(5): p. 896-908.
62. Purcell, E.M. and D.J. Morin, *Electricity and magnetism*. 2013, Cambridge, UK: Cambridge University Press.

References

63. Van der Hoeven, P.C. and J. Lyklema, *Electrostatic stabilization in non-aqueous media*. Adv. Colloid Interface Sci., 1992. **42**: p. 205-277.
64. Carauta, A.N., et al., *Conformational search and dimerization study of average structures of asphaltenes*. J. Mol. Struct.: THEOCHEM, 2005. **755**(1): p. 1-8.
65. Carauta, A.N., et al., *Modeling solvent effects on asphaltene dimers*. Energy Fuels, 2005. **19**(4): p. 1245-1251.
66. Wang, S., et al., *Interaction forces between asphaltene surfaces in organic solvents*. Langmuir, 2009. **26**(1): p. 183-190.
67. Singh, H., et al., *Micelle formation of ionic surfactants in polar nonaqueous solvents*. J. Phys. Chem., 1980. **84**(17): p. 2191-2194.
68. Martinez, C.R. and B.L. Iverson, *Rethinking the term "pi-stacking"*. Chem. Sci., 2012. **3**(7): p. 2191-2201.
69. Allred, A. and E.G. Rochow, *A scale of electronegativity based on electrostatic force*. J. Inorg. Nucl. Chem., 1958. **5**(4): p. 264-268.
70. Wattana, P., et al., *Characterization of polarity-based asphaltene subfractions*. Energy Fuels, 2005. **19**(1): p. 101-110.
71. Gray, M.R., *Consistency of asphaltene chemical structures with pyrolysis and coking behavior*. Energy Fuels, 2003. **17**(6): p. 1566-1569.
72. Tan, X., H. Fenniri, and M.R. Gray, *Pyrene derivatives of 2, 2'-bipyridine as models for asphaltenes: synthesis, characterization, and supramolecular organization*. Energy Fuels, 2007. **22**(2): p. 715-720.
73. Groenzin, H. and O.C. Mullins, *Molecular size and structure of asphaltenes from various sources*. Energy Fuels, 2000. **14**(3): p. 677-684.
74. Groenzin, H. and O.C. Mullins, *Asphaltene molecular size and weight by time-resolved fluorescence depolarization*. Asphaltenes, heavy oils, and petroleomics, 2007: p. 17-62.
75. Alvarez-Ramirez, F., E. Ramirez-Jaramillo, and Y. Ruiz-Morales, *Calculation of the interaction potential curve between asphaltene-asphaltene, asphaltene-resin, and resin-resin systems using density functional theory*. Energy Fuels, 2006. **20**(1): p. 195-204.

References

76. Harris, J., *Simplified method for calculating the energy of weakly interacting fragments*. Phys. Rev. B, 1985. **31**(4): p. 1770.
77. Vosko, S.H., L. Wilk, and M. Nusair, *Accurate spin-dependent electron liquid correlation energies for local spin density calculations: a critical analysis*. Can. J. Phys., 1980. **58**(8): p. 1200-1211.
78. Perdew, J.P. and Y. Wang, *Accurate and simple analytic representation of the electron-gas correlation energy*. Phys. Rev. B, 1992. **45**(23): p. 13244.
79. Delley, B., *An all-electron numerical method for solving the local density functional for polyatomic molecules*. J. Chem. Phys., 1990. **92**(1): p. 508-517.
80. Gray, M.R., et al., *Supramolecular assembly model for aggregation of petroleum asphaltenes*. Energy Fuels, 2011. **25**(7): p. 3125-3134.
81. Murgich, J., *Intermolecular forces in aggregates of asphaltenes and resins*. Pet. Sci. Technol., 2002. **20**(9-10): p. 983-997.
82. Tan, X., H. Fenniri, and M.R. Gray, *Water enhances the aggregation of model asphaltenes in solution via hydrogen bonding*. Energy Fuels, 2009. **23**(7): p. 3687-3693.
83. Stoyanov, S.R., et al., *Computational and experimental study of the structure, binding preferences, and spectroscopy of nickel (II) and vanadyl porphyrins in petroleum*. J. Phys. Chem. B, 2010. **114**(6): p. 2180-2188.
84. Aray, Y., et al., *Exploring the structure–solubility relationship of asphaltene models in toluene, heptane, and amphiphiles using a molecular dynamic atomistic methodology*. J. Phys. Chem. A, 2011. **115**(42): p. 11495-11507.
85. Badre, S., et al., *Molecular size and weight of asphaltene and asphaltene solubility fractions from coals, crude oils and bitumen*. Fuel, 2006. **85**(1): p. 1-11.
86. Nalwaya, V., et al., *Studies on asphaltenes through analysis of polar fractions*. Ind. Eng. Chem. Res., 1999. **38**(3): p. 964-972.
87. Kaminski, T.J., et al., *Classification of asphaltenes via fractionation and the effect of heteroatom content on dissolution kinetics*. Energy Fuels, 2000. **14**(1): p. 25-30.

References

88. Fish, R.H., J.J. Komlenic, and B.K. Wines, *Characterization and comparison of vanadyl and nickel compounds in heavy crude petroleums and asphaltenes by reverse-phase and size-exclusion liquid chromatography/graphite furnace atomic absorption spectrometry*. Anal. Chem., 1984. **56**(13): p. 2452-2460.
89. Ancheyta, J., et al., *Extraction and characterization of asphaltenes from different crude oils and solvents*. Energy Fuels, 2002. **16**(5): p. 1121-1127.
90. Agrawala, M. and H.W. Yarranton, *An asphaltene association model analogous to linear polymerization*. Ind. Eng. Chem. Res., 2001. **40**(21): p. 4664-4672.
91. Teklebrhan, R.B., et al., *Probing structure–nanoaggregation relations of polyaromatic surfactants: a molecular dynamics simulation and dynamic light scattering study*. J. Phys. Chem. B., 2012. **116**(20): p. 5907-5918.
92. Strausz, O.P., T.W. Mojelsky, and E.M. Lown, *The molecular structure of asphaltene: an unfolding story*. Fuel, 1992. **71**(12): p. 1355-1363.
93. George, G.N. and M.L. Gorbaty, *Sulfur K-edge X-ray absorption spectroscopy of petroleum asphaltenes and model compounds*. J. Am. Chem. Soc., 1989. **111**(9): p. 3182-3186.
94. Waldo, G.S., et al., *Determination of the chemical environment of sulphur in petroleum asphaltenes by X-ray absorption spectroscopy*. Fuel, 1992. **71**(1): p. 53-57.
95. Mitra-Kirtley, S., et al., *Determination of the nitrogen chemical structures in petroleum asphaltenes using XANES spectroscopy*. J. Am. Chem. Soc., 1993. **115**(1): p. 252-258.
96. Desando, M.A. and J.A. Ripmeester, *Chemical derivatization of Athabasca oil sand asphaltene for analysis of hydroxyl and carboxyl groups via nuclear magnetic resonance spectroscopy*. Fuel, 2002. **81**(10): p. 1305-1319.
97. Moschopedis, S.E. and J.G. Speight, *Oxygen functions in asphaltenes*. Fuel, 1976. **55**(4): p. 334-336.
98. Ignasiak, T., O.P. Strausz, and D.S. Montgomery, *Oxygen distribution and hydrogen bonding in Athabasca asphaltene*. Fuel, 1977. **56**(4): p. 359-365.

References

99. ISO13321, I., *Methods for determination of particle size distribution part 8: Photon correlation spectroscopy*. International Organisation for Standardisation (ISO), 1996.
100. Nenningsland, A.L., et al., *Comparative study of stabilizing agents for water-in-oil emulsions*. Energy Fuels, 2011. **25**(12): p. 5746-5754.
101. da Costa, L.M., et al., *3D-RISM-KH molecular theory of solvation and density functional theory investigation of the role of water in the aggregation of model asphaltenes*. Phys. Chem. Chem. Phys., 2012. **14**(11): p. 3922-3934.
102. Zhang, L., et al., *Hindered stepwise aggregation model for molecular weight determination of heavy petroleum fractions by vapor pressure osmometry (VPO)*. Energy Fuels, 2013. **27**(3): p. 1331-1336.
103. Mullins, O.C., *The modified Yen model*. Energy Fuels, 2010. **24**(4): p. 2179-2207.
104. Andreatta, G., et al., *Nanoaggregates and structure– function relations in asphaltenes*. Energy Fuels, 2005. **19**(4): p. 1282-1289.
105. Zeng, H., et al., *Critical nanoaggregate concentration of asphaltenes by direct-current (DC) electrical conductivity*. Energy Fuels, 2009. **23**(3): p. 1201-1208.
106. Zhang, L. and M.L. Greenfield, *Molecular orientation in model asphalts using molecular simulation*. Energy Fuels, 2007. **21**(2): p. 1102-1111.
107. Rogel, E., *Thermodynamic modeling of asphaltene aggregation*. Langmuir, 2004. **20**(3): p. 1003-1012.
108. Evdokimov, I.N., N.Y. Eliseev, and B.R. Akhmetov, *Asphaltene dispersions in dilute oil solutions*. Fuel, 2006. **85**(10): p. 1465-1472.
109. Yethiraj, A., *Tunable colloids: control of colloidal phase transitions with tunable interactions*. Soft Matter, 2007. **3**(9): p. 1099-1115.
110. Sharma, A., et al., *Probing order in asphaltenes and aromatic ring systems by HRTEM*. Energy & Fuels, 2002. **16**(2): p. 490-496.
111. Ruiz-Morales, Y. and O.C. Mullins, *Measured and simulated electronic absorption and emission spectra of asphaltenes*. Energy Fuels, 2009. **23**(3): p. 1169-1177.

References

112. Rakotondradany, F., et al., *Hexabenzocoronene model compounds for asphaltene fractions: synthesis & characterization*. Energy Fuels, 2006. **20**(6): p. 2439-2447.
113. Ungerer, P., et al., *Sensitivity of the aggregation behaviour of asphaltenes to molecular weight and structure using molecular dynamics*. Mol. Simul., 2014. **40**(1-3): p. 115-122.
114. Kuznicki, T., J.H. Masliyah, and S. Bhattacharjee, *Molecular dynamics study of model molecules resembling asphaltene-like structures in aqueous organic solvent systems*. Energy Fuels, 2008. **22**(4): p. 2379-2389.
115. Kuznicki, T., J.H. Masliyah, and S. Bhattacharjee, *Aggregation and partitioning of model asphaltenes at toluene– water interfaces: Molecular dynamics simulations*. Energy Fuels, 2009. **23**(10): p. 5027-5035.
116. Jian, C., T. Tang, and S. Bhattacharjee, *Probing the effect of side-chain length on the aggregation of a model asphaltene using molecular dynamics simulations*. Energy Fuels, 2013. **27**(4): p. 2057-2067.
117. Teklebrhan, R.B., et al., *Role of naphthenic acids in controlling self-aggregation of a polyaromatic compound in toluene*. J. Phys. Chem. B, 2016. **120**(14): p. 3516-3526.
118. Skartlien, R., S. Simon, and J. Sjöblom, *DPD Molecular Simulations of Asphaltene Adsorption on Hydrophilic Substrates: Effects of Polar Groups and Solubility*. J. Dispersion Sci. Technol., 2016. **37**(6): p. 866-883.
119. Skartlien, R., S. Simon, and J. Sjöblom, *A DPD study of asphaltene aggregation: The role of inhibitor and asphaltene structure in diffusion-limited aggregation*. J. Dispersion Sci. Technol., 2017. **38**(3): p. 440-450.
120. Pradilla, D., et al., *Sorption and interfacial rheology study of model asphaltene compounds*. Langmuir, 2016. **32**(12): p. 2900-2911.
121. Nordgård, E.L., G. Sørland, and J. Sjöblom, *Behavior of asphaltene model compounds at W/O interfaces*. Langmuir, 2009. **26**(4): p. 2352-2360.
122. Nordgård, E.L.k. and J. Sjöblom, *Model compounds for asphaltenes and C80 isoprenoid tetraacids. Part I: Synthesis and Interfacial Activities*. J. Dispersion Sci. Technol., 2008. **29**(8): p. 1114-1122.

References

123. Liu, L., J. Sjö lom, and Z. Xu, *Nanoaggregation of polyaromatic compounds probed by electrospray ionization mass spectrometry*. Energy Fuels, 2016. **30**(5): p. 3742-3751.
124. Nordgård, E.L., E. Landsem, and J. Sjö lom, *Langmuir films of asphaltene model compounds and their fluorescent properties*. Langmuir, 2008. **24**(16): p. 8742-8751.
125. Rogel, E., *Studies on asphaltene aggregation via computational chemistry*. Colloids Surf., A, 1995. **104**(1): p. 85-93.
126. Rogel, E., *Simulation of interactions in asphaltene aggregates*. Energy Fuels, 2000. **14**(3): p. 566-574.
127. Pacheco-Sánchez, J., F. Alvarez-Ramirez, and J. Martínez-Magadán, *Morphology of aggregated asphaltene structural models*. Energy Fuels, 2004. **18**(6): p. 1676-1686.
128. Aguilera-Mercado, B., et al., *Mesosopic simulation of aggregation of asphaltene and resin molecules in crude oils*. Energy Fuels, 2006. **20**(1): p. 327-338.
129. Metropolis, N., et al., *Equation of state calculations by fast computing machines*. J. Chem. Phys., 1953. **21**(6): p. 1087-1092.
130. Hamaker, H., *The London—van der Waals attraction between spherical particles*. Physica, 1937. **4**(10): p. 1058-1072.
131. Finsy, R., *Particle sizing by quasi-elastic light scattering*. Adv. Colloid Interface Sci., 1994. **52**: p. 79-143.
132. Malvern Instruments, *Dynamic light scattering: an introduction in 30 minutes*. Technical Note Malvern, MRK656-01, 2012: p. 1-8.
133. Pecora, R., *Dynamic light scattering: applications of photon correlation spectroscopy*. 2013, 223 Spring Street, New York, NY 10013, USA: Springer Science & Business Media.
134. Hassan, P.A., S. Rana, and G. Verma, *Making sense of Brownian motion: colloid characterization by dynamic light scattering*. Langmuir, 2014. **31**(1): p. 3-12.

References

135. Vaccaro, A., J. Šefčík, and M. Morbidelli, *Characterization of colloidal polymer particles through stability ratio measurements*. *Polymer*, 2005. **46**(4): p. 1157-1167.
136. Goldfischer, L.I., *Autocorrelation function and power spectral density of laser-produced speckle patterns*. *JOSA*, 1965. **55**(3): p. 247-253.
137. Lattuada, M., et al., *Aggregation kinetics of polymer colloids in reaction limited regime: experiments and simulations*. *Advances in Colloid and Interface Science*, 2003. **103**(1): p. 33-56.
138. Wriedt, T., *Mie theory: a review*, in *The Mie Theory*. 2012, Springer. p. 53-71.
139. Russo, P.S., K.H. Langley, and F.E. Karasz, *Dynamic light scattering study of semidilute solutions of a stiff-chain polymer*. *J. Chem. Phys.* , 1984. **80**(10): p. 5312-5325.
140. Dahneke, B.E., *Measurement of suspended particles by quasi-elastic light scattering*. *J. Polym. Sci., Part C: Polym. Lett.*, 1983.
141. Washington, C., *Particle Size Analysis In Pharmaceuticals And Other Industries: Theory And Practice: Theory And Practice*. 2005: CRC Press.
142. Pusey, P.N., *Introduction to scattering experiments*. Neutrons, X-rays, and light: scattering methods applied to soft condensed matter. Amsterdam: Elsevier, 2002. **46**: p. 3-22.
143. Lindner, P. and T. Zemb, *Neutron, X-ray and light scattering: introduction to an investigative tool for colloidal and polymeric systems*. 1991, North-Holland Delta Series; 1991; 385 p; North-Holland; Amsterdam (Netherlands).
144. Berne, B.J. and R. Pecora, *Dynamic light scattering: with applications to chemistry, biology and physics*. 2000. Mineola, NY: Dover Publications.
145. Swift, J. and A. Brown, *An environmental cell for the examination of wet biological specimens at atmospheric pressure by transmission scanning electron microscopy*. *J. Phys. E: Sci. Instrum.*, 1970. **3**(11): p. 924.
146. Hoo, C.M., et al., *A comparison of atomic force microscopy (AFM) and dynamic light scattering (DLS) methods to characterize nanoparticle size distributions*. *J. Nanopart. Res.*, 2008. **10**(1): p. 89-96.

References

147. Kirichenko, M., et al., *Relation between particle sizes and concentration in undiluted and diluted blood plasma according to light scattering data*. Proc. (Tr.) P. N. Lebedev Phys. Inst., [Acad. Sci. USSR], 2015. **42**(2): p. 33-36.
148. Anderson, W., et al., *A comparative study of submicron particle sizing platforms: accuracy, precision and resolution analysis of polydisperse particle size distributions*. J. Colloid Interface Sci., 2013. **405**: p. 322-330.
149. Amin, S., et al., *Protein aggregation, particle formation, characterization & rheology*. Curr. Opin. Colloid Interface Sci., 2014. **19**(5): p. 438-449.
150. Chandrasekhar, S., et al., *Handbook of Liquid Crystals*. 1998, Demus, D., Goodby, J., Gray, GW, Spiess, H.-W., Vill, V., Eds.
151. Provder, T., *Challenges in particle size distribution measurement past, present and for the 21st century*. Progress in organic coatings, 1997. **32**(1): p. 143-153.
152. Malvern. *Dynamic Light Scattering - Zetasizer*. 2017; Available from: <http://www.malvern.com/en/products/technology/dynamic-light-scattering/>
153. Fraden, S. and G. Maret, *Multiple light scattering from concentrated, interacting suspensions*. Phys. Rev. Lett., 1990. **65**(4): p. 512.
154. Ghosh, S., et al., *Determination of critical micelle concentration by hyper-Rayleigh scattering*. J. Am. Chem. Soc., 2003. **125**(6): p. 1602-1606.
155. Holthoff, H., et al., *Coagulation rate measurements of colloidal particles by simultaneous static and dynamic light scattering*. Langmuir, 1996. **12**(23): p. 5541-5549.
156. Thomson, J.A., et al., *Binary liquid phase separation and critical phenomena in a protein/water solution*. Proc. Natl. Acad. Sci. U. S. A., 1987. **84**(20): p. 7079-7083.
157. San Biagio, P. and M. Palma, *Spinodal lines and Flory-Huggins free-energies for solutions of human hemoglobins HbS and HbA*. Biophys. J., 1991. **60**(2): p. 508-512.
158. Narayanan, J. and X. Liu, *Protein interactions in undersaturated and supersaturated solutions: a study using light and x-ray scattering*. Biophys. J., 2003. **84**(1): p. 523-532.

References

159. Espinat, D., et al., *Effects of temperature and pressure on asphaltenes agglomeration in toluene. A light, X-ray, and neutron scattering investigation.* Energy Fuels, 2004. **18**(5): p. 1243-1249.
160. Yudin, I., et al., *Crossover kinetics of asphaltene aggregation in hydrocarbon solutions.* Phys. A (Amsterdam, Neth.), 1998. **251**(1): p. 235-244.
161. Anisimov, M., et al., *Asphaltene aggregation in hydrocarbon solutions studied by photon correlation spectroscopy.* J. Phys. Chem., 1995. **99**(23): p. 9576-9580.
162. Eyssautier, J.I., D. Frot, and L. Barré, *Structure and dynamic properties of colloidal asphaltene aggregates.* Langmuir, 2012. **28**(33): p. 11997-12004.
163. Hashmi, S.M. and A. Firoozabadi, *Tuning size and electrostatics in non-polar colloidal asphaltene suspensions by polymeric adsorption.* Soft Matter, 2011. **7**(18): p. 8384-8391.
164. Heaps, D.T., et al., *Investigation of the precipitation behavior of asphaltenes in the presence of naphthenic acids using light scattering and molecular modeling techniques.* Energy Fuels, 2012. **26**(3): p. 1862-1869.
165. Holzgrabe, U., I. Wawer, and B. Diehl, *NMR spectroscopy in pharmaceutical analysis.* 2011: Elsevier.
166. Günther, H., *NMR spectroscopy: basic principles, concepts and applications in chemistry.* 2013: John Wiley & Sons.
167. Macomber, R.S., *A complete introduction to modern NMR spectroscopy.* 1998: Wiley New York.
168. Carr, H.Y. and E.M. Purcell, *Effects of diffusion on free precession in nuclear magnetic resonance experiments.* Phys. Rev. Lett., 1954. **94**(3): p. 630.
169. Phillips, J.S. and J.J. Leary, *A qualitative quantitative ¹H-NMR experiment for the instrumental analysis laboratory.* J. Chem. Educ, 1986. **63**(6): p. 545.
170. Peterson, J., *¹H NMR analysis of mixtures using internal standards: A quantitative experiment for the instrumental analysis laboratory.* J. Chem. Educ, 1992. **69**(10): p. 843.

References

171. Griffiths, L., *Assay by nuclear magnetic resonance spectroscopy: quantification limits*. *Analyst*, 1998. **123**(5): p. 1061-1068.
172. Ali, L.H., K.A. Al-Ghannam, and J.M. Al-Rawi, *Chemical structure of asphaltenes in heavy crude oils investigated by nmr*. *Fuel*, 1990. **69**(4): p. 519-521.
173. Ferris, S., E. Black, and J. Clelland, *Aromatic structure in asphalt fractions*. *Ind. Eng. Chem. Prod. Res. Dev.*, 1967. **6**(2): p. 127-132.
174. Dickson, F.E., B.E. Davis, and R.A. Wirkkala, *Weight of unit sheets in petroleum residues by proton nuclear magnetic resonance*. *Anal. Chem.*, 1969. **41**(10): p. 1335-1337.
175. Rongbao, L., S. Zengmin, and L. Bailing, *Structural analysis of polycyclic aromatic hydrocarbons derived from petroleum and coal by ¹³C and ¹H-nmr spectroscopy*. *Fuel*, 1988. **67**(4): p. 565-569.
176. Chaffee, A.L. and C.J. Fookes, *Polycyclic aromatic hydrocarbons in Australian coals—III. Structural elucidation by proton nuclear magnetic resonance spectroscopy*. *Org. Geochem.*, 1988. **12**(3): p. 261-271.
177. Shen, H., C.Y. Airiau, and R.G. Brereton, *Resolution of LC/¹H NMR data applied to a three-component mixture of polyaromatic hydrocarbons*. *J. Chemom.*, 2002. **16**(4): p. 165-175.
178. Calemma, V., et al., *Structural characterization of asphaltenes of different origins*. *Energy Fuels*, 1995. **9**(2): p. 225-230.
179. Gillet, S., et al., *Quantitative carbon-13 and proton nuclear magnetic resonance spectroscopy of crude oil and petroleum products. I. Some rules for obtaining a set of reliable structural parameters*. *Fuel*, 1981. **60**(3): p. 221-225.
180. Dereppe, J.-M., C. Moreaux, and H. Castex, *Analysis of asphaltenes by carbon and proton nuclear magnetic resonance spectroscopy*. *Fuel*, 1978. **57**(7): p. 435-441.
181. Dickinson, E.M., *Structural comparison of petroleum fractions using proton and ¹³C nmr spectroscopy*. *Fuel*, 1980. **59**(5): p. 290-294.
182. Buenrostro-Gonzalez, E., et al., *The overriding chemical principles that define asphaltenes*. *Energy Fuels*, 2001. **15**(4): p. 972-978.

References

183. Resing, H.A. and C.G. Wade, *Magnetic Resonance in Colloid and Interface Science*. 1976: ACS Publications.
184. Szczygiel, A., J. Martins, and L. Timmermans. *NMR characterization of dispersant-particle interactions in the colloidal dispersions*. in *Online Journal for the Basic Principles of Diffusion Theory, Experiment and Application*. 2007.
185. van der Spoel D, L.E., Hess B and The Gromacs Development Team, *Gromacs User Manual Version 4.6.5*. 2013.
186. Van der Spoel, D., E. Lindahl, and B. Hess, *the GROMACS development team*. GROMACS User Manual version, 2013. **4**(5).
187. Van Der Spoel, D., et al., *GROMACS: fast, flexible, and free*. J. Comput. Chem., 2005. **26**(16): p. 1701-1718.
188. Headen, T.F. and E.S. Boek, *Potential of mean force calculation from molecular dynamics simulation of asphaltene molecules on a calcite surface*. Energy Fuels, 2010. **25**(2): p. 499-502.
189. Sedghi, M., et al., *Effect of asphaltene structure on association and aggregation using molecular dynamics*. J. Phys. Chem. B., 2013. **117**(18): p. 5765-5776.
190. Adcock, S.A. and J.A. McCammon, *Molecular dynamics: survey of methods for simulating the activity of proteins*. Chem. Rev., 2006. **106**(5): p. 1589-1615.
191. Lin, J.-H., et al., *Computational drug design accommodating receptor flexibility: the relaxed complex scheme*. J. Am. Chem. Soc., 2002. **124**(20): p. 5632-5633.
192. Jorgensen, W.L., D.S. Maxwell, and J. Tirado-Rives, *Development and testing of the OPLS all-atom force field on conformational energetics and properties of organic liquids*. J. Am. Chem. Soc., 1996. **118**(45): p. 11225-11236.
193. Boek, E.S., D.S. Yakovlev, and T.F. Headen, *Quantitative molecular representation of asphaltenes and molecular dynamics simulation of their aggregation*. Energy Fuels, 2009. **23**(3): p. 1209-1219.

References

194. Headen, T.F., E.S. Boek, and N.T. Skipper, *Evidence for asphaltene nanoaggregation in toluene and heptane from molecular dynamics simulations*. Energy Fuels, 2009. **23**(3): p. 1220-1229.
195. Caleman, C., et al., *Force field benchmark of organic liquids: density, enthalpy of vaporization, heat capacities, surface tension, isothermal compressibility, volumetric expansion coefficient, and dielectric constant*. J. Chem. Theory Comput., 2011. **8**(1): p. 61-74.
196. Costa, J., et al., *Aggregation of model asphaltenes: a molecular dynamics study*. J. Phys.: Condens. Matter, 2016. **28**(39): p. 394002.
197. Allen, M.P. and D.J. Tildesley, *Computer simulation of liquids*. 1989: Oxford university press.
198. Laanait, N., *Ion correlations at electrified soft matter interfaces*. 2013: Springer Science & Business Media.
199. Humphrey, W., A. Dalke, and K. Schulten, *VMD: visual molecular dynamics*. J. Mol. Graphics, 1996. **14**(1): p. 33-38.
200. Accelrys, *Accelrys Draw S.D.-A. Software, Editor*. 2007. p. Academic Version.
201. SchuÈttelkopf, A.W. and D.M. Van Aalten, *PRODRG: a tool for high-throughput crystallography of protein–ligand complexes*. Acta Crystallogr., Sect. D: Biol. Crystallogr., 2004. **60**(8): p. 1355-1363.
202. Ribeiro, A.A., B.A. Horta, and R.B.d. Alencastro, *MKTOP: a program for automatic construction of molecular topologies*. J. Braz. Chem. Soc., 2008. **19**(7): p. 1433-1435.
203. Hibi, R., et al. *Investigation of Asphaltene-Asphaltene Association and Aggregation for Compositional Reservoir Simulators By Quantitative Molecular Representations*. in *International Petroleum Technology Conference*. 2014. International Petroleum Technology Conference.
204. Darden, T., D. York, and L. Pedersen, *Particle mesh Ewald: An $N \cdot \log(N)$ method for Ewald sums in large systems*. J. Chem. Phys., 1993. **98**(12): p. 10089-10092.
205. Hayward, S. and N. Go, *Collective variable description of native protein dynamics*. Annu. Rev. Phys. Chem., 1995. **46**(1): p. 223-250.

References

206. Berendsen, H., *Transport properties computed by linear response through weak coupling to a bath*, in *Computer Simulation in Materials Science*. 1991, Springer: NY, USA. p. 139-155.
207. Berendsen, H.J., et al., *Molecular dynamics with coupling to an external bath*. *J. Chem. Phys.*, 1984. **81**(8): p. 3684-3690.
208. Kelsall, R., I.W. Hamley, and M. Geoghegan, *Nanoscale science and technology*. 2005: John Wiley & Sons.
209. Chen, J.C. and A.S. Kim, *Brownian dynamics, molecular dynamics, and Monte Carlo modeling of colloidal systems*. *Adv. Colloid Interface Sci.*, 2004. **112**(1): p. 159-173.
210. Yu, M., *Computational Modeling of Protein Dynamics with GROMACS and Java*. 2012, Master's Projects. 267. .
211. Latour, R.A., *Molecular simulation of protein-surface interactions: Benefits, problems, solutions, and future directions (Review)*. *Biointerphases*, 2008. **3**(3): p. FC2-FC12.
212. Rabe, M., D. Verdes, and S. Seeger, *Understanding protein adsorption phenomena at solid surfaces*. *Adv. Colloid Interface Sci.*, 2011. **162**(1): p. 87-106.
213. Ortega-Rodríguez, A., et al., *Molecular view of the asphaltene aggregation behavior in asphaltene– resin mixtures*. *Energy & fuels*, 2003. **17**(4): p. 1100-1108.
214. Gao, F., et al., *Molecular dynamics simulation: the behavior of asphaltene in crude oil and at the oil/water interface*. *Energy Fuels*, 2014. **28**(12): p. 7368-7376.
215. Sodero, A.C., et al., *Investigation of the Effect of Sulfur Heteroatom on Asphaltene Aggregation*. *Energy Fuels*, 2016. **30**(6): p. 4758-4766.
216. Venkataraman, P., et al., *Molecular Insights into Glass Transition in Condensed Core Asphaltenes*. *Energy Fuels*, 2017 **31**, 2, 1182-1192.
217. Boduszynski, M.M., *Composition of heavy petroleums. 2. Molecular characterization*. *Energy Fuels*, 1988. **2**(5): p. 597-613.
218. Rodgers, R.P. and A.G. Marshall, *Petroleomics: Advanced characterization of petroleum-derived materials by Fourier transform ion cyclotron*

References

- resonance mass spectrometry (FT-ICR MS)*, in *Asphaltenes, Heavy Oils, and Petroleomics*. 2007, Springer. p. 63-93.
219. Alshareef, A.H., et al., *Formation of archipelago structures during thermal cracking implicates a chemical mechanism for the formation of petroleum asphaltenes*. *Energy Fuels*, 2011. **25**(5): p. 2130-2136.
220. Pisula, W., et al., *Relationship between core size, side chain length, and the supramolecular organization of polycyclic aromatic hydrocarbons*. *Chem. Mater.*, 2005. **17**(17): p. 4296-4303.
221. Kumar, S., *Recent developments in the chemistry of triphenylene-based discotic liquid crystals*. *Liq. Cryst.*, 2004. **31**(8): p. 1037-1059.
222. Van de Craats, A. and J. Warman, *The core-size effect on the mobility of charge in discotic liquid crystalline materials*. *Adv. Mater.*, 2001. **13**(2): p. 130-133.
223. Brown, S.P., et al., *An investigation of π - π packing in a columnar hexabenzocoronene by fast magic-angle spinning and double-quantum ^1H solid-state NMR spectroscopy*. *J. Am. Chem. Soc.*, 1999. **121**(28): p. 6712-6718.
224. Lundblad, R. L., and Noyes, C. M. (1984) *Chemical Reagents for Protein Modification*, Vols. I and II, CRC Press, New York
225. Feng, X., et al., *Towards high charge-carrier mobilities by rational design of the shape and periphery of discotics*. *Nat. Mater.*, 2009. **8**(5): p. 421-426.
226. Hippus, C., et al., *Energy transfer in calixarene-based cofacial-positioned perylene bisimide arrays*. *J. Am. Chem. Soc.*, 2006. **128**(12): p. 3870-3871.
227. Wong, W.W., et al., *A porphyrin-hexa-peri-hexabenzocoronene-porphyrin triad: synthesis, photophysical properties and performance in a photovoltaic device*. *Journal of Materials Chemistry*, 2010. **20**(33): p. 7005-7014.
228. Facchetti, A., *π -Conjugated polymers for organic electronics and photovoltaic cell applications*. *Chem. Mater.*, 2010. **23**(3): p. 733-758.
229. Wong, W.W., et al., *Solution processable fluorenyl hexa-peri-hexabenzocoronenes in organic field-effect transistors and solar cells*. *Adv. Funct. Mater.*, 2010. **20**(6): p. 927-938.

References

230. Díaz-García, M., et al., *Effect of structural modifications in the laser properties of polymer films doped with perylenebisimide derivatives*. Synth. Met., 2009. **159**(21): p. 2293-2295.
231. Choi, H., et al., *Synthesis of annulated thiophene perylene bisimide analogues: Their applications to bulk heterojunction organic solar cells*. Chem. Commun., 2011. **47**(19): p. 5509-5511.
232. Kumar, S., *Triphenylene-based discotic liquid crystal dimers, oligomers and polymers*. Liq. Cryst., 2005. **32**(9): p. 1089-1113.
233. Heeger, A.J., *Semiconducting and metallic polymers: the fourth generation of polymeric materials (Nobel lecture)*. Angew. Chem., Int. Ed., 2001. **40**(14): p. 2591-2611.
234. Archer, M.D., *Nanostructured and photoelectrochemical systems for solar photon conversion*. Vol. 3. 2008, London, Covent Garden, 57 Shelton Street: Imperial College Press.
235. Shaheen, S.E., et al., *2.5% efficient organic plastic solar cells*. Appl. Phys. Lett., 2001. **78**(6): p. 841-843.
236. Marguet, S., et al., *Influence of disorder on electronic excited states: an experimental and numerical study of alkylthiotriphenylene columnar phases*. J. Phys. Chem. B., 1998. **102**(24): p. 4697-4710.
237. Heppke, G., et al., *New chiral discotic triphenylene derivatives exhibiting a cholesteric blue phase and a ferroelectrically switchable columnar mesophase*. J. Mater. Chem., 2000. **10**(12): p. 2657-2661.
238. Korb, J.-P., A. Louis-Joseph, and L.s. Benamsili, *Probing structure and dynamics of bulk and confined crude oils by multiscale NMR spectroscopy, diffusometry, and relaxometry*. J. Phys. Chem. B., 2013. **117**(23): p. 7002-7014.
239. Bushby, R.J. and K. Kawata, *Liquid crystals that affected the world: discotic liquid crystals*. Liq. Cryst., 2011. **38**(11-12): p. 1415-1426.
240. Oh, K., T.A. Ring, and M.D. Deo, *Asphaltene aggregation in organic solvents*. J. Colloid Interface Sci., 2004. **271**(1): p. 212-219.
241. Boden, N., et al., *Mechanism of charge transport in discotic liquid crystals*. Phys. Rev. B, 1995. **52**(18): p. 13274.

References

242. Alameddine, B., et al., *Mesomorphic hexabenzocoronenes bearing perfluorinated chains*. Chem. Mater., 2005. **17**(19): p. 4798-4807.
243. Bast, T. and R. Hentschke, *Molecular dynamics simulation of a micellar system: 2, 3, 6, 7, 10, 11-hexakis (1, 4, 7-trioxaoctyl) triphenylene in water*. J. Phys. Chem., 1996. **100**(30): p. 12162-12171.
244. Percec, V. and T.K. Bera, *Cell membrane as a model for the design of ion-active nanostructured supramolecular systems*. Biomacromolecules, 2002. **3**(1): p. 167-181.
245. Marcos, M., et al., *Dendromesogens: liquid crystal organizations of poly (amidoamine) dendrimers versus starburst structures*. Chem. EU J., 2001. **7**(5): p. 1006-1013.
246. Trejo, F., J. Ancheyta, and M.S. Rana, *Structural characterization of asphaltenes obtained from hydroprocessed crude oils by SEM and TEM*. Energy Fuels, 2009. **23**(1): p. 429-439.
247. Takanohashi, T., et al., *Molecular dynamics simulation of the heat-induced relaxation of asphaltene aggregates*. Energy Fuels, 2003. **17**(1): p. 135-139.
248. Painter, P., B. Veytsman, and J. Youtcheff, *Asphaltene aggregation and solubility*. Energy Fuels, 2015. **29**(4): p. 2120-2133.
249. Bushby, R.J. and O.R. Lozman, *Discotic liquid crystals 25 years on*. Curr. Opin. Colloid Interface Sci., 2002. **7**(5): p. 343-354.
250. Setoguchi, Y., et al., *Infrared studies on hydrogen bond interaction in a homologues series of triphenylene discotic liquid crystals having carboxylic acids at the peripheral chains*. Thin Solid Films, 2003. **438**: p. 407-413.
251. Eyssautier, J., et al., *Insight into asphaltene nanoaggregate structure inferred by small angle neutron and X-ray scattering*. J. Phys. Chem. B., 2011. **115**(21): p. 6827-6837.
252. Eyssautier, J., et al., *Organization of asphaltenes in a vacuum residue: a small-angle X-ray scattering (SAXS)-viscosity approach at high temperatures*. Energy & Fuels, 2011. **26**(5): p. 2696-2704.
253. Hoepfner, M.P., et al., *The fractal aggregation of asphaltenes*. Langmuir, 2013. **29**(28): p. 8799-8808.

References

254. Hashmi, S.M. and A. Firoozabadi, *Effect of dispersant on asphaltene suspension dynamics: aggregation and sedimentation*. J. Phys. Chem. B., 2010. **114**(48): p. 15780-15788.
255. Wattana, P., *Precipitation and characterization of petroleum asphaltenes*. 2004. Ph.D. Theses 3122067.
256. Maqbool, T., A.T. Balgoa, and H.S. Fogler, *Revisiting asphaltene precipitation from crude oils: A case of neglected kinetic effects*. Energy & Fuels, 2009. **23**(7): p. 3681-3686.
257. Maqbool, T., P. Srikiatwong, and H.S. Fogler, *Effect of temperature on the precipitation kinetics of asphaltenes*. Energy Fuels, 2011. **25**(2): p. 694-700.
258. Sheu, E.Y. and S. Acevedo, *Effect of pressure and temperature on colloidal structure of furrial crude oil*. Energy Fuels, 2001. **15**(3): p. 702-707.
259. Wiehe, I.A. and R.J. Kennedy, *The oil compatibility model and crude oil incompatibility*. Energy Fuels, 2000. **14**(1): p. 56-59.
260. Hasan, S.W., M.T. Ghannam, and N. Esmail, *Heavy crude oil viscosity reduction and rheology for pipeline transportation*. Fuel, 2010. **89**(5): p. 1095-1100.
261. Li, S., et al., *Distillation yields from blending Cabinda crude oil and Oman crude oil*. Pet. Sci. Technol., 2006. **24**(6): p. 737-747.
262. Wiehe, I.A., et al., *The paradox of asphaltene precipitation with normal paraffins*. Energy Fuels, 2005. **19**(4): p. 1261-1267.
263. Wang, J. and J. Buckley, *A two-component solubility model of the onset of asphaltene flocculation in crude oils*. Energy Fuels, 2001. **15**(5): p. 1004-1012.
264. Zuo, J.Y., et al., *Advances in the Flory–Huggins–Zuo equation of state for asphaltene gradients and formation evaluation*. Energy Fuels, 2012. **27**(4): p. 1722-1735.
265. Freed, D.E., O.C. Mullins, and J.Y. Zuo, *Theoretical treatment of asphaltene gradients in the presence of GOR gradients*. Energy Fuels, 2010. **24**(7): p. 3942-3949.

References

266. Alboudwarej, H., et al., *Regular solution model for asphaltene precipitation from bitumens and solvents*. AIChE J., 2003. **49**(11): p. 2948-2956.
267. Haji-Akbari, N., et al., *Effect of n-alkane precipitants on aggregation kinetics of asphaltenes*. Energy Fuels, 2015. **29**(4): p. 2190-2196.
268. Mannistu, K., H. Yarranton, and J. Masliyah, *Solubility modeling of asphaltenes in organic solvents*. Energy Fuels, 1997. **11**(3): p. 615-622.
269. Zhang, Y., et al., *Estimating the interaction energy of asphaltene aggregates with aromatic solvents*. Energy Fuels, 2005. **19**(3): p. 1023-1028.
270. Mullins, O.C., et al., *The colloidal structure of crude oil and the structure of oil reservoirs*. Energy & Fuels, 2007. **21**(5): p. 2785-2794.
271. Buckley, J.S., *Predicting the onset of asphaltene precipitation from refractive index measurements*. Energy Fuels, 1999. **13**(2): p. 328-332.
272. Porte, G., H. Zhou, and V. Lazzeri, *Reversible description of asphaltene colloidal association and precipitation*. Langmuir, 2003. **19**(1): p. 40-47.
273. Wiehe, I.A., *Process chemistry of petroleum macromolecules*. 2008: CRC press.
274. Zhao, B. and J.M. Shaw, *Composition and size distribution of coherent nanostructures in Athabasca bitumen and Maya crude oil*. Energy Fuels, 2007. **21**(5): p. 2795-2804.
275. Headen, T.F., et al., *Small angle neutron scattering (SANS and V-SANS) study of asphaltene aggregates in crude oil*. Langmuir, 2008. **25**(1): p. 422-428.
276. Mostowfi, F., et al., *Asphaltene nanoaggregates studied by centrifugation*. Energy Fuels, 2008. **23**(3): p. 1194-1200.
277. Maqbool, T., et al., *Modeling the aggregation of asphaltene nanoaggregates in crude oil- precipitant systems*. Energy Fuels, 2011. **25**(4): p. 1585-1596.
278. Östlund, J.-A., S.-I. Andersson, and M. Nydén, *Studies of asphaltenes by the use of pulsed-field gradient spin echo NMR*. Fuel, 2001. **80**(11): p. 1529-1533.

References

279. Durand, E., et al., *¹H diffusion-ordered spectroscopy (DOSY) nuclear magnetic resonance (NMR) as a powerful tool for the analysis of hydrocarbon mixtures and asphaltenes*. *Energy Fuels*, 2008. **22**(4): p. 2604-2610.
280. Durand, E., et al., *Effect of chemical composition on asphaltenes aggregation*. *Energy Fuels*, 2010. **24**(2): p. 1051-1062.
281. Zielinski, L., et al., *Probing asphaltene aggregation in native crude oils with low-field NMR*. *Langmuir*, 2010. **26**(7): p. 5014-5021.
282. Lijinsky, W. and C.R. Raha, *Polycyclic aromatic hydrocarbons in commercial solvents*. *Toxicol. Appl. Pharmacol.*, 1961. **3**(4): p. 469-473.
283. Acevedo, S., et al., *Thermo-optical studies of asphaltene solutions: evidence for solvent–solute aggregate formation*. *Fuel*, 1999. **78**(9): p. 997-1003.
284. Figueroa-Gerstenmaier, S., et al., *A molecular model for H₂ interactions in aliphatic and aromatic hydrocarbons*. *Phys. Chem. Chem. Phys.*, 2009. **11**(20): p. 3935-3942.
285. Cozzi, F., et al., *Dominance of polar/π over charge-transfer effects in stacked phenyl interactions*. *J. Am. Chem. Soc.*, 1993. **115**(12): p. 5330-5331.
286. Etter, M.C., *Encoding and decoding hydrogen-bond patterns of organic compounds*. *Acc. Chem. Res.*, 1990. **23**(4): p. 120-126.
287. Henderson, P., et al., *Complex ordering in thin films of di- and trifunctionalized hexaalkoxytriphenylene derivatives*. *J. Am. Chem. Soc.*, 1997. **119**(20): p. 4740-4748.
288. Gallivan, J.P. and G.B. Schuster, *Aggregates of hexakis (n-hexyloxy) triphenylene self-assemble in dodecane solution: intercalation of (-)-menthol 3, 5-dinitrobenzoate induces formation of helical structures*. *J. Org. Chem.*, 1995. **60**(8): p. 2423-2429.
289. Rogel, E., et al., *Aggregation of asphaltenes in organic solvents using surface tension measurements*. *Fuel*, 2000. **79**(11): p. 1389-1394.

References

290. Kumar, S. and J.J. Naidu, *Novel hexasubstituted triphenylene discotic liquid crystals having three different types of peripheral substituent*. *Liq. Cryst.*, 2002. **29**(7): p. 899-906.
291. McKenna, M.D., et al., *Discotic liquid crystalline poly (propylene imine) dendrimers based on triphenylene*. *J. Am. Chem. Soc.*, 2005. **127**(2): p. 619-625.
292. Gherghel, L., et al., *Pyrolysis in the mesophase: a chemist's approach toward preparing carbon nano-and microparticles*. *J. Am. Chem. Soc.*, 2002. **124**(44): p. 13130-13138.
293. Wu, J., et al., *Controlled self-assembly of hexa-*p* eri-hexabenzocoronenes in solution*. *J. Am. Chem. Soc.*, 2004. **126**(36): p. 11311-11321.
294. Kastler, M., et al., *Influence of alkyl substituents on the solution and surface-organization of hexa-*peri*-hexabenzocoronenes*. *J. Am. Chem. Soc.*, 2005. **127**(12): p. 4286-4296.
295. Kim, H.-S., et al., *Phase behavior of hexa-*peri*-hexabenzocoronene derivative in organic solvent*. *J. Phys. Chem. B.*, 2011. **115**(22): p. 7314-7320.
296. Hughes, J.M., et al., *High quality dispersions of hexabenzocoronene in organic solvents*. *J. Am. Chem. Soc.*, 2012. **134**(29): p. 12168-12179.
297. Kastler, M., et al., *Influence of alkyl substituents on the solution-and surface-organization of hexa-*peri*-hexabenzocoronenes*. *J. Am. Chem. Soc.*, 2005. **127**(12): p. 4286-4296.
298. Rathore, R. and C.L. Burns, *A practical one-pot synthesis of soluble hexa-*peri*-hexabenzocoronene and isolation of its cation-radical salt*. *Am. J. Org. Chem.*, 2003. **68**(10): p. 4071-4074.
299. Dechaine, G.P. and M.R. Gray, *Membrane diffusion measurements do not detect exchange between asphaltene aggregates and solution phase*. *Energy Fuels*, 2010. **25**(2): p. 509-523.
300. Yudin, I., et al., *Mechanisms of asphaltene aggregation in toluene–heptane mixtures*. *J. Pet. Sci. Eng.*, 1998. **20**(3): p. 297-301.

References

301. Feng, X., et al., *Towards high charge-carrier mobilities by rational design of the shape and periphery of discotics*. *Nature materials*, 2009. **8**(5): p. 421-426.
302. Wasserfallen, D., et al., *Suppressing aggregation in a large polycyclic aromatic hydrocarbon*. *J. Am. Chem. Soc.*, 2006. **128**(4): p. 1334-1339.
303. Tanga, M., R. Davis, and E. Reist, *Synthesis of phenanthro [9, 10-g] isoquinoline*. *J. Heterocycl. Chem.*, 1987. **24**(1): p. 39-41.

Appendices

Appendices

The following contains supplementary information relevant to anyone attempting to verify, replicate or continue this work.

Appendix A. Molecular dynamics simulations: additional information

The simulation steps described in Chapter 2 were accomplished with on an Ubuntu-Linux operating system, with a GROMACS 4.6.5 software package.

A.1. Command lines for simulations and data analysis

To start the simulation, the key files (*.mdp*, *.pdb*, *.itp*) corresponding to the molecules used in the simulation must be in the same directory-folder. At this point, the simulation box may be generated:

```
$ genconf -f molecule.pdb -nbox 1 2 3 -dist 1.5 1.5 1.5 -o box.gro
```

This line creates a box with 6 molecules (*nbox 1x2x3*) at a distance of 1.5 between them. However, this simple method does not give a high degree of randomness to the position of the molecules, which may impact on the results later on. Hence, a more complex but risk free command was employed that positions the 7 model compound molecules at equidistant positions through the simulation box:

```
$ genconf -f molecule.pdb -dist 0 4 0 -nbox 1 2 1 -o boxtestvertical.gro
```

```
$ editconf -f boxtestvertical.gro -box 7 7 7 -center 3.5 3.5 3.5 -o vertical.gro
```

```
$ genconf -f molecule.pdb -dist 0 0 0 -nbox 1 1 1 -o boxtestx.gro
```

```
$ editconf -f boxtestx.gro -box 7 7 7 -center 3.5 3.5 3.5 -rotate 90 0 0 -o horizontal.gro
```

```
$ genconf -f molecule.pdb -dist 0 0 5 -nbox 1 1 2 -o boxtestz.gro
```

Appendices

```
$ editconf -f boxtestz.gro -box 7 7 7 -center 3.5 3.5 3.5 -o editboxz.gro
```

```
$ editconf -f boxtestz.gro -box 7 7 7 -center 3.5 3.5 3.5 -rotate 0 90 0 -o  
editboxy.gro
```

```
$ genbox -cp vertical.gro -cs horizontal.gro -o box1.gro
```

```
$ genbox -cp box1.gro -cs editboxz.gro -o box2.gro
```

```
$ genbox -cp box2.gro -cs editboxy.gro -o aspbox.gro
```

The next step is to solvate the box with the chosen solvent molecule.

```
$ genbox -cp aspbox.gro -ci solvent.gro -nmol 700 -try 10 -o  
asphsolventbox.gro
```

This line loaded the box with 700 solvent molecules as can be seen in Figure 2.12. More than one solvent can be loaded in the box by modifying the command line to:

```
$ genbox -cp aspbox.gro -ci solvent1.gro -nmol 350 -try 10 -o  
asphsolvent1box.gro
```

```
$ genbox -cp asphsolvent1box.gro -ci solvent2.gro -nmol 350 -try 10 -o  
asphsolvent2box.gro
```

These two command lines will solvate the box with 350 *solvent1* and 350 *solvent2* molecules.

Appendices

As mentioned in Chapter 2, after the box contains all the required molecules, several steps need to be performed to allow the system to establish thermodynamic equilibrium.

- EM (Energy minimization)

```
$ grompp -f em.mdp -c asphsolventbox.gro -p box.top -o em.tpr -maxwarn 1
```

```
$ mdrun -deffnm em -v
```

- NVT (Number of particles, system volume and temperature)

```
$ grompp -f nvt.mdp -c em.gro -p box.top -o nvt.tpr
```

```
$ mdrun -deffnm nvt -v
```

- NPT (Number of particles, system pressure and temperature)

```
$ grompp -f npt.mdp -c nvt.gro -p box.top -o npt.tpr
```

```
$ mdrun -deffnm npt -v
```

After these steps have been completed, the full-length simulation can be carried out by using the command line:

```
$ grompp -f md.mdp -c npt.gro -p box.top -o md.tpr
```

```
$ mdrun -deffnm md -v
```

The output files of main interest for data analysis and further processing will be the *output.gro* and the *output.trr*, as they contain the final parameters of the file (*.gro*) and the molecular trajectories (*.trr*).

Appendices

A.2. Software operation instructions

The Visual Molecular Dynamics (VMD) software package was employed for capturing, viewing, animating, and analysing simulation boxes, using 3D graphics and built in scripting.

The *.gro* output files are loaded into the VMD software along with the *.trr*. When the loading process is complete the *Graphics>Representation* menu is accessed. The names of the model molecules (*DRG*) were written in the “*Selected Atoms*” box to render all other atoms invisible. The option for *Coloring Method – ResID* and *Drawing Method – Dynamic Bonds* were selected for improving the quality of the snapshots.

The VMD software cannot assemble video files, so it is utilised to generate snapshot images of the simulations at customised time intervals. The following steps are taken for this purpose:

At *Display* on the main window:

- Remove the *Axis Indicator*
- Change the *Projection* to *Orthographic*
- Uncheck the box for *Depth Cueing*

The *movie generator* tool is then used: Main window: *Extensions>Visualisation>Movie Generator*. The options employed there are:

- *Renderer – Snapshots*
- *Movie Settings – Change to Trajectory*.
- Format: *AVI(VideoMatch)*

Appendices

In the movie generator window:

- Set a directory for your movie
- If you already use the *Stride* option to refine the number of frames you can use step size = 1. You could also load the whole trajectory and change the *Step size* in a different way.
- *Rotation* = 0
- Press *Make Movie*

The snapshot images will be sent to the selected directory, after which Windows Movie Maker was used to convert the obtained images into a *.wma* movie file.

Appendix B. Triphenylene-cored model compounds synthesis and quality analysis

The triphenylene cored model compounds were synthesised and quality checked by the group members of Professor Jon Preece in the School of Chemistry, University of Birmingham, UK. The model chemical structures are presented above in Table 2.1.

While the TPN-C0 (triphenylene core) was readily purchased from Sigma Aldrich (Dorset, UK), the model compounds were produced in two synthesis groups, by alkoxy group addition (TPN-C1/C3/C5/C10), and by functional group (TPN-CN/CNAcid).

Triphenylene carboxylic acid (**1**) was prepared using the synthesis described by Reist *et al* [303]. All other reagents were used directly from the suppliers (Sigma Aldrich-Dorset, UK) without further purification unless otherwise stated. All solvents used were reagent grade unless otherwise stated. Reflux apparatus used

Appendices

had been previously dried at 140 °C for at least a period of 3 h before use. Column chromatographic separations were performed using silica gel 120 (ICN Chrom 32-63 60 Å). Analytical techniques used as confirmation were Electron Impact Ionisation Mass Spectrometry (EIMS), Electrospray Mass Spectrometry (ES⁺MS), infra-red spectroscopy and NMR spectroscopy. ¹H NMR, and ¹³C NMR spectroscopy, correlation spectroscopy (COSY), heteronuclear single quantum coherence (HSQC) and heteronuclear multiple bond correlation (HMBC).

B.1. Synthesis of alkoxy group model compounds

A solution of **5a-5c** (15.2 mmol) in anhydrous dichloromethane (30 mL) was charged to **5a-5c** anhydrous iron (iii) chloride (7.4 g; 46 mmol). The slurry was stirred under N₂ for 30 min. Ice-cold methanol (100 mL) was added slowly. Afterwards the slurry was cooled to -10 °C and left for 48 h. The slurry was filtered under vacuum and the resulting precipitate was washed with ice-cold methanol (5 x 40 mL). The crude solid was further purified by flash column chromatography (silica, 98% *n*-hexane: 2% ethyl acetate) to afford **6a** (70%), **6b** (30%) and **6c** (56% yield) as off-white solids.

A solution of **5a-5c** (15.2 mmol) in anhydrous dichloromethane (30 mL) was charged to **5a-5c** anhydrous iron (iii) chloride (7.4 g; 46 mmol). The slurry was stirred under N₂ for 30 min. Ice-cold methanol (100 mL) was added slowly. Afterwards the slurry was cooled to -10 °C and left for 48 h. The slurry was filtered under vacuum and the resulting precipitate was washed with ice-cold methanol (5 x 40 mL). The crude solid was further purified by flash column chromatography (silica, 98% *n*-hexane: 2% ethyl acetate) to afford **6a** (70%), **6b** (30%) and **6c** (56% yield) as off-white solids.

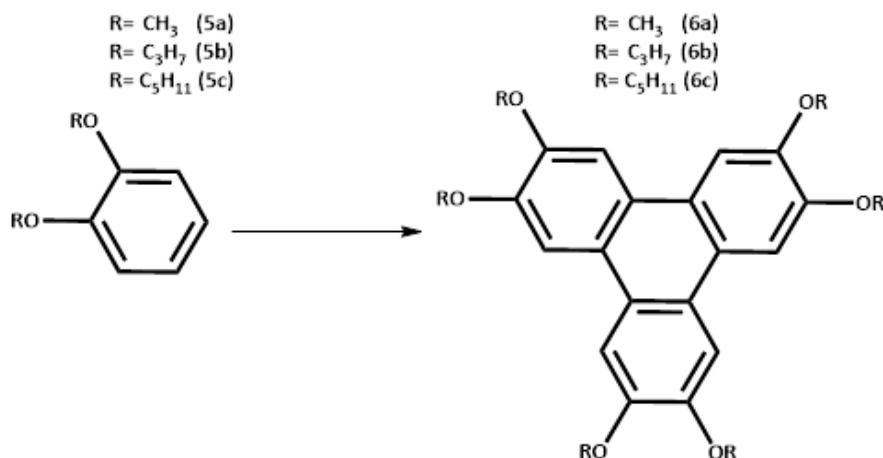


Figure A.1. Depiction of the reaction synthesis into **6a** (70%), **6b** (30%) and **6c** (56% yield)

- **6a** $^1\text{H NMR}$ (300 MHz, CDCl_3) δ_{H} : 7.78 (6H, s), 4.13 (18H, s) ppm.
- $^{13}\text{C NMR}$ (400 MHz, CDCl_3) δ_{C} : 148.9, 123.3, 104.4, 56.1 ppm.
- **MALDI** $^+$ m/z : 408.3 ($[\text{M}]^+$ 100%).
- **IR** Cn^{-1} (neat): 2986w (C-H), 2827w (C-H), 1516m (benzene ring), 1459m (benzene ring), 1264s (C-O), 1159 (C-O) cm^{-1}
- **6b** $^1\text{H NMR}$ (300 MHz, CDCl_3) δ_{H} : 7.84 (6H, s), 4.20 (12H, t, J 6.6 Hz), 2.43 (3H, h, J 7.1 Hz), 1.14 (18H, t, J 7.4 Hz) ppm.
- $^{13}\text{C NMR}$ (400 MHz, CDCl_3) δ_{C} : 149.1, 123.7, 107.5, 71.3, 22.9, 10.7 ppm.
- **MALDI** $^+$ m/z : 408.3 ($[\text{M}]^+$ 100%). **IR** λ^{-1} (neat): 2963w (C-H), 2882w (C-H), 1508m (benzene ring), 1431m (benzene ring), 1254s (C-O), 1167 (C-O) cm^{-1} .
- **6c** $^1\text{H NMR}$ (300 MHz, CDCl_3) δ_{H} : 7.84 (6H, s), 4.24 (12H, t, J 6.6 Hz), 2.43 (12H, p, J 6.8 Hz), 1.58 (24H, m), 0.98 (18H, t, J 7.2 Hz) ppm.
- $^{13}\text{C NMR}$ (400 MHz, CDCl_3) δ_{C} : 149.3, 124.0, 107.7, 70.1, 29.5, 28.8, 23.0, 14.5 ppm.
- **ES** $^+$ **MS** m/z : 745.5 ($[\text{M}+\text{H}]^+$ 100%), 744.5 ($[\text{M}]^+$ 60%).

- **IR** Cn^{-1} (neat): 2931w (C-H), 2858w (C-H), 1514m (benzene ring), 1437m (benzene ring), 1259s (C-O), 1167 (C-O) cm^{-1} .

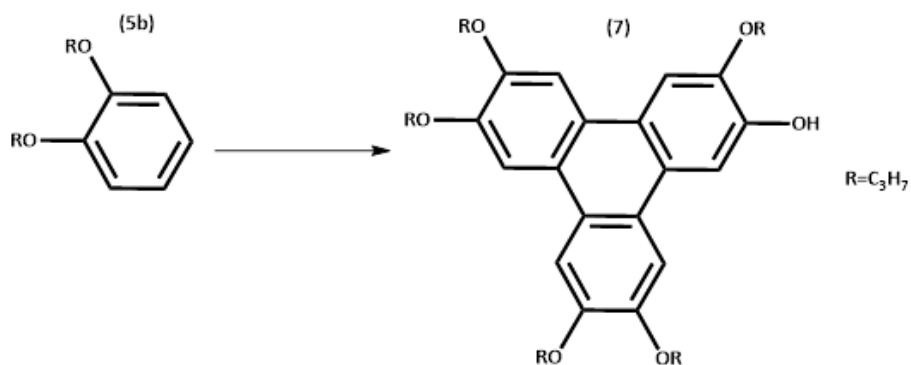


Figure B.2. Depiction of the reaction synthesis of 3,6,7,10,11-pentapropoxytriphenylen-2-ol (**7**).

A solution of **5b** (2.95 g; 15.2 mmol) in anhydrous dichloromethane (30 mL) and sulfuric acid (98% w/w; 0.1 mL) was charged to **5a-5c** anhydrous iron (iii) chloride (7.4 g; 46 mmol). The slurry was stirred under N_2 for 30 min. Ice-cold methanol (100 mL) was added slowly. Afterwards the slurry was cooled to $-10\text{ }^\circ\text{C}$ and left for 48 h. The slurry was filtered under vacuum and the resulting precipitate was washed with ice-cold methanol (5 x 40 mL) to afford a mixture of **7** as the minor product of **6b** as an off-white solid. The crude mixture was used with no further purification in the next step.

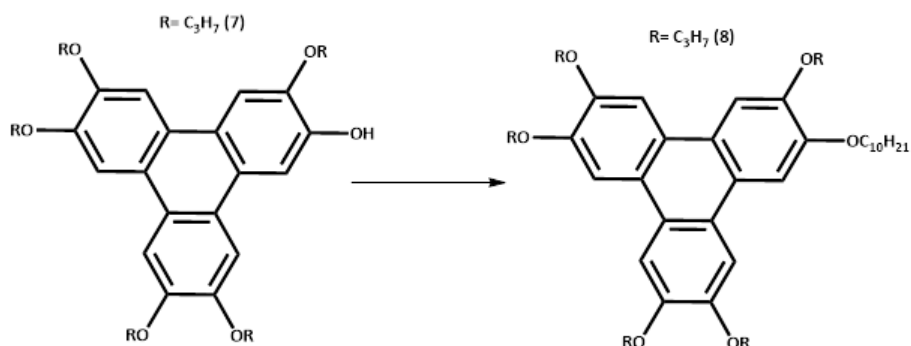


Figure B.3. Depiction of the reaction synthesis of 3,6,7,10,11-pentapropoxytriphenylen-2-ol (**7**) into 2-(decyloxy)-3,6,7,10,11-pentapropoxytriphenylene (**8**).

Appendices

Under atmospheric conditions a solution of **7** (150 mg; 0.28 mmol) in acetonitrile (20 mL) was stirred at room temperature for 20 min in a vessel fitted with a CaCl₂ drying tube. Potassium carbonate (77 mg; 0.56 mmol) and potassium iodide (16 mg; 0.10 mmol) was charged to the vessel and the resulting slurry was stirred for 15 min. The vessel was warmed to 40 °C. 1-bromodecane (71 µL; 0.336 mmol) was added *via* syringe to the mixture over a period of 10 min. The slurry was heated under reflux for 48 h. The reaction contents were cooled to room temperature. The slurry was filtered and the resulting solid was washed with CH₂Cl₂ (3 x 10 mL). The combined filtrates were washed with sodium hydroxide (20 mL; 1 M) followed by water (20 mL). The organic phase was dried with MgSO₄ and filtered. The filtrate was evaporated to dryness under reduced pressure and further purification using flash chromatography (silica, 99.5% *n*-hexane: 0.5% ethyl acetate) to afford **8** (45 mg; 23% yield) as a white solid.

- **¹H NMR** (300 MHz, CDCl₃) δ_H: 7.86 (6H, s), 4.22 (12H, t, *J* 6.6 Hz), 2.05-1.98 (12H, m), 1.65-1.58 (2H, m), 1.45-1.30 (12H, m), 1.16 (15H, t, *J* 7.4 Hz), 0.90 (3H, t, *J* 6.2 Hz) ppm.
- **¹³C NMR** (400 MHz, CDCl₃) δ_C: 149.3, 124.0, 107.9, 71.5, 70.1, 32.3, 30.0, 29.9, 29.9, 29.8, 29.7, 26.5, 23.2, 23.1, 14.4, 11.0 ppm.
- **MALDI⁺ *m/z***: 674.4 ([M]⁺ 100%).
- **IR Cn⁻¹** (neat): 2924w (C-H), 2851w (C-H), 1508m (benzene ring), 1431m (benzene ring), 1261s (C-O), 1168 (C-O) cm⁻¹

B.2. Synthesis of functional group model compounds

Under atmospheric conditions a solution of **1** (100 mg; 0.37 mmol), EDC (107 mg; 0.56 mmol), HOBt (60 mg; 0.44 mmol), 1-amino-octane (73 μ L; 0.44 mmol) and NMM (120 μ L; 1.11 mmol) in DMF (5 mL) was stirred at room temperature for 24 h.

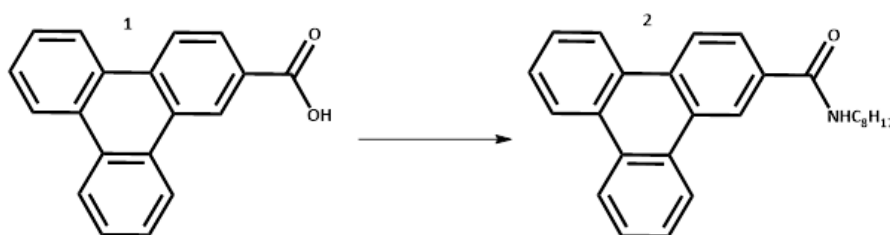


Figure B.4. Depiction of the reaction synthesis of N-octyltriphenylene-2-carboxamide (**2**).

The solution was diluted with EtOAc (20 mL), and washed with water (3 x 20 mL). The organic phase was evaporated to dryness and purified using column chromatography (*n*-hexane: EtOAc), providing a white solid 55 mg (39% yield).

- **$^1\text{H NMR}$** (300 MHz, CDCl_3) δ_{H} : 9.09 (1H, d, *J* 1.8 Hz), 8.72-8.69 (1H, m), 8.65-8.59 (4H, m), 6.41 (1H, exc), 3.59-3.52 (2H, m), 1.75-1.65 (4H, m), 1.43-1.30 (8H m), 0.91-0.87 (3H m) ppm.
- **$^{13}\text{C NMR}$** (400 MHz, CDCl_3) δ_{C} : 168.0, 133.4, 132.2, 130.6, 130.2, 130.0, 129.7, 129.3, 128.3, 128.9, 127.7, 125.9, 125.0, 124.0, 123.8, 123.7, 123.6, 123.1, 40.8, 30.2, 30.7, 30.2, 29.7, 29.6, 27.5, 23.0, 14.5 ppm.
- **ES⁺MS** *m/z*: 447.5 ($[\text{M}+\text{Na}+\text{MeCN}]^+$ 100%)
- **IR Cn^{-1}** (neat): 3296b (N-H), 2953w (C-H), 2921w (C-H), 2858w (C-H) 1631s (C=O), 1537s (C-C)

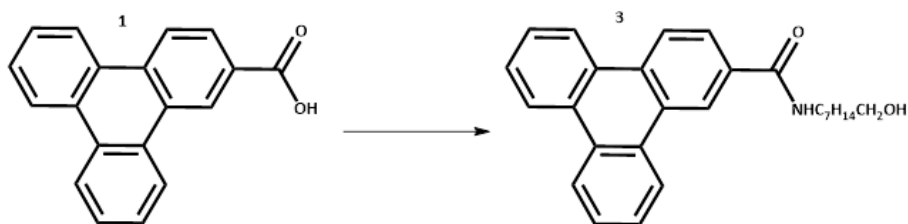


Figure B.5. Depiction of the reaction synthesis of N-(8-hydroxyoctyl)triphenylene-2-carboxamide (**3**)

Under atmospheric conditions a solution of **1** (100 mg; 0.37 mmol), EDC (107 mg; 0.56 mmol), HOBt (60 mg; 0.44 mmol), 8-amino-octan-1-ol (64 mg; 0.44 mmol) and NMM (120 μ L; 1.11 mmol) in DMF (5 mL) was stirred at room temperature for 24 h. The solution was diluted with EtOAc (20 mL) and washed NaHSO₃ (1 M: 10 mL) and then with water (3 x 20 mL). The organic phase was evaporated to dryness and purified using column chromatography (*n*-hexane: EtOAc) followed by recrystallization using EtOAc (2 mL) : *n*-hexane (20 mL). This provided **3** as a white solid 46 mg (31% yield).

- **¹H NMR** (300 MHz, CDCl₃) δ_{H} : 9.13 (1H, *d*, *J* 1.9 Hz), 8.77-8.74 (1H, *m*), 8.70-8.65 (4H, *m*), 7.95 (1H, *dd*, *J* 8.6, 1.8 Hz), 7.72-7.69 (4H, *m*), 6.34 (1H, *exc*), 3.65 (2H, *t*, *J* 6.5 Hz), 3.60-3.53 (2H, *m*), 1.73-1.66 (2H, *m*), 1.56 (6H, *m*), 1.38 (4H, *m*) ppm.
- **¹³C NMR** (400 MHz, (CD₃)₂SO) δ_{C} : 167.7, 135.2, 133.1, 131.7, 131.4, 131.1, 130.8, 130.6, 130.3, 129.8, 129.7, 128.3, 126.1, 125.8, 125.7, 124.2, 62.7, 34.5, 31.2, 30.9, 30.9, 28.6, ppm.
- **ES⁺MS** *m/z*: 422.2 ([M+Na]⁺ 100%)
- **IR Cn⁻¹** (neat): 3408b (N-H), 3081w (C-H), 2934w (C-H), 2858w (C-H) 1630s (C=O), 1532s (C-C) cm⁻¹.

Appendices

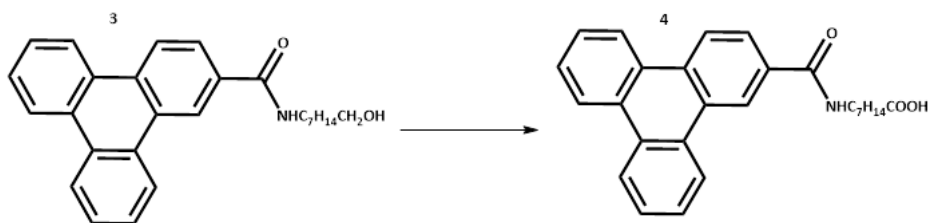


Figure B.6. Depiction of the reaction synthesis of 8-(triphenylene-2-carboxamido)octanoic acid (**4**).

A solution of **3** (50 mg; 0.13 mmol), periodic acid (95 mg; 0.42 mmol) and CrO_3 (5 mg; 0.05 mmol) in DMF (5 mL) were stirred for 1- 2 h. The solution was diluted with EtOAc (20 mL) and washed with water (3x 10 mL) followed by HCl (10 mL; 0.1 M). The organic phase was evaporated to dryness and purified by column chromatography (*n*-hexane: EtOAc) providing **4** as a white solid.).

- **$^1\text{H NMR}$** (300 MHz, $(\text{CD}_3)_2\text{SO}$) δ_{H} : 12.04, (1H, exc), 9.30 (1H, s), 8.97-8.85 (5H, m), 8.22 (1H, dd J 8.5, 1.6 Hz), 7.82-7.76 (4H, m), 3.44-3.38 (2H, m), 2.24 (2H, t, J 7.3 Hz) 1.65-1.54 (4H, m), 1.42-1.30 (6H, m) ppm.
- **$^{13}\text{C NMR}$** (400 MHz, $(\text{CD}_3)_2\text{SO}$) δ_{C} : 175.4, 166.6, 134.1, 132.0, 130.6, 130.3, 130.0, 129.7, 128.9, 128.7, 128.6, 127.2, 125.0, 124.7, 124.6, 123.1, 40.3, 34.6, 30.1, 29.5, 27.4, 25.4 ppm.
- **ES-MS** m/z : 412.2 ($[\text{M}]^-$ 100%);
- **IR** Cn^{-1} (neat): 3309b (N-H), 2921w (C-H), 2849w (C-H), 2638vw (O-H) 1698s (C=O), 1631s (C=O), 1536s (C-C) cm^{-1} .

Appendix C. DOSY NMR spectroscopy of triphenylene-cored model compounds in toluene

The aggregation characteristics of triphenylene-cored model compounds were further investigated by a collaboration with Dr Rob Evans in the Department of Physical Chemistry at Aston University, Birmingham, UK.

Appendices

DOSY NMR experiments in toluene were conducted on the TPN-C3 and TPN-C10 model compounds. No significant changes were observed in the diffusion coefficients over time (0-300 hours) and at different concentrations (0.1 – 10 mg/ml) of the TPN-C3 and TPN-C10 molecules dissolved in deuterated toluene. However, the diffusion coefficients are lower than expected for a single molecule, suggesting the existence of stable nanoaggregates (3-5 molecules/aggregate) in toluene. This data is consistent with the GROMACS simulations, which suggest the aggregation of these molecules, as well as helps to explain the hydrodynamic diameter of ~ 1 nm obtained by DLS measurement. Further DOSY NMR experiments are scheduled that will focus on the other model compound molecules in both toluene and *n*-heptane.

Appendix D. HTBHBC one pot synthesis

The synthesis of HTBHBC was carried out based on a previous procedure [298], by the group members of Prof William Kerr in the Department of Pure and Applied Chemistry, WestCHEM, University of Strathclyde, Glasgow, UK. Hexaphenylbenzene (HPB), 2-chloro-2-methylpropane (t-BuCl), anhydrous iron(III) chloride (FeCl₃), dichloromethane (DCM), methanol (MeOH), nitromethane (MeNO₂), petroleum ether, ethyl acetate purchased from Sigma-Aldrich (Dorset, UK) and used as received.

Appendices

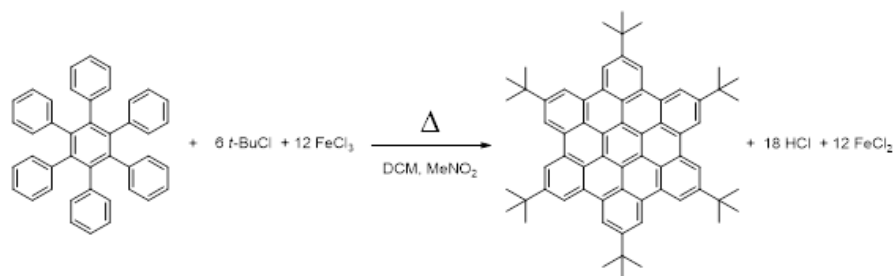


Figure D.7. Depiction of the reaction synthesis of the HPB (raw material) with *t*-BuCl and FeCl₃ to obtain the HTBHBC molecule.

Hexaphenylbenzene (HPB) was subjected to Friedel-Craft alkylation with 2-chloro-2-methylpropane (16 equivalents added compared to the 8 equivalents used by the reference [298], to increase the reactivity of the synthesis) to obtain the HTBHBC compound, based on the one-pot synthesis established by Rathore and Burns [298]. Anhydrous iron(III) chloride was used both as a Lewis acid and stoichiometric oxidant. A one-pot synthesis was performed in a 3-necked 250 mL round bottom flask, flame dried under vacuum, and set to cool under a blanket of argon. It was then filled with HPB (0.2 g, 0.374 mmol), *t*-BuCl (0.36 mL, 3.28 mmol) and dry DCM (12 mL), followed by FeCl₃ (1.213 g, 7.48 mmol) dissolved in 7.5 mL MeNO₂. The solution was heated to and kept at 40 °C for 2 h while a gentle stream of argon was bubbling through. The mixture was allowed to cool to room temperature in remaining solution (up to 9.6 g) of FeCl₃ was added to the flask. The mixture was stirred further for 3 hours, followed by introduction of 40 mL of cold (5°C) MeOH. The yellow precipitate obtained was filtered and washed with cold MeOH (20 mL x 2). The crude material obtained was further purified via flash chromatography (petroleum ether/ ethyl acetate 9:1) yielding 185 mg of a dark orange powder.